Investigations on the role of Cr, Mn and Ni on the formation, structure, and metastability of nitrogen-expanded austenite on Fe-based austenitic alloys under triode-plasma nitriding

A dissertation submitted in partial fulfilment of the requirements for the degree of Doctor of Philosophy

by

Xiao Tao

Supervisor: Dr A. Leyland, Prof. A. Matthews

Department of Materials Science and Engineering

University of Sheffield, UK

March 2018

Acknowledgement

First and foremost, I would express my sincere gratitude to my supervisors, Dr. Adrian Leyland and Prof. Allan Matthews for their generous guidance and invaluable supervision through this PhD study.

I would like to express my appreciation to my family and friends whose constant encouragement I have relied on throughout my study in Sheffield. I wholeheartedly thank to my parents and my wife, whose love and persistent confidence in me supported me during the years I have been working on this study.

My sincere thanks also goes to the experimental officers of electron microscopes, including Dr. Peter Korgul, Dr. Le Ma, Dr, Peng Zeng, and Dr. Cheryl Shaw from Sorby Centre, and Dr. Ian Ross from Department of Electronic and Electrical Engineering (EEE), for the generous supports and discussions with their expertise in electron microscopy.

I am also indebted to many of my colleagues and staffs who supported me throughout these years. I would also like to send great thanks to Dr. John Kavanagh for the training provided on triode-plasma PVD unit used in this work, to Mr. John Lowndes for the technical support and to Mr. Rhod Turner for his invaluable advice on plasma nitriding unit. Many thanks go Ms. Dawn Bussey for her assistance using nanoindentation and Mr. Michael Bell for his assistance on sample preparation.

I would also like to thank ATI Allvac (Sheffield) Ltd. for their kind provision of Staballoy AG17® alloy, NeoNickel (Blackburn) Ltd. for supply of RA 330® alloy and City Special Metals (Sheffield) Ltd. for supply of Invar 36® for this study.

My last gratitude goes to this broad, deep and diverse world, where I had a great time in my life, focusing on this research project.

Abstract

Thermochemical diffusion treatments (such as nitriding and carburising) are widely applied to metallic components to improve material surface hardness and wear/tribological performance. AISI 304 (Fe-18Cr-8Ni, in wt.%) and AISI 316 (Fe-18Cr-11Ni-3Mo, in wt.%) type ASS, as two of the most commonly used ASS, have been investigated extensively under low-temperature thermochemical diffusion treatments (e.g. < ~450°C for nitriding and < ~550°C for carburising). The unusual crystallographic structures – i.e. anisotropically-expanded austenite (or so-called S phase) − observed on ASS (or other alloys) under low-temperature thermochemical diffusion treatments and the remarkable enhancement of surface mechanical/tribological properties that these structures provided (without loss of corrosion resistance) led to a drive to try to understand their origin.

The principal aim of this study was to contribute to a roadmap for design of 'nitridable' austenitic alloys (capable of being nitrogen interstitially-supersaturated under low-temperature nitriding). The objectives were i) to study the nitrogen-expanded structure and decomposition of ASS with either high-Ni or high-Mn content (other than AISI 304 or 316 type ASS) after nitriding, ii) to access the performance of the nitrided ASS, and iii) to explore the possibility of nitrogen-supersaturation on Cr-free high-Ni or high-Mn austenitic steels under low-temperature nitriding. AISI 304 and four other selected steels (with different Ni/Mn level and with/without Cr) were triode-plasma nitrided under low (and close to monoenergetic) ion energy of ~200 eV at different temperatures for 4-20hrs. Auxiliary radiant heating was used to facilitate different treatment temperatures under a deliberately controlled substrate current density (e.g. at ~0.13 A/cm^2), in which case material surface crystallographic structure obtained under nitriding was mainly influenced by the different treatment temperatures and times applied.

Firstly, the role of SFE on the crystallographic structure and stability of γ_N has been revealed and discussed with the vastly available literature. At low treatment temperature (400°C), low SFE ASS (with high-Mn content) tended to exhibit superior nitrogen absorption and relative high lattice expansion, while high SFE ASS (with high-Ni content) tended to absorb less nitrogen – reaching a saturated lattice expansion quite quickly during treatment. Dislocation dissociation and dislocation glide were proposed and discussed for the different plastic deformation structures observed. Nevertheless, at elevated treatment temperatures (425 and 450°C), lattice instabilities (SFs and SF-associated local lattice distortions) developed on the low SFE alloy under nitrogen 'over-supersaturation', tending to accelerate the decomposition of γ_N, while low SF density (or SF-free) γ_N developed on high SFE ASS, tending to exhibit relatively sluggish decomposition. Secondly, the wear and corrosion performance of the nitrided high-Mn/Ni ASS were investigated. The surface hardened ASS after low-temperature TPN exhibited superior wear performance under dry sliding condition owing to enhanced load-bearing capacity and reduced adhesive wear, but not under selected wet SiC slurry abrasive wear conditions potentially owing to layer brittleness and insufficient layer thickness under the selected nitriding parameters. Improved corrosion performance was observed for ASS under nitrogen-supersaturation and loss of corrosion resistance was evident after CrN formation in γ_N. Last but not the lease, the necessity of Cr in substrate alloy on the formation of γ_N after nitriding has been demonstrated. Formation of iron nitrides (rather than γ_N) was evident on both of the Cr-free austenitic steels (Invar and Hadfield steel) under TPN at selected low treatment temperatures, which indicates that nitride-forming elements (such as Cr) played an important role in the formation of expanded austenite.

Table of Contents

List of acronyms and abbreviations

ASS(s): austenitic stainless steel(s)

AG17: Staballoy AG17 ®

BCC: body-centred cubic

BCT: body-centred tetragonal

BF-TEM: bright-field transmission electron microscopy

BSE: back-scattered electron microscopy

DC: direct current

DF-TEM: dark-field transmission electron microscopy

EDP: electron diffraction pattern

EDX: energy dispersive x-ray spectroscopy

FCC: face-centred cubic

HAD: Hadfield steel

HCP: hexagonal-closed packed

HR-TEM: high-resolution transmission electron microscopy

Invar: Invar 36®

GAXRD: grazing angle x-ray diffraction

OCP: open circuit potential

OM: optical microscopy

PVD: physical vapour deposition

SEM: scanning electron microscopy

SF: stacking fault

TEM: transition electron microscopy

TPN: triode-plasma nitriding

XRD: X-ray diffraction

$\gamma(N)/\gamma(C)$: nitrogen/carbon solid solution in austenite

γ_N/γ_c: nitrogen/carbon stabilised expanded austenite

I_{corr}: Tafel current density

E_{corr}: Tafel potential

E_{pit}: critical pitting potential

304: AISI 304

List of Figures

List of Tables

1 Introduction

After the pioneering work by Adolph Machlet and Dr. Adolf Fry in the early 20th century [1, 2], nitriding techniques have been developed for various metallic materials, providing beneficial enhancements in material mechanical/tribological performance after treatment. The interaction of nitrogen with different alloy compositions after nitriding has been investigated as early as in 1921, when Fry [2] indicated a "special increase of hardness" of alloyed steels (i.e. with additions of Al, Cr, Mn and Si to a few weight percent) after gaseous nitriding − and led to the development of a specific group of low alloy nitriding steels (i.e. 'Nitralloy') for Krupp Steel [3]. The presence of nitride-forming elements such as Cr, Ti, V, Al and Zr in steel accelerates the interstitial diffusion of N and leads to formation of hard nitrides.

Austenitic stainless steel (ASS), as the most commonly used group of stainless steels nowadays, is undoubtedly an important material class. However, the low hardness and poor wear performance of ASS [4] limits their tribological applications. Nitriding of ASS has been investigated as a potential solution to improve material surface hardness and wear performance. However, nitriding processes that were carried out at conventional treatment temperatures (e.g. plasma nitriding at ~570°C [5], above ~500°C [6] and gaseous nitriding at ~585°C [7]) resulted in formation of chromium nitride precipitates on the ASS surfaces being treated, which degraded material corrosion performance and limited the application of this technique on stainless steels. Nevertheless, from the mid-1980s, an intriguing 'new' surface structure was identified at the surface of ASS after plasma nitriding at ~400°C, providing good surface wear performance without the loss of corrosion resistance [5, 8]. At low treatment temperatures, the parent austenitic lattice is able to accommodate enormous amounts of interstitial nitrogen without the formation of chromium nitrides (and therefore no localised Cr depletion that could damage the corrosion resistance).

This interstitially supersaturated structure is now commonly referred to as 'expanded austenite' [9], which describes a metastable, anisotropically expanded FCC austenite − generated under 'paraequilibrium' conditions − at low temperatures and (typically) over long timescales far from thermodynamic equilibrium. This surface structure was also evident on ASS after carburising, nitrocarburising and carbonitriding at low treatment temperatures [10]. Fundamentally, the FCC lattice expands in accordance with extreme supersaturation of interstitial elements, where their reported 'paraequilibium' solubility after thermochemical treatments was extremely high (i.e. colossal amount) as compared to their equilibrium solubility in ASS (e.g. up to ~19 at.% C [11] or ~38 at.% N [12] at paraequilibrium after carburising or nitriding, respectively, compared to < 0.015 at.% C [13] and <0.65 at.% N [10] at thermodynamic equilibrium in AISI 316 type ASS). Under paraequilibium conditions, there is no phase transformation of the modified (anisotropically expanded) austenitic lattice [10, 14, 15]; nevertheless, phase decomposition occurs eventually with chromium nitride/carbide formation, either after prolonged treatment or at elevated temperature, which leads to Cr-depletion adjacent to the grain boundaries − and thereby deteriorates alloy corrosion resistance [16-19].

1.1 Research objectives strategy

As will be described later in a literature review of expanded austenite (**Section 2.3**, **Chapter 3**), AISI 304 (i.e. Fe-18Cr-8Ni, in wt.%) and AISI 316 (i.e. Fe-18Cr-11Ni-3Mo, in wt.%) ASS were investigated extensively after low-temperature thermochemical diffusion treatment such as nitriding. Given the colossal interstitial content in expanded austenite and the low equilibrium solubility of interstitial elements (e.g. C and N) in commercial ASS, the pre-existing interstitial content in the unmodified stainless steel substrates should have limited influences on determining the interstitial-introduced lattice expansion and decomposition

during low-temperature thermochemical diffusion treatments. However, considering the large atomic percentage of substitutional elements in the FCC lattice, substitutional alloying elements (such as Cr, Mn and Ni) in ASS should be able to influence the formation, structure and decomposition of expanded austenite synthesised after low temperature thermochemical diffusion treatments.

Whereas (historically) significant effort has been expended in designing "nitridable" ferritic alloys for commercial applications, little or no effort has been made to develop analogous austenitic grades amendable to low-temperature plasma diffusion treatment − due in no small part to the sheer complexity of the chemical composition-dependent issues which the metallurgical behaviour of an elastically anisotropic parent lattice (with strong composition-dependent strain behaviour and lattice instability) introduces. This study takes several tentative steps towards improved material selection criteria − and a basic design methodology − for developing improved 'nitridable' austenitic engineering alloys for specific applications, as follows:

i) The role of substitutional Ni or Mn on lattice expansion and decomposition of ASS upon nitrogen diffusion treatments
ii) The material performance of ASS after nitriding treatments
iii) The role of Cr on the formation of expanded austenite and structure-property evolution of austenitic steels after low temperature nitriding

Five commercial austenitic steels were selected with respect to their Cr, Mn and Ni content as shown in **Fig. 1.1**. To elucidate the role of Cr and Mn/Ni on the formation of expanded austenite, alloy compositions could be divided into two groups for comparison, as highlighted

in **Fig. 1.1**, i.e. i) ASS having similar level of Cr (17-19 wt.%) but different Ni/Mn content, and ii) austenitic steels having similar content of Ni (~35-36 wt.%) with/without Cr. Additionally, an austenitic manganese steel (Hadfield steel) was also selected to explore the possibility of γ_N formation in high-Mn steel after low temperature nitriding.

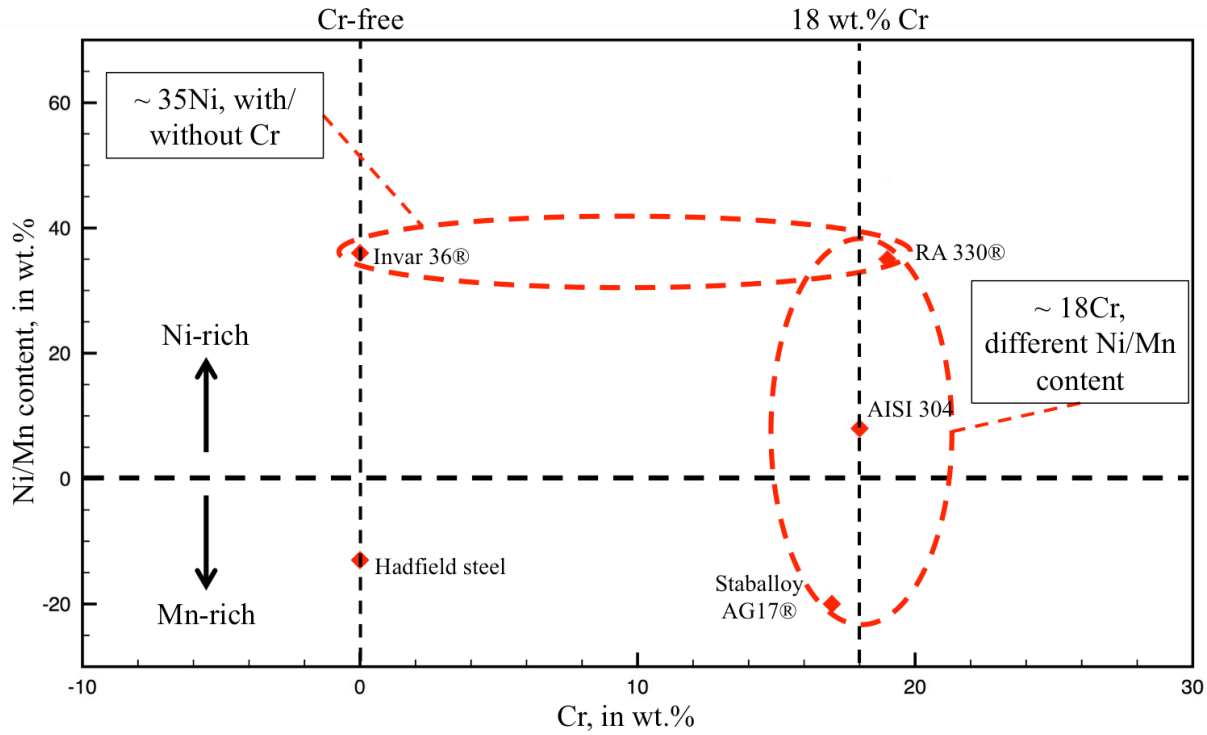

Fig. 1.1 Illustration of material selection criteria based on Cr, Ni and Mn content

The selected steels were all plasma nitrided at low ion energy (and near mono-energetic at ~200 eV) under a low-pressure triode-plasma configuration [20-23]. Enabled with an additional electron emitter, cathode current density was deliberately controlled and kept nearly constant at a rather low value for the nitriding processes at temperatures from 400 to 450°C. Under the deliberately controlled low cathode current density, plasma heating alone was insufficient to achieve and maintain the selected treatment temperatures (at 400-450°C), in which case auxiliary radiant heating was used together with plasma heating. Noticeably, the nitriding unit used was fully capably to achieve treatment temperatures above 450°C

using plasma heating alone, the auxiliary radiant heating used was for comparison reasons (rather than achieving the best process efficiency), in which case the material surface nitrogen absorption and crystal structure evolution under TPN was mainly as a result of the different treatment temperatures and times employed, rather than a result from different plasma current densities. Differently, during nitriding processes at a rather low treatment temperature of 300°C (for Hadfield steel), plasma heating was used (without radiant heating) to achieve maximum ion bombardment under the selected low treatment temperature. After the inward diffusion of nitrogen at these selected treatment temperatures for 4-20hrs, the surface crystallographic structure, hardness and the performances were investigated.

1.2 Thesis structure

After this introduction, **Chapter 2** provides background information of this study, covering nitriding techniques, Fe-N phase diagram and a literature review of expanded austenite. Experimental procedures are given in **Chapter 3**. Experimental results are presented and discussed in **Chapter 4-6**. Conclusions and recommendations for studies in the future are drawn at the end of this thesis.

Chapter 4 presents a study mainly on the crystal structure of a high-Mn and a high-Ni ASS (i.e. Fe-17Cr-20Mn-0.5N and Fe-19Cr-35Ni, respectively, in wt.%) after TPN at 400-450°C for 4hrs and 20hrs. For comparison, AISI 304 ASS was also investigated after TPN at selected equivalent conditions. Both lattice supersaturation and decomposition are achieved and investigated. The crystallographic structure of the surface layers generated within the selected temperature/time envelope is discussed mainly with XRD and TEM observations.

After the investigations on the crystallographic structure of three ASS under TPN in **Chapter 4**, **Chapter 5** discusses material performance before and after treatment. The wear performance of untreated and 400°C 20hrs nitrided ASS (i.e. without nitride formation) are investigated under sliding/abrasion wear conditions. The corrosion performance of ASS is investigated before TPN, after TPN at 400°C for 20hrs and after TPN at 450°C for 20hrs (i.e. polished untreated samples, CrN-free nitrided samples and CrN-containing nitrided samples, respectively).

Chapter 6 includes studies on two Cr-free austenitic steels after TPN, attempting to explore the possibility of nitrogen-supersaturation in high-Ni and high-Mn steels. This chapter focuses on the structure of the treated surface, where no evidence in the formation of γ_N was observed. The wear and corrosion performance of treated surfaces were not investigated, since the scope of this study was typically on nitrogen-expanded austenite. In the first part of this chapter, high-Ni Invar alloy (i.e. Fe-35Ni, in wt.%) is compared to high-Ni alloy 330 ASS (i.e. Fe-19Cr-35Ni, in wt.%) after TPN at 400-450°C. The role of Cr in the surface structures formed after nitriding is discussed with the XRD and TEM analysis and material hardness-depth profiles. In the second part of this chapter, plasma nitrided Hadfield steel (Fe-13Mn-1.2C, in wt.%) samples are investigated via XRD and indentation hardness measurements.

2 Background

Nitriding, as a thermochemical diffusion treatment developed initially for alloy steels, involves i) heat-treating of materials in nitrogen-bearing media (**Section 2.1**) and ii) diffusion and absorption of nitrogen at the material surface that leads to metallurgical phase transformations (**Section 2.2**). Nitrogen-expanded austenite, as an 'unusual' crystallographic structure obtained under nitrogen-supersaturation at low treatment temperatures, was first identified on ASS after low-temperature plasma nitriding from the 1980s [5, 8] and has been the subject of extensive research interest since then. A literature review on expanded austenite is given in **Section 2.3**.

2.1 Nitriding techniques

This section covers nitriding techniques, including brief introductions on nitriding techniques with respect to different nitrogen-bearing media (**Section 2.1.1**), some physics background for vacuum direct current (DC) glow discharge plasma (**Section 2.2.2**), and discussions of the triode-plasma nitriding (hot-filament electron-emission intensified plasma) technique adopted in this study (**Section 2.1.3**).

2.1.1 Three main nitriding techniques

2.1.1.1 Gaseous nitriding

The development of the nitriding process can be traced back to the early 1900s, when Adolph Machlet (U.S) in 1907 firstly developed and patented a gaseous nitriding process (using ammonia and hydrogen) on red-hot plain iron and low carbon steel, which generated a hard rust-preventing "silvery casing" [1]. In 1921, Dr. Adolf Fry (Germany) patented a surface hardening technique applied at approximately 580°C using a flow of ammonia for steel alloys [2]. During gaseous nitriding, materials are heated in a retort under a flow of nitrogen-bearing

gas (usually a gas mixture of ammonia and hydrogen). At elevated temperature, thermally catalytic dissociation of ammonia occurs as follows [3, 24, 25]:

$$2NH_3 \leftrightarrow N_2 + 3H_2$$

Nascent nitrogen is released through a gas-solid reaction at the metallic workpiece surface [25]:

$$\frac{1}{2}N_2 \leftrightarrows N$$

A key gaseous nitriding process parameter – the so-called nitriding potential, r_N (bar$^{-1/2}$) – describes the 'nitridability' of the gaseous atmosphere, as determined by following equation [3, 24, 25]:

$$r_N = \frac{pNH_3}{p^{3/2}H_2}$$

where pNH_3 is the partial pressure of ammonia (bar) and $p^{3/2}H_2$ is the partial pressure of hydrogen (bar$^{3/2}$). Via altering gas compositions and total pressure at constant treatment temperature, different nitrogen supply rates (to workpiece surfaces) could be achieved (see Ref. [25] for details of the gaseous process). It was therefore argued that, unlike liquid and ion nitriding, gaseous nitriding offers good control of layer composition and microstructure [25].

2.1.1.2 Liquid nitriding/nitrocarburising

Compared to gas-solid reactions, the liquid-solid reaction was thought to offer more uniform chemical exchange at the workpiece surface and led to research on liquid nitriding shortly after the invention of gaseous nitriding [3]. A process named Tufftride was introduced and gained popularity from the 1950s [3]. Workpieces are usually immersed in a hot bath of molten salts. Compared to gaseous or ion nitriding, liquid nitriding has several advantages, i). low cost in operation and maintenance, ii). easiness of operation, and iii). less spacious

equipment [3]. Nevertheless, the cyanides used during the process impose operational and disposal hazards [3, 26, 27]. Wastewater (i.e. predominantly iron cyanide complexes) from liquid nitriding processes needed to be neutralised to reduce pollution and meet environmental regulations, which increased the total cost and limited the application of liquid nitriding techniques.

Nevertheless, cyanide-free liquid nitriding was developed and widely used in industries [27], such as the Melonite® process. This process, which was first patented in 1977, enabled liquid nitriding using salt compositions of cyanates and carbonates [28]. Both Tufftride® and Melonite® are currently registered trademarks of Durferrit GmbH and widely used in heat treatment and surface engineering industries. Noticeably, both Tufftride® and Melonite® process are nitrocarburising treatments, where both nitrogen and carbon are released in the liquid salt bath medium and diffuse into the immersed workpiece. In a modern system (e.g. Melonite® Process), the molten salt can be aerated and a catalytic reaction occurs to release nascent nitrogen and carbon monoxide, as shown in following reactions [24]:

$$2NCO^- + O^2 \rightarrow CO_3^{2-} + CO + 2N$$

$$3NCO^- \rightarrow CO_3^{2-} + CN^- + 2N + C$$

$$4NCO^- \rightarrow CO_3^{2-} + CO + 2CN^- + 2N$$

2.1.1.3 Plasma nitriding

Plasma nitriding was first investigated by Wehnheldt [29], but the first plasma nitriding process was developed and patented by Dr. Bernhard Berghaus in the 1930s as an alternative to gaseous nitriding [30, 31]. The workpiece is usually biased negatively in a gas mixture of nitrogen (or ammonia) and argon (or hydrogen). The working chamber is normally evacuated to low pressure (e.g. ~500 Pa) and gaseous molecules are ionised [3]. Ions are driven towards

workpiece surface under an applied electrical potential. Further discussions will be given in **Section 2.1.2** and **Section 2.1.3**. Plasma-based techniques enable nitriding using inert nitrogen-bearing media (such as nitrogen, argon or hydrogen) rather than the more chemically reactive ones (such as ammonia and cyanide), which dramatically reduces process hazards [3, 29]. Most of the current plasma nitriding equipment offers computer monitoring/control, which leads to good treatment quality and reproducibility. The operation cost is much lower due to small gas and energy consumption [3, 29]. However, plasma nitriding techniques require large initial capital for equipment in association with vacuum system and plasma generation, monitoring and control [24].

2.1.2 Vacuum and glow-discharge plasma

Plasma, as the fourth state of matter (after solid, liquid and gas) was firstly identified as 'radiant matter' by William Crookes in 1879 and named as 'plasma' by Irvine Langmuir in 1923 [32]. Essentially, plasma is (partially) ionised gas − a mixture of randomly moving electrons, ions and neutrals (and photons, X-ray…) − which is electrically neutral as a whole but highly conductive [33-35]. A plasma state requires charge separation, which could be achieved simply by thermally heating substances to several thousands of Kelvin (e.g. ~4000 K for cesium) as shown in **Fig. 2.1**, but it is impractical to generate plasma simply by heating since not many solid materials could withstand such high temperatures [34, 35]. One simple way of generating plasma is via application of DC potential between two metallic plates in vacuum (i.e. a low pressure gas), which could be referred to as cold plasma [32-36]. In **Section 2.1.2.1**, several concepts and terms in kinetic theory of gas are introduced to depict the equilibrium gaseous condition. Then, in **Section 2.1.2.2**, the physics for plasma generation is introduced.

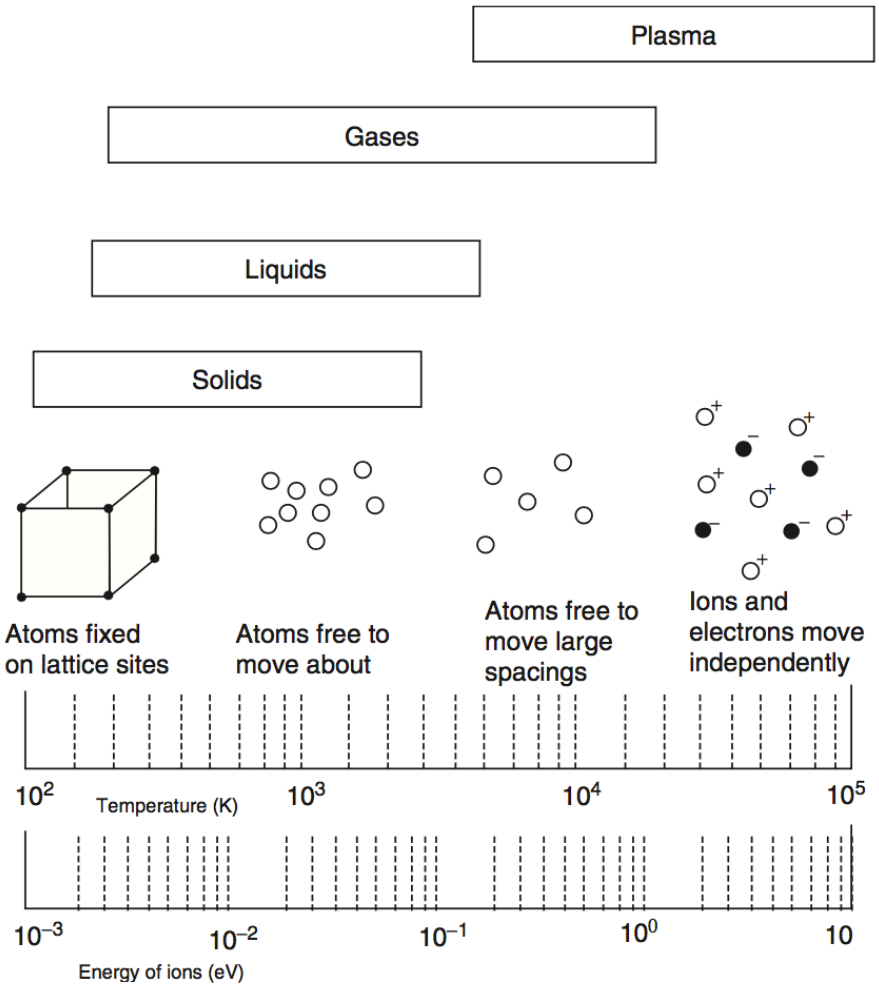

Fig. 2.1 State of matter as a function of temperature (reproduced from Ref. [34])

2.1.2.1 Vacuum and kinetic theories of gas

Several gaseous terms will be introduced, including the number of molecules (N), kinetic energy of each molecule (KE), molecular speeds (μ and μ_{RMS}**)**, thermal impingement rate of molecules onto heterogeneous surfaces (Φ**)**, mean free path (λ**)** and collision frequency (υ). These terms are commented on and calculated with respect to variations in pressure and/or temperature, as tabulated in **Table 2.2**.

Consider an isolated chamber of volume, V (m^3), filled with gas at a temperature, T (K), the gas inside could be observed as a group of randomly moving molecules, which exert a net pressure, P (Pa), on the interior walls of chamber. Assuming the internal energy of a gas is composed of kinetic energy, the ideal gas law applies as follows:

$$\boldsymbol{PV = Nk_BT} \quad \textbf{Equation 2.1}$$

where k_B is Boltzmann constant (i.e. ~1.38×10^{-23} kg m^2/s^2 K), T is temperature (K), and N is number of molecules. The speed of molecules in gas could be described by the Maxwell-Boltzmann distribution [37-39]. The mean kinetic energy per molecules, KE (J), is a function of temperature:

$$\boldsymbol{KE = \frac{3}{2}k_BT} \quad \textbf{Equation 2.2}$$

Assuming a particle of mass, m (kg), its average speed, μ (m/s), and root mean square speed, μ_{RMS} (m/s), could be derived as a function of temperature and mass as follows:

$$\boldsymbol{\mu = \sqrt{\frac{8k_BT}{m\pi}}} \quad \textbf{and} \quad \boldsymbol{\mu_{RMS} = \sqrt{\frac{3k_BT}{m}}} \quad \textbf{Equation 2.3}$$

Using the average speed of μ, the impingement rate of gaseous molecules onto a solid surface, Φ (molecules/m^2 s), could be derived [40]:

$$\boldsymbol{\Phi = \frac{P}{\sqrt{2\pi mk_BT}}} \quad \textbf{Equation 2.4}$$

The above equations facilitate numerical descriptions of the equilibrium gaseous state in a vacuum chamber before/during TPN. If this chamber is 1 m^3 and is filled with gaseous nitrogen at 101 kPa (atmospheric pressure) and 300 K (room temperature), there are 2.4×10^{25} nitrogen molecules in the chamber and each molecule has a kinetic energy of 6.2×10^{-21} J (i.e. ~0.04 eV). Taking the atomic mass of N as 14 g/mol (so m = 4.65×10^{-26} kg for N_2), the mean and root mean square speed of N_2 molecule are ~416 m/s and ~517 m/s, respectively. Every

second inside this chamber, each face of the interior wall (in a cubic chamber of 1 m^3) is bombarded with ~2.9×10^{27} nitrogen molecules.

If this isolated chamber is now connected to a working vacuum pump, practically it would reach a pressure lower than atmospheric pressure of 101 kPa. This state is referred to as vacuum. Other non-SI units might be used, as shown at atmospheric pressure in **Table 2.1**. If pressure drops to 0.4 Pa at room temperature, the number of N_2 molecules reduces to ~9.7×10^{19}, whilst the energy and speeds of the molecules remain unchanged.

Table 2.1 Pressure units at atmospheric pressure

Atmospheres	Pascal	Torr	Bar	Pound/square inch
1 atm	101325 Pa	760 Torr (mmHg)	1.01325 bar	14.6959 psi

Since the total number of molecules decreases, each molecule in chamber has more space to move around. The molecular interactions need more comments here. Gaseous molecules collide elastically with each other that direction of motion changes randomly with a 'zigzag' shape [34, 35]. The probability of a collision is referred to as the collision cross-section, σ (m^{-2}). Collision mean free path, λ (m), could be defined as the average distance that a molecule is able to travel without collision [41]. The mean free path of monomolecular N_2 in the vacuum chamber could be describe using the following equation [34]:

$$\boldsymbol{\lambda = \frac{1}{n\sigma} = \frac{k_B T}{\sqrt{2}\pi P d^2}} \quad \textbf{Equation 2.5}$$

where n is the number density of particles (m^{-3}), σ is the collision cross-section (m^2), and d is the diameter of molecule (m). The collision frequency of molecules, υ (s^{-1}), could be obtained from average speed and mean free path [34]:

$$\upsilon = \frac{\mu}{\lambda} \qquad \textbf{Equation 2.6}$$

Therefore, when pressure decreases from 101325 Pa to 0.4 Pa, taking 375 pm as diameter of N_2 molecule [42], mean free path increases dramatically from ~65.4 nm to ~16.6 mm and collision frequency reduces from ~7.3×10^9 s^{-1} to ~2.5×10^4 s^{-1}.

Furthermore, if the temperature rises to 700 K (and assuming that the chamber pressure remains at 0.4 Pa), the gaseous condition could be predicted similarly with above equations, with calculated values tabulated in **Table 2.2**.

Table 2.2 Equilibrium gaseous state of nitrogen in a 1 m^3 chamber

Temperature and pressure	N	KE, eV	μ, m/s	μ_{RMS}, m/s	Φ, $m^{-2}s^{-1}$	λ, mm	υ, s^{-1}
101 kPa, 300 K	2.4×10^{25}	0.04	476	517	2.9×10^{27}	0.065	7.3×10^9
0.4 Pa, 300 K	9.7×10^{19}	0.04	476	517	1.1×10^{22}	16.6	2.9×10^4
0.4 Pa, 700 K	4.1×10^{19}	0.09	727	789	7.5×10^{21}	38.7	1.9×10^4

In case of gas mixture (e.g. N_2:Ar ratio at 7:3) used, owing to Penning effect (viz. increase in effective ionisation rate or decrease in breakdown voltage of gas due to presence of a small number of foreign atoms), during plasma nitriding, Dalton's Law applies:

$$P = P_1 + P_2 = N_1 k_B T + N_2 k_B T$$

where N_1, N_2 are the numbers of each molecule and P_1, P_2 are the partial pressures for each type of molecule. Thus, there were ~2.9×10^{19} N_2 molecules and ~1.2×10^{19} Ar molecules at 0.4 Pa 700 K. For such binary gas mixture, the following equation could be used to determine mean free path [43]:

$$\boldsymbol{\lambda_1 = \frac{1}{\pi(d_1/2+d_2/2)^2 N_2}\sqrt{\frac{M_2}{M_1+M_2}}} \quad \textbf{and} \quad \boldsymbol{\lambda_2 = \frac{1}{\pi(d_1/2+d_2/2)^2 N_1}\sqrt{\frac{M_1}{M_1+M_2}}} \qquad \textbf{Equation 2.7}$$

where λ_1 (m) and λ_1 (m) are mean free path for each molecules; d_1 (m) and d_2 (m) are diameter of each molecules; M_1 (kg) and M_2 (kg) are molar weight of each molecules; N_1 and N_2 are the number of each molecules. Taking ~342 pm and ~375 pm as the molecular diameter of Ar and N_2 [42], Mean free path of Ar and N_2 in a 7:3 volumetric ratio at 0.4 Pa, 700 K could be estimated as ~38.2 mm and ~13.7 mm, respectively.

2.1.2.2 DC glow discharge plasma

As elucidated in the section above, the impingement rate of neutral (onto workpiece surface) is enormous even in vacuum (e.g. ~7.5×10^{21} $m^{-2}s^{-1}$ for pure nitrogen gas at 0.4 Pa, 700 K). However, the thermal energies carried by neutrals (e.g. ~0.09 eV at 700 K), which are negligible compared to ion energy during plasma nitriding (e.g. ~200 eV during TPN), are insufficient for nitriding process. In a typical 'diode' DC plasma configuration, workpiece is biased negatively at (normally) >1 kV. This applied potential in conventional DC plasma is essential for plasma generation.

Consider two parallel metallic plates (with flat face facing each other) inside the abovementioned vacuum chamber, plasma could be generated via applying direct current potentials between two plates (electrodes), which is normally referred to as DC plasma and exhibit characteristics as shown in **Fig. 2.2**. Positively charged nitrogenous ions are driven to cathode and electrons to anode. With respect to current densities and potentials between two electrodes, **Fig. 2.2** could be divided into dark current region (i.e. before D), glow discharge region (i.e. D to G) and arc discharge (i.e. after G).

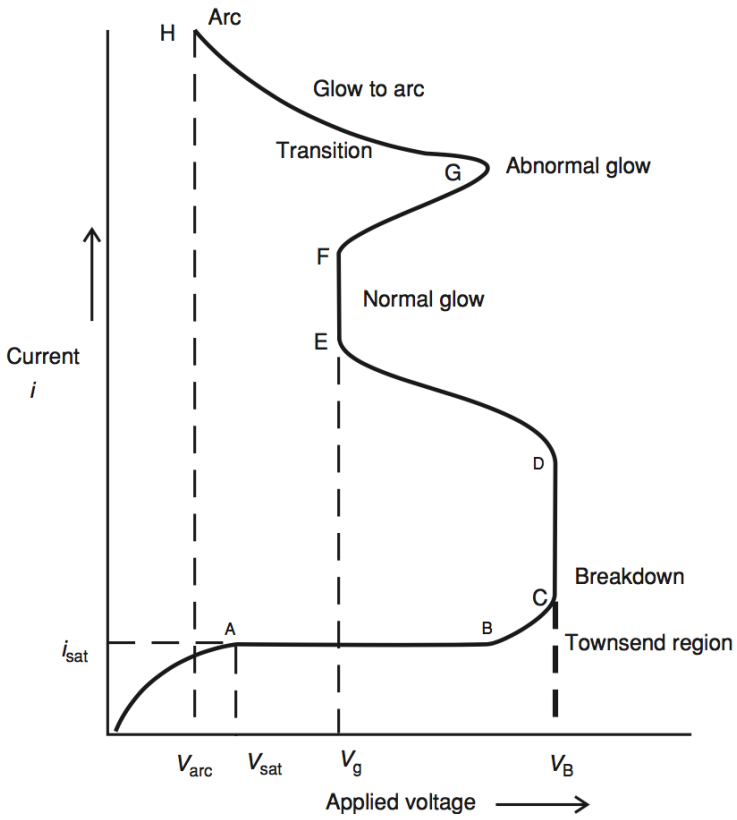

Fig. 2.2 Inter-electrode current verses inter-electrode potential for DC discharge (reproduced from Ref. [34])

If the potential between plates (i.e. inter-electrode potential) is increased slowly from zero, there will initially be a very small inter-electrode current, which will soon reach saturation at i_{sat}. In this stage, the small current corresponds to the migration of the small number of charge carriers, which are generated under background radiation (e.g. cosmic radiation, natural radioactivity and ultraviolet radiation) [34]. The applied potential is insufficient for ionisation. If potential is further increased (beyond point B, **Fig. 2.2**), electrons start to gain energy to interact with neutrals through inelastic collision. Neutrals are ionised liberating extra electrons, which in turn ionise neutrals under the applied electric field, releasing more electrons (i.e. multiplication of electrons) that leads to exponential increase of current.

Under excitation collision beyond breakdown voltage (at point D in **Fig. 2.2**), plasma becomes luminous. Ions start to strike rapidly (and glow) at small regions of cathode surface [34]. The conductivity of gas between two electrodes increases rapidly so that the inter-electrode voltage drops with the increase of current. The ionised gas becomes "negatively resistant", as compared to the external circuit of power supply. The strikes of energetic ions onto cathode (e.g. workpiece) lead to emission of secondary electrons from cathode surface [34], which are repelled from cathode to plasma – contributing to further ionisation in plasma and secondary electron emission at cathode surface. Eventually, plasma becomes self-sustaining at a voltage of V_g (point E, **Fig. 2.2**), which is lower than the breakdown voltage. The glow area at cathode surface enlarges with the increase of total applied electrical power until it covers entire cathode (at point F, **Fig. 2.2**). In the abnormal glow region beyond point F, ionic bombardment occurs over the entire cathode surface, where inter-electrode current increases with inter-electrode voltage. Glow-discharge plasma nitriding is carried out in this region. Additionally, glow discharge transits to arc discharge at the upper end of abnormal glow region, where the cathode carries very high current densities and is heated up consequently to temperatures sufficiently high for thermionic electron emission [34]. Inter-electrode voltage decreases further with increase of current in this region.

2.1.3 Triode plasma fundamentals and configurations

In a conventional DC plasma, the workpiece is usually biased negatively at ≥1 kV in a 0.1-1 kPa chamber (cathode), where the chamber wall is coupled to earth (anode). Different to conventional diode DC plasma, triode plasma involves an extra independent (thermionic) electron emission system, which is a self-circuited and biased (hot) tungsten filament. As will be shown in the following discussions, the ionic bombardment becomes more "efficient" in triode plasma, as compared to the conventional DC plasma.

2.1.3.1 Cathode sheath

Due to the difference in mass and size between electrons and ions (i.e. $m_e << m_{ion}$, m denotes mass; and $d_e << d_{ion}$, d denotes size), electrons travel faster than ions in plasma. Plasma itself is electrically neutral (i.e. $N_e = N_{ion}$, N denotes number of species) that there are equal number of electrons and ions in plasma. Consider a metallic solid surface exposed to plasma; the solid surface receive more electrons than ions in a unit time, which consequently possess a floating potential of V_f (V) that is relatively negative to the plasma potential of V_p (V). There naturally forms a sheath, across which cations are accelerated (and electrons flux is reduced), above the solid surface in plasma. The sheath potential is given by [34]:

$$V_p - V_f = \frac{k_B T}{2e} \ln\left(\frac{m_i T_e}{m_e T_i}\right) \quad \textbf{Equation 2.8}$$

where T_e (K) and T_i (K) are temperature of electron and ion, respectively; m_e (kg) and m_i (kg) are mass of electron and ion, respectively; e is electronic charge (i.e. 1.6×10^{-19} C). Such sheath still exists on top of cathode and anode during nitriding process. If anode (e.g. chamber wall) is grounded (i.e. $V_{anode} = V_f = 0$ V), V_p can be estimated using **Eq. 2.8** (e.g. 0-10V for DC argon discharge [44]). Considering the several hundreds of Volts applied on the cathode during nitriding, V_p appears negligible and the cathode potential, V_c (V), can be considered equivalent to the applied bias potential.

If one assumes an ion being accelerated with zero initial energy from the plasma side of the cathode sheath towards the cathode, the cathode sheath thickness, *L* (m), could be evaluated from the Child-Langmuir equation of cathode free-fall [20, 45, 46]:

$$L = \left(\frac{4\varepsilon_0}{9J}\right)^{1/2} \left(\frac{2q}{m_{ion}}\right)^{1/4} V_c^{3/4} \quad \textbf{Equation 2.9}$$

where ε_0 is permittivity of free space (i.e. $\sim 8.85 \times 10^{-12}$ s^4 A^2/m^3 kg); J is current density (A/m^2); q (A/s) is the ionic charge; m_{ion} (kg) is the ion mass. This equation also assumes, i)

one flat cathode surface with an infinite exposure area in plasma, and ii) one type of cation in plasma [44].

2.1.3.2 Energy distribution of ions

In the cathode sheath, ions inevitably collide with neutrals, for example, through symmetrical charge exchange collision [47], $M^+_{fast} + M_{slow} \rightarrow M_{fast} + M^+_{slow}$. The kinetic energy of ions (given under the applied potential) is consumed via collision with neutrals on their path towards the cathode. The energy distribution of incident ions is associated with such collisions between ions and neutrals in cathode sheath. The relative energy distribution of incident ions could be estimated by Rickard's modification of the Davis and Vanderslice equation [47, 48]:

$$\frac{dN}{dE} = \frac{N_0}{m_f}\frac{L}{\lambda_c}(1-E)^{(1/m_f-1)}\, exp\left[-\frac{L}{\lambda_c}+\frac{L}{\lambda_c}(1-E)^{1/m_f}\right] \quad \textbf{Equation 2.10}$$

where $\frac{dN}{dE}$ denotes the number of ions per energy interval; E is the ratio of the ion energy arriving at the cathode normalised to V_c (i.e. ranging from 0 to 1); N_0 is the number of ions entering the cathode sheath; m_f is the field distribution parameter (m_f = 4/3 if this electric field is considered space charge limited) [46]. Noticeably, this modification is based on assumptions that i) the incident ions all originate from plasma outside the cathode sheath, ii) ions are accelerated across the cathode sheath from zero initial energy to a theoretical maximum of qV_c, and iii) charge exchange collision is the only (or, at least, the predominant) mechanism in the cathode sheath [44, 47, 48].

L/λ_c could be used as a key factor to describe the energy distribution of ions arriving at cathode. As shown in **Fig. 2.3**, low L/λ_c values (e.g. < 0.1) lead to preferred "efficient" ionic bombardment. The L/λ_c value of DC plasma is, for example, ~10-15 for Ar discharge [46],

which is relatively high. One could either reduce bias potential (to reduce cathode sheath thickness, **Eq. 2.9**) or pressure (to increase collision mean free path, **Eq. 2.6**) to achieve low L/λ_c values. Nevertheless, plasma generation in conventional DC configuration depends on the secondary electron emission from cathode surface, whereby changes in both pressure and bias potential will influence the plasma generation itself.

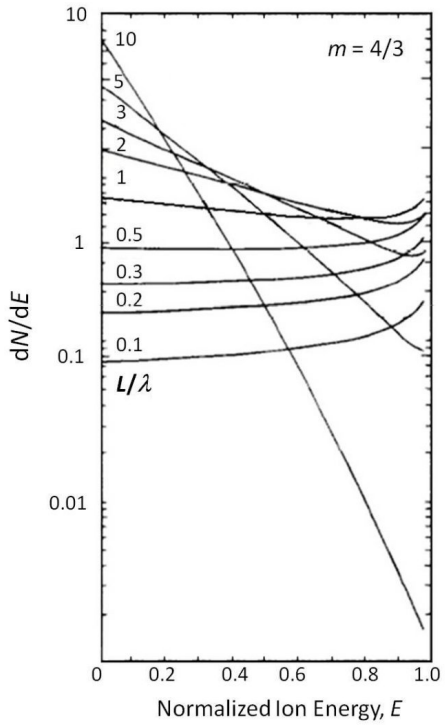

Fig. 2.3 Ion energy distribution at various L/λ values from Eq. 2.10 (reproduced from Ref. [48])

2.1.3.3 Triode plasma configurations and plasma enhancement

Thermionically enhanced DC plasma nitriding was studied from the late 1980s with several traceable publications and patents from the early 1990s [20-23]. Essentially, a DC plasma configuration was modified with an additional electron-emitting unit, which is a self-circuited and biased hot tungsten filament. Both workpiece and filament are negatively biased (i.e.

cathode) during process, while chamber wall is grounded (i.e. anode). There are three electrodes, so it is also referred to as triode configuration. This configuration is also adaptable for physical vapor deposition (PVD), as shown in **Fig. 2.4**, so that nitriding could be performed in-situ prior to PVD processes.

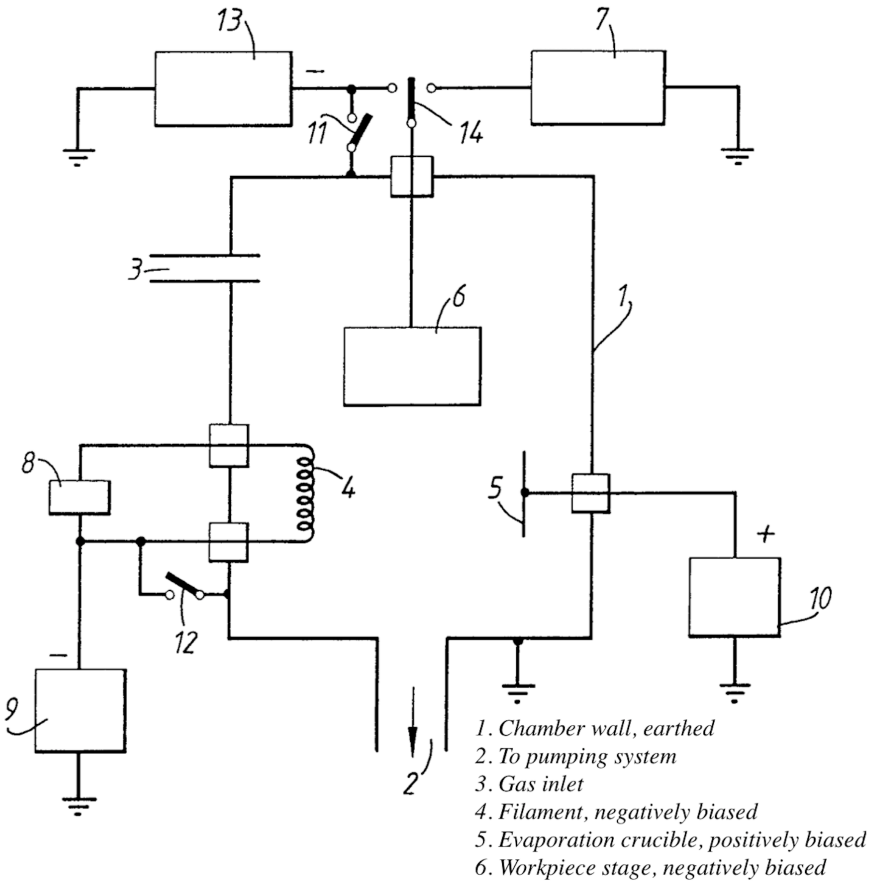

Fig. 2.4 Schematic illustration of the triode plasma PVD unit used in this study for triode plasma nitriding (reproduced from Ref. [21]), the evaporation system (for PVD coating, involving element 5 and 10 in the above figure) was not used in this study

During treatment, the tungsten filament is resistively heated and emits thermionic electrons into a low-pressure environment. In addition to the secondary electron emitted from workpiece upon ionic bombardment, the thermionic electrons from hot filament enhance the

degree of ionisation in plasma. Triode-plasma configuration dramatically lowered the workpiece potentials and chamber pressures required for plasma treatments, providing sufficient cathodic current density for nitriding (or coating) processes with dramatically reduced L/λ_c values (e.g. ~0.01 for Ar discharge [20]). Compared to diode-plasma nitriding, ions are accelerated over a relatively short distance and experience less collision under triode-plasma in cathode sheath before bombarding the cathode surface (i.e. low L and high λ_c).

2.2 Incorporation of nitrogen in iron

Owing to the continuous plasma-solid interaction and adsorption of nitrogenous atoms/ions/molecules at material surface, a chemical potential gradient is developed at workpiece surface during nitriding. Given sufficient time and temperature, nitrogen atoms diffuse interstitially into bulk material from high chemical potential to low. In **Section 2.2.1**, interstitial diffusion is discussed. Crystallographically, the accommodation of N in substrate could lead to lattice distortion, rearrangement and/or formation of nitrides. The diffused nitrogen may i) dissolve in solid solution in the parent lattice, and/or ii) trigger metallurgical phase transformations. In **Section 2.2.2**, the crystallographic structure of iron after N absorption is discussed using Fe-N binary phase diagram as a guide.

2.2.1 Interstitial diffusion

Chemical potential gradient is the driving force for nitrogen migration in bulk material [49]. Although interstitial diffusion could occur "uphill" from low concentration to high in some special cases [50], the chemical concentration gradient is generally considered equivalent to the chemical potential gradient in this section. The following discussion is based on one-dimensional mass migration from high N concentration to low.

Steady state diffusion (i.e. constant concentration gradient) could be described as a mass-flux, depicted via Fick's first law:

$$\boldsymbol{J_N = D_N \frac{\partial C_N}{\partial x}} \qquad \textbf{Equation 2.11}$$

where J_N denotes atomic diffusion flux density of diffusion species (atoms/m^2s), D_N the diffusivity (m^2/s), C_N the concentration (atoms/m^3), and x the diffusion depth (m). However, concentration gradient changes with respect of time. Fick's second law can be applied to predict concentration-limited diffusion:

$$\boldsymbol{\frac{\partial C_N}{\partial t} = D_N \frac{\partial^2 C_N}{\partial x^2}} \qquad \textbf{Equation 2.12}$$

where C_N denotes the time and depth dependent concentration (atoms/m^3), and t the time (s). Diffusivity, D_N, could be expressed in simplified form of Arrhenius equation [49, 51]:

$$\boldsymbol{D_N = D_0 e^{-\Delta H_m/RT}} \qquad \textbf{Equation 2.13}$$

where D_0 is a pre-exponential factor (m^2/s), ΔH_m is the activation energy per mole (J) for nitrogen to jump between each interstitial sites, R the universal gas constant (i.e. ~8.31 J/Kmol), and T the temperature (K). Consider that interstitial elements are free to migrate to the neighboring interstitial sites, D_0 could be described as [51]:

$$\boldsymbol{D_0 = \alpha\, a^2 p v e^{\Delta S_m/R}} \qquad \textbf{Equation 2.14}$$

where α is a geometrical factor (e.g. 1/12 for face-centred cubic lattice), a is the lattice parameter (m), p is the number of nearest interstitial sites, v is the vibration frequency of nitrogen in the interstitial site and ΔS_m is the change in lattice entropy per mole of nitrogen atoms accommodated. The distribution of nitrogen could be described using complementary error functions:

$$\mathrm{erf}(z) = \frac{2}{\sqrt{\pi}} \int_0^z e^{-y^2} dy \quad \text{and} \quad \mathrm{erfc(x)} = 1 - \mathrm{erf\,(x)}$$

Assuming a constant surface nitrogen concentration (i.e. C_s), the concentration of nitrogen at a displacement (or depth) x below surface could be described as [52]:

$$C_x = C_s \operatorname{erfc} \frac{x}{2\sqrt{Dt}} \qquad \textbf{Equation 2.15}$$

There appears only one variable, $\sqrt{Dt}$, in **Eq. 2.15**, that the following empirically relationship is derived for nitriding [26, 49, 52, 53]:

$$Diffusion\ depth \propto \sqrt{Dt} \qquad \textbf{Equation 2.16}$$

The abovementioned equations contain fundamental aspects of diffusion and present a convenient way of estimating case depth for diffusion treatments [53]. However, they are based on theoretical assumptions (e.g. constant diffusion diffusivity and perfect lattice). The diffusion mechanisms in real applications are complex. The interstitial diffusivity in austenitic iron was reported as increasing with carbon content during carbon diffusion, as shown in **Fig. 2.5** [54]. Furthermore, phase transformations (especially for those occurring during nitrogen absorption) and lattice imperfections (e.g. dislocations, grain boundaries and stacking faults) also have profound influences on interstitial diffusion. For example, enhanced nitrogen diffusivity in α-Fe was reported at low temperature after the grain size was mechanically reduced (from ~100 μm to ~13 nm), where diffusion occurred predominantly along grain boundaries rather than within the grains [55].

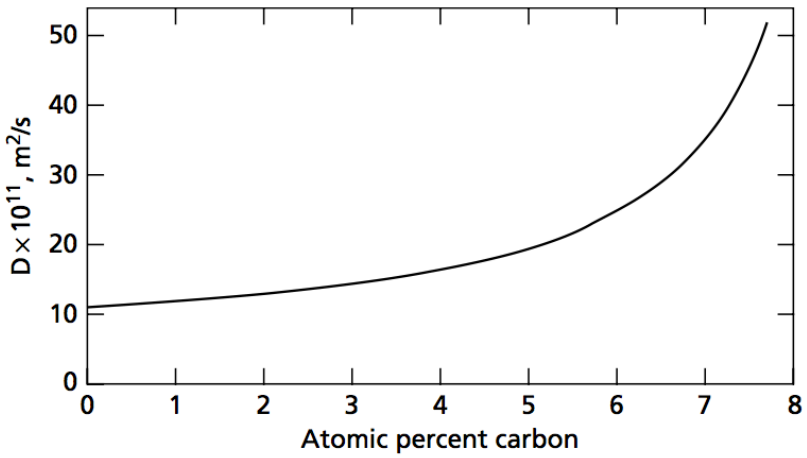

Fig. 2.5 Diffusion coefficient of carbon in FCC-Fe at 1400 K (reproduced from Ref. [54])

2.2.2 Nitrogen in iron

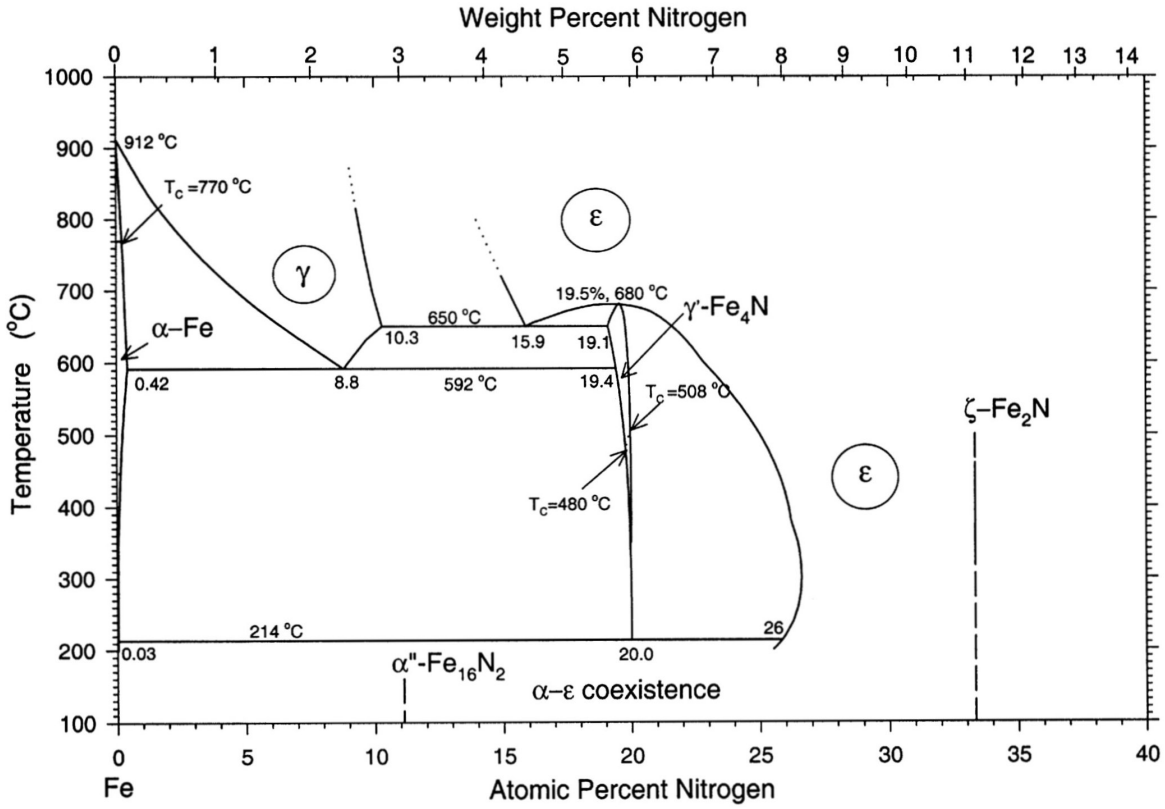

Fig. 2.6 Fe-N binary phase diagrams (reproduced from Ref. [56])

The Fe-N binary system has been investigated extensively since 1920s, but the first binary phase diagram was published by Jack [57] in 1951, which was based on X-ray diffraction results of gaseous nitrided iron powders. An extended version of the Fe-N binary phase diagram was published with more details in 1987 [58], which can be found in widely-available ASM International publications from the 1990s [59, 60]. The latest Fe-N phase diagram was extended to lower temperatures [56], as shown in **Fig. 2.6**. From low nitrogen concentration to high, there are ferrite α(N), martensite α′(N), austenite γ(N), α′′-$Fe_{16}N_2$, γ′-Fe_4N, ε-Fe_3N_{1+x}, ζ-Fe_2N and γ′′-FeN in the Fe-N binary phase diagram. Apart from γ′′-FeN, all iron nitrides are ferromagnetic [61]. After commercial nitrogen surface modification processes, the enhancement of material properties occurs mainly due to i) solid solution strengthening by interstitially-located N, and ii) formation of iron nitrides (mainly γ′-Fe_4N and ε-Fe_3N_{1+x}) [62].

2.2.2.1 Nitrogen in solid solution – α(N), γ(N) and α′(N)

As depicted in **Fig. 2.6**, α-Fe dissolves up to 0.42 at.% N at 592°C and γ-Fe dissolves up to 10.3 at.% N at 650°C; i.e. it becomes clear that solid solubility of N in iron depends strongly on the matrix structure. Interstitial elements preferably occupy the octahedral sites in the crystal lattice of iron [63]. If N occupies an octahedral site in the body-centred cubic (BCC) unit cell (**Fig. 2.7**), a large anisotropic (i.e. tetragonal) strain is generated. In this case, BCC-α(N) could only accommodate a small amount of interstitial nitrogen before phase transformation occurs. If N occupies an octahedral site of the face-centred cubic (FCC) unit cell (**Fig. 2.7**), an isotropic strain is generated, such that austenite is capable of accommodating interstitial nitrogen to a much higher amount.

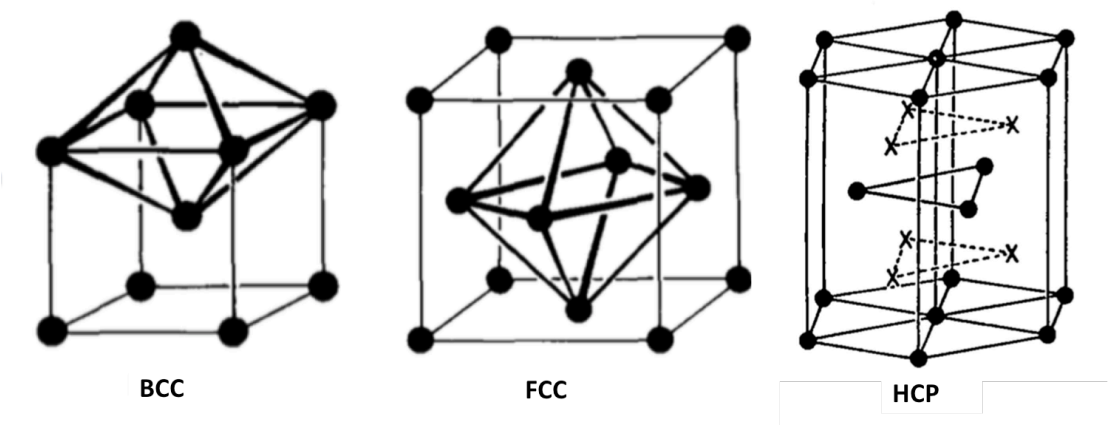

Fig. 2.7 Illustration of octahedral sites in BCC, FCC and HCP unit cells (×-octahedral centres) (reproduced from Ref. [63, 64])

If γ(N) is cooled rapidly, martensitic shear transformation can occur, where interstitial N has no time to escape the octahedral site of the original FCC structure. This could results in diffusionless shear of γ(N) to body-centred tetragonal (BCT) martensite α′(N), which could be considered as a highly-distorted N-supersaturated ferrite [63]. Before reaching N-solubility in FCC-γ(N), N addition can suppress the M_s temperature (i.e. the temperature below which martensite starts to form) to below room temperature, in which case martensitic transformation does not occur after quenching [65]. In that case, α′(N) is capable of accommodating N amount higher than α(N) but lower than γ(N).

2.2.2.2 Iron nitrides

α′′-$Fe_{16}N_2$

In α′′-$Fe_{16}N_2$, N resides at the octahedral centre of a distorted BCC lattice of Fe [63]. Jack [57] described α′′-$Fe_{16}N_2$ by space group I4/mmm (139) as 2×2×2 distorted BCC cells, as shown in **Fig. 2.8**, which can be considered as an intermediate structure between α′ and γ′- Fe_4N.

Nitrogen atoms reside at the centres of every other corner-sharing octahedron. Lattice parameters were defined later as: a = 0.5710 nm and c = 0.6283 nm.

γ′-Fe_4N

In γ′-Fe_4N, N atoms occupy the centres of corner-sharing octahedra in the FCC lattice of Fe [63]. Single crystal γ′-Fe_4N has the space group $Fm\bar{3}m$ and a lattice parameter of 0.379 nm [66]. This phase has a narrow regime of homogeneity from ~19-20 at.% N at temperatures from 214°C to 680°C, while it coexists with ε-Fe_3N_{1+x} nitride from ~20-27 at.%N (**Fig. 2.6**).

ε-Fe_3N_{1+x}

The crystal arrangement of ε-Fe_3N_{1+x} could be described by the space group of P312 or $P6_322$, with its lattice parameter influenced by N content and degree of ordering [67]. Typical lattice parameters are i) a = 0. 46919 nm; c = 0.43670 nm for Fe_3N [66] and ii) a = 0.48016 nm; c = 0.44269 nm for $Fe_3N_{1.47}$ [68]. The wide range of homogeneity for ε-Fe_3N_{1+x} (as shown in the Fe-N phase diagram, **Fig. 2.6**) extends from ~25 at.%N to (theoretically) ~33.3 at.%N; ε-Fe_3N_{1+x} could also be formulated as ε-Fe_2N_{1-z} or ε-$Fe_{2-3}N$.

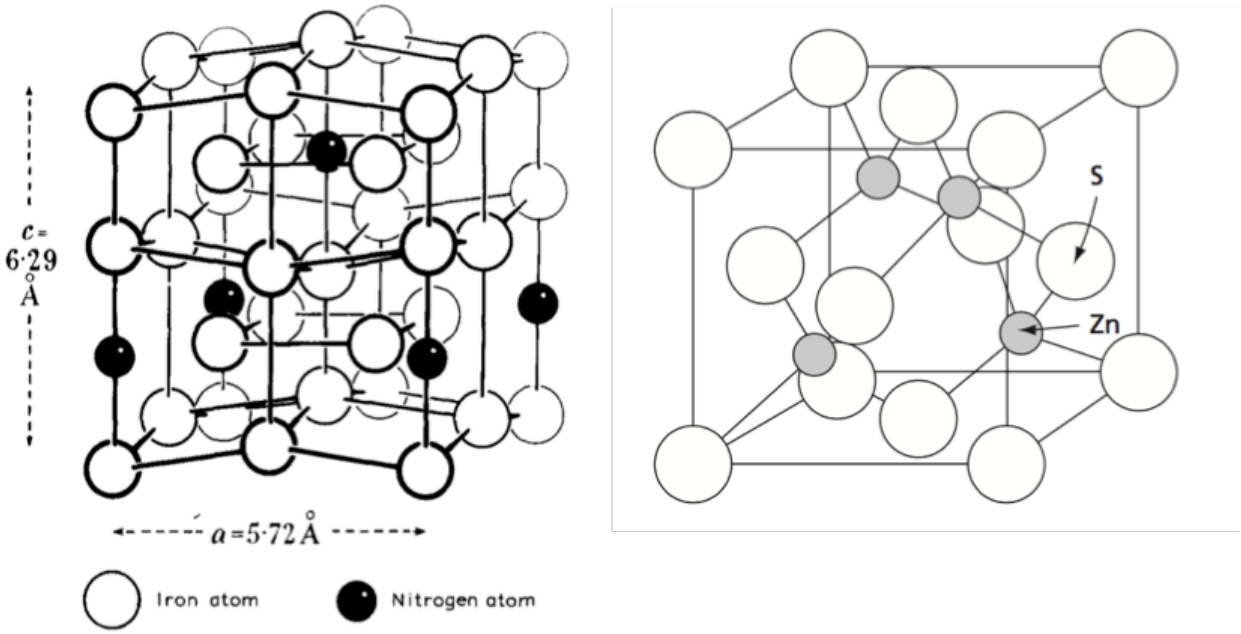

Fig. 2.8 The crystal structure of α″-$Fe_{16}N_2$ (reproduced from Ref. [57]) and ZnS (reproduced from Ref. [51])

ζ-Fe_2N

ζ-Fe_2N (i.e. 33.3 at.% N) has a orthorhombic lattice, where N occupies half of the octahedral interstices in each layer, leaving unoccupied sites above and below them [63, 64]. Typical lattice parameters are a = 0.4426 nm, b = 0.5529 nm and c = 0.4831 nm [69].

γ″-FeN

In γ″-FeN, N resides at corner-sharing tetrahedral centres of the FCC sublattice of Fe (i.e. ZnS type structure, **Fig. 2.8**) [69, 70], under a space group of $F\bar{4}3m$ where a = ~0.433 nm [69]. In Ref. [70], γ″-FeN thin film was synthesised experimentally on top of a Cu(001) film via deposition of Fe in a nitrogenous atmosphere, which is less likely to be synthesised via nitriding of steels.

2.3 Austenitic stainless steels after low temperature nitriding

The 'new' surface phase, which is known as 'expanded austenite' (γ_N or γ_C for nitrogen-expanded or carbon-expanded austenite, respectively) or 'S-phase' (S_N or S_C, for nitrogen-rich or carbon-rich, respectively), is introduced in **Section 2.3.1**. The origin of expanded austenite is discussed in **Section 2.3.1.1**. The crystal structure of nitrogen-expanded austenite is discussed in **Section 2.3.1.2**, which focuses on intensive XRD and TEM studies of low temperature nitrided AISI 316 (and/or AISI 304) from literature. The role of substrate composition on the formation of expanded austenite is also discussed in **Section 2.3.2**. The commercial processes and applications of expanded austenite after low-temperature thermochemical diffusion treatments are reviewed in **Section 2.3.3**.

2.3.1 Expanded austenite

2.3.1.1 Origin and early studies of expanded austenite (~1960s-1990s)

Unanticipated corrosion-introduced carbon transportation in nuclear reactors

In 1958, low temperature carburising of austenitic stainless steels was first investigated 'accidentally' by Shepard [71] (in a technical report) for AISI 304 applied in a "carbon-contaminated" liquid sodium nuclear reactor cooling system (at ~454-650°C), in which the unanticipated corrosion-induced carbon transportation was initially a concern for the surface embrittlement (and cracking) after carbide formation. This subject was studied systematically by the nuclear power generation industry from the early 1960s onwards [72-75]. Despite the main focus being on carbon transportation from liquid sodium at service temperatures, Anderson and Sneesby [73] in 1960 indicated a possible "metastable super-saturation of austenite with respect to precipitation of carbide" for the carburised surface of AISI 304; however, no clear metallurgical evidence was provided. Later in 1970, Litton and Morris [75] clearly presented a surface layer described as a "solid solution of carbon in austenite" on AISI 316 carburised in liquid sodium at 550°C for 24hrs, as shown in **Fig. 2.9a.** Compared to

the unmodified ASS core, the carbon-rich surface layer showed unambiguously different (slightly better) corrosion resistance to the etchant used. Nevertheless, no crystallographic information was provided in these early studies (before 1980s).

A potential solution for the poor wear performance of stainless steels

In the open literature of surface engineering, nitrogen-expanded austenite was investigated from the 1980s, with its unusual crystallographic structure (XRD pattern) firstly revealed by Ichii et al. [8] and the enhanced surface hardness (without loss of corrosion resistance) demonstrated by Zhang and Bell [5]. In the mid-1980s, Zhang and Bell [5] reported a CrN-free surface layer on AISI 316 after plasma nitriding at 400°C (**Fig. 2.9b**) with no significant decrease of material pitting potential after treatment, which was presumed to be a mixture of FCC γ′-$(Fe, Cr, Ni)_4N$ and matrix austenite. Similarly, Ichii et al. [8] claimed a "white layer" at the surface of 18-8 ASS (AISI 304) after plasma nitriding at 400°C − with five new broad XRD peaks that were not listed in the ASTM standard (peaks of S1-S5 in **Fig. 2.9c**) − which were again believed to be an M_4N (i.e. M-metallic elements, such as Fe, Cr, Ni…) phase, owing to the ~5.9 wt.% N (~ 20 at.% N) detected under EPMA (electron probe micro analysis) and the ferromagnetism of this surface layer. This apparently mono-phased (but clearly crystallographically 'different') surface region generated after low temperature plasma nitriding of ASS was initially denoted as 'S-phase' by Ichii et al. [8].

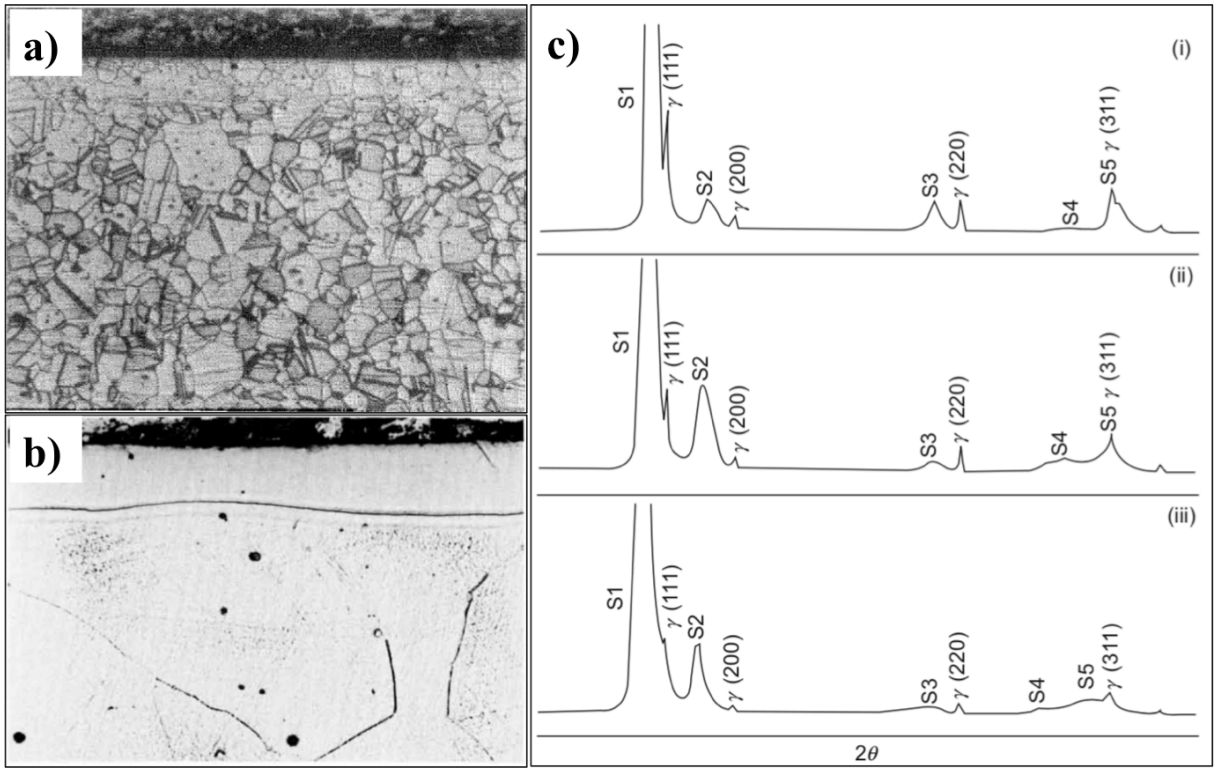

Fig. 2.9 a) Transverse OM of AISI 316 surface carburised at 550°C for 24hrs in carbon-containing liquid sodium (reproduced from Ref. [75]), b) Transverse OM of AISI 316 surface after plasma nitriding at 400°C for 60hrs (reproduced from Ref. [5]), c) XRD patterns of 18-8 ASS surface after plasma nitriding at 400°C for 4hrs at three N_2:H_2 gas ratios (from top to bottom, ratios are 1:1000, 1:9, 4:1, reproduced from Ref. [8])

The terminology of 'expanded austenite' was used in 1989 by Hannula et al. [76] to describe the low-nitrogen surface phase (with lattice parameters of ~0.371-0.374 nm in-between γ′-nitride and nitrogen solid solution) generated after treatment on AISI 304 and AISI 316 after plasma nitriding at 350°C for 15mins. However, in the 1989 study by Hannula et al. [76], the high-nitrogen surface phase (with lattice parameters larger than stoichiometric γ′-nitride) generated after nitriding at 350°C for 6hrs and 24hrs were (mis-)claimed as ε′ (as first claimed by Angelini et al. [77] in 1988) and/or FCC nitride phase of MN_{1-x}.

The ‘expanded austenite’ terminology was re-defined by Leyland et al. [22] in 1993 as a “heavily strained austenitic structure” to describe the precipitation-free nitrogen (and/or carbon) induced austenitic (anisotropic) lattice expansion generated after low temperature plasma nitriding (or carburising) regardless of N (and/or carbon) content – although, as will be shown later, the anisotropic expansion effect tends to occur at very high levels of interstitial supersaturation by N and/or C. Based on terminology of ‘expanded austenite’, the surface XRD peaks (at lower 2θ angles) observed after treatment can be regarded as being shifted from the substrate austenite XRD peaks. The larger peak shift of (200)γ after nitriding could be attributed to the elastic anisotropy of the FCC structure that, under elastic strain, the γ(200) peak will in any case shift more than γ(111), since the {200}γ planes are more compliant than {111}γ. The systematic study of elastic anisotropy in cubic crystals can be dated back to the early research works in the 1950s such as Zener [78].

The anisotropic elastic strain of expanded austenite was further discussed in 2000 by Mandl and Rauschenbach [79], who pointed to plastic accommodation of the N-interstitial induced strain in expanded austenite owing to the extremely large lattice expansion (~10%) observed. Additionally, Sun et al. in 1999 [80] proposed a “disordered” and “distorted” FCC structure, which involved consideration of stacking faults in the N-rich surface layer. In Sun’s paper [80], the anomalous XRD peak positions (**Fig. 2.10a**) after plasma nitriding was attributed to the combined effect of the hkl-dependent elastic lattice constants (and residual stress in the surface layer) according to the argument of Wagner et al. [81] and the hkl-dependent stacking fault parameters (and stacking fault generation in the surface layer) according to Paterson [82] and Warren [83]; in either case (200)γ planes would be expected to shift more than (111)γ planes.

Similar to 'expanded austenite', this surface phase was also referred to as metastable FCC 'γ_N' by Williamson et al. from 1990 [84-87]. The phase metastability was illustrated in 1994 [85], where the diffusivities of small interstitial elements (i.e. C and N) were calculated to be several orders of magnitude higher than those of the relatively 'immobile' substitutional elements (e.g. Fe, Cr, Ni and Mn) at low treatment temperatures [85]. Thus, interstitial nitrogen (or carbon) is able to diffuse inward from the substrate surface (following a chemical potential gradient) during typical low treatment temperatures of nitriding (or carburising), while the formation of thermodynamically-favorable nitrides (or carbides) is suppressed, owing to the low substitutional diffusivity of nitride-/carbide-forming substitutional elements, such as Cr.

Nevertheless, it is worth mentioning that the precise nature of the crystallographic structure (reflected in the various names allocated) of the surface phase synthesised on ASS after low-temperature nitriding has been a controversial point of discussion, owing to the anomalous XRD peaks observed. In 1988, Angelini et al. [77] assigned plasma nitrided (at 500°C and 600°C) surfaces of AISI 316 with a structure of ε′-(Fe, Cr, Ni, Mo)$_2$N$_{1-x}$, since the surface phase was able to have a wide range of N content similar to that of ε-Fe$_2$N$_{1-x}$. However, as indicated by Marchev et al. [88] in 1998, one of a weak peak at ~81.2° cannot be satisfactorily indexed to confirm unequivocally an ε′ structure. Based on the XRD profiles observed by Marchev et al. [88-90], a body-centred or face-centred tetragonal martensitic structure was proposed for such surface layers (generated on ASS after low-temperature plasma nitriding), which was denoted by these authors as 'm-phase'. After years of intellectual effort (as will be discussed in **Section 2.3.1.2**), both of these denotations (ε′ and m-phase) misconstrue the crystal structure of this metastable interstitially supersaturated surface phase. Noticeably, both S phase and expanded austenite suggests an FCC structure of

this phase; however, compared to S phase (which could be misinterpreted to a compound ceramic phase), expanded austenite appears to be a more suitable denotation.

'Nitrogen-doped' PVD coatings

Over a parallel time frame, similarly structured ferrous materials have also been synthesised and investigated as thin coatings using various sputtering (and other) physical vapour deposition techniques [91-97]. Most of the coating deposition studies were carried out at low temperatures (~300°C). As early as 1978, Hirohata et al. [91] reported unknown XRD peaks for the unusual "Fe-N_x type" phase layers generated in an Fe-N_2 reactively deposited coating system on glass substrates. Similar unexpected phases were identified by Frantz et al. [92] in 1985 – believed to be iron nitrides − in the nitrogen-containing stainless steel coating produced. In subsequent studies of chemistry (using EPMA), structure (using XRD and TEM) and properties (e.g. adhesion, internal stress and hardness) of N-containing AISI 310 coatings, Frantz [93, 94] claimed i) a structure of "metastable supersaturated disordered" FCC solid solution for the nitrogen-doped (~2-40 at.% N measured via EMPA) ASS films generated, and ii) "some structural analogies" to diffusion layers that were generated on ASS after low-temperature plasma nitriding. Noticeably, the anomalous $(200)\gamma_N$ lattice parameter of expanded austenite coating was correlated to the anisotropic internal stress, which was more intense on $(200)\gamma_N$ planes than others [93]. Several investigations on metastable N-doped ferrous coatings could be found from the early-1990s, e.g. nitrogen-doped AISI 316 coatings by Stebut et al. [95, 96], 'expanded austenite' coatings by Matthews et al. [97] and 'S-phase' coatings by Dearnley et al. [98].

2.3.1.2 Crystallographic structure of nitrogen-expanded austenite

Crystallography − XRD

The crystallographic structure of expanded austenite, as determined from the hkl-dependent peak shifts and broadening in X-ray diffractograms, deviates from the ideal FCC structure, as shown via d_{111}/d_{200} ratios in **Fig. 2.10a**. That is, expansion of the FCC lattice under extreme interstitial supersaturation differs from the uniform, isotropic lattice expansion at nitrogen content below equilibrium solubility. Attempts were made by Sun et al. [80] in 1999 to describe the anomalous XRD profile of γ_N layers with hkl-dependent elastic constant and/or stacking fault generation, which led to a conclusion that the lattice structure of γ_N originates from a combined effects of high residual stress and stacking fault generation. After a high-order diffractometry study of expanded austenite layers (on low-temperature plasma nitrided AISI 316) in 2008, Fewell and Priest [99] tried to match the structures observed to several existing candidate structures, from which it was concluded that "distortion and faulting" were the main contributory factors. Residual stress analysis of expanded austenite layer (on 430°C 20hrs nitrided AISI 316) was carried out via successive layer removal and glancing angle XRD techniques by Fernandes et al. [100] in 2015, which suggested non-linear nitrogen dependency of elastic constants (i.e. E_{111} and E_{200} in his study).

After decades of intellectual effort [80, 99-102], the anomalous anisotropic lattice expansion for expanded austenite could be attributed to the combined effects of two aspects: i) lattice stress associated with the hkl-dependent planar elastic constants, and ii) stacking fault (SF) generation associated with the hkl-dependent stacking fault parameters. Nevertheless, together with the concentration gradient of the interstitial species from surface to core for the expanded austenite formed on bulk materials (i.e. heterogeneous expanded austenite), the abovementioned interrelated two aspects complicate the scientific interpretation of

observable XRD peak shifts to lower angles. No consistent structural model is currently available to comprehensively depict the anomalous XRD peak shift and broadening of expanded austenite [102].

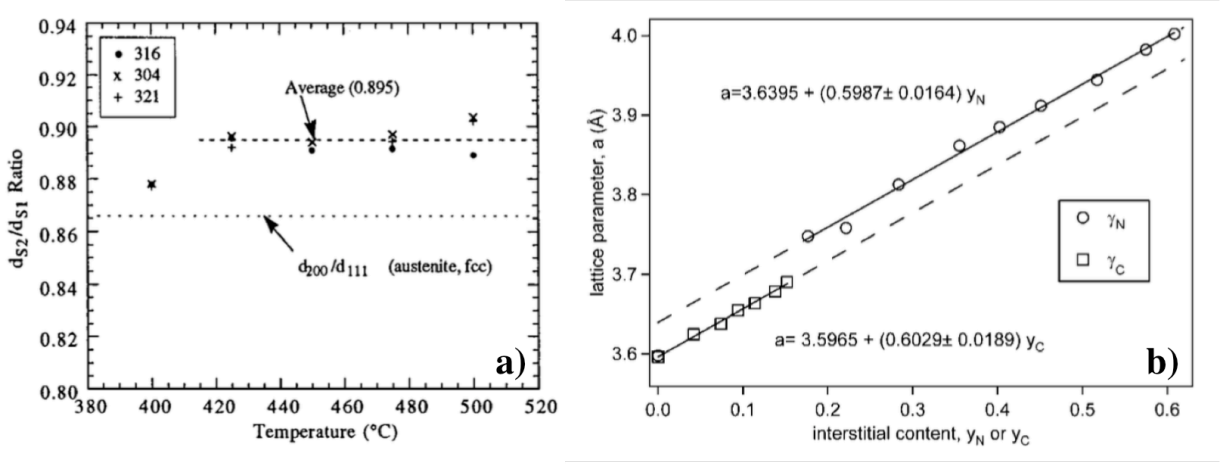

Fig. 2.10 a) Left: Ratio of d_{200}/d_{111} (as determined from respective X-ray diffraction peak positions) for AISI 316, 304 and 321 austenitic stainless steels after plasma nitriding for 4hrs at various temperatures (reproduced from Ref. [80]); b) Right: Plot of lattice parameters of homogenous nitrogen and carbon expanded austenites (as determined from $\gamma_N(220)$ and $\gamma_C(220)$ X-ray diffraction peak positions) against interstitial N or C per metal atom (reproduced from Ref. [12])

Since 2004, Somers et al. [101-105] synthesised and investigated "homogenous" (stress-free) expanded austenites. Rather than thick (~several mm) stainless steel substrates, thin (~7.5 or ~ 50 μm) AISI 316 foils were nitrided or carburised at low temperatures, which powdered naturally during treatment or during ultrasonic bath after treatment. Having a nitrogen content of 25-30 at.%, the N-rich AISI 316 powders clearly exhibited an expanded FCC structure with a slight systematic deviation from ideal (fault-free) FCC line profiles [101]; the

deviations could be accurately described by stacking faults (taking a stacking fault probability of ~ 0.03) using following equation from Warren [106]:

$$\boldsymbol{\Delta(2\theta_{hkl}) = 0.2756 \cdot \alpha \cdot G_{hkl} \cdot \tan\theta} \quad \textbf{Equation 2.17}$$

where $2\theta_{hkl}$ is the Bragg angle (in degrees), α is the stacking fault probability and G_{hkl} is the stacking fault parameter. The synthesis technique for homogenous expanded austenite powders was then further improved with, for example, high temperature (~1080°C) austenitising before treatment and low temperature (≤ 500°C) homogenisation after treatment (see Ref. [12] for detail procedure). Using these techniques, Christiansen et al. [103] later revealed a linear relationship between lattice parameters (determined from XRD peak positions) and interstitial content (determined via thermogravimeteric analysis) of homogenous expanded austenites, as shown in **Fig. 2.10b**, where expanded austenite evidently retains an FCC structure [101, 103].

Nevertheless, Velterop et al. [107] argued that Warren's approach is based on unrealistic assumptions, such as i) small and hkl-independent stacking fault probabilities, and ii) randomly-orientated crystallites. Compared to homogenous powders, the XRD anomaly of expanded austenite is more pronounced on expanded austenite layers (on top of thick substrates) − owing to high residual stress developed in material that cannot be relaxed via breaking into powders − where stacking fault probabilities of expanded austenite layers must be remarkably greater than homogenous powders. Additionally, EBSD studies by Templier et al. [108-110] demonstrated nitrogen concentration-dependent lattice rotation (and texture development) of polycrystalline AISI 316L after low-temperature nitriding. Therefore, Warren's equation appeared unreliable on predicting the lattice parameter of expanded austenite.

In this case, homogenous expanded austenites were later studied via Derby simulation (instead of Warren's method) in 2017 by Brink et al. [102], who revealed that stacking faults alone cannot explain the anomalous XRD peak shifts of the 'homogenous' γ_N powders. Thus, it was argued that the interstitially-supersaturated powders – which are chemically homogenous − could still contain "micro-stress" [102]. Together with the previous elastic constant studies by Fernades et al. [100] and a self-consistent plasticity model by Clausen et al. [111], Brink et al. [102] argued that the anomalous lattice expansion could originate from the "elastic anisotropy of plastically deformed (expanded) austenite".

Crystallography − TEM

In contrast to the structures reported from XRD studies, expanded austenite was consistently reported as being mono-phased, precipitation-free and FCC structured under TEM [14, 15, 112-114], where the absence of diffraction anomalies is believed to be due to stress relaxation after sample preparation from bulk materials to TEM thin foils. The TEM signatures of nitrogen-expanded austenite associated with lattice defects, including stacking faults [14, 15], twinning [112, 113] and HCP lamellae [114]. Additionally, forbidden FCC reflections were reported in nitrogen-expanded austenite [14, 15, 112-114], which were attributed to ordered occupation of N in octahedral interstices.

A series of TEM investigations on plasma nitrided AISI 316 (at 420-460°C) by Li and Sun [112] showed micro-twins (**Fig. 2.11**) and forbidden FCC reflections in an "expanded and distorted austenite". Lattice expansion decreased from surface to core. Phase decomposition of γ_N thin foils was studied further by in-situ heating in a TEM chamber, where fine coherent lamellae of CrN and Cr-depleted austenite were observed, revealing a "cellular precipitation

mechanism" for phase decomposition [112]. Incubation time for phase decomposition decreased with increasing heating temperature.

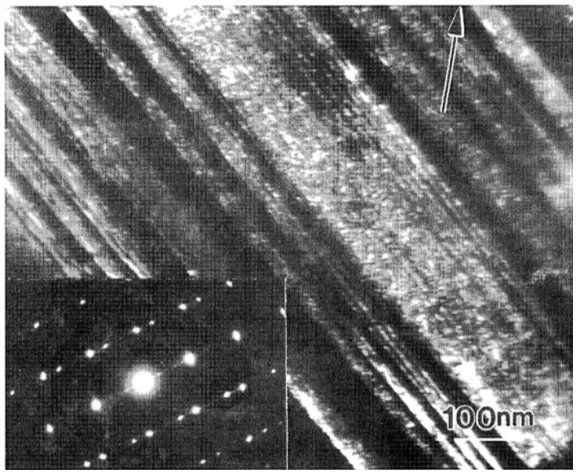

Fig. 2.11 DF-TEM image and its EDP showing twinning lamellae in AISI 316 ASS after low temperature plasma nitriding (reproduced from Ref. [112])

Low-temperature (i.e. 400°C) plasma nitrided AISI 316 was investigated by Meletis et al. [14, 15], for the first time, under HR-TEM as shown in **Fig. 2.12**. The <111> streaking observed in EDPs (**Fig. 2.12a**) was attributed to stacking faults (**Fig. 2.12b**). Forbidden FCC reflections (**Fig. 2.12d**) were correlated to the domain structure observed (**Fig. 2.12c, e**), which was believed to be due to different local ordering of nitrogen occupancy. After these observations, it was argued that expanded austenite formed simply by introducing one nitrogen atom into one octahedral centre of the FCC Bravais unit cell [15] − giving a theoretical upper nitrogen saturation point of 20 at.% − which is apparently not true; for example, ~38 at.% N in nitrided AISI 316 measured by Christiansen et al. [12].

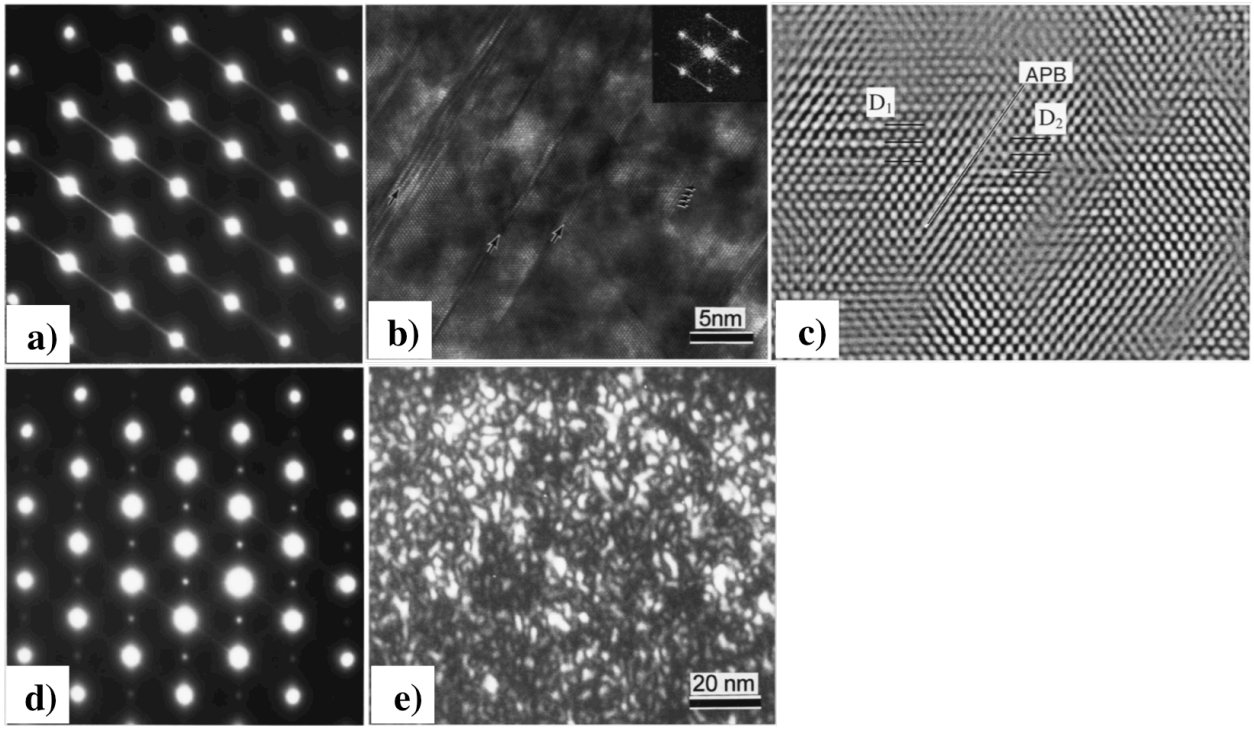

Fig. 2.12 a) EDP of high stacking fault region in expanded austenite, b) HRTEM image of region with stacking faults indicated with arrows, c) Fourier filtered image of image b (after omission of noncrystallographic information) showing antiphase domains (D1 and D2) and antiphase boundary (APB), d) EDP of region in expanded austenite containing forbidden FCC reflections, e) DF-TEM image using one of the (010) reflection in image d showing domain structure rather than precipitate structure (reproduced from Ref. [15])

Furthermore, twinning was observed by Li and Sun [112] in low-temperature nitrided AISI 316 surfaces, but not by Meletis et al. [14, 15]. In a later study by Stronz and Psoda [113], nano-twinning was evident in low-temperature nitrided AISI 316L under HR-TEM. Determined from the $\gamma_N(111)$ XRD peak positions, lattice parameters of expanded austenite can be determined as ~0.381 nm on AISI 316 by Meletis et al. [14] and ~0.391 nm on AISI 316L by Stroz and Psoda [113]. Therefore, it appeared that nano-twinning in nitrogen-expanded austenite depends on the extent of lattice expansion. That is, the absence of

twinning in expanded austenite reported by Meletis et al. [14, 15] was attributable to the relatively small lattice expansion of AISI 316 achieved in their studies – owing to the selected treatment conditions (e.g. short treatment time or low treatment temperature). In both TEM studies by Meletis et al. [14, 15], AISI 316 samples were nitrided for relatively short time (i.e. 1hr and 4hrs), whereby their argument (based on ~6% lattice expansion) was clearly not representative of nitrogen-expanded austenite, especially for those with lattice expansions larger than ~6%.

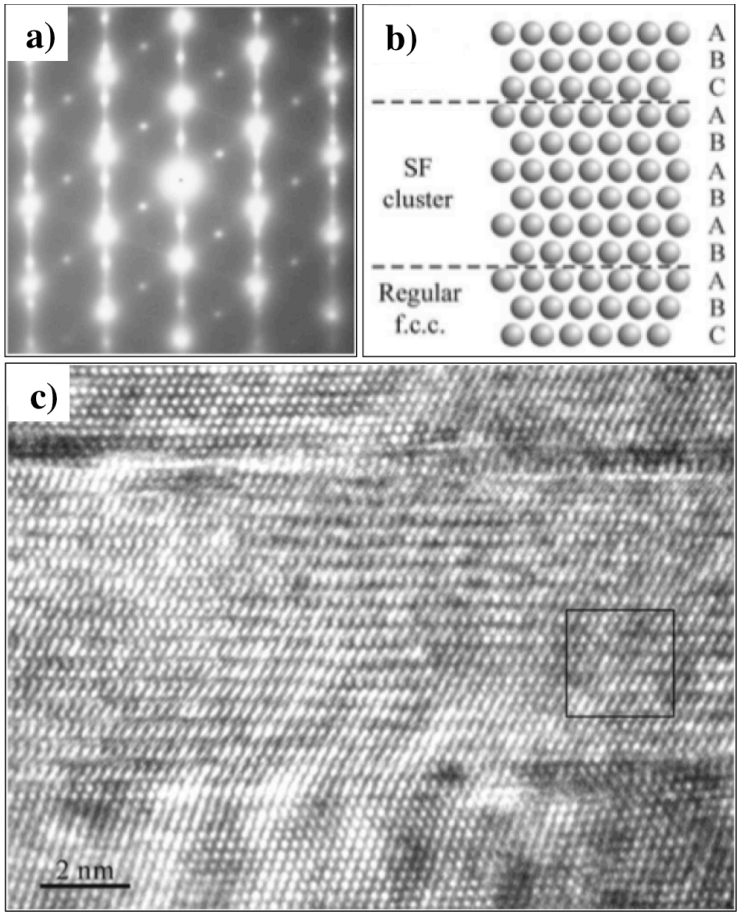

Fig. 2.13 a) EDP of expanded austenite generated on AISI 304L at <110>γ_N zone axis, b) illustration of stacking fault clusters equivalent to a HCP structure, and c) HR-TEM image of HCP structure (reproduced from Ref. [114])

In 2016, Tong et al. [114] investigated nitrogen-expanded austenites (generated on AISI 304L after plasma nitriding at 400°C) under TEM and HR-TEM. Similar to those observed in plasma nitrided AISI 316 and AISI 316L, <111> streaking, forbidden FCC reflections and twinning were evident in EDPs of plasma nitrided AISI 304L (**Fig. 2.13a**), suggesting stacking faults, ordered nitrogen occupancy and nano-twins (or ordered twin lamellae), respectively. More importantly, in addition to the abovementioned TEM features, HCP lamellae were observed by Tong et al. [114] in nitrogen-supersaturated AISI 304L (see EDP in **Fig. 2.13a** and HR-TEM images in **Fig. 2.13b**), which were attributable to local accumulation of SFs (see SF cluster in **Fig. 2.13b**). Noticeably, these HCP lamellae were crystallographically equivalent to ε-martensite, but were still considered as "SF clusters" in Tong's study.

2.3.2 Role of substrate elements

2.3.2.1 Role of substitutional elements of Cr, Mn, Ni and Mo in ASS

Several early studies on this topic can be found from the 1990s, when Menthane et al. [115] in 1995 reported that γ_N (which was referred to as S-phase) formed on austenitic AISI 304L and duplex 1.4460 (equivalent to AISI 329, Fe-27Cr-5Ni-1.5Mo, in wt.%), but did not form on binary steels of Fe-13Cr (in wt.%) and Fe-42Ni (in wt.%) after plasma nitriding for 5hrs over a temperature range of 400-600°C. In 1998, Yasumaru [116] also indicated that, γ_N (which was referred to as Y_N) formed on ternary Fe-Cr-Ni alloys (i.e. Fe-18Cr-8Ni, Fe-18Cr-20Ni and Fe-18Cr-48Ni, in wt.%) after plasma nitriding at 350°C, while γ′-Fe_4N type nitride − instead of γ_N − formed on Fe-Ni binary alloys (i.e. Fe-30Ni and Fe-36Ni, in wt.%), Fe-Mn-C alloy (i.e. Fe-26Mn-0.2C, in wt.%) and Fe-Cr binary alloy (i.e. Fe-17Cr, in wt.%). It was thus thought that both Cr and Ni are required for the formation of expanded austenite.

ASS are based fundamentally on a ternary system of Iron-Chromium-Nickel (Fe-Cr-Ni), where Ni can be replaced with Mn (wholly, or in part) for economic or other (e.g. biocompatibility) reasons. Cr has been widely referred to as being an 'essential' element in the formation of γ_N, believed to assist in 'trapping' the inwardly-diffusing interstitial species and (in the case of nitrogen) forming short-range ordered Cr-N clusters [10, 17, 87, 104, 117].

Ni addition is thought to lower the equilibrium N solubility in austenite − and hence reduce N uptake during nitriding, whereas Mn addition is thought to increase it. For example, Williamson et al. [87] illustrated that austenitic Ni-based alloys possess lower surface N-absorption compared to austenitic Fe-based alloys. However, the austenitic Fe-based alloys in their study contained varying concentrations of either Cr or other strong nitride forming elements (e.g. Al and Ti), such that the effect of Ni content was not clearly demonstrated in Fe-based alloy.

In 2009, Buhagiar [118] investigated Fe-17Cr-14Ni-3Mo (AISI 316 type) and a Ni-free Fe-17Cr-11Mn-3Mo-0.5N alloy after plasma nitriding at 430°C, carburising and nitrocarburising. The formation of γ_N on Ni-free Fe-Cr-Mn ASS was evident. Replacement of Ni with approximately the same mass content of Mn enhanced nitrogen uptake in expanded austenite during plasma nitriding [118]. Clearly, Ni is not crucial for the formation of γ_N. However, the synergistic effects of Ni and Mn on the structural response (i.e. lattice expansion and/or phase decomposition) during thermochemical treatment with nitrogen (and/or carbon) are still unclear.

Decomposition of γ_N (via long-range ordering of chromium nitrides) is principally influenced by substitutional diffusion (i.e. migration of substitutional elements towards or away from nitride embryos), the potency of which varies with alloy compositional factors (such as Ni/Mn content). Due to its low substitutional diffusivity in the Fe-Cr-Ni-Mo system (i.e. AISI 316), Ni was reported as retarding the formation of carbides in AISI 316 during low temperature carburising [17]. In contrast, Mn possesses a higher solid solution diffusivity than both Fe and Cr in the Fe-Cr-Mn system [119], in which case Mn_3N_2 precipitation was reported in γ_N for a Ni-free Mn-stabilised ASS after low temperature nitriding [118].

Last but not least, the different substitutional contents of Mn/Ni (as major substitutional austenite-stabilising elements in ASS) will influence the decomposition mechanisms in a nitrogen-supersaturated FCC lattice, by varying the ferrite-austenite transformation temperature. The decomposition mechanism of γ_N is known for AISI 304L to be $\gamma_N \rightarrow \alpha$-ferrite + CrN, whereas for AISI 316L, having higher Ni content (an Mo content), $\gamma_N \rightarrow \gamma$-austenite + CrN is commonly reported [112, 120, 121].

As one of the main compositional differences between AISI 304 and AISI 316 type ASS, the influence of Mo content could also be found from the early studies on these two types of ASS after low temperature nitriding. The presence of Mo does not seem to influence the paraequilibrium solubility of N in expanded austenite, since the homogenous nitrogen-expanded austenite powders of both alloys showed similar saturated nitrogen occupancy after nitriding [12]. However, Mo content tends to enhance the thermal stability of nitrogen-expanded austenite. Bell and Sun [122] investigated Fe-19Cr-11Ni-3Mo (AISI 316) and Fe-18Cr-11Ni (AISI 304) after plasma nitriding, where the presence of ~3 wt.% Mo in AISI 316

retarded the formation of nitrides to higher treatment temperatures and to longer treatment times. A similar effect was also reported by Christiansen et al. [120], who reported a decomposition activation energy of ~187 kJ/mol for AISI 316L and of ~128 kJ/mol for AISI 304L. Noticeably, there is also a significant difference in Ni content between the AISI 316 and AISI 304 type ASS.

2.3.2.2 Ni-Cr and Co-Cr alloys after low temperature diffusion treatments

Apart from Fe-Cr alloys (such as ASS), similar N-rich metastable layers were reported in Ni-Cr and Co-Cr alloys after plasma nitriding. As early as 1998, Williamson [87] investigated a wide range of Fe-based and Ni-based alloys after nitrogen ion implantation at 400°C. Following an order from Fe-rich to Ni-rich alloys, 16 FCC alloys exhibited a decreasing trend in layer depth and surface nitrogen content after nitrogen implantation [87]. Taking the abnormal XRD peak shift as an indicator of γ_N formation, γ_N only formed on Fe-Cr alloys and Ni-Cr alloys, but did not form on pure Ni and Ni-20Fe after treatment, which suggested the necessity of Cr for the formation of expanded austenite. Nevertheless, similar to the γ_N formed on the Cr-containing FCC alloys in his study, conspicuous highly-expanded and less-expanded expanded FCC structures (γ_{N1} and γ_{N2} in his paper, respectively) were observed on Fe-35Ni binary steel (Invar) after low energy N-implantation [87]. However, the relative XRD peak shifts of γ(111) and γ(200) of Invar after implantation are not significantly different (i.e. no strong expansion anisotropy), suggesting nitrogen-expanded austenite might not be formed.

In 2004, Makishi and Nakata [123] systematically investigated Ni-based metallic systems after plasma nitriding at 400-800°C, which involved i) 31 types of Ni binary alloys containing nitride-forming elements (such as Ti, V, Nb, Ta, Cr, Mo, Mn, Fe, Al and Si) up to

their solid solubility limit in Ni, and ii) 8 commercial Ni alloys. Apart from the 8 commercial Ni-Cr alloys, surface diffusion layers were also observed on Ni-Ti, Ni-V, Ni-Nb and Ni-Cr binaries after treatments. The low-temperature nitrided layers on Ni-Ti, Ni-V, Ni-Nb and Ni-Cr alloys exhibited XRD peaks "not detected in the ASTM Powder Diffraction File", which appear analogous to the XRD peak shift and broadening of expanded austenite. These low-temperature nitrided layers on Ni-alloys also presented other features, such as homogenous distribution of substitutional elements and metastability − similar to the metastable nitrogen-expanded austenite formed on ASS. This leads to a strong suggestion that strong nitride-forming elements other than Cr could also facilitate the formation of metastable N-rich expanded-FCC layers after low temperature nitrogen insertion. Nevertheless, different to the TEM diffraction features of nitrogen-expanded austenite layers (as shown in **Fig. 2.11-2.13**), large diffused diffraction spots were observed in the N-rich layers on Ni binaries in the study by Makishi and Nakata [123], which were attributed to fine nitride particles and large microstrain in the diffusion layer. Fine (~6 nm) disk-like particles were reported at low temperature (e.g. in Ni-7Ti and Ni-30Cr) coherent to the FCC matrix (**Fig. 2.14a,b**), which transformed to ~10-15 nm incoherent spheroid precipitates at high treatment temperature (**Fig. 2.14c,d**) [123]. Strictly speaking, it is still a question whether these metastable N-rich layers (produced on Ni binaries) could be denoted as expanded austenite or not, since no such metastable zones or particles could be seen in the γ_N synthesised on ASS after low-temperature nitriding.

Li et al. [124] (probably firstly) investigated Co-Cr alloys after low temperature carburising, where precipitation-free carbon-expanded austenite was generated at low treatment temperatures – with clear enhancement of material surface hardness and corrosion resistance. In 2008, Lutz et al. [125] reported formation of metastable γ_N on three Co-Cr alloys (i.e. Co-

28Cr-5Mo, Co-20Cr-10Ni-15W-3Fe and Co-22Cr-22Ni-14W-3Fe, in wt.%) after plasma immersion ion implantation (PIII) at ~230-580°C for 2hrs. Characteristic XRD peak shifts of γ_N were observed on both AISI 304 and Co-22Cr-22Ni-14W-3Fe at temperatures less than 400°C, whist CrN formation was observed for both alloys at higher temperatures. Compared to those formed on ASS, γ_N layers were thinner on Co-Cr alloys.

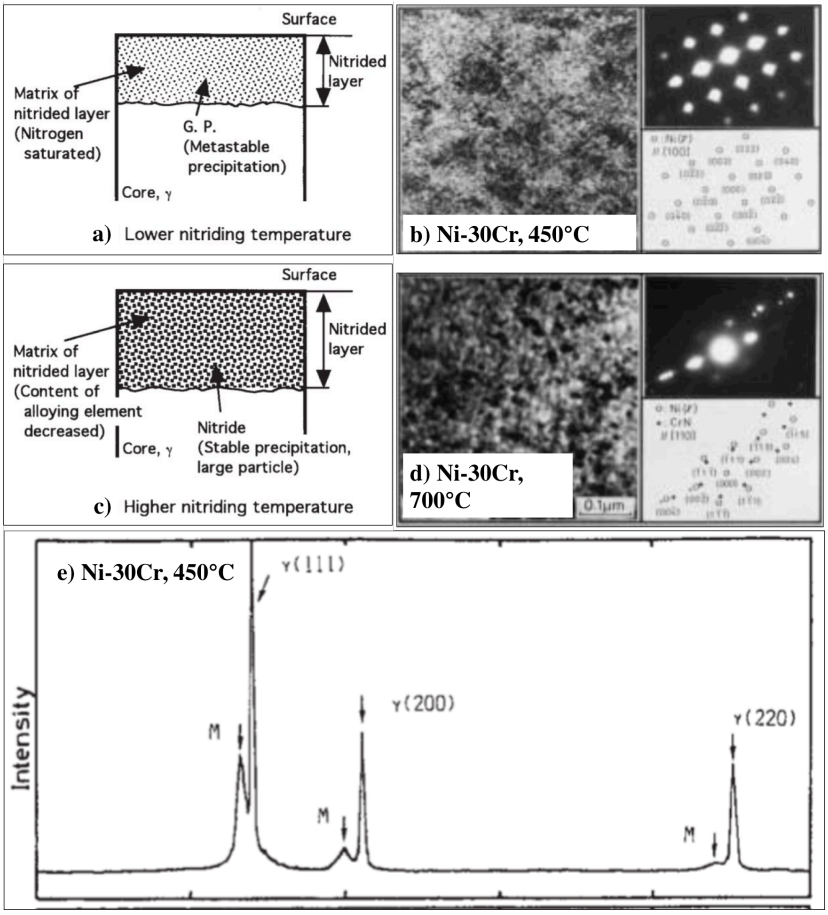

Fig. 2.14 Schematic illustration of Ni-binary alloys and TEM images (and EDPs) of Ni-30Cr alloy after plasma nitriding at low temperature (a, b, respectively), and at high temperature (c, d, respectively); and e) XRD of Ni-30Cr after plasma nitriding at 450°C (reproduced from Ref. [123])

Intriguingly, Dong [10] pointed out in his review paper that the matrix elements of Fe, Co and Ni are all 3d transitional metals, having outer electron structure of $3d^6 4s^2$, $3d^7 4s^2$ and $3d^8 4s^2$, respectively. The metallic elements associated with the formation of metastable expanded austenite − which were reported in the open literature as discussed above in this section − are Ti, V, Cr, Mn, Fe, Co, Ni and Nb. Apart from Nb (in the case of metastable N-rich layers formed on Ni-Nb binaries [123]), these elements are all 3d transition metals having outer electron shell form $3d^2 4s^2$ (for Ti) to $3d^8 4s^2$ (for Ni), whilst the outer electron shell is $2s^2 2p^2$ for carbon and $2s^2 2p^3$ for nitrogen. The formation of metastable expanded austenite, with respect to electron theories of alloys, could also be investigated on the electronic structure, chemical bonding and magnetism (not in the scope of this study). For example, Fewell [126] reported in 2000 that the γ_N layer (produced on AISI 316) changed from ferromagnetic to paramagnetic as the nitrogen content decreased from surface to unmodified core, whereas a later (in 2016) study by Brink et al. [126, 127] clearly demonstrated the composition-dependent magnetic properties for the γ_N layer produced (on AISI 316).

2.3.3 Commercial low-temperature diffusion treatment processes and applications

2.3.3.1 Carburising − Kolsterising (Bodycote Plc.) and SAT12 (Swagelok Co.)

Commercial exploitation of low-temperature thermochemical diffusion treatment of stainless steels can be traced back to as early as 1983, when Kolster [128-130] first claimed a surface treatment for stainless steel, capable of enhancing material wear performance without loss of corrosion performance. The development of this successful proprietary gaseous carburising treatment (the so-called 'Hardcor' process of Hardcor B.V. − later renamed as 'Kolsterising®' by Bodycote Plc. in honour of the ground-breaking work by Kolster) could be traced back to investigations at the Netherlands Organisation for Applied Scientific Research (TNO) during

the 1970s, when Kolster investigated the transport of alloying elements of steels in liquid sodium cooling systems for nuclear power industry applications [131]. No process details were ever openly published; however, from the early 1990s, Kolsterising® (or Hardcor) has been routinely applied on ASS − where both wear and corrosion resistance are required − such as in the food processing, automotive, offshore and medical industry sectors [129].

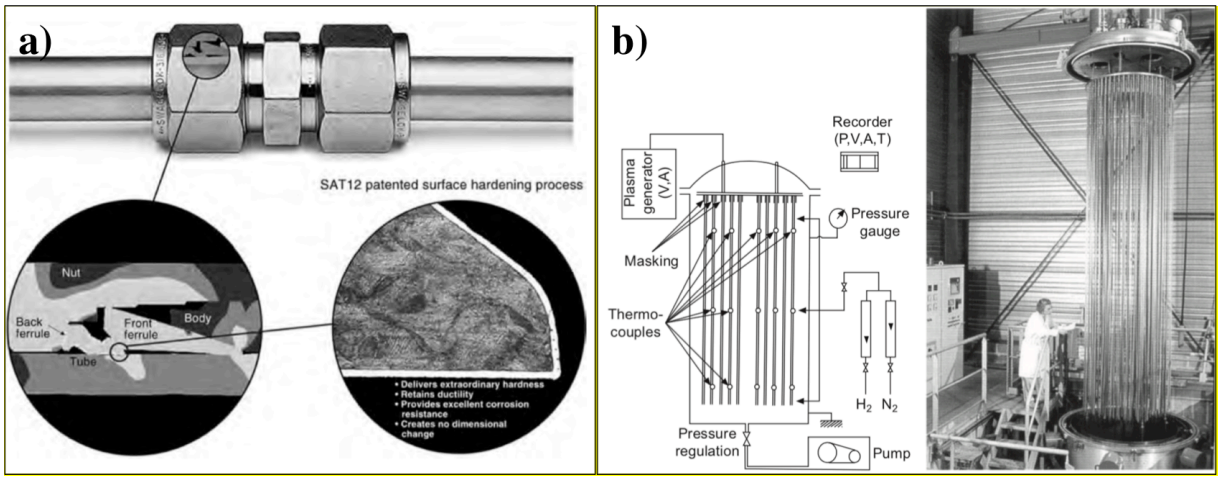

Fig. 2.15 Illustrations of two typical applications of low-temperature thermochemical treatments, a) SAT12 for Swagelok tube fitting (AISI 304 or 316), and b) Nivox 2 for rod clusters control assembly (AISI 316L) used in pressurised water nuclear reactors (reproduced from [132])

After a research project (involving Swagelok, Case Western Reserve University, and Oak Ridge National Lab) from 2004, Collins and Williams [133] published a low temperature colossal supersaturation process (LTCSS or SAT12), for which general process details can be found in patents of Swagelok Co. from 2000 [134-137]. Gaseous HCl was used during an activation processes to remove the surface chrome-oxide film from the stainless steel before gaseous carburising at ~470°C. This process was developed specifically for new types of tube

fitting ferrules of Swagelok Co, which enabled strong and vibration-resistant grip between fitting component and ferrules, as shown in **Fig. 2.15a**.

2.3.3.2 Nitriding – Nivox 2 (Bodycote Plc.)

As recently reviewed by Somers and Christiansen [9], Lebrun et al. [138] reported in 1972 a zone of supersaturated austenite (with a lattice parameter of ~0.368 nm) in-between the topmost compound nitride layer and the unmodified core on 18-8 ASS (i.e. AISI 304) after plasma nitriding at 550°C. This early study on plasma nitriding of ASS led to the establishment of Nitruvid S.A in 1985. Nitruvid S.A was specialised in low temperature (pulsed DC) plasma nitriding of ASS [139] (see Ref. [140] for process details) before the acquisition by Bodycote Plc. in 2010. "Nivox 2", as a low-temperature plasma nitriding process developed by Nitruvid S.A, has been applied on control rods (AISI 316L type ASS) in nuclear reactors as shown in **Fig. 2.15b**. Owing to the metastability of N-expanded austenite, a service life of no more than 5000hrs was recommended for a service temperature of 350°C [139]. Noticeably, "Nivox 2", which was known as a competitive commercial low-temperature plasma nitriding process in the market from 2002 [139], had first been published in ~1994 [141]. The establishment of the low-temperature diffusion treatment (i.e. plasma nitriding) by Nitruvid was clearly somewhat later than Kolster's Hardcor process in 1983 [128].

3 Experimental Procedure

3.1 Materials Investigated

The nominal substrate compositions are shown, according to ASTM standards, in **Table 3.1**. The composition of proprietary Staballoy AG17® (ATI Allvac Ltd.), since not listed in the ASTM system, is shown according to the company datasheet [142]. Some minor elements (such as P, S and B that these alloys might also contain) are not listed in this table, since their contents are negligible in these commercial alloys. RA 330® (NeoNickel Ltd.) and Invar® 36 (City Special Metals Ltd.) were obtained in solution-annealed condition. Invar 36 was sliced as ~4 mm thick 20 mm diameter disks. AISI 304, Staballoy AG17, RA330, and Hadfield steel were prepared as ~50×25×4 mm rectangular coupons.

Table 3.1 Nominal material compositions, in wt.%

Material	ASTM	Fe	Cr	Ni	Mn	N	C	Others
AISI 304	ASTM A240, UNS S30400	Bal.	17.5-19.5	8-10.5	2	0.1	0.07	0.75 Si
Staballoy AG17	/	Bal.	17	0.8	20	0.5	0.03	0.3 Si, 0.05 Mo
RA 330	ASTM B536-07, UNS N08330	Bal.	17-20	34-37	2 max	/	0.08 max	0.75-1.5 Si, 1 max Cu
Invar 36[A]	ASTM F1686-06, UNS K93603	Bal.	0.25	36	0.6	/	0.05	0.4 Si, 0.5 Co, 0.1 Al, 0.1 Mg, 0.1 Zr, 0.1 Ta
Hadfield steel	ASTM A128 Grade B2	Bal.	/	0.2	11.5-14	/	1.05-1.2	1 max Si

[A] The total amount of Al, Mg, Ti and Zr is below 0.2 wt.%

One flat surface of the substrate coupons/disks was ground using silicon carbide paper with grit sizes from P400 to P1200 and then polished to mirror finish using Buehler MetaDi^{TM} monocrystalline diamond suspensions (6 μm to 1 μm, successively). The measured mean surface roughness, Ra, was ~0.02 ±0.01 μm after polishing.

3.2 The Triode Plasma Nitriding Process

3.2.1 Treatment strategy and sample designations

A designation system (as presented in **Table 3.2**) was derived, based on the treatment history and substrate composition of each sample. Apart from treatment temperature and time, other treatment conditions were kept constant for each chamber configuration. Detailed procedure is shown in **Sections 3.2.2** and **3.2.3**. The untreated samples, which are denoted with 'U', are all characterised and evaluated after polishing. Treated samples were denoted correspondingly with the treatment temperature and time as shown in **Table 3.2**. For example, untreated Hadfield steel is designated as U-Had; 400°C and 20hrs treated RA 330 is designated as 400C20h-330.

Table 3.2 Sample designation system

Chamber configuration	Temperature	Time	Substrate materials
A	400°C − 400C 425°C − 425C 450°C − 450C	4 hours – 4h 20 hours – 20h	AISI 304 − 304 Staballoy AG17 − AG17 RA 330 − 330 Invar 36 − Invar
B	300°C − 300C	4 hours – 4h 8 hours – 8h 12 hours −12h 20 hours – 20h	Hadfield steel − Had

3.2.2 Triode plasma nitriding – equipment and chamber configurations

Nitriding was performed in a low-pressure triode-plasma configuration using a modified Tecvac IP70L commercial PVD coating unit, where an additional tungsten filament was used as a thermionic electron emitter to enhance ionisation during processing [20-23]. The vacuum process chamber (~70×70×70 cm) was at earth potential during the entire process. As shown in **Fig. 3.1a**, the vacuum chamber is connected with two diffusion pumps during processing. Evacuation directions are indicated with white arrows. Inside the chamber, the substrate

holder is surrounded by four auxiliary radiant heating units (two at the back and one at each side). A tungsten filament (~900 mm long and 0.75 mm diameter) at the bottom of chamber provides independent control of electron emission impact ionisation during the triode process.

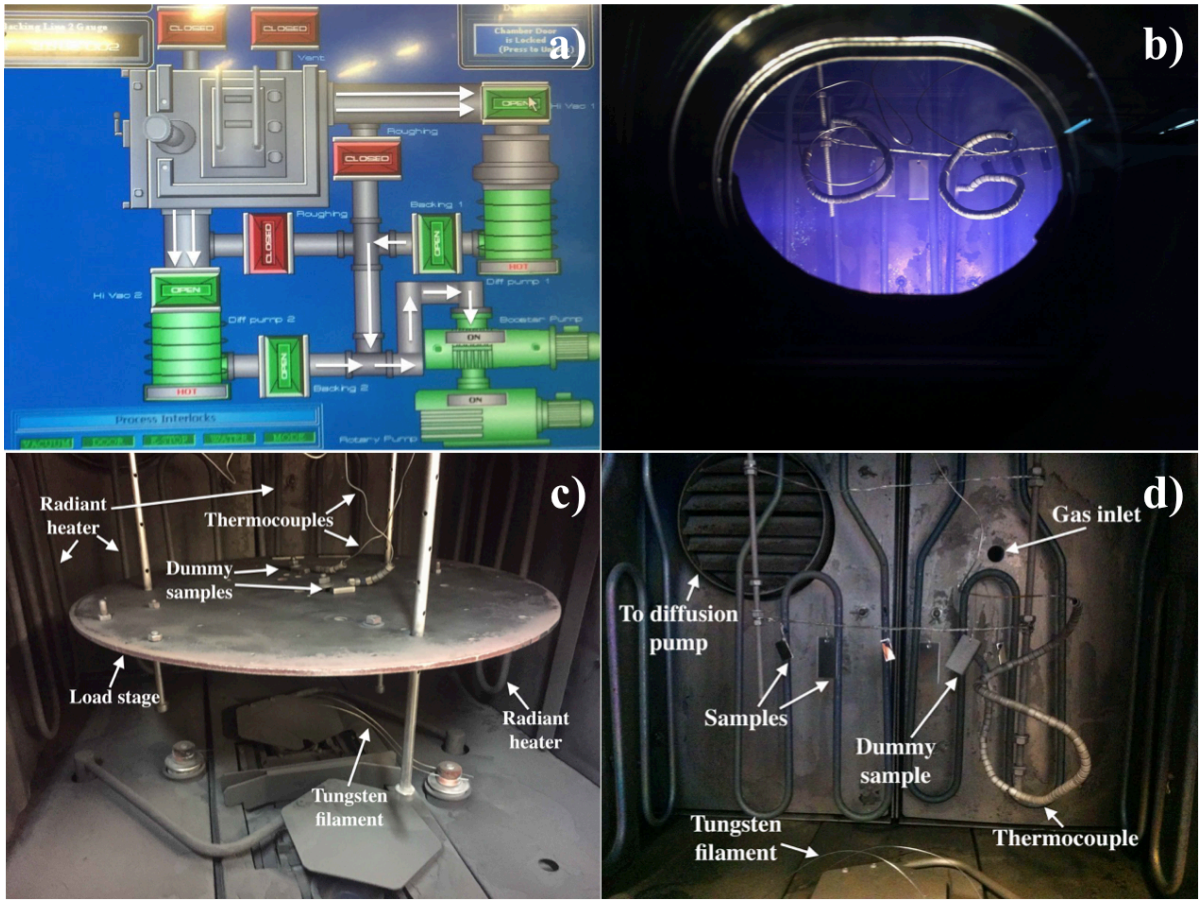

Fig. 3.1 a) Illustration of vacuum system, b) a photo through observation window during a TPN process, c) chamber configuration A, d) chamber configuration B

Two chamber configurations were used in this work (**Fig. 3.1c,d)** for the substrates and treatment conditions shown in **Table 3.2**. Configuration A was adopted for the majority of the treatments in this study, for comparison purposes at temperature regime of 400-450°C. As shown in **Fig. 3.1c**, samples were mounted on top of a 5 mm thick 500 mm diameter stainless steel load stage, which is located in the middle of chamber. Two additional dummy stainless steel samples of size ~50×25×4 mm were also mounted on the load stage. A type-K

thermocouple was inserted into each dummy sample for temperature monitoring and control. The measured temperature variation across the load stage (i.e. from center to edge) was ~1-2°C during TPN processing at 400-450°C.

Hadfield steel is susceptible to carbide precipitation after prolonged treatments at temperatures above ~300°C. Configuration B provided relatively better surface exposure to plasma, which enabled sufficient ion bombardment of the sample at low treatment temperature such as 300°C. As shown in **Fig. 3.1d**, samples were hung on stainless steel wires in the middle of the chamber. An additional dummy stainless steel sample, inserted with a type-K thermocouple, was also hung at the same chamber height for temperature monitoring and control. The measured temperature variation across the steel wire (i.e. from middle to both sides) was ~1-3°C during a typical 300°C TPN process.

3.2.3 Triode plasma nitriding − process procedure

Before TPN treatment, the polished samples were cleaned ultrasonically in acetone for 15mins, in isopropanol for 10mins, and then dried using dry compressed air. Process parameters were observed, adjusted and logged during TPN. Operator visually checked the chamber periodically through a glass window to ensure plasma generation and free of arcing (**Fig. 3.1b**). For different research purposes, the treatment procedure varies; nevertheless, following a chronologic order, a typical triode-plasma nitriding process could involve the following steps:

1. Evacuation and pre-heating: The chamber was evacuated to a base pressure of 2×10^{-3} Pa. Samples were then pre-heated to (and held at) ~300°C using radiant heating to aid evacuation for process cleanliness, until reaching the base-pressure. This temperature is insufficient to

cause any significant metallurgical transformation in the substrates investigated. Additionally, in vacuum, the oxidation of steel surfaces is minimal and (if already present) surface oxides will be removed by the plasma sputter cleaning in step 2.

2. Plasma sputter cleaning and triode plasma heating: After pressure stabilised < 2×10^{-3} Pa at 300°C, gaseous Ar was introduced into chamber and samples was negatively biased at 800V. Plasma sputtering was performed at 2 ±0.2 Pa Ar atmosphere for ~10-15 mins. Substrate bias was then reduced to -200V for plasma heating. Filament power was switched on and biased at -200V. Ar flow rate was reduced to maintain a chamber pressure of 0.3-0.5 Pa. Typical heating rates were ~7-10°C/min for plasma heating. This step helped to remove surface oxides and/or contamination from sample surfaces (especially to remove protective chromium oxides from stainless steels) so that material surfaces were ready for the subsequent nitrogen diffusion process.

3. Triode plasma nitriding: Once the target temperature was reached, argon flow rate was reduced and gaseous N_2 was introduced into chamber. All triode-plasma nitriding treatments were performed at a chamber pressure of 0.4 ±0.04 Pa in a N_2:Ar atmosphere (7:3 volumetric ratio). Both substrates (i.e. cathode) and filament unit (i.e. another cathode) were negatively biased at 200V.

4. Cooling and venting: When the target treatment time was reached, both radiant heater and plasma units were turned off. Samples were cooled under vacuum (i.e. < 1×10^{-3} Pa) until 180°C. Typical cooling rates were ~2-3°C/min. The chamber was then vented to atmosphere and samples were extracted.

Apart from the different treatment temperatures and times, TPN was performed at a constant chamber pressure of 0.4 Pa, a 7:3 N_2:Ar gas volumetric ratio, substrate and filament bias at -200V. Nevertheless, for chamber configuration A, auxiliary radiant heating was used (together with plasma heating) to support different treatment temperatures, whilst substrate current density was deliberately kept constant at ~0.13 mA/cm^2 (i.e. almost constant plasma heating at different treatment temperatures achieved) via altering the filament electron emission current. In this case, nitrogen diffusion and crystallographic structure at the treated surfaces would be mainly influenced by the different treatment temperatures and times applied during nitriding rather than different ion bombardment energy/intensity. For chamber configuration B, plasma heating was used (without radiant heating) to achieve an ultra-low nitriding temperature and to provide as much ion bombardment as possible under the selected treatment condition for Hadfield steel.

3.2.4 L/λ value for this study

For chamber configuration A, treatment parameters were V ≈ 0.3 m^3, P = 0.4 Pa, T = 673-723 K, V_c = 200 V and J ≈ 0.13 mA/cm^2. The predominant ions are N^+, N_2^+ and Ar^+. An optical emission spectroscopy study showed that N_2^+ is the major nitrogenous species (i.e. over 80%) in the cathode sheath when using gas mixtures of argon and nitrogen under a triode plasma configuration [23]. The charge exchange collision cross-section, σ_C, for N_2^+ could be taken as ~3×10^{-19} m^2 for the low ion energy of 200 eV [143]. In this case, the cathode free-fall model, as mentioned in **Section 2.1.3**, could be used to estimate the L/λ_c value. Recall **Eq. 2.6** and **Eq. 2.9** in **Chapter 2,** the L/λ_c value could be estimated as being as low as 0.01. In other words, ions were nearly collisionless when travelling through cathode sheath, that the incident ions were almost mono-energetic at ~200 eV. Nevertheless, the above calculation

does not take account of other potential species, such as Ar^{2+}, N^{+} and/or the sputtered species from substrate surfaces.

3.3 Statistical Considerations

Data in this study is presented as mean ± error. The mean value (i.e. sample mean, x) was calculated from a number of measurements. The sampling size, n_m, is given in the following sections with testing procedures. Sampling distribution is assumed to be normally distributed. Error is based on 95% confidence interval and is calculated from the standard error of the sample mean, SE(x), as follows:

$$\boldsymbol{Error = 1.96 \times SE(x) = 1.96 \times \frac{s}{\sqrt{n_m}}} \qquad \textbf{Equation 3.1}$$

where s is the sample standard deviation. That is, there is 95% confidence that the population mean is located in the interval of ±error around the sample mean.

3.4 Energy Dispersive X-ray Spectroscopy

Compositions of untreated and nitrided surfaces were examined quantitatively with Energy Dispersive X-ray (EDX) spectra using Oxford Instruments INCA EDX system via a XL30S FEG electron microscope. The beam acceleration voltage, spot size and working distance were 15 kV, 5 and 5 mm, respectively. Beam intensity was calibrated with a cobalt standard. The untreated (substrate) compositions were evaluate and shown in **Table 4.2**. After nitriding, material surface nitrogen content was averaged from 10 X-ray spectra, which were taken at random sites (with an area of 65×45 μm for each site) across the treated surface.

Table 3.3 Material compositions, compositions were normalised in wt.%

Material	Fe	Cr	Ni	Mn	N	C	Others
AISI 304	70.6	19.2	8.1	1.7	/	/	0.4 Si
Staballoy AG17	61.7	17.4	0.8	18.6	0.5*	/	0.3 Si, 0.7 Co
RA 330	41.3	19.4	34.1	1.6	/	/	1.5 Si, 0.1 Cu, 0.2 Al
Invar 36	61.4	0.1	35.1	0.5	/	/	0.2 Si
Hadfield steel	85.2	0.2	0.2	12.7	/	1.2*	0.5 Si

*Nitrogen content of Staballoy AG17 and carbon content of Hadfield steel were determined in Sheffield Assay Office, via in-house method (thermoconductivity and IR absorption, ATM 149) and combustion/Infra-red analysis (ATM 82), respectively

3.5 Optical Microscopy

The optical images in this work were extracted from a Nikon Eclipse LV150 Optical Microscope (OM) equipped with Buehler Omni Met software. For each triode-plasma nitriding treatment set, material surfaces were firstly examined under OM. After wear and corrosion testing, the worn or corroded surfaces were also examined.

3.6 Back-scattered Electron Microscopy

Flat sample coupons or disks were cut transversely using an abrasive cutting wheel (i.e. Struers Secotom-50) and mounted with conductive Bakelite resin. The mounted sample cross-sections were polished. Diffusion-introduced chemical composition-depth profiles were revealed transversely under back-scattered electron (BSE) imaging using a FEI Nova NanoSEM 450 instrument. The acceleration voltage and spot size were 20kV and 5.5, respectively.

Diffusion layer depths of the ASS after nitriding were determined based on BSE imaging, since nitrogen-rich diffusion layers (having relatively lower mean atomic weight) and unmodified core materials (having relatively high mean atomic weight) present sharp contrast/brightness at the layer/core boundary. The mean layer depth was measured and averaged from a total number of 50 measurements (10 measurements per electron micrograph, 5 micrographs in total).

3.7 Hardness Indentation Measurements

3.7.1 Vickers Indentation

Vickers hardness was evaluated on top of the untreated and treated material surfaces via a Struers Durascan 70 instrument. Indentation load and dwell time were 0.025 kg and 15 s, respectively. The mean surface hardness of material (before and after TPN) was calculated from 12 random indents.

3.7.2 Nanoindentation depth-profiles

The treated layer hardness-depth profiles were evaluated in polished cross-section with nanoindentation via a Hysitron Triboscope® Nanoindentor equipped with a Berkovich diamond indenter. Indentation load was 5 mN. The displacements of nanoindents to sample surface were measured using the instrumented atomic force microscope (AFM) after indentation. Nanoindents were placed from near surface (at depths of ~2-4 μm) to core at a ~4 μm separation. The mean hardness value at each depth level was calculated from at least 5 nanoindentations.

3.8 Phase Characterisations

3.8.1 X-ray Diffraction analysis

X-ray diffraction (XRD) analysis was carried out on top of sample surfaces before and after TPN under Bragg-Brentano θ-2θ geometry via a Bruker D2 PHASER (Cu-$K\alpha_{average}$, 0.15418 nm). Tube voltage and current were 30 kV and 10 mA, respectively. Invar and Hadfield steel samples were also characterised under Seeman-Bohlin geometry (at 2° glancing angle) via a monochromated PANalytical Xpert^3 diffractometer ($CuK\alpha_1$, 0.15406 nm). Tube voltage and current were 45 kV and 40 mA, respectively. Peak intensity of samples could vary significantly (e.g. after nitrogen-supersaturation or phase decomposition); for clarity, X-ray

intensity at each 2θ angle was divided by the maximum intensity of the X-ray profile for each sample (i.e. normalised profiles).

X-ray attenuation depths, as shown in **Table 3.4** with respect to sample compositions (using AbsorbDX software), are shallower under glancing-angle XRD (GAXRD) compared to those under θ-2θ XRD. To identify depth-related material phase composition changes, Invar and Had at selected treatment conditions were successively ground using P1200 grit paper and characterised under GAXRD.

Table 3.4 X-Ray attenuation depths in materials (95% of X-ray signal)

Material, atomic%	Bragg-Brentano θ-2θ geometry	Seeman-Bohlin geometry (2° glancing angle)
304 – Fe-19Cr-8Ni	~1.8-3.5 μm	/
AG17 – Fe-18Cr-20Mn-2N	~1.7-3.3 μm	/
330 – Fe-19Cr-35Ni	~2.4-4.7 μm	/
Invar – Fe-35Ni	~2.3-4.4 μm	~0.6 μm
Had – Fe-13Mn-5C	~1.7-3.3 μm	~ 0.4 μm

3.8.2 Transmission Electron Microscopy

Transmission electron microscopy (TEM) analysis was carried out via a Philips EM420 instrument at beam acceleration voltage of 120 kV and a FEI Tecnai T20 instrument at beam acceleration voltage of 200 kV. The low-magnification images and electron diffraction patterns (EDPs) were extracted from Philips EM420, while high-resolution images were extracted from FEI Tecnai T20. The diameters of three diffraction apertures for Philips EM420 were ~540 nm, ~1400 nm and ~5800 nm. A cross-sectional TEM foil was prepared from U-330 and examined under EM 420, as shown in **Fig. 3.2**. The diffraction camera length of the Philips EM420 could be calibrated using EDPs extracted from the U-330 steel sample (as shown in **Fig. 3.2b,c**), taking lattice constant of U-330 sample as ~0.358 nm (determined from the XRD peak positions of U-330).

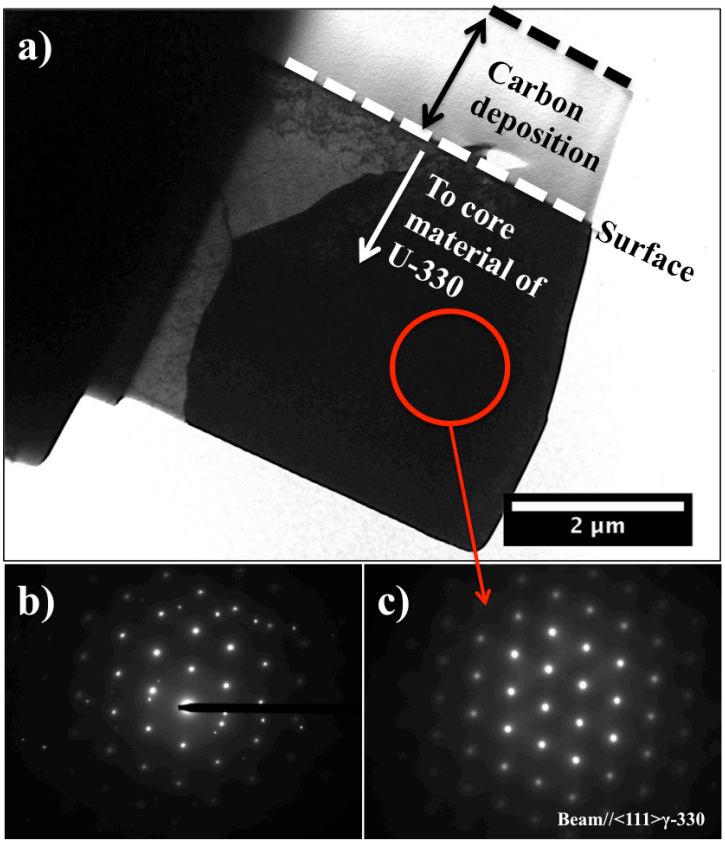

Fig. 3.2 FIB prepared TEM thin foil of untreated RA330 (U-330) under Philips EM420, a) BF-TEM image, b) EDP of the entire foil using the largest diffraction aperture (~5800 nm diameter), and c) EDP of an austenitic grain using (~1400 nm diameter) diffraction aperture at its <111> zone axis

3.8.3 Focused Ion Beam Method

Thin cross-sectional TEM foils were prepared from sample surfaces using the focused ion beam (FIB) milling method via a FEI Quanta 200 3D electron microscope as shown in **Fig. 3.3**. A gallium ion beam was used at beam acceleration voltage of 30 kV for milling, cutting and thinning.

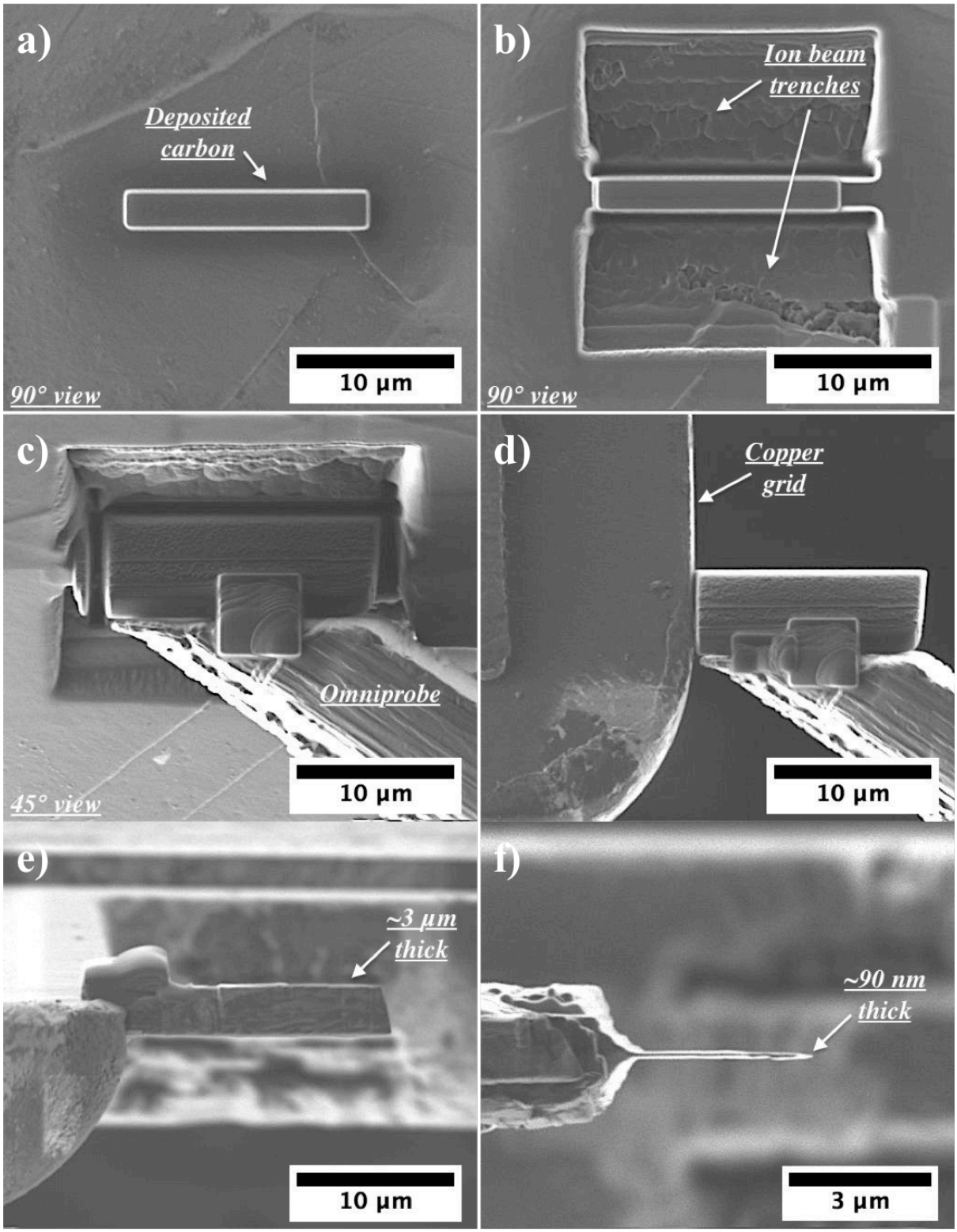

Fig. 3.3 Ion beam images during FIB process (chronological order from a to f)

A carbon layer (~2-3μm thick) was firstly deposited on top of sample surface to protect material from ion beam damage in the following process steps (**Fig. 3.2a**). Two trenches were milled, using a high ion beam current of 5 nA, above and below the carbon deposition (**Fig. 3.2b**). Material under the carbon deposition (i.e. from material surface to ~4-8 μm deep) was attached to an omniprobe and cut out using a lower ion beam current of 0.5 nA (**Fig. 3.2c**), and was then extracted from the material surface. The extracted material was attached to a copper grid (**Fig. 3.2d**) for further thinning. The sample was finally thinned to <100 nm thickness (**Fig. 3.2e** to **Fig. 3.2f**) for TEM examination. In order to reduce ion beam damage during thinning, beam current was gradually reduced to i) 0.5 nA for sample thickness from ~2-3 μm to ~500 nm, ii) 300 pA for sample thickness from ~500 nm to ~150 nm, and iii) 10-30 pA to thickness <100 nm.

3.9 Material Wear and Corrosion Performance

3.9.1 Wear testing

3.9.1.1 Reciprocating-sliding wear testing

Sliding wear (dry) performance was evaluated using a (homemade) reciprocating-sliding tribometer. The sample was mounted on a flat stage with surface of interest facing upward. A 10 mm diameter WC-6 wt.% Co ball (Spheric-Trafalgar Ltd.) was loaded at ~9.8 N on top of sample surface. Before each test, sample coupon and ball were ultrasonically cleaned and rinsed with isopropanol for 10 mins, and dried using dry compressive air.

During sliding, the sample stage was set to move horizontally at 8 Hz with a reciprocation amplitude of 10 mm. Relative humidity, temperature and friction coefficient were recorded during each sliding test. All sliding tests were performed under room conditions at temperatures between 20 and 25°C and at relative humidities between 15 and 25%. A total sliding distance

of 500 m was used, for which the measured wear depths were all shallower than the diffusion layer thicknesses of nitrided samples tested. Two repetitions of sliding test were performed.

3.9.1.2 Micro-abrasion wear testing

Abrasion wear performance was evaluated using a Plint TE-66 abrasion tester, as shown in **Fig. 3.4a**. Sample coupon was mounted at abrasion tester with surface of interest facing sideway. A preconditioned 25.4 mm diameter steel ball (SAE52100) was loaded at 0.1 N or 0.2 N against the sample surface. The preconditioning process, which roughened the ball surface to assist entrapment of abrasives, involved five micro-abrasion runs (i.e. 300 ball rotation revolutions) against a U-304 stainless steel coupon. Ball rotation speed was set at ~0.1 m/s. Slurry concentration was 0.8 g/ml or 0.24 volume fraction (i.e. SiC powder in distilled water). The abrasive silicon carbide powder (Grade P1200 SiC, Logitech Ltd.) had a mean powder size of ~3.1 μm [144], as shown in **Fig. 3.4b**. The abovementioned parameters were also selected to achieve 3-body abrasion mode (i.e. spherical crater without abrasion grooving inside) as shown in **Fig. 3.5c,d**.

Before each test, both sample and ball were cleaned with isopropanol in an ultrasonic bath for 10mins and dried using dry compressed air. During abrasion, the ball was rotated against the sample surface and silicon carbide slurry was added via a syringe. Abrasion distances of ~2.39 m (i.e. 30 ball rotation revolutions) and ~3.99 m (i.e. 50 ball rotation revolutions) were used under normal loads of 0.2 N and 0.1 N, respectively, to obtain 'non-perforating' abrasion craters − with measured depths less than the diffusion layer thickness. A minimum of two repetitions were performed for each abrasion distance.

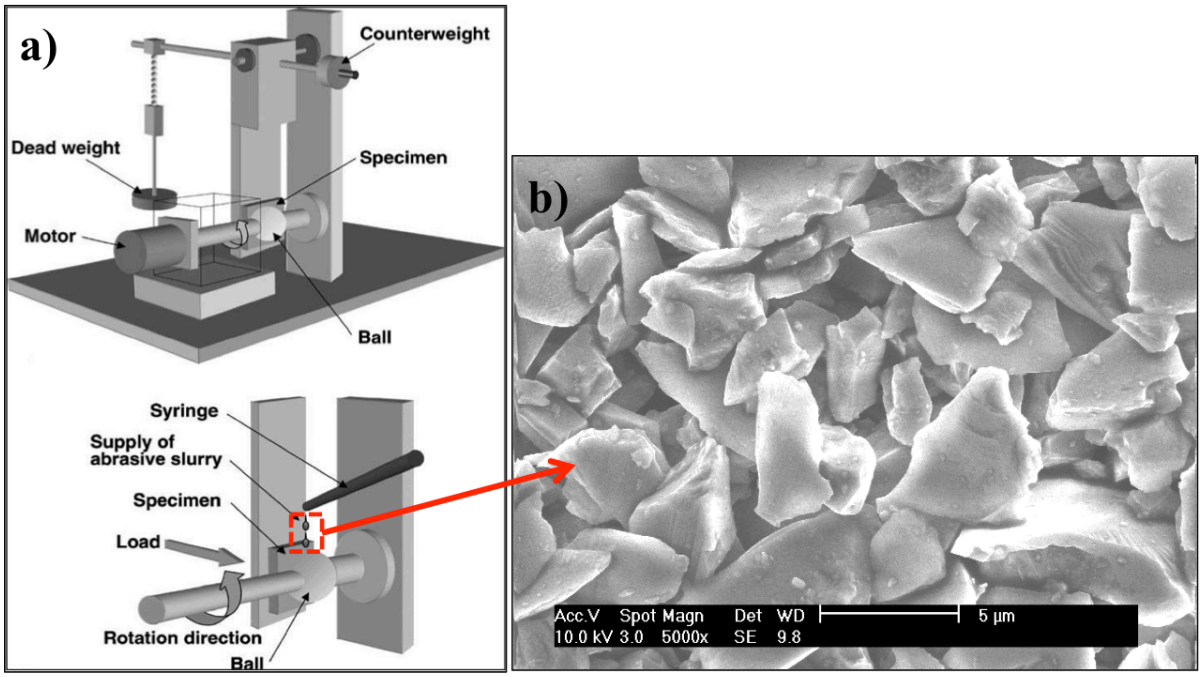

Fig. 3.4 a) Schematic illustration of abrasion tester (reproduced from Ref. [145]) and b) scanning electron micrograph of SiC powder

3.9.1.3 Surface profilometry and evaluations of wear

Worn surfaces were evaluated with a two-dimensional mechanical profilometer (Veeco Dektak 150), equipped with a 12.5 µm radius diamond tip, which was loaded at 3 mg onto the sample surface during each scan. Different scan lengths and durations were used for the different features, but were adjusted for resolutions better than 0.01 µm. Untreated sample surfaces were also examined (after polishing) before TPN, showing mean surface roughness, Ra, of ~0.02 µm for all polished surfaces. Mean surface roughness was measured and averaged from five random (randomly oriented and randomly located) scans on top of material surfaces at a scan length of 800 µm.

Parallel scans were performed perpendicular to the sliding direction at five locations along each sliding track. The cross-sectional area of each sliding scar was extracted from the

surface profile and then multiplied by the length of scar (i.e. 10 mm). The product of them was taken as the sliding wear volume.

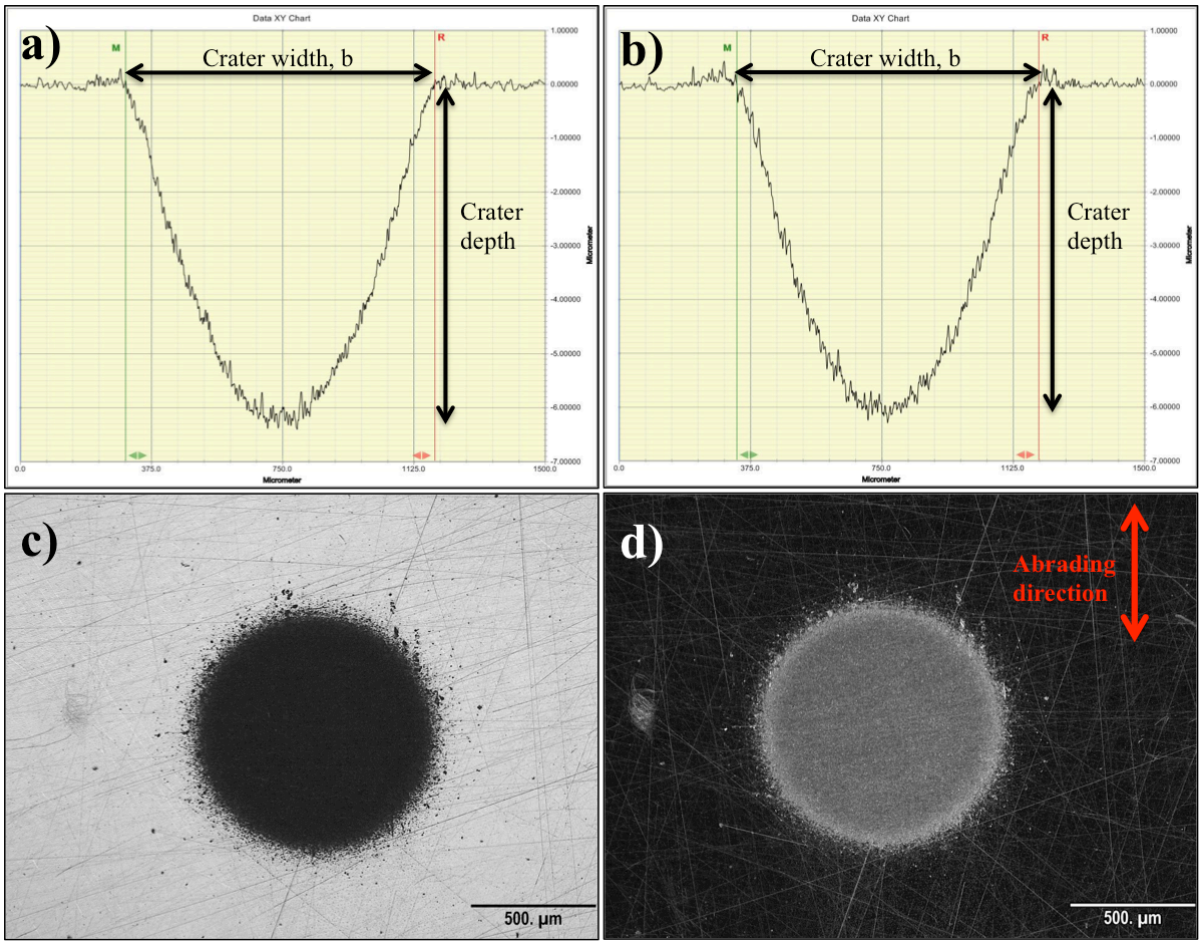

Fig. 3.5 Illustration of surface profiles obtained from an 3-body abrasion crater at scan direction a) parallel and b) perpendicular to abrading direction; Light optical images of an 3-body abrasion crater under c) bright field illumination, and d) dark field illumination

Each abrasion crater was scanned across the crater diameter, both parallel and perpendicular to the abrading direction (**Fig. 3.5a,b**). Crater diameter was evaluated from the profiles obtained. 3-body abrasion was achieved (without 2-body grooving) and craters show a spherical cap shape (**Fig. 3.5**). Abrasion wear volume, V, was calculated by:

$$V = \frac{\pi b^4}{64R} \qquad \textbf{Equation 3.2}$$

where b is the mean crater diameter and R is the ball radius (b<<R). Sliding/abrasion wear rates, κ, can be determined by:

$$\kappa = \frac{V}{SN} \qquad \textbf{Equation 3.3}$$

where S is the abrasion/sliding distance and N is the load.

3.9.2 Corrosion Testing

Material corrosion performance was evaluated using proprietary Scribner/Solartron CorrWare® software in an electrochemical cell equipped with a saturated calomel reference electrode (i.e. SCE, Hg/Hg_2Cl_2 in saturated KCl solution, E_{SCE} = 0.241 V) and a platinum counter electrode. After ultrasonic cleaning in acetone for 10mins and isopropanol for 10mins, the sample was located at the bottom of the cell. Then, 3.5wt.% sodium chloride solution (i.e. NaCl in distilled water) was added, with a sample surface area of ~0.785 cm^2 exposed to the chemical solution. Counter electrode and reference electrode were also immersed in 3.5wt.% sodium chloride solution, with the untreated/treated samples acting as the working electrode during corrosion testing.

3.9.2.1 Open circuit potential

After setting up the electrochemical cell, the exposed material surface was immersed in solution for 3600 s for open circuit potential (OCP) measurement. Potential (V) was recorded, with respect to reference electrode, and was plotted as a function of time. During OCP, corrosion reactions could be considered to be in equilibrium, where the oxidation current, I_a, for anodic reactions equaled the reduction current, I_c, for cathodic reactions. Nevertheless, corrosion reactions changed the exposed metallic surface and the chemical solution at OCP, during which it took time to reach a stabilised corrosion potential measurement.

3.9.2.2 Potentiodynamic polarisation

Immediately after stable open circuit potential measurement, potentiodynamic polarisation was carried out. An external potential was applied from -1 V to +2 V, with respect to the reference electrode, at a scan rate of ~1.667 mV/s. The working electrode current density (A/m^2) was recorded and plotted (in log scale) as a function of potential. During potentiodynamic polarisation, corrosion reactions in the electrochemical cell were forced from cathodic to anodic reactions, from which the corrosion equilibrium could be found at the lowest corrosion current between cathodic region and anodic region. The Tafel potential and current of each sample could be determined by extrapolation of the linear cathodic and anodic regions in the polarisation curve.

4 Characterisation of two proprietary austenitic stainless steels after triode plasma nitriding

AISI type 304 (i.e. Fe-18Cr-8Ni, in wt.%) and 316 (i.e. Fe-18Cr-11Ni-3Mo, in wt.%) austenitic stainless steels (ASS) have both been studied extensively after low-temperature nitriding. ASS are based fundamentally on a ternary system of Iron-Chromium-Nickel (Fe-Cr-Ni), where Ni can be replaced with Mn (wholly, or in part) for economic or other (e.g. biocompatibility) reasons. Cr has been widely referred to as an 'essential' element in the formation of γ_N, believed to assist in 'trapping' the inwardly-diffusing species and (in the case of nitrogen) forming short-range ordering of Cr-N pairs [10, 17, 87, 104, 117]. However, the synergistic effects of Ni and Mn on the structural response (i.e. lattice expansion and/or phase decomposition) during thermochemical diffusion treatment with nitrogen (and/or carbon) are still unclear.

In this chapter, two proprietary commercial alloys, ATI Staballoy AG17® (i.e. Fe-17Cr-20Mn-0.5N, in wt.%) and RA 330® (i.e. Fe-18Cr-35Ni, in wt.%), were selected for reasons of i) an equivalent Cr content (i.e. ~17-18 wt.%) without other strong nitride forming elements present and, ii) a high content of the austenite-stabilising element (i.e. 20 wt.% Mn and 35 wt.% Ni, respectively). A range of experimental treatment parameters were chosen, such that both lattice expansion and phase decomposition could be achieved in AG17 and 330 via the low-temperature triode-plasma nitriding (TPN) technique [20, 22]. A conventional AISI 304 ASS was also triode plasma nitrided at 400°C, 425°C and 450°C for 20hrs under equivalent conditions.

In **Section 4.1**, some general information about the treated surfaces − including surface nitrogen content, surface morphology and treatment layer depth − are presented and discussed. In **Section 4.2**, the crystallographic structure of surface diffusion layers is discussed with their X-ray diffractograms. Then, in **Section 4.3,** TEM diffraction features are discussed (and compared with previous literature work), to explore the analogy between nitrogen-interstitial introduced strain and mechanical strain, which leads to a discussion in **Section 4.4** of the potential influence from SFE on material crystallographic structure during low-temperature nitriding (and the SFEs of the two ASSs investigated).

In **Section 4.5**, the crystallographic structures of the surface layers synthesised are discussed (with TEM observations) – and are compared to the scientific literature. Notwithstanding the plasticity phenomena observed in heavily-expanded γ_N, in this study 'phase decomposition' is defined with respect to the formation of chromium nitrides – which requires segregation and redistribution of substitutional elements to nucleate and grow new precipitates (of a fundamentally different chemical composition and crystallographic structure) – in particular because of its significance to material corrosion properties in practical applications (see **Chapter 5** for material corrosion performances).

After a discussion on the lattice parameters extracted from TEM in **Section 4.5.1**, detailed TEM observations for the expanded and/or decomposed lattices are shown in **Section 4.5.2** and **Section 4.5.3**, respectively. Two possible 'diffusionless' plasticity mechanisms and two possible phase decomposition (and segregation) mechanisms are proposed for ASS after nitriding at low and elevated treatment temperatures, respectively. The evolutions of lattice defects generated in AG17 and 330 (and also in 304) after TPN are shown and discussed in **Section 4.5.2.1**. Evidence of lattice decomposition is given in **Section 4.5.3.1**. The influence

of material SFE (altered mainly by Mn/Ni content) on the lattice expansion and decomposition is discussed in **Section 4.5.2.2** and **Section 4.5.3.2**, respectively.

4.1 Surface composition and morphology

4.1.1 Surface nitrogen content

Surface nitrogen atomic percentages (at.% N) are presented in **Table 4.1**. The measured surface nitrogen contents all exceeded the equilibrium N solubility (c.f. ~10.3 at.% in austenitic iron [58] and < 0.65 at.% for AISI 316 ASS [10]). Under a given treatment temperature, surface N content shows an expected increasing trend with treatment time (**Table 4.1**). This increasing trend is significant on AG17 but very limited on 330.

Table 4.1 Surface nitrogen content (at.%) of 304, AG17 and 330 after TPN

Treatment	AISI 304	Staballoy AG17	RA 330
400°C 4hrs		27.8 ± 0.2	23.1 ± 0.6
400°C 20hrs	26.9 ± 0.5	34.4 ± 0.6	24.0 ± 0.8
425°C 4hrs		29.6 ± 0.4	24.1 ± 0.5
425°C 20hrs	29.3 ± 0.7	34.3 ± 0.7	25.7 ± 0.9
450°C 4hrs		26.5 ± 0.5	22.6 ± 0.8
450°C 20hrs	19.2 ± 0.3	29.2 ± 0.3	25.1 ± 0.5

The surface nitrogen contents of samples after 4hrs and 20hrs of TPN are plotted separately in two bar charts, as shown in **Fig. 4.1**. Under a given treatment time (**Fig. 4.1)**, surface N content increases slightly from 400°C to 425°C of all three ASS after TPN. However, a clear drop in surface N content is observed from 425°C to 450°C for both 304 and AG17, but not for 330. These drops of material surface N content with treatment temperature could be attributed to the lattice decomposition on ASS at this upper treatment temperature (see **Section 4.2**).

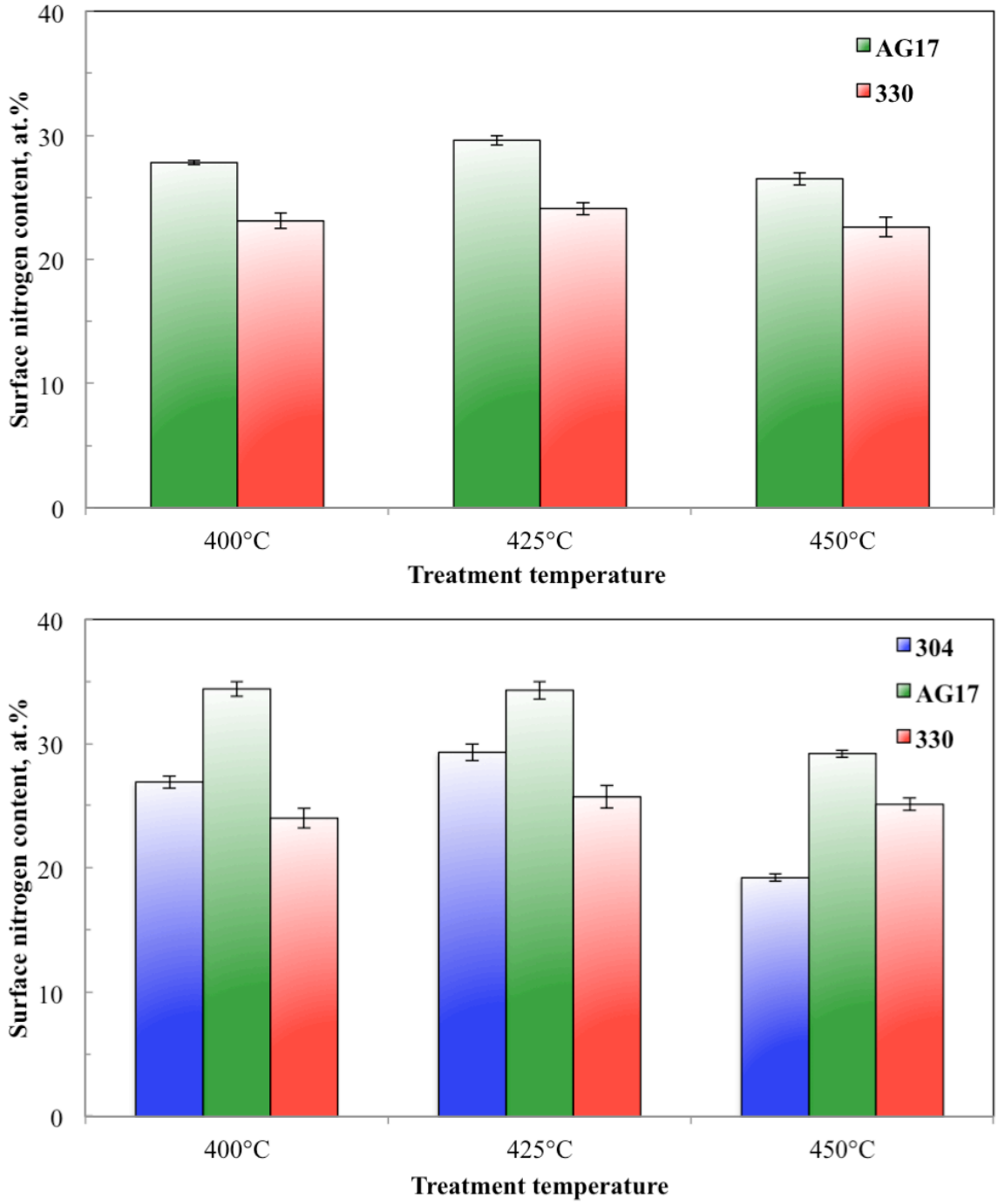

Fig. 4.1 Surface nitrogen content (in at.%) of three ASS after TPN at different treatment temperatures for a) 4 hours and b) 20 hours

As clearly shown in **Fig. 4.1**, surface N contents of the nitrided 330 (which range narrowly from ~23 to 26 at.% N) are much lower than those of the nitrided AG17 (i.e. ~26 to 35 at.% N). For prolonged treatments at low temperatures (400°C and 425°C in **Fig. 4.1b**), the surface

nitrogen contents of the nitrided 304 stay between those of the nitrided AG17 and 330 alloys, under equivalent conditions. The nitrogen contents of the low-temperature nitrided surfaces diminish – following an order from Mn-stabilised (or low Ni) ASS to high-Ni ASS, in the sequence: AG17 → 304 → 330.

4.1.2 Surface morphology under OM

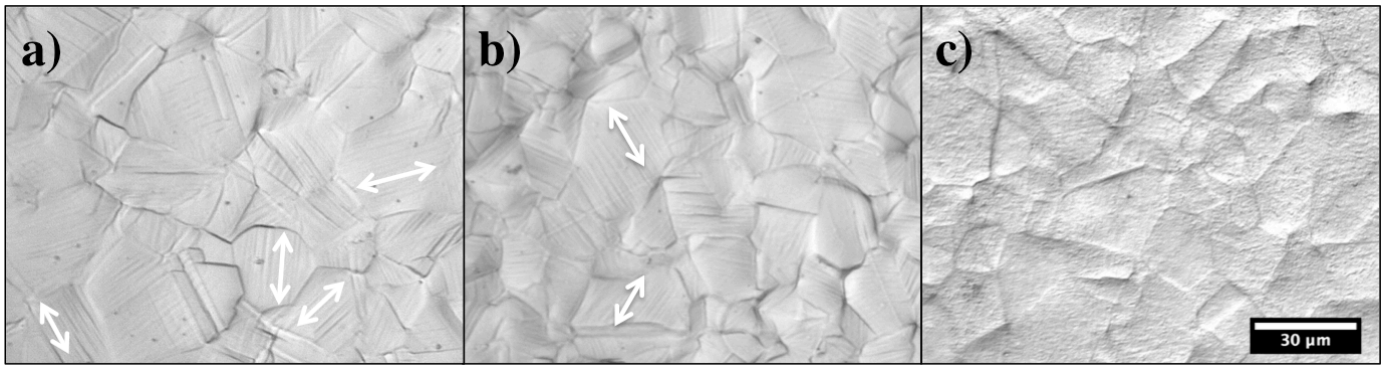

Fig. 4.2 Optical micrographs of AISI 304 after triode-plasma nitriding at a) 400°C 20hrs, b) 425°C 20hrs, c) and 450°C 20hrs

Optical micrographs of the TPN-treated surfaces are shown in **Figs. 4.2-4.4**. Individual grains are clearly observed, due to different plasma etching effects on grains of varying crystallographic orientation − showing an equiaxed polycrystalline microstructure (without 'macrozone'-like directionality) for the three ASS. The treatment temperatures are insufficient to cause grain growth for the three ASS, such that their grain sizes observed after TPN are representative of the original grain size. The 330 prior grain size is clearly larger than that of 304 and AG17, but all ASSs have a grain size range within 30-100 µm.

Groups of parallel traces are observed within grains at the surface of 400C20h-304 and 425C20h-304 (with their directions indicated by white arrows, as shown in **Fig. 4.2**), which

could be due to the nitrogen-interstitial introduced strain. Rather than parallel traces, a 'dimpled' surface is observed on 450C20h-304, hinting to an absence of γ_N (ie. low or no lattice strain), which could be due to phase decomposition expected at elevated temperature.

For AG17, parallel traces are also observed (but much lighter as compared to 304) at low treatment temperatures (with their directions indicated by white arrows in **Fig. 4.3a-c**). The surface of 425C20h-AG17 also shows an anomalous morphology with small 'hills' (**Fig. 4.3d**), which could correspond to 'incomplete phase decomposition' (with phase morphology discussed later with BSE images). Similar to 450C20h-304, 450C20h-AG17 (**Fig. 4.3f**) presents 'dimpled' surface morphology, which also hints at phase decomposition. For alloy 330 shown in **Fig. 4.4**, parallel traces are also observed, but surface 'dimpling' was not seen, suggesting no phase decomposition. However, several sharp surface traces appear conspicuous on the 450C20h-330 sample (as indicated with red arrows in **Fig. 4.4f**), which could be due to grain boundary cracks (as shown later by BSE imaging).

Optical microscopy, as a widely accessible characterisation technique, is able to reveal distinguishable surface morphologies for low-temperature nitrided surfaces. The parallel traces and 'dimples' at the treated surface could be useful to generally identify nitrogen-supersaturation and decomposition of the ASS surfaces after nitriding. As will be seen in the following part of **Chapter 4** (especially in **Section 4.2**), the crystallographic structures of treated surfaces (determined from XRD and TEM analyses) match with the phase compositions hinted at by simple OM.

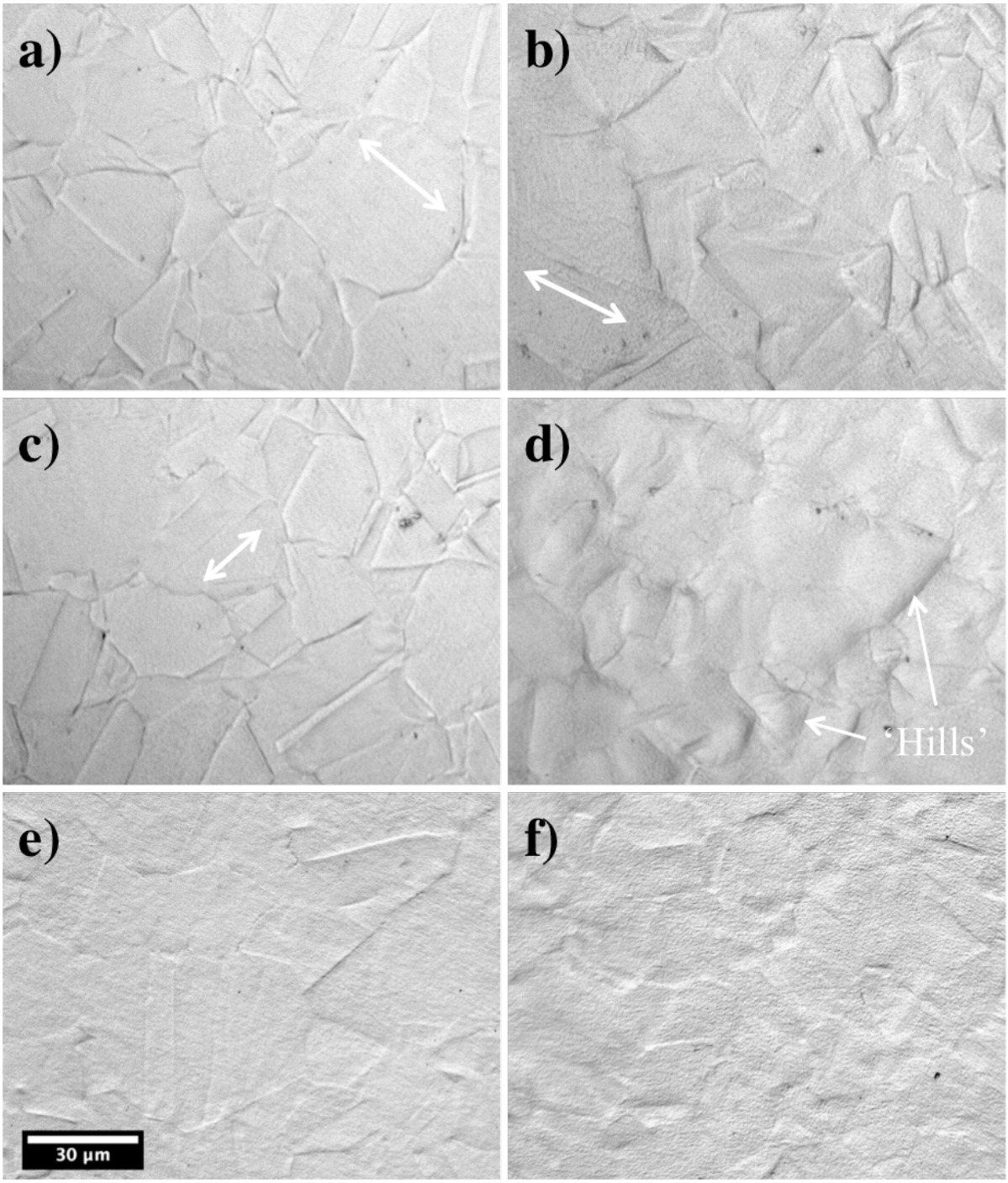

Fig. 4.3 Optical micrographs of AG17 after triode-plasma nitriding at a) 400°C 4hrs, b) 400°C 20hrs, c) 425°C 4hrs, d) 425°C 20hrs, e) 450°C 4hrs, f) and 450°C 20hrs

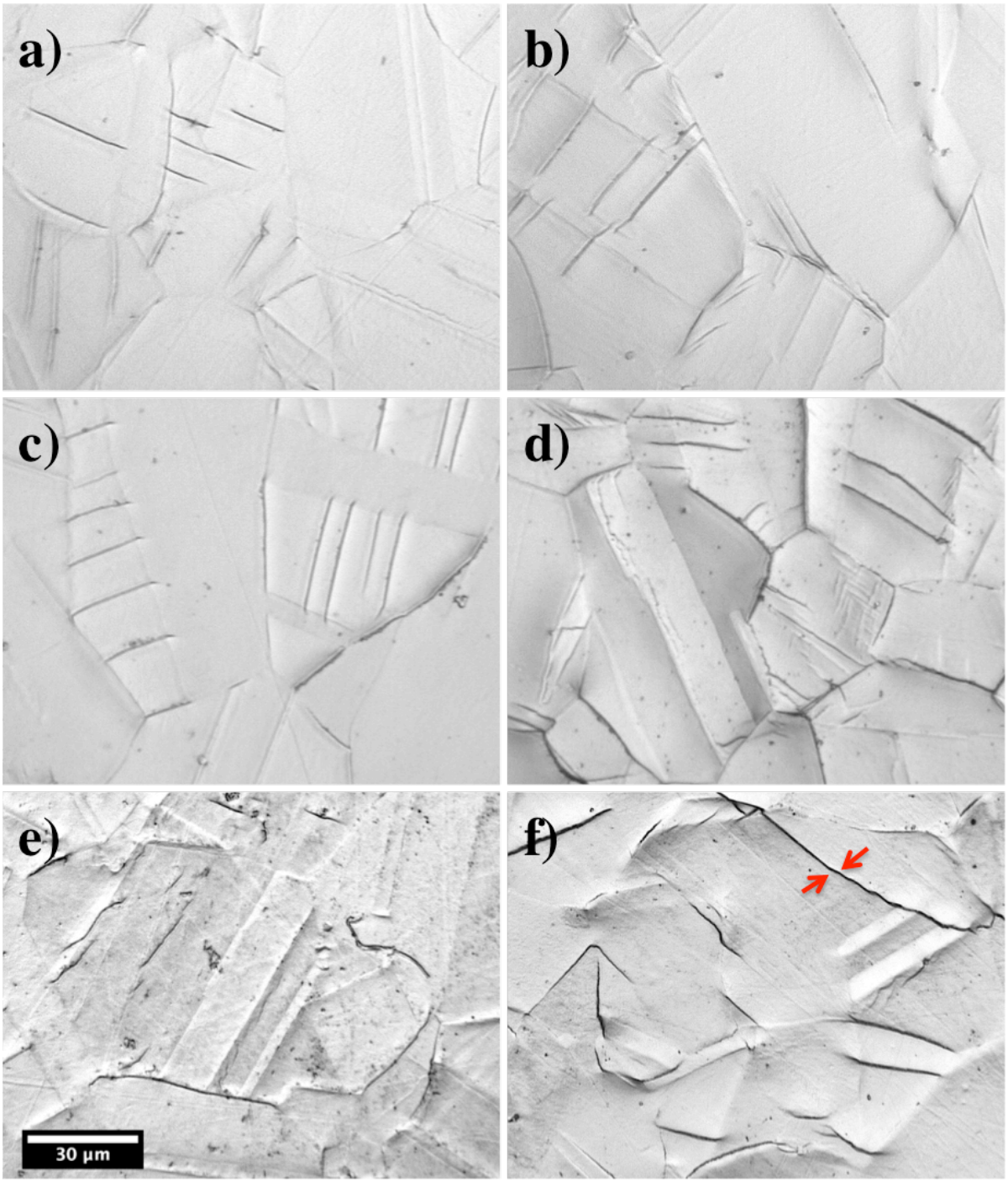

Fig. 4.4 Optical micrographs of 330 after triode-plasma nitriding at a) 400°C 4hrs, b) 400°C 20hrs, c) 425°C 4hrs, d) 425°C 20hrs, e) 450°C 4hrs, f) and 450°C 20hrs

4.1.3 Transverse BSE imaging

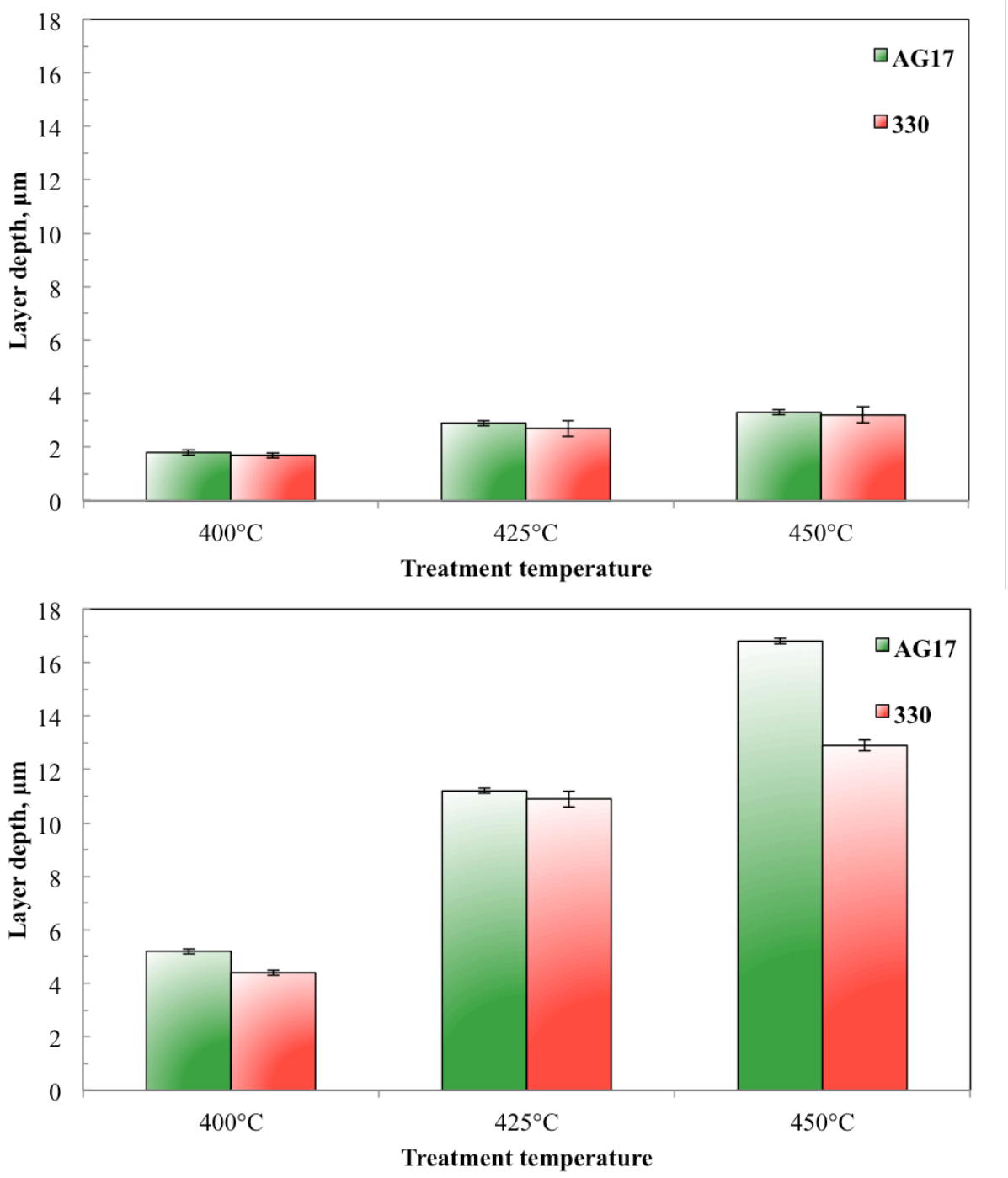

Fig. 4.5 Layer depths of two proprietary ASS after TPN for a) 4hrs and b) 20hrs

Layer depths determined from BSE images are plotted in **Fig. 4.5**. Treatment depths (especially for the prolonged treatments) are slightly higher in the high Mn(-N) AG17 alloy compared to the high-Ni alloy 330. The significantly thicker surface layer on 450C20h-AG17, as compared to 450C20h-330, could be attributed to an accelerated nitrogen diffusion rate – with associated austenite lattice decomposition.

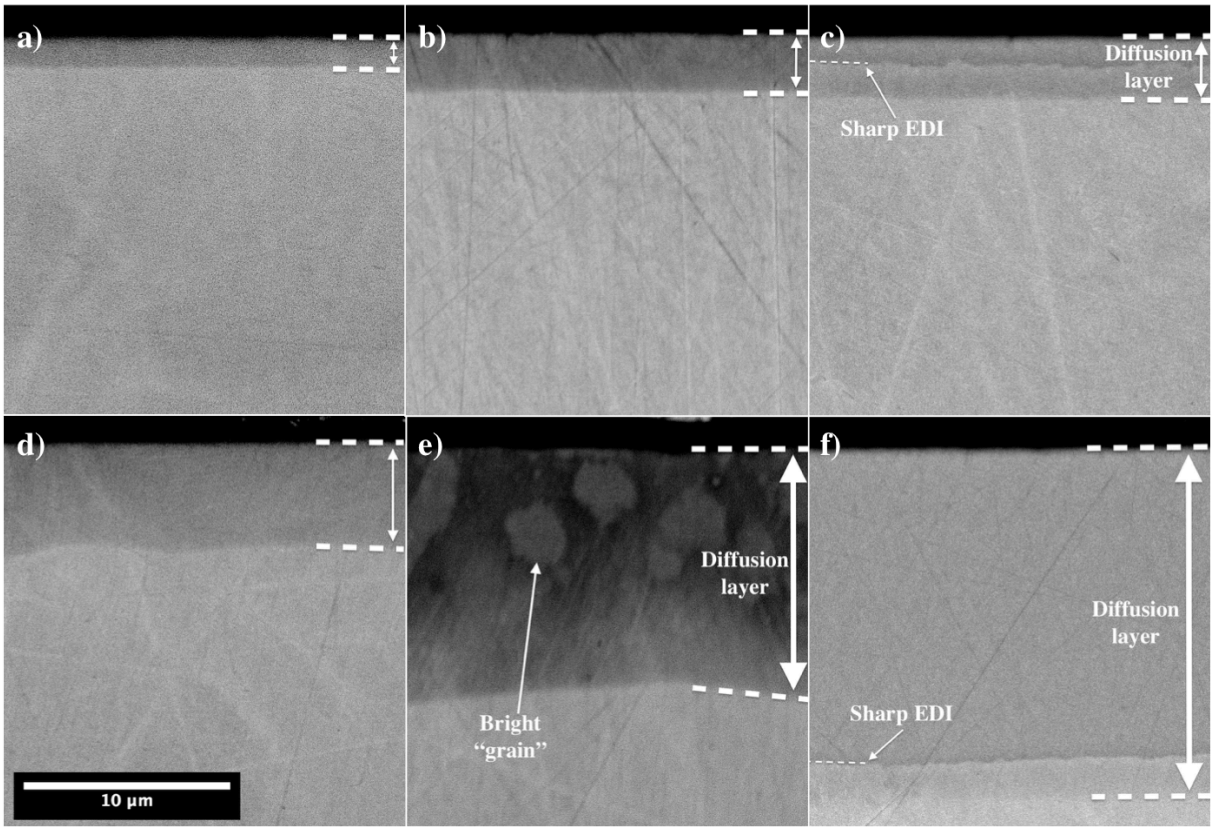

Fig. 4.6 Back-scattered electron images of AG17 after triode-plasma nitriding at a) 400°C for 4hrs, b) 425°C for 4hrs, c) 425°C for 4hrs, d) 400°C for 20hrs, e) 425°C for 20hrs, f) and 450°C for 20hrs

Transverse BSE images of the modified surfaces of alloys AG17 and 330 are shown in **Figs. 4.6** and **4.7**. Imaging contrast originates mainly from differences in local atomic mass. The uptake of light elements (in this case N) in a matrix of heavy elements (i.e. Fe, Cr, Ni and Mn) reduces the average atomic mass; hence the backscattered electron signal is weakened and N-enriched diffusion zones appear darker than the core material in BSE imaging. For both AG17

and 330, dark surface diffusion layers are observed, with a clear boundary at the unmodified core interface, presumably owing to the abrupt drop in N concentration.

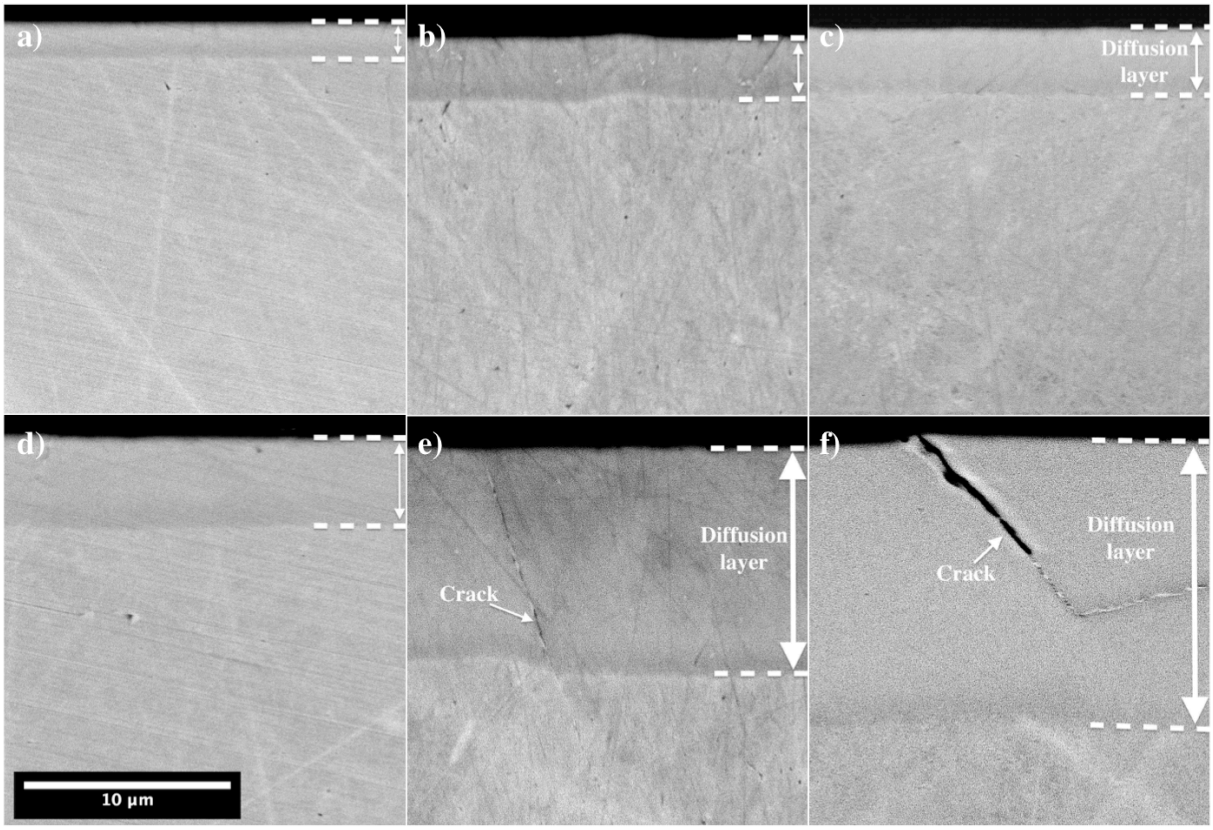

Fig. 4.7 Back-scattered electron images of 330 after triode-plasma nitriding at a) 400°C for 4hrs, b) 425°C for 4hrs, c) 450°C for 4hrs, d) 400°C for 20hrs, e) 425°C for 20hrs, f) and 450°C for 20hrs

Diffusion layers appear featureless on nitrided AG17 until treatment at 425°C for 20hrs, when relatively bright (low N content) "grains" are revealed in the dark (high N content) matrix in the top region of the treated layer (**Fig. 4.6e**). This special transverse (phase) morphology of 425C20h-AG17 leads to the small 'hills' observed under OM (**Fig. 4.3d**). The diffusion zones of 450C4h-AG17 and 450C20h-AG17 show a similar double-layered structure (**Fig. 4.6c** and **Fig. 4f**), with a sharp elemental distribution interface (EDI) between the two layers. On the other hand, surface layers appear homogeneous in cross-section for all nitrided 330

samples under BSE; however, micro-cracks could initiate on 425C20h-330 along grain boundaries and are obvious on 450C20h-330 (**Fig. 4.7**). In that case, the dark surface traces of 450C20h-330 under top-viewing (see OM, **Fig. 4.4f**) are most likely grain boundary cracks.

4.2 XRD analysis

4.2.1 Phase identifications

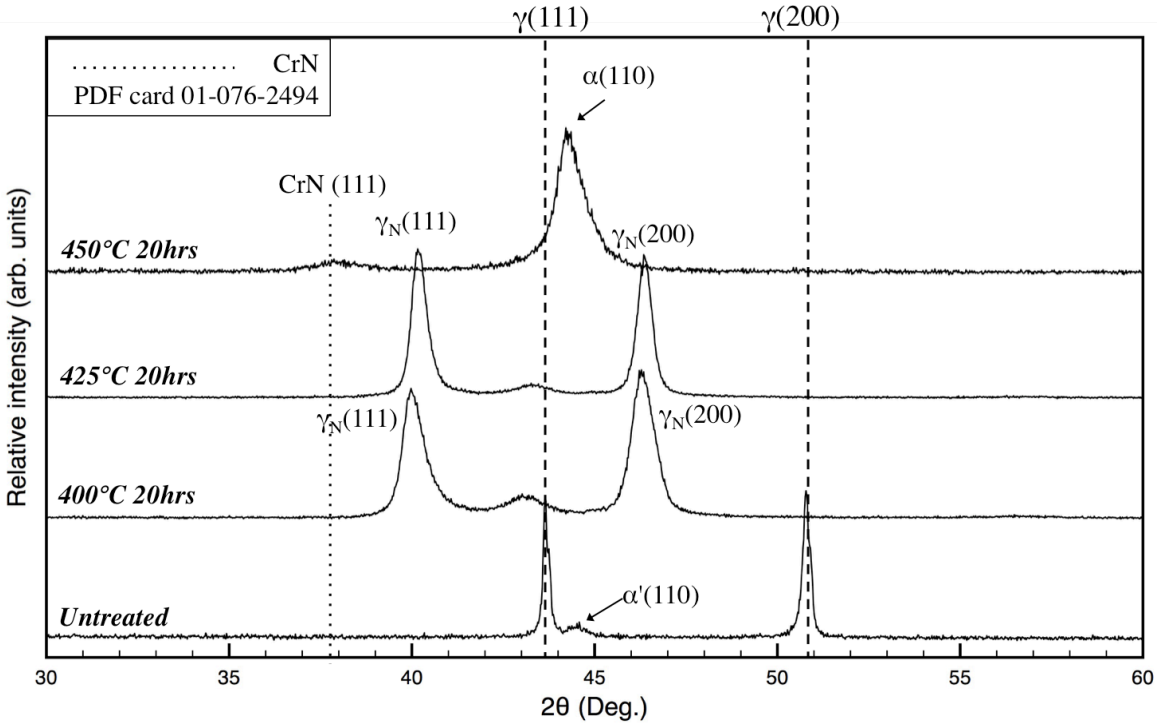

Fig. 4.8 X-Ray diffraction patterns of AISI 304 before and after TPN for 20hrs

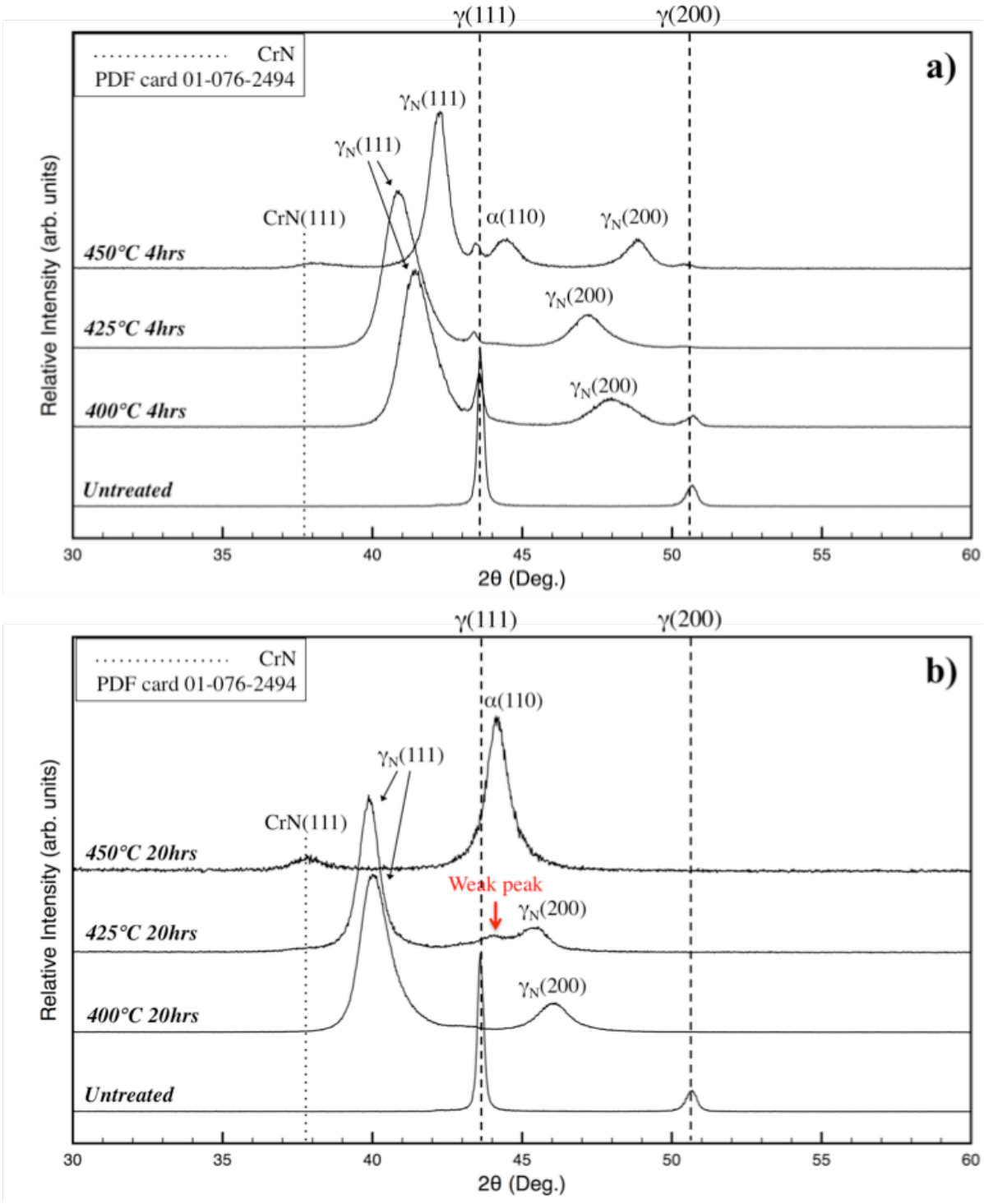

Fig. 4.9 X-Ray diffraction patterns of AG17 before and after TPN for a) 4hrs and b) 20hrs

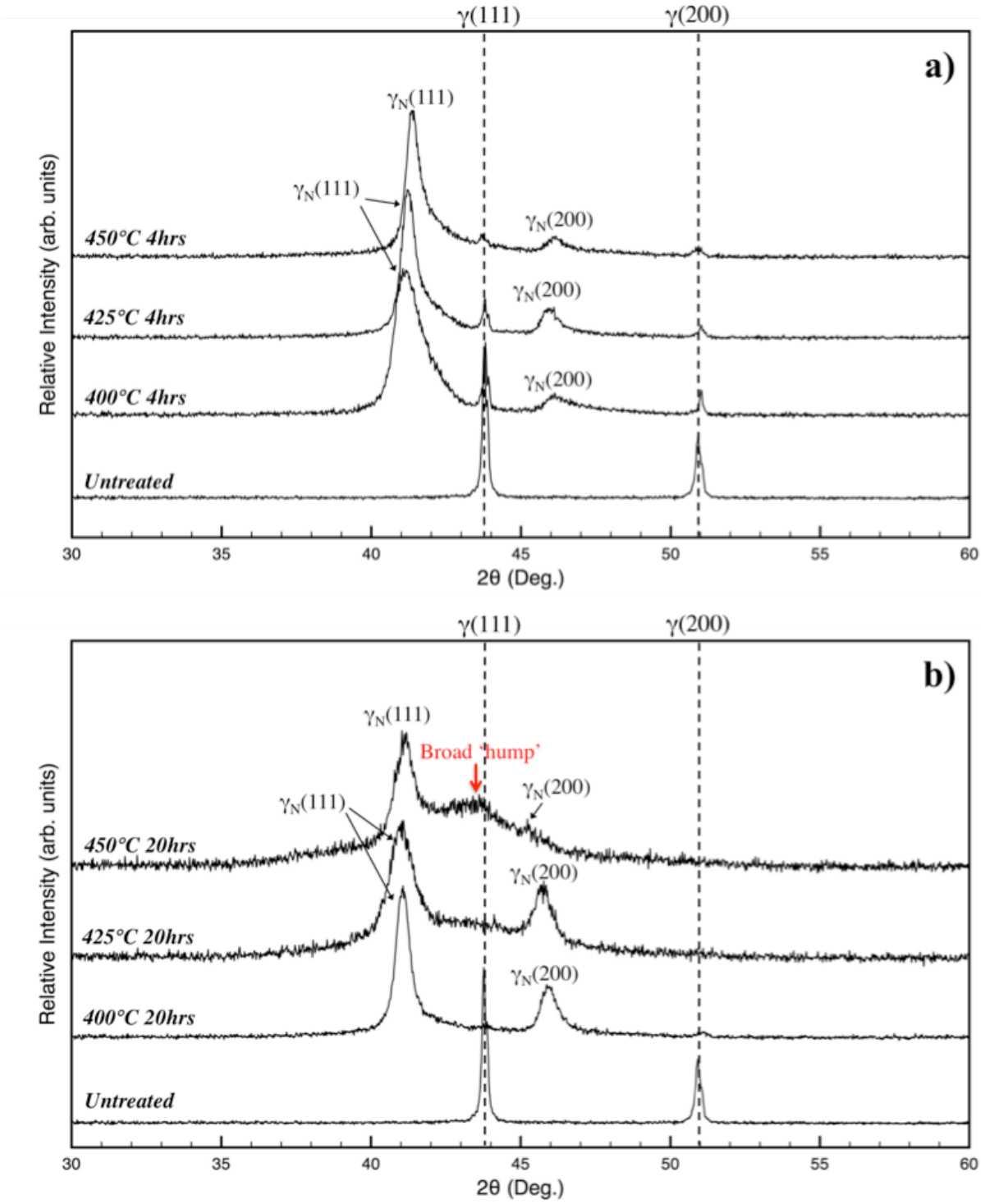

Fig. 4.10 X-Ray diffraction patterns of 330 before and after TPN for a) 4hrs and b) 20hrs

XRD patterns, as shown in **Figs. 4.8-4.10**, suggest the formation of γ_N on all three ASSs after TPN treatment, according to the characteristic peak shifts to lower angles. The observable CrN(111) and α-Fe(110) peaks on both 304 and AG17 at 450°C 20hrs imply that the same phase decomposition mechanism is shared between these two alloys. Compared to 425C20h-304, which showed no CrN and ferrite decomposition peaks, γ_N-AG17 decomposed after only 4hrs at 450°C − with a clear α(110) and a weak CrN(111) reflection seen. The γ_N peak intensities are still strong at 4hrs but (with increasing phase decomposition) disappear after 20hrs at 450°C. Moreover, two γ_N XRD peaks are observed on 425C20h-AG17; nevertheless, a weak peak (as indicated in **Fig. 4.9b**) between 43.6° and 44.6° is also seen on this sample, which corresponds to ferrite (as discussed further in **Section 4.5.3**).

With XRD analysis, the BSE features of nitrided AG17 (see images in **Fig. 4.6**) can be discussed further. At 425°C 20hrs (**Fig. 4.6d**), the dominant dark matrix phase corresponds to untransformed γ_N-AG17 and the relatively bright spherical "grains" correspond to decomposed regions. The bottom layer is also untransformed γ_N-AG17 due to its insufficient N concentration for nitride precipitation. The γ_N phase appears much darker (i.e. higher N content) in the top region compared to the bottom region, possibly due to the formation also of body-centred cubic (BCC) α-ferrite in the top region, which can accommodate only negligible amounts of interstitial N [63] − and consequent rejection of excess N to the adjacent γ_N matrix during the later stages of treatment. At the higher temperature of 450°C, the surface diffusion zone is composed of a topmost layer of decomposition products and an underlying layer of γ_N-AG17 (**Fig. 4.6c,f**). The sharp EDI between the two layers therefore corresponds in this case to a phase boundary. The XRD signals of the underlying γ_N-AG17 layer are still observable at 450°C 4hrs, owing to a thin topmost layer; however, as the topmost layer (decomposed region) grew sufficiently thick to exceed the X-ray attenuation

depth, only CrN and ferrite are detected after 20hrs of treatment. Under BSE imaging (**Fig. 4.6f**), there is a ~2μm thick underlying layer, which appears just slightly darker than the unmodified core. Due to this slight contrast difference, it is determined to be a layer of γ_N-AG17. Moreover, the different transverse morphologies at 425°C and 450°C could be attributed to the slightly different treatment temperatures, resulting in a topmost 'incomplete' decomposed region at lower temperature and a completely decomposed top layer at higher temperature.

From BSE imaging and XRD analysis of alloy 330 (**Fig. 4.7** and **Fig. 4.10**), there is no direct evidence of CrN formation in γ_N-330 under the selected nitriding conditions of this study. However, a broad XRD 'hump' (as indicated in **Fig. 4.10b**) is observed near the substrate γ(111) peak position (i.e. ~43.8°), adjoined to the γ_N(111) and γ_N(200) peaks at 450°C 20hrs − hinting at crystallographic arrangements other than γ_N. The transverse BSE of 330 after TPN (**Fig. 4.7**) always appear homogenous even at 450°C 20hrs, but there could be some lattice decomposition that is not detected under BSE (see TEM observations in **Section 4.5.3**).

4.2.2 XRD Lattice parameters of γ_N

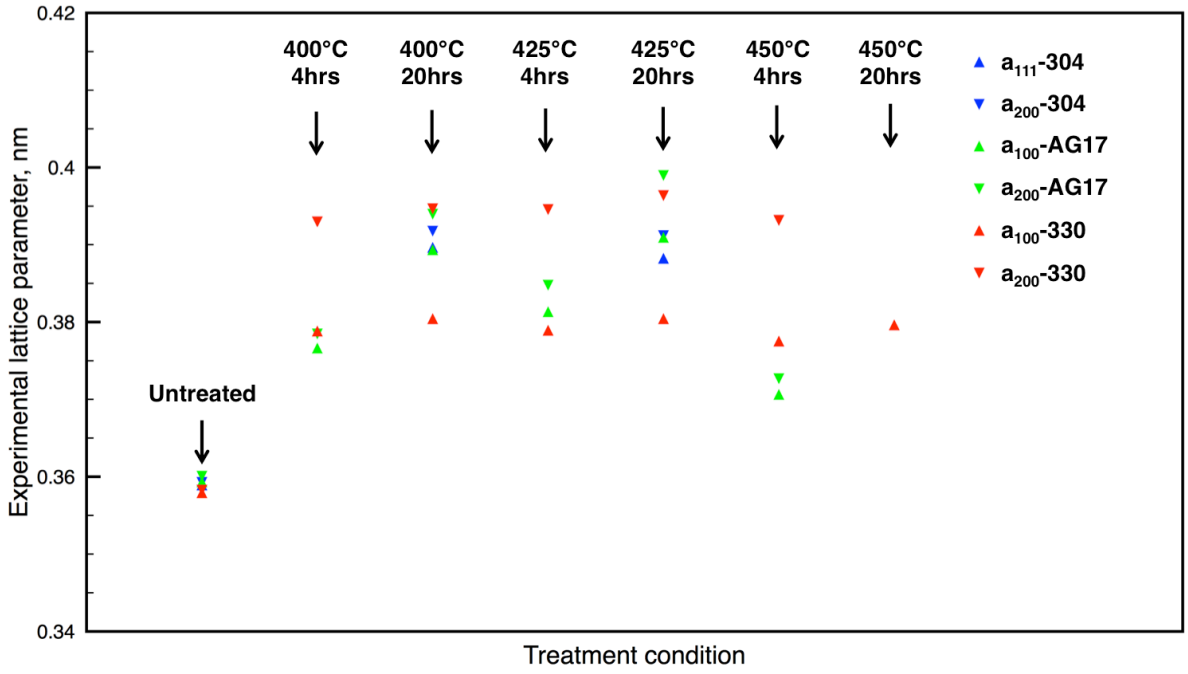

Fig. 4.11 Lattice parameters of nitrogen-expanded austenite (i.e. a_{111} and a_{200} as determined by d_{111} and d_{200}, respectively) from experimental XRD peak positions

The effective interplanar spacing (d_{hkl}) of untreated and expanded austenite are calculated from XRD peak positions ($2\theta_{hkl}$ angles) measured at full width at half maximum (FWHM) taking Cu K-α radiation (λ = 0.15418 nm) under Bragg's law, i.e. $2d_{hkl}\sin\frac{2\theta_{hkl}}{2} = \lambda$. Lattice constants ($a_{111}$ and a_{200}) are calculated via $a_{hkl} = d_{hkl}\times\sqrt{h^2+k^2+l^2}$ and are plotted in **Fig. 4.11**. Detailed lattice parameters are shown in **Table 4.2**. Only a_{111} is plotted for the 450°C 20hrs nitrided 330 alloy, because the $\gamma_N(200)$ peak position of this sample cannot be correctly determined at FWHM from XRD. However, the $\gamma_N(200)$ maximum peak intensity of this sample is located at ~45.3°, which gives a lattice parameter of ~0.401 nm − similar to the a_{200} of the other 20hrs nitrided 330 samples (**Table 4.2**).

Table 4.2 Lattice constants of nitrogen-expanded austenite, measured from i) experimental X-ray peak positions of $\gamma_N(111)$ and $\gamma_N(200)$, and ii) from experimental diffraction spacings of $\gamma_N(111)$ and $\gamma_N(200)$ diffraction spots in EDPs (at <110>γ_N zone axis) extracted under TEM, using U-330 TEM sample for calibration

	XRD lattice parameters, nm		TEM lattice parameters, nm	
	a_{111}	a_{200}	a_{111}	a_{200}
U-304	0.359	0.360	0.366	0.367
400C20h-304	0.390	0.392	0.383	0.380
425C20h-304	0.389	0.392	0.380	0.381
U-AG17	0.360	0.360	0.368	0.369
400C4h-AG17	0.377	0.379	0.376	0.378
400C20h-AG17	0.390	0.394	0.393	0.392
425C4h-AG17	0.382	0.385	0.374	0.375
425C20h-AG17	0.391	0.399	0.386	0.390
450C4h-AG17	0.371	0.373	0.367	0.368
U-330	0.358	0.359	0.358	0.359
400C4h-330	0.379	0.393	0.374	0.379
400C20h-330	0.381	0.395	0.382	0.387
425C4h-330	0.379	0.395	/	/
425C20h-330	0.381	0.397	/	/
450C4h-330	0.378	0.393	/	/
450C20h-330	0.380	0.401	0.369	0.370

Evidently, XRD peak shift of 200 planes is always higher than that of 111 planes for both ASS substrates after TPN treatment, in accordance with the first clearly documented XRD patterns published by Ichii et al. in 1986 [8]. This is due to the fundamental elastic anisotropy of FCC structures (i.e. hkl-dependent lattice elastic constants) such that, under a specific elastic strain, the γ(200) peak will in any case shift to lower 2θ angles than does γ(111), since the non-close packed {200}γ planes are more compliant than are the close packed planes of {111}γ. An anisotropically-expanded "heavily strained austenitic structure" was the basis of the (now widely-accepted) 'expanded austenite' terminology introduced by Leyland et al. in 1993 [22].

As elucidated in more detail by Sun et al. in 1999 [80], such anomalous expansion could also originate from the hkl-dependent SF parameters (based on Warren's theoretical study [83]), in addition to the hkl-dependent lattice constants in the surface layer (or to a combination of both factors). In the study by Sun et al. [80], a_{111} ranged from ~0.374 nm to ~0.386 nm and a_{200} ranged from ~0.374 nm to ~0.398 nm for AISI 304 and AISI 316 after plasma nitriding at temperatures between 400°C and 500°C. The lattice parameters of γ_N-AG17, γ_N-304 and γ_N-330 synthesised in this study all fall with within this range. Comparisons between the lattice parameters (a_{111} and a_{200}) of AG17 and 330 indicate that γ_N-AG17 changes its lattice parameters with both treatment time and temperature, while γ_N-330 exhibits rather invariant lattice parameters over the selected time/temperature range. Together with the narrow range of surface nitrogen content for 330 after TPN (**Fig. 4.1**), one could argue that nitrogen-interstitial introduced lattice expansion is rapidly saturated in the (high-Ni) 330 alloy within a relatively short treatment time during TPN (i.e. $\leq$ 4hrs) at the selected treatment temperatures.

4.3 TEM diffraction features of γN

Apart from the characteristic XRD peak shifts and broadening, various TEM signatures were reported previously for nitrogen-expanded austenite. Under TEM, local lattice distortion of γ_N bears close analogy to the deformation structure of plastically deformed Mn/N-stabilised ASS reported by Lee et al. [146]. Further to a TEM study by Tong et al. [114], electron diffraction patterns of the high SF density regions in γ_N [14, 15, 112-114] appear strikingly similar to SFs, deformation twinning and/or stress-induced hexagonal closed packed (HCP) ε-martensite of (plastically) mechanically-deformed ASS [146] as illustrated (at the $[110]_{matrix}$ zone axis) in **Fig. 4.12**. That is, the FCC lattice undergoes plasticity mechanisms, such as generation of SFs [14, 15], twinning [112, 113] and/or martensitic shear transformation [114], with {111}γ habit planes similar to those obtained under mechanical deformation.

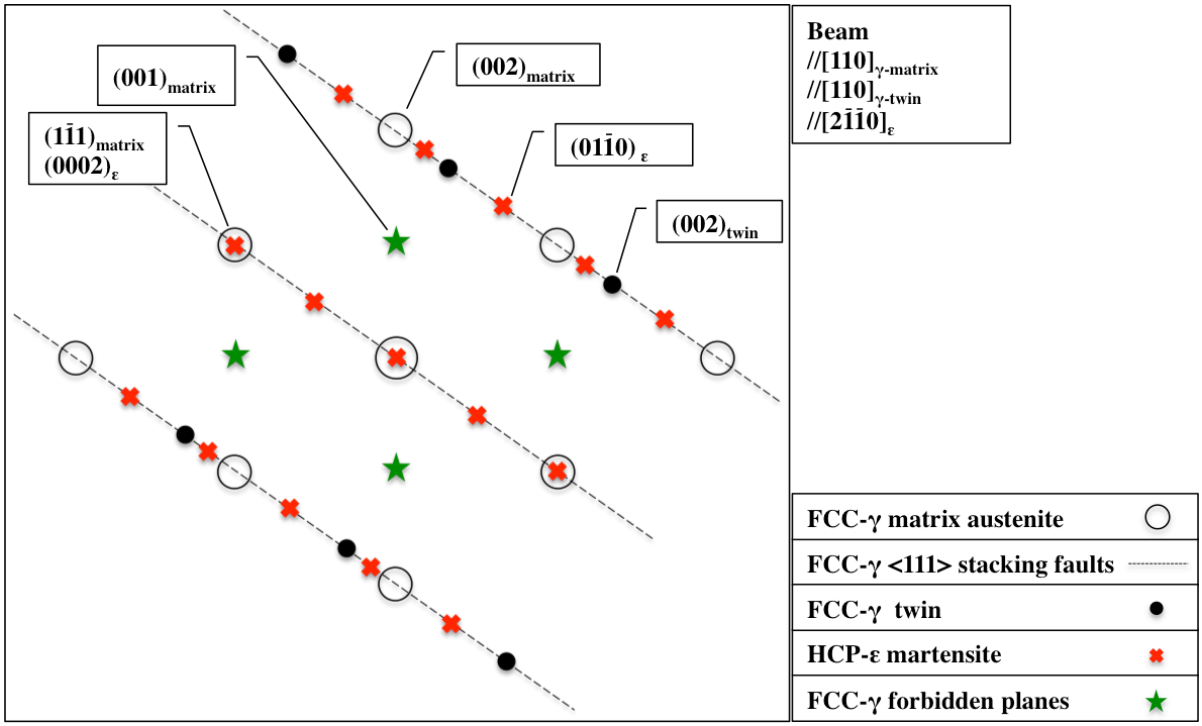

Fig. 4.12 Illustration of electron diffraction features observable for high SF density regions in γ_N. Apart from the forbidden reflections of FCC planes, the other features (i.e. <111> SFs, twinning and local HCP arrangement in γ_N) are consistent with those of mechanically deformed ASS [146]

Various local features of lattice distortion, including SFs on {111}γ_N planes, twinning and/or local 'martensitic' SF clusters, have been reported and studied in expanded austenite layers synthesised on AISI 304L [114], AISI 316 [14, 15, 112] or AISI 316L [113] after plasma nitriding. Noticeably, local HCP structure has been reported in γ_N-304L [114], but not in γ_N-316 [112] and γ_N-316L [113]. Even though the HCP structures in γ_N-304L showed the same crystallographic structure to ε-martensite in the paper by Tong et al. [114], the HCP-structured 'bright strips' were still considered by these authors as clustered (i.e. locally ordered) SFs − which was attributed to the small widths of the HCP features observed (no more than about ten nanometers wide). However, the 'primary ε bands' identified in the study by Lee et al. [146] are clearly also less than ten nanometers wide. The HCP strips observed in

γ_N could actually be considered as ε-martensite, equivalent to regions (in bands or strips) with high SF densities on $\{111\}\gamma_N$ planes having ABABAB arrangement (ε-martensite) rather than ABCABC arrangement (γ-austenite).

4.4 The potential influences of material SFE

Lee et al. [146] experimentally identified and discussed three SFE regions for mechanically-strained high interstitial ASS, which were i) SFE < 15 mJ/m^2 for only strain-induced martensitic transformations; ii) 15 mJ/m^2 < SFE < 20 mJ/m^2 for the co-existence of deformation twins and martensite; iii) SFE > 20 mJ/m^2 for the occurrence of deformation twins only. Additionally, modeling of SFE using the Gibbs free energy of the austenite to martensite transformation, $\Delta G^{\gamma \rightarrow \varepsilon}$, suggests a threshold SFE at ~18 mJ/m^2 [147, 148]. In other words, the strain-induced HCP ε-martensite transformation is energetically favourable for materials with SFE below ~18-20 mJ/m^2. Similar to the effects of mechanical strain, one could postulate local displacive transformations of N-strained FCC lattices (i.e. γ_N) to i) ε-martensite with SFE < 15 mJ/m^2; ii) a mixture of martensite and twins with SFE from 15 to ~18-20 mJ/m^2; iii) twins only with SFE > 20 mJ/m^2. In this case, the coexistence of ε-martensite and twins in γ_N-304L [114] correlates well to its low substrate SFE (below 18 mJ/m^2), while the twinned-only γ_N-316 [112] (or γ_N-316L [113]) correlates to a slightly higher substrate SFE (certainly exceeding 18 – and possibly above 20 − mJ/m^2), implying a likely correlation between substrate SFE and specific, localised lattice distortion under nitrogen-interstitial induced strain.

The stacking fault energy (SFE) of a material which is, for example, ~18 mJ/m^2 for AISI 304 [149, 150] − where both deformation twinning and/or martensitic transformation may occur under mechanical deformation − will directly influence the propensity of the strained lattice to undergo twinning, martensitic shear or conventional dislocation-mediated slip transformations

(or combinations thereof). In this case, the SFE of the particular ASS substrate material being treated must contribute significantly to the structure and phase stability of expanded austenite structures formed upon supersaturation of interstitial element(s).

A high density of lattice defects might aid the accommodation of extra nitrogen, increasing the paraequilibrium solubility and the resulting lattice expansion. Ernst et al. [17] also indicated that decomposition of expanded austenite (γ_C in their study) requires i) substantial lattice expansion to reduce the volume-misfit stress for precipitation, and ii) a high density of lattice defects (e.g. SFs) to locally enhance substitutional segregation. Taking the available SFE data of the substrate compositions at room temperature as reference points, (the relatively low SFE) AG17 alloy should be able to accommodate more interstitial N than (the high SFE) alloy 330 during nitriding (via the generation of SFs during treatment), leading to higher lattice expansion; however, the expected higher SF density and lattice expansion of AG17 will also result in a lower thermodynamic stability of γ_N-AG17, as compared to γ_N-330.

Both substitutional (Ni, Mn) and interstitial (N, C) species will influence the SFE of ASS; however, there is a lack of SFE data for the precise compositions of the AG17 and 330 proprietary alloys. From the literature, a higher Ni content clearly increases SFE (from ~17 mJ/m^2 at 8 at.% Ni to ~31 mJ/m^2 at 30 at.% Ni) in an Fe-Cr-Ni ternary system containing ~18-20 at.% Cr [151, 152]. Alloy 330 is thus likely to possess a much higher SFE than 304 (probably in excess of 30 mJ/m^2) for this positive effect of Ni on SFE; in which case, planar dislocation glide tends to be promoted under strain. Secondly, Gavriljuk et al. [153] measured experimentally a SFE of ~21 mJ/m^2 for an alloy composition quite similar to AG17 (Fe-15Cr-17Mn-0.5N) – i.e. slightly higher than (but approximately equivalent to) AISI 304 (at ~18 mJ/m^2). Based on a thermodynamic model for the Fe-Cr-Mn-N system developed by

Mosecker et al. [147], the SFE of AG17 should in principle lie between ~10 to 18 mJ/m^2 for the occurrence of martensitic transformation and twinning (or martensitic transformation only); i.e. values similar to (or slightly lower than) those reported for AISI 304 [149, 150].

The effect of nitrogen on SFE will strongly depend on the host composition. The interactions between nitrogen and the ternary metal alloy systems of interest (i.e. Fe-Cr-Ni and Fe-Cr-Mn) will result in incomparable N-dependence of SFE between these two systems. Experimentally, SFE was reported as decreasing with increasing N content in the Fe-Cr-Ni-N system [149], while the effect of N on SFE appeared non-monotonic in the Fe-Cr-Mn-N system [146, 147, 153]. Increasing N content in the Fe-Cr-Mn solid solution initially decreases SFE, due to Suzuki segregation of N into SFs at low N concentration and then increases SFE at higher N contents, due to a less effective interstitial segregation [147]. However, available literature (e.g. [146, 147, 149, 153]) was based on measurements/models for N contents in the low concentration regime − i.e. below 0.8 wt.% (~3 at.%) − at room temperature. SFE increases with temperature for FCC ASS, but the N-dependence of SFE is still unclear for the metastable γ_N formed in Fe-Cr-Ni-N and Fe-Cr-Mn-N systems. The 'locking' effect of interstitial N on SFs is likely to be reduced by the thermally-enhanced mobility of interstitial N at typical thermochemical diffusion treatment temperatures (increasing SFE), but the much higher local N content (and short range ordering) of Cr-N could contribute to SFE in an opposite way, creating energy barriers for dislocation glide (reducing SFE). Additionally, the extremely high atomic fraction of N, in itself, introduces strain to the metastable lattice; the real effect of N in the "colossal supersaturation" [13, 133] concentration region is complex – and requires further systematic investigation (beyond the scope of this study).

4.5 TEM analysis

4.5.1 TEM Lattice parameters of γ_N

Assuming the same camera constant (i.e. $\lambda \times L$) for all EDPs – and using a FIB-prepared TEM sample of U-330 for calibration (taking $a_{111} \approx a_{200} \approx$ ~0.358 nm) – TEM lattice parameters (a_{111} and a_{200}) of γ_N can be calculated from the distances of the respective diffraction spots to the centre spot using EDPs generated at the <110>γ_N zone axis, which are shown in **Table 4.2**. The measured lattice constants (near the surface of the cross-sectional samples) for 400C20h-304, 400C20h-AG17, and 400C20h-330 are ~0.390, ~0.390 and ~0.382 nm, respectively, which clearly indicates lattice expansion under stress-free (or 'micro-stress') conditions, as compared to the lattice constants of untreated samples. However, as the high compressive stress of γ_N diminished (i.e. stress relaxation when the anisotropically strained γ_N is no longer constrained by material volumes in bulk form) during preparation of thin TEM foils, TEM lattice parameters appear hkl-independent, revealing isotropically expanded austenite ($a_{111} \approx a_{200}$) − as observed also in TEM studies of γ_N-316 [14]. The measured TEM lattice constants of γ_N decrease from surface to core.

Generally, lattice parameters are higher in (high-Mn) alloy AG17 and lower in (high-Ni) alloy 330. Nevertheless, the abovementioned 'quantitative' TEM analysis for γ_N is, strictly speaking, non-representative (and probably inaccurate), owing to the small sampling areas, the small error in the camera length (despite placing the sample at eucentric height), influences from the FIB preparation process (using a high voltage gallium beam), etc. The lattice constants extracted from TEM are not discussed further therefore, with the following section focused on more reliable/convincing evidence observed in the selected treatment temperature/time envelope.

4.5.2 TEM observations and discussions on lattice expansion

4.5.2.1 TEM observations

As discussed in **Section 4.3**, the HCP 'strips' reported in γ_N-304L by Tong et al. [114] were not observed in either γ_N-316L [113] or γ_N-316 [14, 112]. The TEM observations on γ_N-304L by Tong et al. [114] are however reproducible under the selected TPN conditions in this study. The HCP structured lamellae (or ε-martensite) are obtained in the γ_N-304 synthesised in this study, as shown in **Fig. 4.13**. Streaking is observable in the γ_N-304 as shown in EDPs, indicating generation of SFs. The 'forbidden' FCC reflections are also evident, indicating ordered nitrogen occupation in austenite lattice octahedra [15]. Under TEM, no evidence of CrN formation can be found in the foils prepared from 400C20h-304 and 425C20h-304, which agrees with XRD profiles. Although the γ_N-304 in this study has XRD lattice parameters almost identical to those of γ_N-304L in Tong's study [114] (i.e. $a_{111} \approx 0.389$ nm, $a_{200} \approx 0.392$ nm for γ_N-304L), the twinning reported for γ_N-304L is not seen in γ_N-304, as shown by the EDPs in **Fig. 4.13**. This could be attributed to substrate compositional differences with respect to the relatively wide composition window for AISI 304, where variations in Cr and Ni (or N, C, Si and Mn) within the composition window will result in slight change in SFE that is, however, sufficient to alter the 'deformation' mode. More importantly, AG17 and 330, having significantly different compositions and SFEs, show very different lattice-expansion behaviour with treatment time/temperature, as already shown with XRD profiles (**Figs. 4.8-4.10**). Lattice defects created after TPN at low temperature are observable under TEM, as shown in **Figs. 4.14-4.15**.

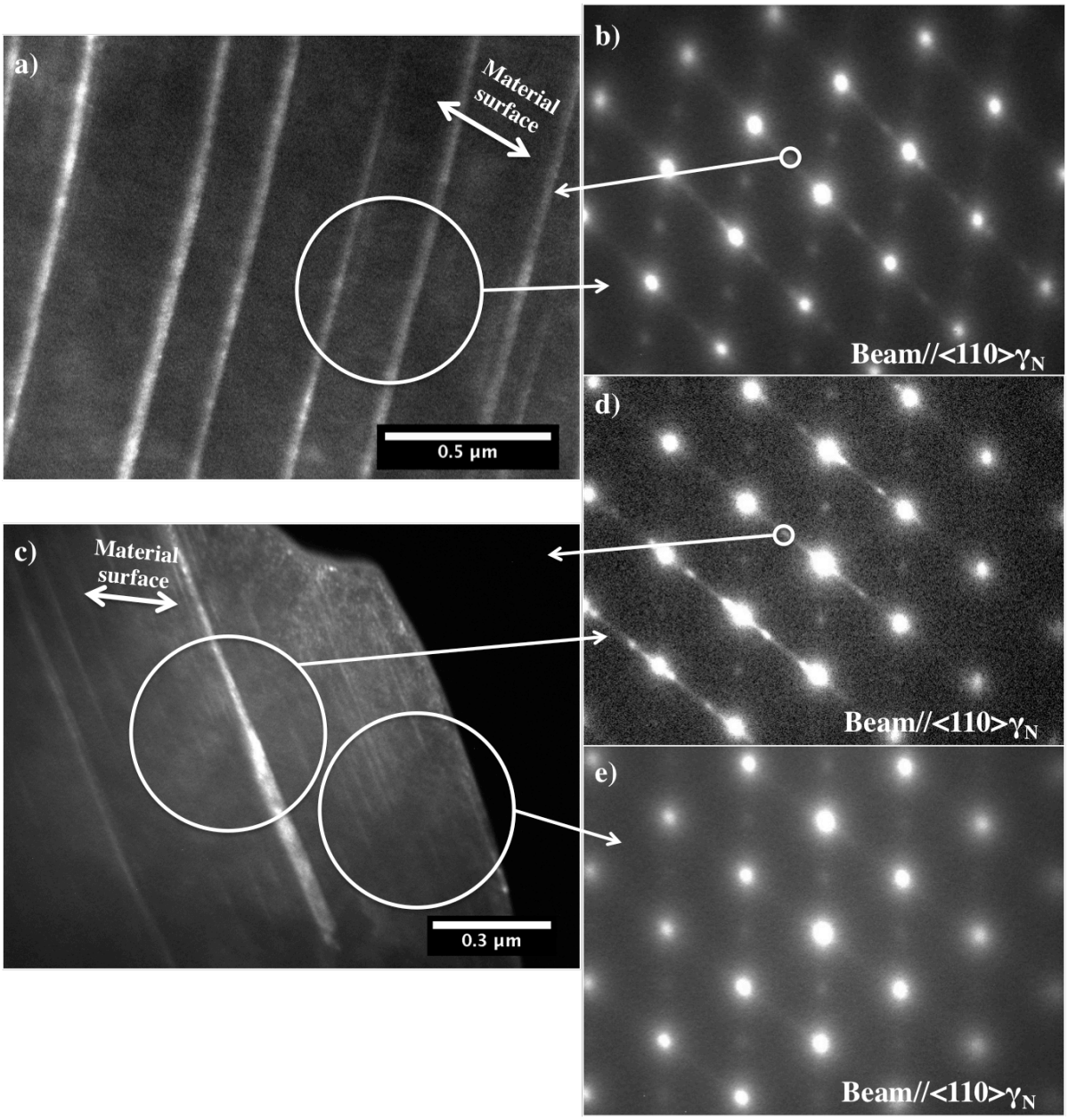

Fig. 4.13 DF-TEM images and selected area EDPs of AISI 304 after plasma nitriding for 20hrs at 400°C (a, b, respectively) and at 425°C (c, d, e, respectively) (DF-TEM images were constructed from diffraction electrons as indicated in EDPs of image b, d; diffraction aperture were located as indicated in DF-TEM images of image a, c)

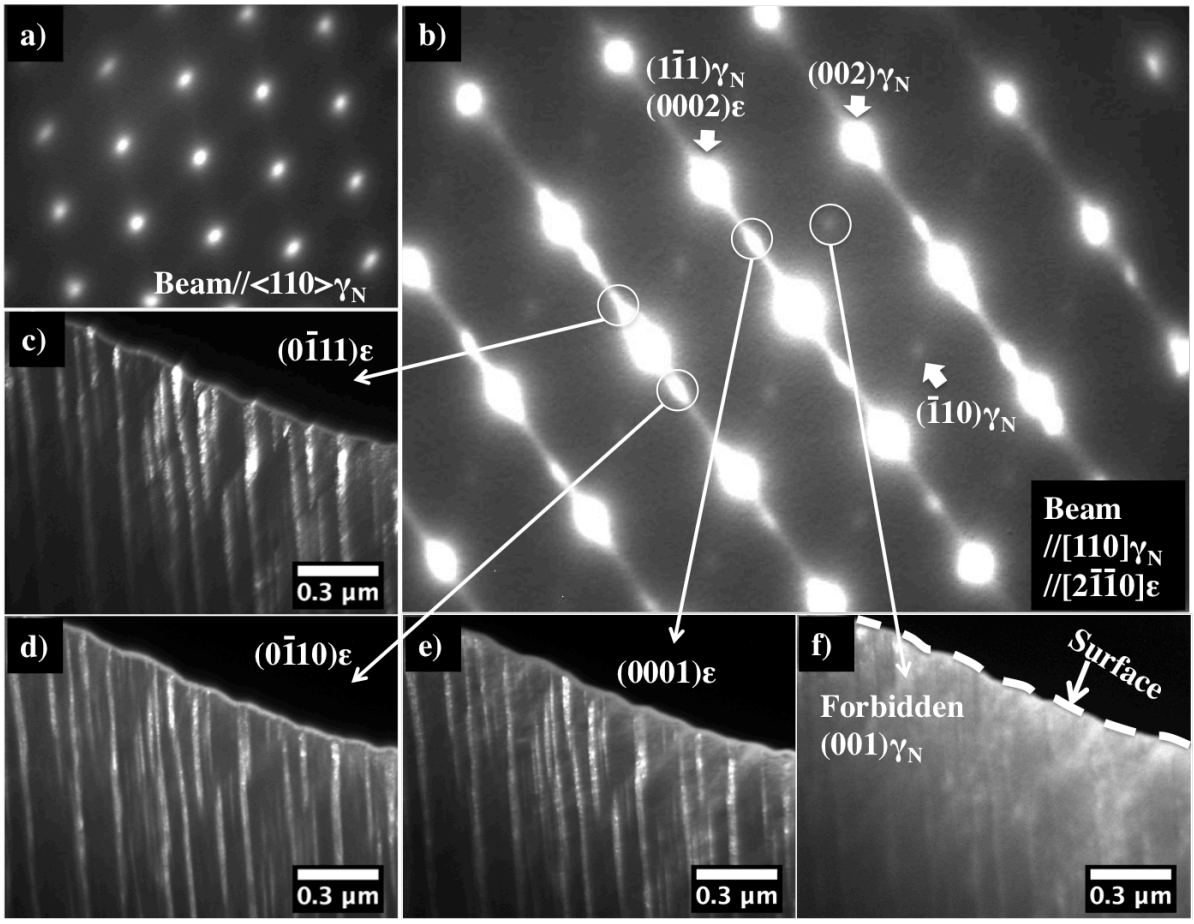

Fig. 4.14 EDP of region at the surface of AG17 after plasma nitriding a) at 400°C for 4hrs, b) at 400°C for 20hrs, and c-f) corresponding DF-TEM images of the 400°C 20hrs nitrided AG17 surface (DF-TEM images were constructed from different diffraction electrons as indicated in the figure)

More importantly, AG17 and 330, having significantly different compositions and SFEs, show very different lattice-expansion behaviour with treatment time/temperature, as already shown with XRD profiles (**Figs. 4.8-4.10**). Lattice defects created in AG17 surface after TPN at low temperature are observable under TEM, as shown in **Figs. 4.14-4.15**.

The increasing XRD peak shift of γ_N-AG17 (to lower 2θ angles) with temperature/time correlates well to the evolution of lattice distortion observed under TEM. After 4hrs of

nitriding at 400°C, γ_N-AG17 shows only austenitic diffraction intensity maxima under TEM (**Fig. 4.14a**), whilst a high SF density is obtained in γ_N-AG17 after 20hrs of treatment at the same temperature (**Fig. 4.14b**). The <111>γ_N 'streaking' (**Fig. 4.14b**) corresponds to a high SF density located preferentially on {111}γ_N planes, which correlates to further composition-induced lattice expansion with increasing treatment time. Although it was not unambiguously observed or reported in the open literature of expanded austenite, this <111>γ_N streaking (under N-induced strain) could occur as a result of dissociation of 'perfect' dislocations into Shockley partials on the {111}γ_N slip planes (e.g. $\frac{a}{2}[110] \rightarrow \frac{a}{6}[211] + \frac{a}{6}[12\bar{1}]$, where a denotes lattice parameter), which is normally considered responsible for the <111>γ streaking observed in mechanically deformed austenite. Through dislocation dissociation, lattice strain is accommodated by the generation of SFs on {111}γ_N planes. A secondary set of intensity maxima are observed on the <111>γ_N streaks, corresponding to the same bright strip-shaped regions at the nitrided surface, revealed by DF-TEM imaging of the intensity maxima (**Fig. 4.14c-e**). These maxima are indexed as HCP ε-martensite. After 20hrs of nitriding at 400°C, the parallel bright strips are ~10-40 nm wide and occupy a significant volume fraction of approximately ~24% at the material surface. Similar to the 'clustered SFs' reported by Tong et al. [114] in γ_N-304L or 'primary ε bands' by Lee et al. [146] in plastically deformed low SFE ASS, the ε-martensite and parent γ_N-AG17 follow the Shoji-Nishiyama (S-N) structure-orientation relationship, i.e. <110>γ_N//<$2\bar{1}\bar{1}0$>ε and {111}γ_N//{0001}ε. These strips can thus be considered as local distortion of the FCC austenitic structure (with a high SF probability of ~0.5), in which case SFs are present on every second {111}γ_N plane. Noticeably, no evidence of twinning was observed in EDPs under TEM. A third set of weak intensity maxima is observed − and was examined more closely under DF-TEM (**Fig. 4.14f**). No clearly distinguished responsible features could be found, indicating that these weak diffraction reflections are unlikely to originate from the ε-martensite strips. Such weak

reflections are however evident in γ_N-AG17, γ_N-304 [114], γ_N-316 [14, 15, 112] and γ_N-316L [113]. In the model of Jiang et al. [15], these weak diffraction patterns are claimed to correspond to 'forbidden' reflections of γ_N − and are attributed to ordered occupation by N at the centre of corner-sharing octahedra in the FCC lattice.

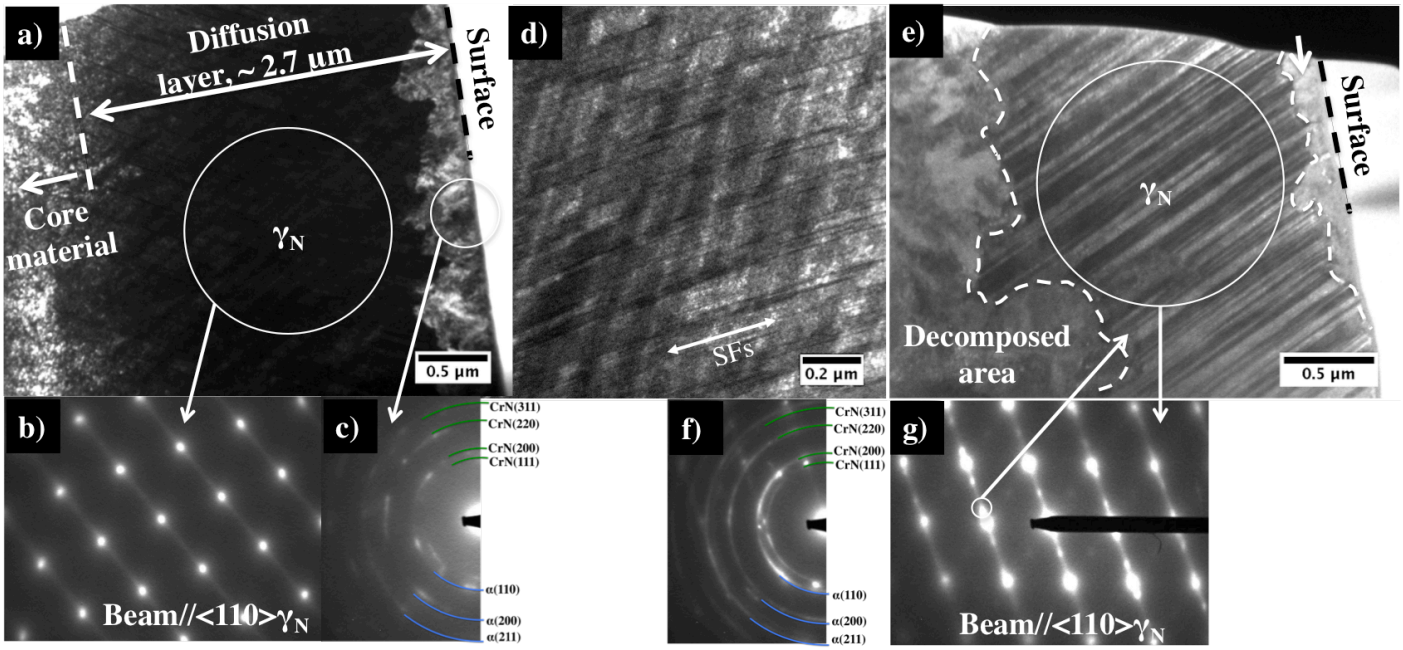

Fig. 4.15 TEM images, EDPs of AG17 after plasma nitriding at 425°C for 4hrs and 20hrs. a-c) BF-TEM image of 425°C 4hrs nitrided AG17 and corresponding selected area EDPs, d) BF-TEM image of the γ_N-AG17 in image a showing extensive SFs, e) DF-TEM image of 425°C 20hrs nitrided AG17, f) EDP covering entire region shown in image d, g) Selected area EDP of the untransformed γ_N in image d (DF-TEM was constructed from diffraction electrons as indicated in the figure)

At a treatment temperature of 425°C, similar structural evolution is revealed in γ_N-AG17 as compared to that generated at 400°C for the same alloy. The EDP of γ_N-AG17 treated at 425°C for 4hrs (**Fig. 4.15b**) presents γ_N spots and <111>γ_N streaking, where extensive SFs were revealed in γ_N-AG17 at this treatment condition in BF-TEM image (**Fig. 4.15d**). The EDP of γ_N-AG17 treated at 425°C for 20hrs (**Fig. 4.15g**) presents γ_N spots, <111>γ_N

streaking – and also HCP spots and 'forbidden' γ_N spots. In the DF-TEM image of the 425°C 20hrs nitrided AG17 surface, using a single HCP spot (**Fig. 4.15e**), parallel strips are revealed inside an untransformed volume of γ_N-AG17 that has not decomposed to CrN + α. Comparisons between the 400°C treated γ_N-AG17 sample and the 425°C one reveal also a structural evolution with treatment temperature. The extra <111>γ_N streaking in the EDP of γ_N-AG17 at 425°C 4hrs, as compared to γ_N-AG17 at 400°C 4hrs, corresponds to a slightly larger lattice expansion. The EDP features of the γ_N-AG17 at 425°C 20hrs (**Fig. 4.15e**) are the same as its counterpart at 400°C 20hrs (**Fig. 4.14b**); however, comparing the DF-TEM images of γ_N-AG17 at 400°C 20hrs (**Fig. 4.14d**) and at 425°C 20hrs (**Fig. 4.15e**), the HCP lamellae evidently grow in width (from ≤ 30 nm to ≤ 50 nm) and in volume fraction (from ~24 vol% to ~37 vol%) with the increase in treatment temperature.

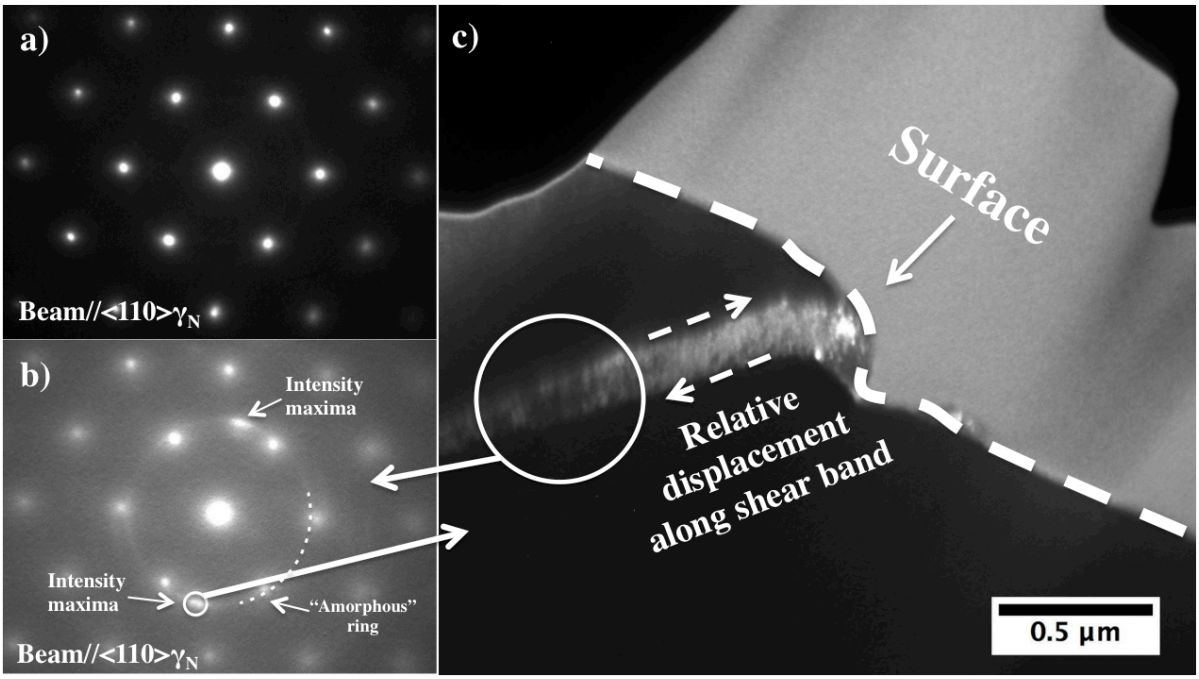

Fig. 4.16 a) EDP of expanded austenite generated on 330 after nitriding at 400°C 20hrs, b) selective area EDP of localized lattice distortion from region shown in image c, c) DF-TEM image showing a shear band, DF-TEM image was constructed from diffraction electrons as indicated in the figure

In contrast, mainly γ_N diffraction spots are observed in EDPs of γ_N-330 synthesised at 400°C 20hrs (**Fig. 4.16a)**. Different to the SFs observed in γ_N-316 [14], no evidence of SFs, twins or HCP martensite is observed in the γ_N-330 produced in this study. The nearly 'perfect' FCC lattice (with low SF density) of alloy 330 was retained, however, after nitrogen-interstitial introduced lattice expansion. In this case, the rapid saturation of the lattice expansion observed for γ_N-330 could be correlated primarily to dislocation-mediated slip (e.g. $\{111\}\gamma_N<110>\gamma_N$ as active primary slip systems for the FCC lattice) under the thermochemically-induced lattice strain. Intriguingly, the forbidden γ_N reflections are absent in γ_N-330, despite the interstitial nitrogen content apparently exceeding the level required to saturate the FCC lattice octahedral interstices. In contrast to the ordered occupation suggested by Jiang et al. [15], the occupation of interstitial sites by nitrogen might therefore be random in γ_N-330, i.e. not always in the corner-sharing octahedra of the FCC lattice.

However, microscopic shear bands (i.e. localised accumulation and interaction of shear planes) can be observed inside individual austenite grains (**Fig. 4.16b, c**). Similar shear bands, which initiate through structural instability (and contain layered dislocation walls), have been reported on plastically deformed (i.e. cold-rolled) high or medium SFE materials [154, 155]. If the precursory obstacles for forming the shear bands are walls of dislocations (rather than fine twin lamellae), the shear band is of copper-type (rather than brass-type). The shear band investigated here can be classified as a 'copper-type' shear band (rather than 'brass-type') − according to the terminology introduced by Wagner et al. [156] − since there is no evidence of twin lamellae. In the EDP of **Fig. 4.16b**, apart from γ_N diffraction spots (arising from an adjacent γ_N-330 grain), the obvious 'spot-and-stripe' intensity pairs and weak 'amorphous' diffraction rings suggest lattice mis-orientation and distortion within shear band under highly-localised strain.

Under DF-TEM imaging, using one of the intensity maxima (**Fig. 4.16c**), the shear band discussed above appears to be ~120 nm wide. Extensive dislocation interactions within this shear band have caused the volume to the left of the shear band (**Fig. 4.16c)** to be displaced out from the material surface − presumably under compression parallel to the material surface. This observation of high-level plasticity confirmed the surface patterns observed from top viewing under OM (**Fig. 4.4**). Unlike the large volume fraction of HCP lamellae observed at the surface of γ_N-AG17 (where such volume displacements were small and gradual), the shear bands in γ_N-330 are 'macroscopically' located several microns from each other in the austenite grains (based on OM observations of **Fig. 4.4)**. Given such localised dislocation-mediated microstructural evolution inside grains, one could assume dislocation accumulation and interactions at grain boundaries. In addition to the expansion/strains developed between adjoining γ_N-330 grains, without the generation of SFs inside γ_N-330 grains to relax the high compressive stress, such dislocation accumulations could initiate voids and eventually micro-cracking along grain boundaries, as observed in the 330 samples treated at 425°C for 20hrs (see BSE image in **Fig. 4.7e**).

4.5.2.2 Influence of SFE on lattice expansion

In plastic accommodation of composition-induced strain, extremely high densities of SFs (forming HCP lamellae) are believed to be generated via dislocation dissociation in the FCC lattice of low-SFE AG17 alloy, whilst the (presumed) dislocation-mediated slip in the FCC lattice of high-SFE alloy 330 led to a relatively 'perfect' FCC lattice structure, but also generated a small volume fraction of shear bands. The generation of SFs (and the potential lattice twinning or local martensitic transformation) in γ_N-AG17 during treatment, owing to lattice strain induced by N-absorption, in turn assists further N-uptake and lattice expansion. Due to the retention of a 'perfect' austenitic lattice with little or no SFs, nitrogen saturation of

γ_N-330 (and an associated limit of lattice expansion) is rapidly reached during the early stage of diffusion treatment. The shear bands formed inside a γ_N-330 grain lead to significant displacement of large lattice volumes out from the material surface. In this regard, a low substrate SFE appears to be beneficial for low-temperature nitriding, which could be argued owing to a (hypothesised) SF-enhanced N-absorption and lattice expansion. However, this hypothesis still needs to be confirmed with more direct evidence in future experimentations. In conjunction with solid solution strengthening, the work hardening via local martensitic shear transformation and dislocation slip in γ_N-AG17 contributes to a hardening mechanism, which should be different to the hardening mechanism in γ_N-330 (via dislocation slip).

The deformation modes discussed so far have been correlated to the SFEs of unmodified substrates, which are hinted at by the literature and – as confirmed in this study for γ_N-AG17 and γ_N-330 – present distinguishably different 'deformation structures'. However, the distortion mechanisms are in practice determined by the 'dynamic' (nitrogen-concentration mediated) SFEs of the near-surface FCC lattices generated during treatment − rather than the 'textbook' room-temperature (unmodified) substrate SFE values – with consideration of effects of treatment temperature and inhomogeneous near-surface chemical composition on 'local' SFE values across the treated layer. Interstitial nitrogen, which induces a composition-dependent lattice strain similar to that of mechanical strain, will also simultaneously influence material behaviour. SFE increases with temperature for FCC material, with a commensurate rise in the energy required to generate stacking faults. In this case, the 'distorted' structures in low SFE γ_N-AG17 (i.e. only ε-martensite lamellae for SFE < 15 mJ/m^2) must be attributable to the extensive short-range-ordered Cr-N clusters, which create energy barriers within the primary slip systems (reducing SFE), offsetting the influence of elevated temperature. The SF-free or low SF density features of γ_N-330 (with high Ni content) could certainly be attributed to its

high SFE – and to the increase in SFE with temperature. However, the high N content could also offset the influence of raised temperature in γ_N-330. The initiation of strain localisation (i.e. shear banding) in γ_N-330 might have something to do with the effect on dislocation glide of local interaction of Cr-N clusters.

Obviously, the N-dependence of SFE varies also between Fe-Cr-Ni(-N) and Fe-Cr-Mn(-N) systems – another consideration requiring further systematic study beyond the immediate scope of the work presented in this thesis. However, from our studies (and the available literature), one could tentatively rank the SFE of γ_N (at considerably saturated N absorption under a typical nitriding temperature of ~400°C) qualitatively from low to high as: γ_N-AG17 → γ_N-304(L) → γ_N-316(L) → γ_N-330 − which follows the SFE trend of substrate compositions from Mn-stabilised ASS to Ni-stabilised ASS. It is also worth reiterating at this point that, despite being a potent austenite stabiliser, the bulk N content of unmodified AG17 alloy probably has a negligible effect on the lattice SFE of γ_N during thermochemical treatment − since the N content in the resulting γ_N is, by comparison, extremely high. The SFE of γ_N during nitriding should mainly be influenced by the various substitutional alloying elements (or, to a lesser extent, by interstitial elements other than N) already present in the substrate.

4.5.3 TEM observation and discussions on lattice decompositions

4.5.3.1 TEM observations

The strong chemical affinity of Cr for N eventually leads to CrN precipitation in all three ASS compositions after TPN. In comparison with XRD and SEM–BSE data, TEM analysis indicates slightly different (and arguably more precise) results. The threshold decomposition condition for γ_N-AG17 is determined, almost exactly, as 4hrs at a treatment temperature of

425°C (**Fig. 4.15**). The selected area EDP of **Fig. 4.15c** reveals CrN and α-ferrite diffraction rings (identified by PDF cards 01-076-2494 and 00-006-0696, respectively) in the topmost region of the diffusion layer only, which presumably has the highest nitrogen content and associated lattice distortion. The precipitation morphology of CrN in plasma nitrided AG17 is compared to that of 304 at the upper treatment temperature/time condition of 450°C 20hrs, which is shown in **Fig. 4.17**. Fine lamellar CrN precipitates (with an inter-lamellar spacing of only 1-3 nm) were observed for both 304 and AG17 (**Fig. 4.17c,f**). Similar thin, lamellar CrN precipitation (with inter-lamellar spacing of 3-5 nm) has also been reported by Li et al. [112] in decomposed γ_N-316 − which was attributed to a cellular precipitation mechanism under low substitutional diffusivity of Cr. Noticeably, γ(111) halos are observed in between the CrN(111) ring and the α-Fe(110) ring in the EDPs of **Fig. 4.17b** and **Fig. 4.17e**, suggesting residual austenitic structure in the decomposed lattice for both AG17 and 304. Therefore, γ_N-AG17 experienced a eutectoid phase transformation similar to that of γ_N-304, which is: $\gamma_N \rightarrow$ CrN + α (+ γ). However, considering the phase decomposition mechanism of γ_N-304L to CrN + α-ferrite [120], the observed residual γ(111) halos are most likely due to incomplete phase transformation caused by sluggish substitutional-element diffusion kinetics at the treatment temperature. It is also worth mentioning that Mn_3N_2 precipitation, which was reported for the high-Mn alloy Fe-18Cr-11Mn-3Mo [118] after plasma nitriding, is not observed in γ_N-AG17.

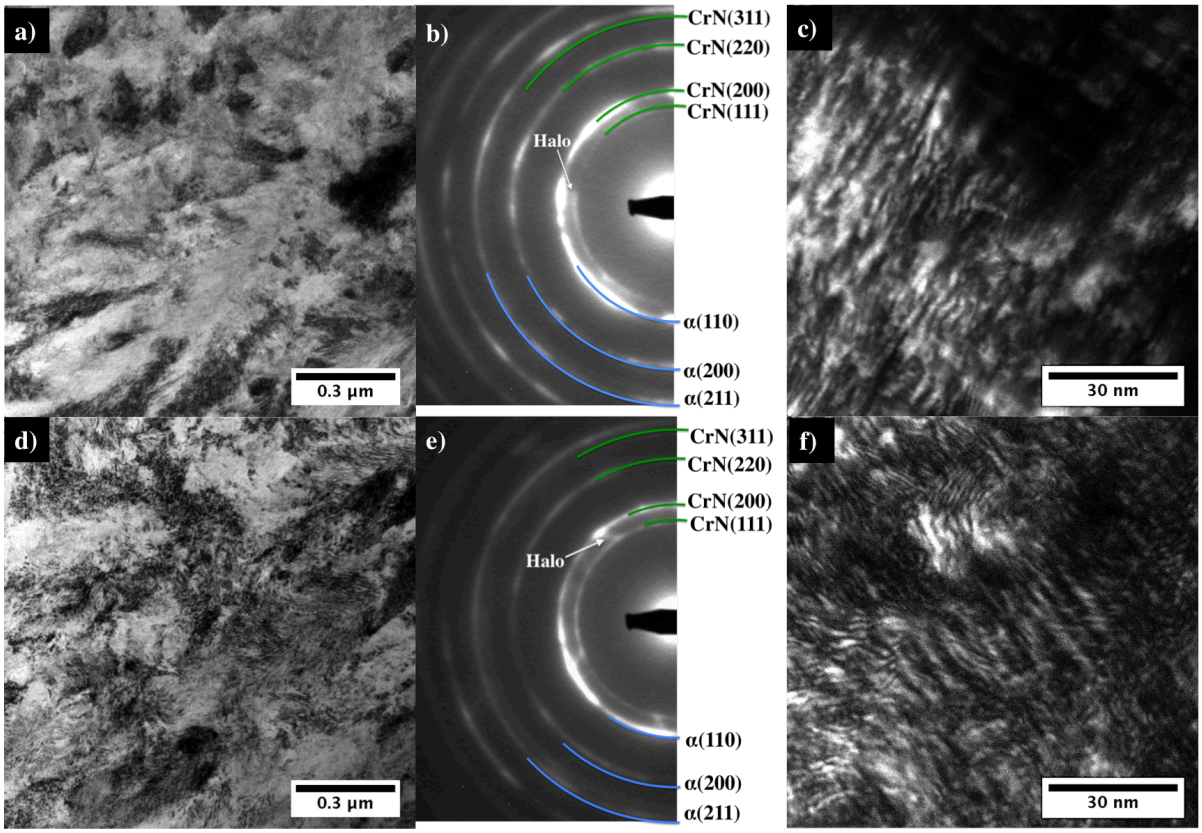

Fig. 4.17 BF-TEM images, EDPs, and DF-TEM images of 450°C 20hrs plasma nitrided 304 (a, b, c, respectively) and AG17 (d, e, f, respectively). DF-TEM images were constructed from CrN(111) diffraction electrons

For alloy 330, phase decomposition is clearly revealed at grain boundaries after 450°C 20hrs treatment (**Fig. 4.18c, d**). In the EDP of **Fig. 4.18c**, the large diffraction spots originate from two adjacent grains of γ_N-330 within the diffraction aperture, whilst the polycrystalline diffraction rings correspond to CrN and γ-Fe co-located at (or near) the grain boundary (identified by PDF cards 01-076-2494 and 00-052-0513, respectively). The DF-TEM image of **Fig. 4.18d** reveals nanometric clusters of spheroidal CrN precipitates located at the grain boundary; the precipitation zone being ~150nm wide. The high Ni content in alloy 330 stabilises the Cr-depleted austenite volume as polycrystalline γ-(Fe, Ni), which is co-precipitated with CrN. Thus, the decomposition mechanism can be determined for γ_N-330 as being: $\gamma_N \rightarrow$ CrN + γ-(Fe, Ni).

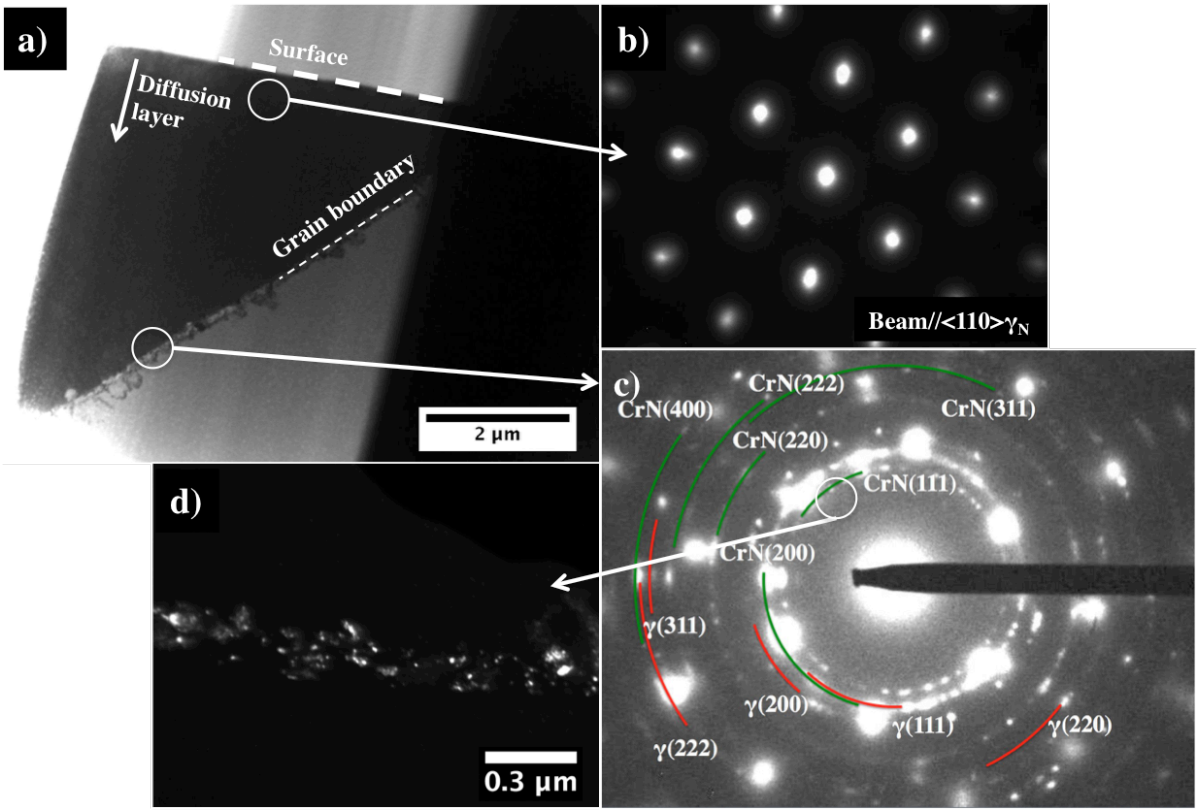

Fig. 4.18 a) low magnification BF-TEM image of the 450°C 20hrs plasma nitrided 330, b-c) corresponding selected area EDPs, d) DF-TEM image of the grain boundary region, DF-TEM image was constructed from CrN(111) diffraction electrons as indicated in figure c

More importantly, further to the broad XRD 'hump' (**Fig. 4.10**) and 'stretched' diffraction spots observed (**Fig. 18b**) on alloy 330 after plasma nitriding at 450°C for 20hrs, partial phase decomposition occurs inside the γ_N-330 grains under this treatment condition. Fine spheroidal nano-particles are observed in BF-TEM imaging (**Fig. 4.19a, c**) and double diffraction is evident in EDPs (**Fig. 4.19b, d**). Different to the sharp diffraction polycrystalline spots observed at grain boundaries, double diffraction spots for the γ_N-330 grains (**Fig. 4.19b, d**) suggest lattice coherency between secondary phase(s) and the matrix. It is difficult to generate a DF-TEM image for the secondary phase(s), because the adjacent diffraction spots are very close together. However, taking the lattice parameters of CrN, γ-Fe

and γ_N-330 as respectively ~0.414 nm (PDF card 01-076-2494), ~0.366 nm (PDF card 00-052-0513) and ~0.380 nm (the latter being determined from the peak position of close-packed plane from the X-ray diffractogram of alloy 330 at this treatment condition), lattice parameter ratios can be calculated as i) ~1.09 between CrN and γ_N-330, and ii) ~1.13 between CrN and γ-Fe. The ratio of diffraction spot distances of the adjacent FCC spots (in **Fig. 4.19b, d)** is ~1.10, which is very close to ~1.09 that is expected between CrN and γ_N-330, suggesting CrN nano-precipitates inside γ_N-330 grains.

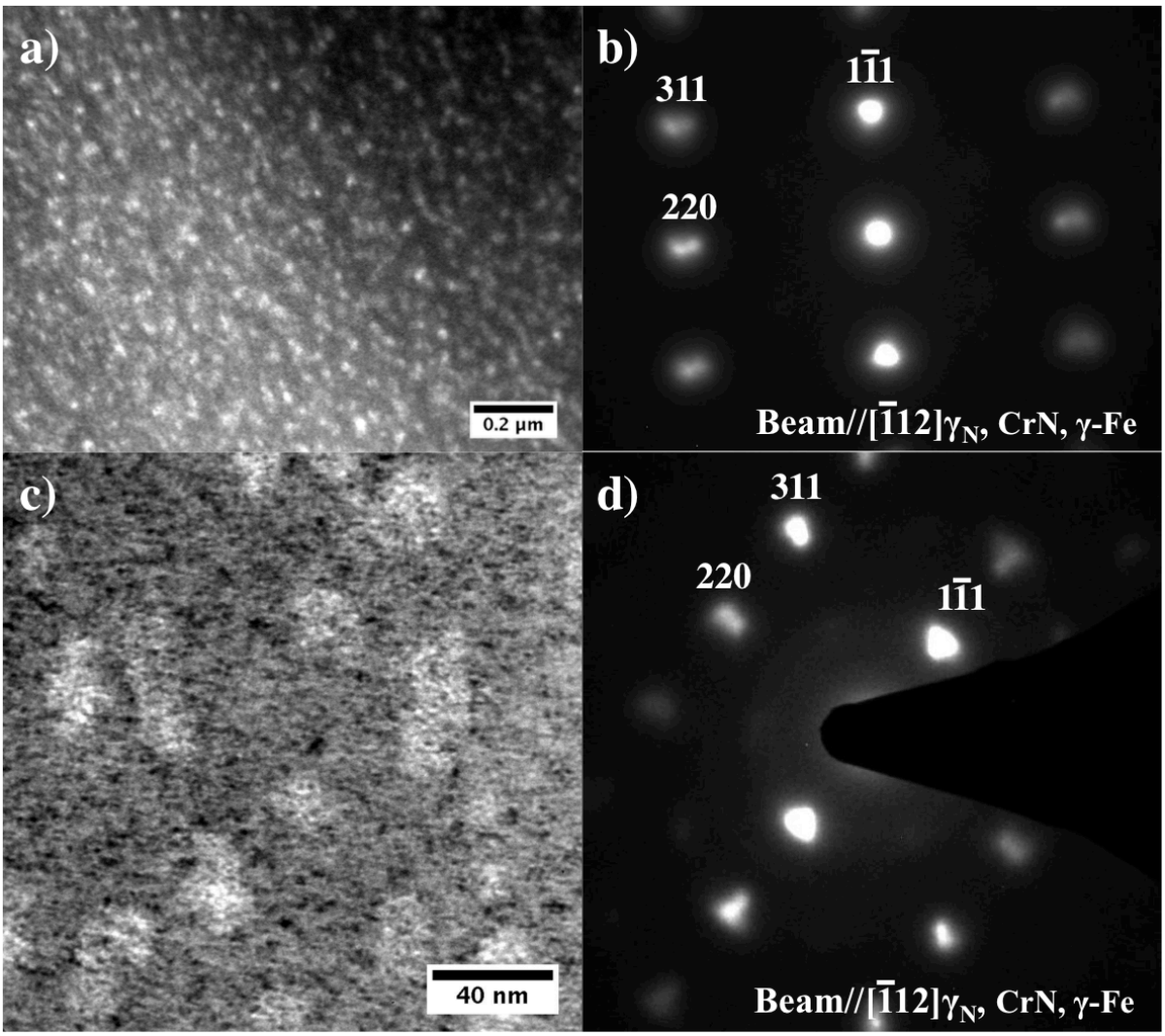

Fig. 4.19 BF-TEM images and EDPs of the 450°C 20hrs plasma nitrided 330 extracted via Philips EM420 (a, b, respectively) and FEI Tecnai T20 (c, d, respectively)

The abovementioned morphology and diffraction features are observed in the γ_N-330 grains of the TEM foil shown in **Fig. 4.18a**, which covers material to a sub-surface depth of ~5.5 μm, that is sufficiently deep with respect to the X-ray attenuation depth. In this case, γ-Fe could form inside γ_N-330 grains to give rise to the broad XRD 'hump' near the γ(111) position, in which the γ-Fe reflections might overlap with γ_N-330 reflections in EDPs (**Fig.4.19b, d**) owing to their relatively close lattice parameters and the lattice coherency. Owing to the potential coherency-microstrain (between precipitates and matrix) and the nitrogen-concentration or microstrain gradient (from surface to core) in the γ_N-330 layer, a broad 'hump' is eventually observed in the X-ray diffractogram of the 450°C 20hrs nitrided alloy 330 (**Fig. 4.10**). Such decomposed structure inside γ_N-330 grains should be metastable, where the precipitate coherency must reduce with increasing treatment temperature (or prolonged treatment time).

4.5.3.2 Influence of SFE on lattice decomposition

The formation of nitrides in γ_N is limited − and is controlled mainly by the diffusivity of substitutional elements, which clearly varies with material composition (i.e. primarily the Mn/Ni content, in commercial alloys) at a specific TPN treatment temperature. Moreover, given the limited substitutional diffusivity at the low treatment temperatures involved, lattice defects (e.g. SFs) plays a vital role in promoting the formation of distinct nitride crystallographic phases during treatment, through i) further increased N-uptake (and consequent lattice strain under supersaturation) and ii) locally enhanced substitutional diffusivity [17]. Phase decomposition of γ_N-AG17 at 425°C initiates from the topmost region of the nitrided surface, where lattice expansion and SF density is highest. The precipitation of CrN in γ_N-AG17 is facilitated by substantial lattice strain and high SF density. Phase decomposition of γ_N-AG17 occurred allotropically to α-Fe + CrN in a similar way to that commonly reported for γ_N-304,

but lattice decomposition is more thermodynamically favourable in AG17 than 304 after TPN, which can be correlated to the lower SFE expected in AG17 during nitriding ($10 \leq 18$ mJ/m^2 for unmodified AG17, compared to ≥ 18 mJ/m^2 for unmodified 304).

On the other hand, compared to the relatively 'complete' phase decomposition in γ_N-AG17 and γ_N-304 at the upper treatment condition of 450°C and 20hrs, the γ_N-330 grains were still at an early stage of decomposition under this treatment condition, whereby fine (metastable) nano-particles were observed in the expanded austenite matrix. Owing to the free surface (i.e. high interfacial energy planar defects) provided and the relatively high substitutional diffusivity at grain boundaries, phase decomposition of γ_N-330 occurred more readily at grain boundaries, where polycrystalline CrN and γ-Fe precipitates were clearly observed. Such sluggish decomposition of γ_N-330 could be attributed to the minor lattice defects in γ_N-330 grains, which correlates well to the significantly higher SFE of unmodified alloy 330 at room temperature (or of N-supersaturated lattice for this alloy during treatment). High SFE materials appear thermodynamically more stable, compared to low SFE ones (e.g. 304 and AG17) after TPN.

4.6 Summary

In this chapter, the crystal structures of the expanded and/or decomposed FCC lattice − as synthesised on two proprietary ASS after TPN at 400°C, 425°C and 450°C for 4hrs and 20hrs, respectively − were investigated systematically under EDX, XRD, BSE and on (FIB-prepared) TEM thin foils. Several findings on the paraequilibium structures of ASS after TPN could be summarised as follows:

- Lattice distortion in γ_N under nitrogen-supersaturation bears strong analogy with that of austenitic materials subjected to mechanical deformation (**Fig. 4.12**). Plasticity mechanisms of dislocation glide and/or dissociation in the nitrogen composition-strained FCC lattice are proposed with respect to material SFE under extremely high nitrogen absorption after low-temperature TPN, after the TEM observation of i) HCP lamellae (or ε-martensite) in a high SF density expanded austenitic lattice (i.e. low SFE γ_N-AG17) (**Figs. 4.13-4.15**) and ii) shear banding in a relatively low SF density expanded austenitic lattice (i.e. high SFE γ_N-330) (**Fig. 4.16**).

- Other than providing the basic (meta)stable room-temperature austenitic phase composition of the parent alloy, neither Mn nor Ni is essential for the formation of γ_N, but each element has a pronounced effect on the expanded lattice structure and stability under conditions of low-temperature thermochemical treatment, via their influence on SFE – and particularly with regard to the onset of crystallographic phase instability at the point of alloy 'over-supersaturation' with nitrogen (in Fe-Cr-Ni/Mn-N systems) for specific, alloy composition-dependent, critical temperature/time envelopes.

- At elevated treatment temperature, two possible 'diffusional' phase transformation mechanisms were identified in association with CrN formation, which were: i) a uniformly-distributed eutectoid decomposition mechanism to CrN + α-Fe in alloy AG17 (similar to that seen in AISI 304) (**Fig. 4.17**), and ii) sluggish precipitation inside grains but complete decomposition to CrN + (Ni-stabilised) γ-Fe at grain boundaries in alloy 330 (**Figs. 4.18-4.19**).

- The symbiotic relationship between SF number density and nitrogen uptake in a low SFE alloy such as γ_N-AG17 during thermochemical treatment appears beneficial in achieving high nitrogen absorption and lattice expansion at a relative low treatment temperature, but tends also to result in accelerated phase decomposition at higher treatment temperatures. Given the potential for dislocation glide under lattice strain, high SFE alloys such as 330 tend to accommodate less interstitial nitrogen overall (with rapid saturation – and relatively low anisotropic expansion − occurring under thermochemical treatment), but exhibit better structural integrity and thermodynamic stability.

- Under low-temperature nitrogen-supersaturation, the anomalous lattice expansion of ASS – and resulting material surface property or mechanical/tribological performance (as will be discussed in **Chapter 5**) – is influenced by both the residual stress development and SF generation, and could eventually be attributed to the elastic/plastic response of the substrate alloy (varying with ASS substrate compositional factors) to the nitrogen composition-induced stress/strain.

5 Mechanical and tribological evaluation of three austenitic stainless steels after triode plasma nitriding

As discussed in **Chapter 4**, colossally N-supersaturated surface layers were synthesised on three ASSs after low-temperature TPN treatment, by which different extents of phase decomposition were revealed on different ASS substrates after TPN with increasing treatment temperature or extended treatment time. Enhanced wear resistance was reported for AISI 316 after low-temperature nitriding [157]; however, the formation of CrN at the substrate surface is known to degrade material corrosion performance [5]. Previous investigations were mainly based on results from AISI 304 or 316 type ASS after low-temperature nitriding. Additionally, enhancements in wear performance after thermochemical diffusion treatment were mainly investigated under conditions of sliding wear. Details of the abrasion resistance of γ_N can hardly be found in the open literature.

In this chapter, the mechanical property (i.e. hardness) and tribological/electrochemical behaviour (i.e. sliding/abrasion wear resistance and corrosion resistance) of three ASSs after TPN treatment are evaluated. Vickers hardness values measured on the treated surfaces are presented in **Section 5.1**. In **Section 5.2**, the wear performance of the untreated and the 400°C 20hrs nitrided ASS is evaluated under dry sliding wear against a WC-Co ball (at 9.8 N for 500 m) and under wet slurry 3-body abrasion wear against a SAE 52100 steel ball (at 0.1 N for 3.99 m and at 0.2 N for 2.39 m). In **Section 5.3**, the corrosion performance of ASS before and after TPN (typically at 400°C 20hrs and at 450°C for 20hrs) is evaluated in 3.5 wt.% NaCl solution.

5.1 Vickers Surface Hardness

Vickers surface hardness values for untreated and TPN-treated alloys are shown in **Table 5.1** and plotted in **Fig. 5.1**. Hardness enhancement is evident for all three ASS after TPN, which could be attributed to i) the colossal amount of interstitial nitrogen absorbed, ii) defects (such as SFs) generated, iii) compressive residual stress developed at material surface (in case of nitrogen-supersaturation) and/or iv) the formation of hard CrN (in the case of phase decomposition). Nevertheless, indentation hardness also depends on layer depth at the treated surfaces. Generally, surface hardness increases with treatment time or treatment temperature.

Table 5.1 Surface hardness, HV0.025

Treatment	**AISI 304**	**Staballoy AG17®**	**RA 330®**
Untreated	235 ± 6	419 ± 6	210 ± 4
400°C 4hrs	/	692 ± 6	515 ± 10
400°C 20hrs	1325 ± 36	1808 ± 37	1048 ± 62
425°C 4hrs	/	892 ± 13	520 ± 17
425°C 20hrs	1518 ± 25	1890 ± 48	1494 ± 21
450°C 4hrs	/	1776 ± 55	786 ± 26
450°C 20hrs	1656 ± 38	2053 ± 58	1573 ± 18

Despite the (early stage of) lattice decomposition observed at the surface of 450C20h-330, TPN-treated alloy 330 surfaces present similar surface nitrogen contents and lattice expansion across the selected range of treatment conditions (as shown in **Chapter 4**). One could argue that the increase in surface hardness for alloy 330 is mainly due to the growth in diffusion layer depth. As shown in **Fig. 5.1**, the hardness values of the treated 330 samples generally correlate well to layer thickness (**Fig. 4.5**, **Chapter 4**). Nevertheless, the presumably high residual stress of γ_N-330 – partially released to different extents after volume displacements and/or cracking (already shown in **Chapter 4**) – must also contribute to the variation of surface hardness under different treatment conditions.

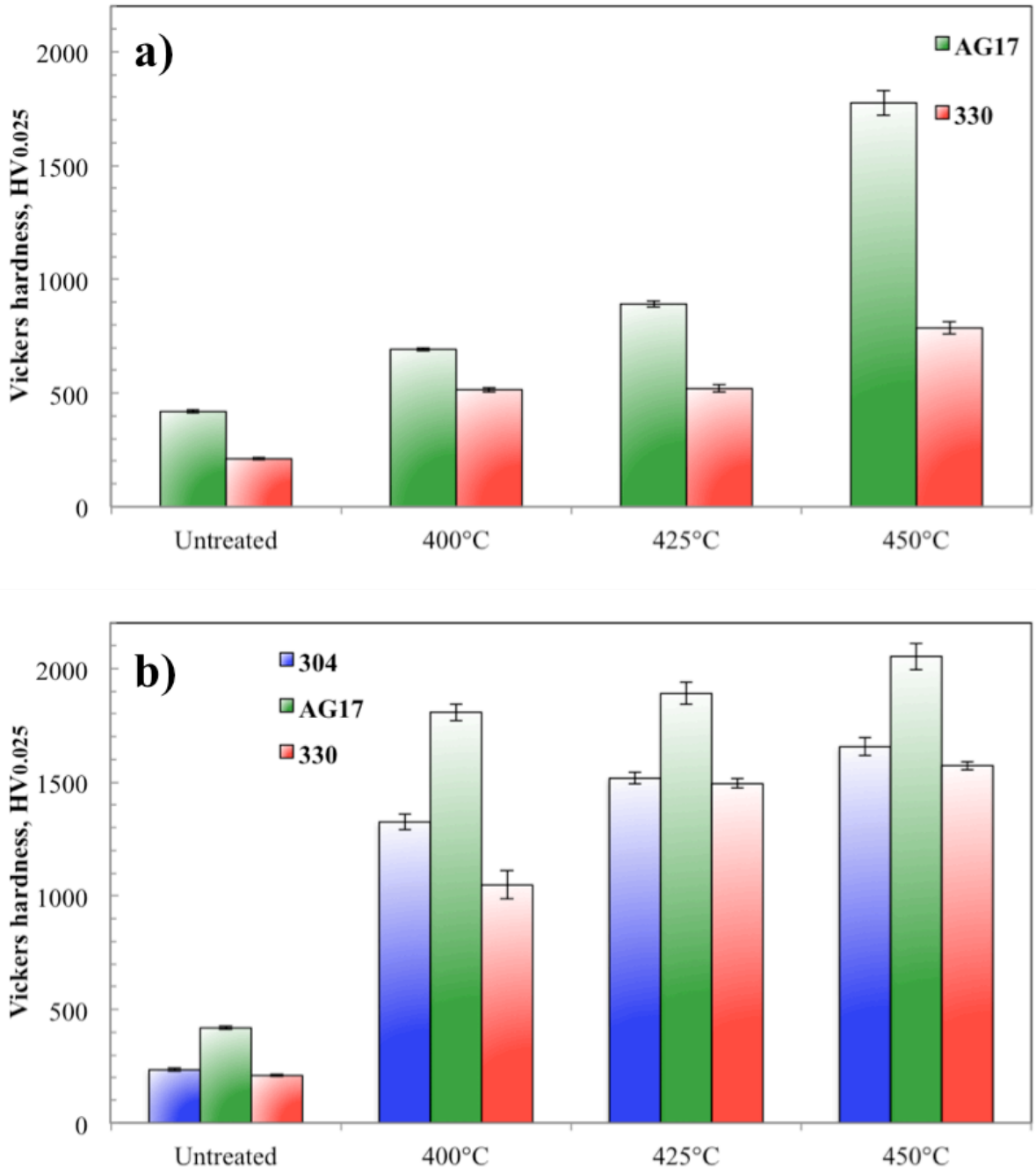

Fig. 5.1 Vickers surface hardness, $HV_{0.025}$, of ASS before and after TPN a) for 4hrs and b) for 20hrs

Compared to alloy 330, TPN-treated AG17 surfaces present significantly different surface nitrogen content and crystal structure after different treatment temperatures/times (**Chapter 4**).

At 400°C, the significant increase in hardness of AG17 with treatment time originates from i) the increasing accommodation of nitrogen in γ_N-AG17 (and the resulting lattice expansion, SF density and residual stress) and ii) the inward growth of the γ_N-AG17 layer.

At elevated treatment temperature, the formation of CrN could also lead to an increase in surface hardness. As already shown in **Fig. 4.6** (**Chapter 4)**, layer depths of 425C4h-AG17 and 450C4h-AG17 are similar (~2.7 μm and ~3.3 μm, respectively), but 450C4h-AG17 contains a ~1.5 μm thick topmost CrN-containing decomposed layer. Noticeably, 425C4h-AG17 also presents a CrN-containing decomposed layer at the surface, as shown under TEM, **Fig. 4.15**, **Chapter 4**), but the decomposed layer is discontinuous and much thinner (i.e. ~0.2-0.5 μm). Admittedly, the slightly higher layer thickness of 450C4h-AG17 (as compared to 425C4h-AG17, **Chapter 4**) should provide a higher measured surface hardness for this sample, but the remarkably higher hardness of 450C4h-AG17 compared to 425C4h-AG17 (**Fig. 5.1a**) should be mainly due to the thick decomposed layer. Nevertheless, comparing the surface hardness between 400C20h-AG17 and 450C20h-AG17 (**Fig. 5.1b**) there is a clear indication that a thin γ_N-AG17 layer of ~5.2 μm (with surface nitrogen content reaching, or at least not far below, the paraequilibrium nitrogen solubility at the selected treatment temperature) is able to provide a hardness level (at ~1800$HV_{0.025}$ under microindentation testings) similar to that of a ~14.7 μm thick CrN-containing surface layer after phase decomposition (at ~2000$HV_{0.025}$).

More importantly, as shown in **Fig. 5.1**, the high-Mn AG17 and the high-Ni 330 tend to have the highest and lowest surface hardness, respectively, after nitriding at equivalent conditions. Looking at three 400°C and 20hrs TPN-treated ASS samples – where γ_N layers were synthesised on all three ASS substrates at (presumably) saturated nitrogen absorption and

lattice expansion − the layer thicknesses of 400C20h-304, 400C20h-AG17 and 400C20h-330 are not significantly different (i.e. ~5.4 μm, ~5.3 μm, and ~4.3 μm, respectively, as shown in **Fig. 5.2**); however, 400C20h-AG17 (~1808 $HV_{0.025}$) exhibits an exceptionally higher surface hardness than 400C20h-304 (~1325 $HV_{0.025}$) and 400C20h-330 (~1048 $HV_{0.025}$), as shown in **Fig. 5.1b**. In this case, the ability of AG17 to generate SFs in plastic accommodation of nitrogen under nitrogen-supersaturation appears beneficial for material surface hardness enhancement, whereby low SFE ASS tends to have higher surface hardness after prolonged low-temperature treatment.

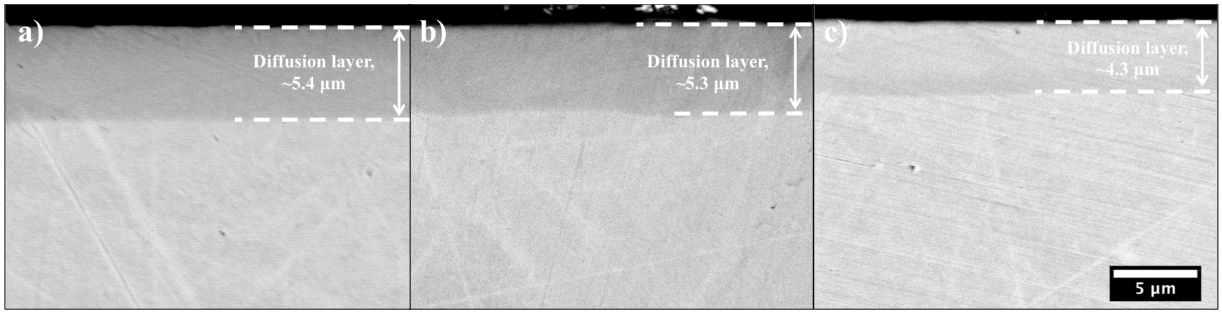

Fig. 5.2 Transverse BSE images of a) 400C20h-304, b) 400C20h-AG17, and c) 400C20h-330

5.2 Wear Performance

5.2.1 Dry sliding wear against WC-Co ball

The calculated sliding wear rates and measured wear track depths are tabulated in **Table 5.2**. The maximum Hertzian contact stress for 10 mm WC-Co ball pressing on untreated ASS substrate (taking an elastic modulus at 200 GPa and Poisson ratio at 0.3 for three ASS) was ~1.27 GPa. After low-temperature TPN, both the sliding wear rates and depths indicate remarkable enhancement in material sliding wear resistance. Wear rates were reduced by more than two orders of magnitude after introducing a nitrogen-supersaturated layer on top of ASS. The mean wear depths on the 400°C 20hrs nitrided ASS suggest that wear did not penetrate to the unmodified core on these samples under the selected sliding condition.

Table 5.2 Wear rates and depths of the untreated and the 400°C and 20hrs nitrided ASS after (dry) sliding against WC-Co ball at 9.8 N for 500 m

	Sliding wear rate, mm^3/Nm	Sliding wear depth, µm
U-304	$1.2 (\pm 0.1) \times 10^{-4}$	51.6 ± 2.9
400C20h-304	$4.8 (\pm 0.9) \times 10^{-7}$	1.1 ± 0.2
U-AG17	$1.4 (\pm 0.1) \times 10^{-4}$	62.5 ± 4.1
400C20h-AG17	$1.3 (\pm 0.3) \times 10^{-7}$	0.7 ± 0.1
U-330	$2.7 (\pm 0.2) \times 10^{-4}$	91.1 ± 4.7
400C20h-330	$12.5 (\pm 0.6) \times 10^{-7}$	3.0 ± 0.4

As indicated by Sun and Bell [157], the hard surface layer synthesised after nitriding reduces plastic deformation and adhesive wear during sliding. In this study, large amount of wear products were observed in the wear tracks on untreated ASS after sliding (**Fig. 5.3a, c, e**). The wear tracks on the low-temperature nitrided ASS, however, were revealed without such massive amount of wear products, which could be attributed to less adhesive wear after TPN (**Fig. 5.3b, d, f**). The severe adhesive wear on untreated ASS under sliding [4] was dramatically reduced after introducing a hard nitrogen-supersaturated surface layer. Consistent with surface hardness, 400C20h-AG17 showed the lowest wear rate and 400C20h-330 showed the highest wear rate amongst the nitrided samples. One could argue that 400C20h-AG17, which has the highest hardness as compared to 400C20h-304 and 400C20h-330, is more resistant to plastic deformation and provides better load-bearing capacity during sliding wear against a WC-Co ball counterface. Additionally, in all of the sliding wear tracks, wear grooves were seen parallel to the sliding direction. Intriguingly, extensive cracks were observed perpendicular to the sliding direction in the sliding wear track on 400C20h-330 (as highlighted next to **Fig. 5.3d**), which were not seen in the wear tracks on other two nitrided ASSs. These cracks might be associated with the high residual compressive stress state in γ_N-330.

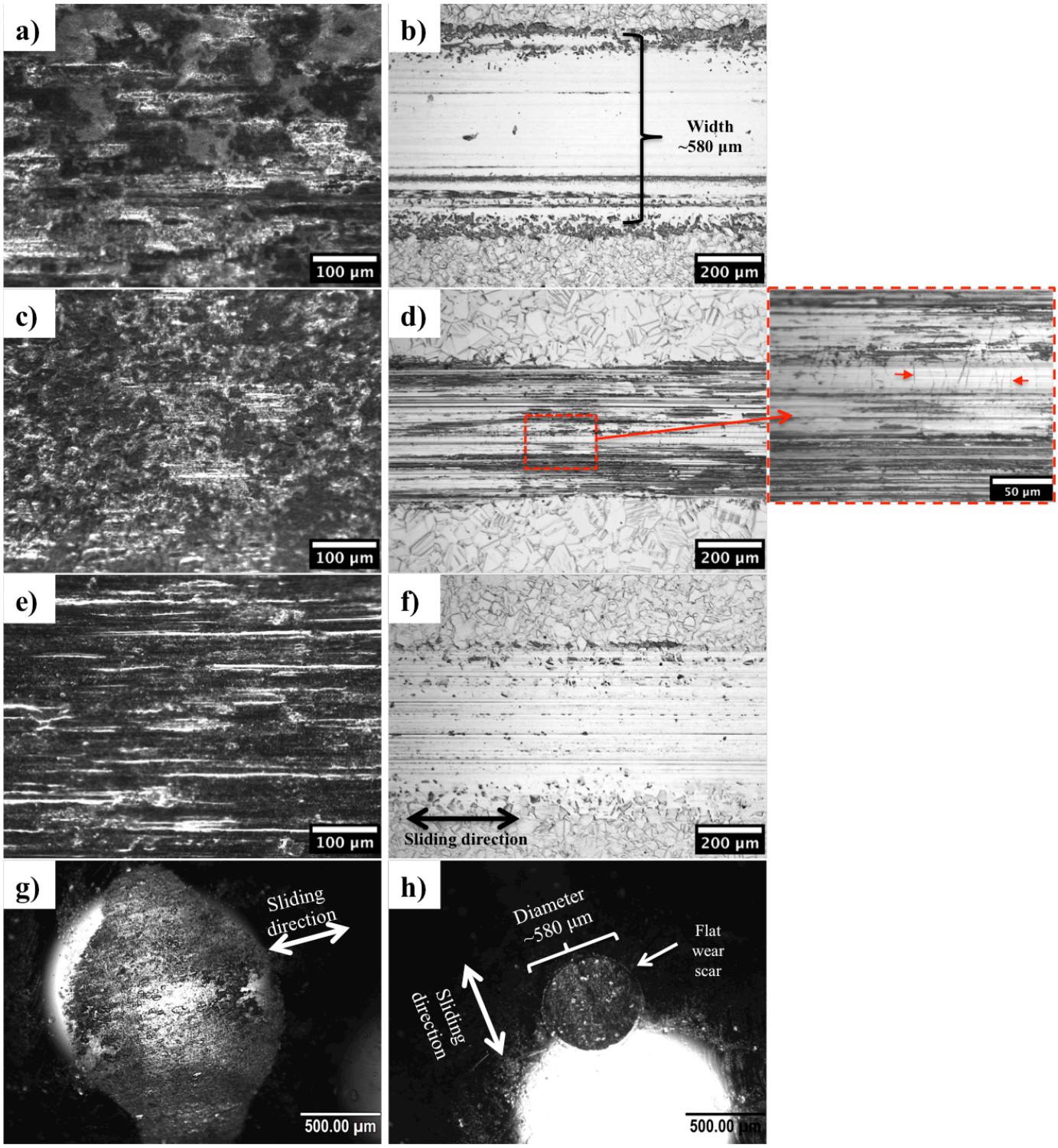

Fig. 5.3 Light optical images of sliding wear tracks on a) U-304, b) 400C20h-304, c) U-330, d) 400C20h-330, e) U-AG17, f) 400C20h-AG17 (a local region of image d is highlighted as indicated in figure); Light optical images of WC-Co ball after sliding g) against U-304 and h) 400C20h-304

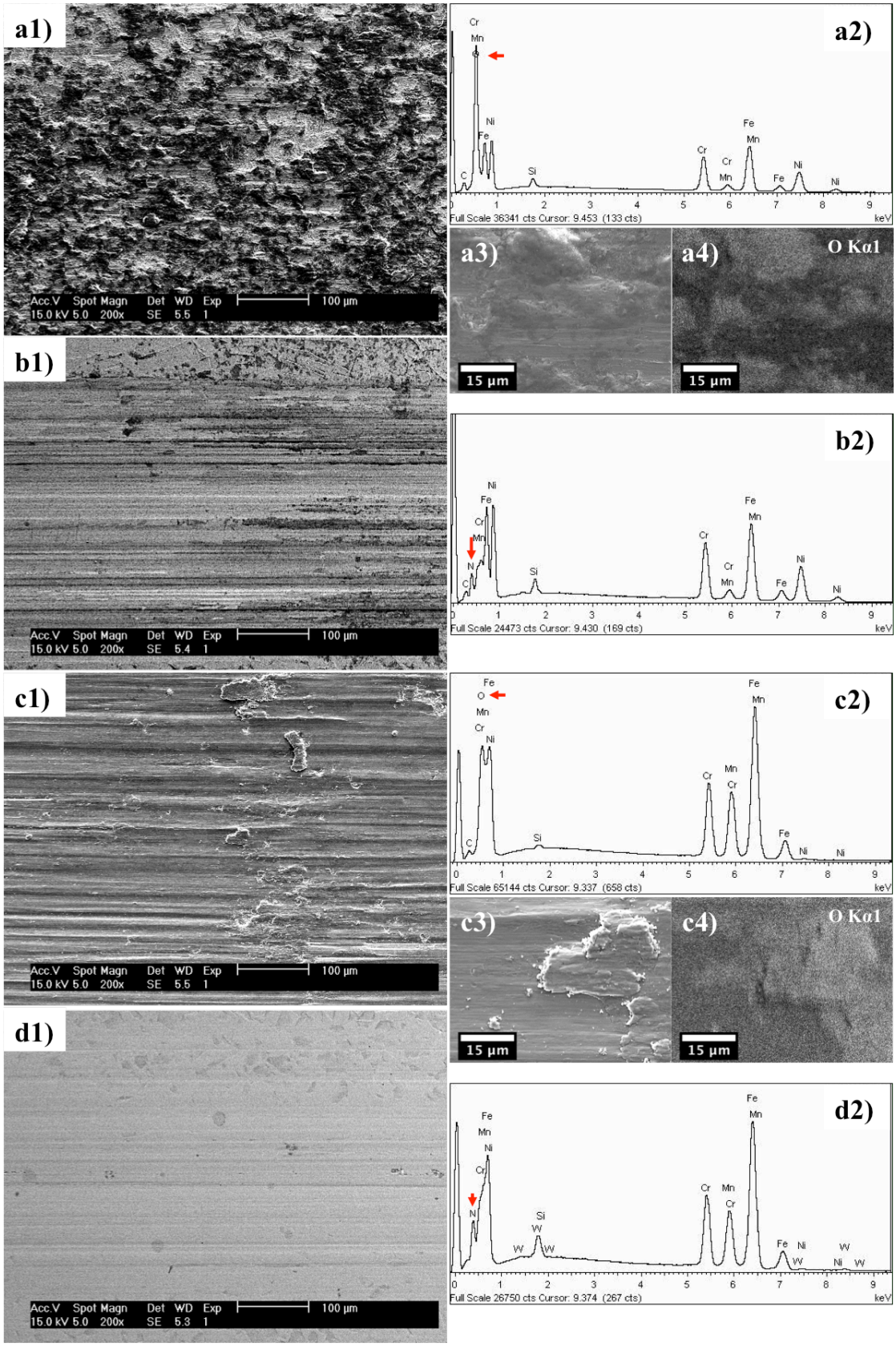

Fig. 5.4 SEM images of sliding wear tracks on a1) U-330, b1) 400C20h-330, c1) U-AG17 and d1) 400C20h-AG17; EDX profiles of local regions on wear tracks (covering an area of ~65 µm × 45 µm for each profile) of a2) U-330, b2) 400C20h-330, c2) U-AG17 and d2) 400C20h-AG17; SEM images for the local regions and corresponding element map of oxygen for U-330 (a3 and a4, respectively) and U-AG17 (c3 and c4, respectively).

After sliding tests, the WC-Co balls used were ultrasonically cleaned with isopropanol for 10 mins (to expose the wear scar on ball) and then also inspected under OM. Owing to the superior hardness and wear resistance of WC-Co (as compared to the low hardness and the known poor wear resistance of ASS), no significant wear can be seen on the ball after sliding against untreated ASS. As shown in **Fig. 5.3g**, the natural curvature of ball is retained in the contact region after sliding against U-304, but a significant amount of firmly attached wear product can be seen on top of WC-Co ball. The 'oval-shaped' attachment of wear products on WC-Co ball could be due to the adhesive junctions between ball and wear track during sliding. After sliding against TPN-treated samples, however, the contact region on the ball is flattened, without any signs of adhesive wear product attached. The diameter of the rounded wear scar on the WC-Co ball is consistent with the width of the sliding track on the nitrided sample surface (e.g. ~580 μm for 400C20h-304 sliding against WC-Co ball, **Fig. 5.3b** and **Fig. 5.3h**). Therefore, despite of the fact that low-temperature nitriding is capable of reducing sliding wear on ASS components, the hardened surfaces could introduce severe wear on the counterface material (even on hard and wear resistant materials such as WC-Co).

The SEM-EDX analyses of these sliding wear tracks on untreated ASSs indicate the presence of O (without significant W or Co from counterface material) in the attached wear products (**Fig. 5.4a1-4 and Fig. 5.4c1-4**), suggesting oxidation of untreated ASSs (probably in form of wear debris) under the heat generated during sliding. In contrast, the SEM-EDX profiles of the low-temperature nitrided surfaces under sliding show strong N Kα peak (as indicated in **Fig. 5.4b2, d2**) without any sign of O. Noticeably, the O Kα peak (at 0.525 keV) is very close to and overlaps with low energy peaks of Cr (at 0.5, 0.572 and 0.582 keV). The sliding wear track of nitrided ASSs might still have oxides, but oxygen should be in much smaller amount that was insufficient to be detected. It could be argued that the oxidation reaction of the TPN-

treated ASSs was reduced, as compared to untreated ASSs. The reduced oxidation might associate with (chemically) the high N content of γ_N. Additionally, small W peaks are seen in **Fig. 5.4d2**. W could be transferred from the conterface ball during sliding, since severe wear was observed on the WC-Co ball after sliding against the surface hardened ASSs (**Fig. 5.3h**).

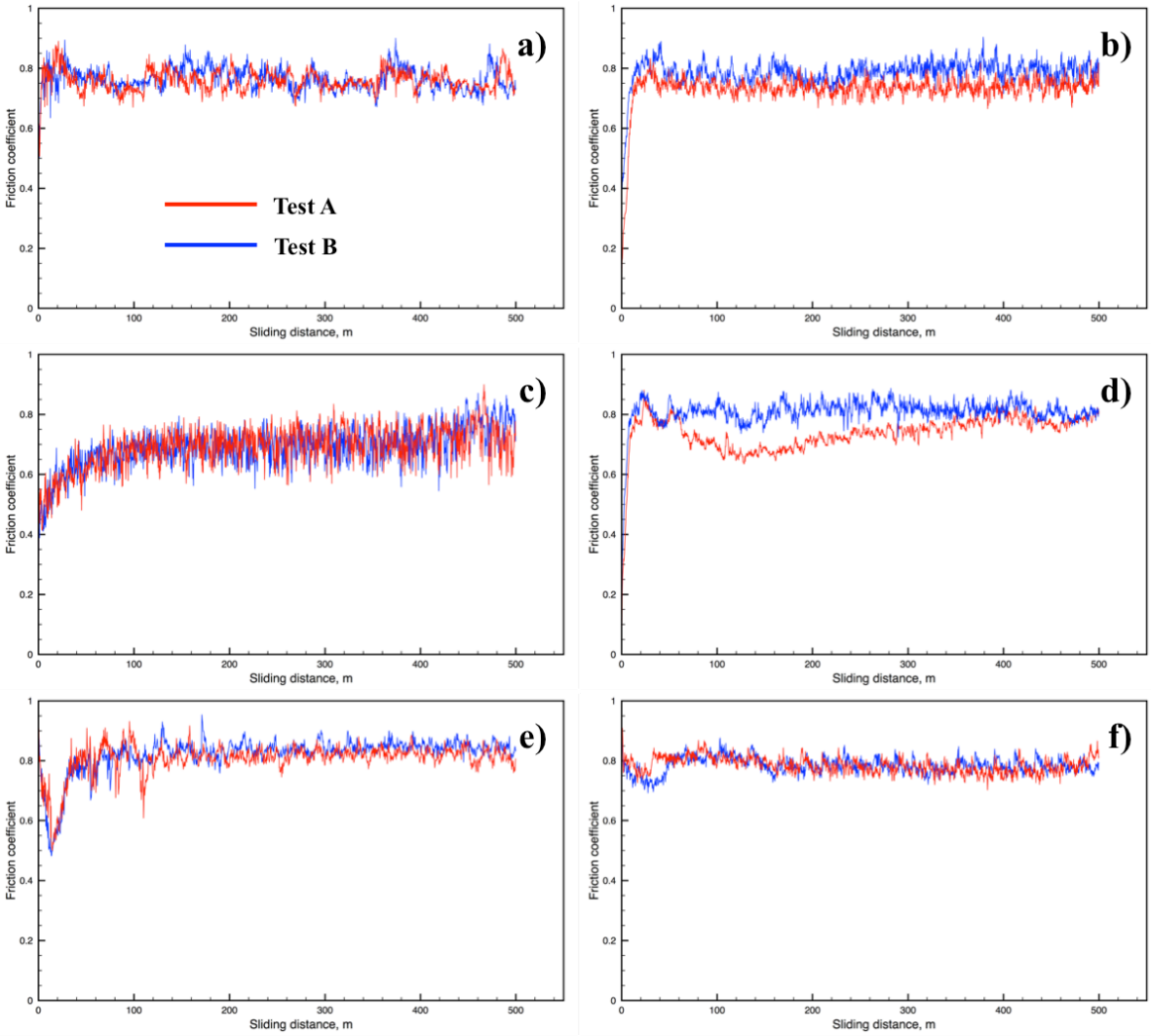

Fig. 5.5 Friction coefficient curves of a) U-304, b) 400C20h-304, c) U-AG17, d) 400C20h-AG17, e) U-330 and f) 400C20h-330 sliding against WC-Co ball for 500 m

Friction coefficient curves (of two repetitions for each sample) are shown in **Fig. 5.5**. After the first ~100 m, the friction coefficient stabilised at approximately 0.7-0.8 for almost all

tested samples. No significant change in steady state friction coefficient can be seen for ASSs before and after TPN.

5.2.2 Wet slurry microabrasion wear against bearing steel ball

Abrasion wear rates and crater depths of the 400°C 20hrs treated ASS are tabulated in **Table 5.3**. The maximum Hertzian contact stress for the 25.4 mm ball pressing on untreated ASS substrates (taking an elastic modulus at 200 GPa and Poisson ratio at 0.3 for three ASS) were ~0.11 GPa and ~0.14 GPa at normal load of 0.1N and 0.2N, respectively. OM inspection indicates 3-body abrasion mode (or rolling-abrasion [158]) for all craters, as expected for the low load and high slurry concentration employed. Due to the conformal spherical contact between craters and test balls (typically in 3-body abrasion mode), wear rates could be calculated from the measured crater widths [159]. Crater width typically ranged from ~500 to ~700 μm in this study, in which case craters were sufficiently large for the polycrystalline samples tested. The measured crater depths on the nitrided samples were all smaller than the diffusion layer depth; such tests can generally be regarded as 'non-perforation' tests (according to standard BS ISO 26424:2008).

Despite the remarkable enhancement in material sliding resistance after surface hardening (**Table 5.2**), there was no evidence of enhancement in wear performance under the selected abrasion conditions (**Table 5.3**). On the contrary, a degradation in abrasive wear performance was seen for both 304 and AG17 after introducing nitrogen-supersaturated surface layers at material surface via prolonged low-temperature TPN, whilst the abrasion wear rate of alloy 330 was almost unchanged. The decrease in abrasion wear resistance was the largest on AG17 after TPN, where the abrasion wear rate was doubled (**Table 5.3**).

Table 5.3 Abrasion wear rates and crater depths at selected abrasion parameters for the untreated and the 400°C 20hrs nitrided samples

	At 0.2 N for 2.39 m		At 0.1 N for 3.99 m	
	Abrasion wear rate, 10^{-4} mm^3/Nm	**Depth, µm**	**Abrasion wear rate, 10^{-4} mm^3/Nm**	**Depth, µm**
U-304	11.7 ± 1.2	2.5 ± 0.1	8.8 ± 0.6	2.2 ± 0.1
400C20h-304	16.2 ± 0.7	2.8 ± 0.1	14.8 ± 2.7	2.5 ± 0.1
U-AG17	11.8 ± 1.5	2.3 ± 0.1	11.9 ± 0.7	2.4 ± 0.1
400C20h-AG17	24.3 ± 3.5	3.1 ± 0.1	25.9 ± 5.2	2.8 ± 0.1
U-330	14.1 ± 1.0	2.7 ± 0.1	13.1 ± 1.3	2.5 ± 0.1
400C20h-330	14.7 ± 1.2	2.8 ± 0.1	13.3 ± 3.2	2.4 ± 0.1

Considering sample coupons being repetitively indented by (sharp) SiC particles under 'multi-indentation' rolling-abrasion, hard material surface should be worn less than soft material. However, the abrasion wear rate of the treated surfaces appeared somehow inversely correlated to the extend of surface hardness enhancement after TPN treatment at 400°C for 20hrs (as shown in the hardness bar chart of **Fig. 5.1b**). The counterintuitive increased abrasion wear rate is attributable to the brittleness of γ_N layer, sharp layer/core interface and lack of sufficient layer thickness.

Firstly, under 'multi-indentation' scenario during abrasion, the nitrided ASS could potentially experience brittle fracture, which accelerated abrasion wear rate. As illustrated by Christiansen et al. [103, 160], due to the strong chemical affinity between Cr and N (as compared to Cr and C), γ_N is able to accommodate much greater interstitial nitrogen (as compared to the accommodation of C in γ_C), giving rise to extremely high composition-induced residual stress under high nitriding potential (a term in gaseous nitriding in **Section 2.1.1.1**), and thus prone to brittle cracking. Apart from the stress relaxation as "brittle fracture" or as "grain elevation" (pushed-out) under high residual stress [103], the surface brittleness (after gaseous nitriding at high nitriding potential) has also been correlated to the potential

formation of ε-martensite "nucleated on SFs", but no evidence of ε-martensite formation was given in their study [160].

Furthermore, after tensile testing (instrumented with in-situ optical microscopy viewing) of AISI 316 "dogbone"-shaped samples after plasma immersion ion implantation (PI^3) at 360°C-520°C, Hoeft et al. [161] suggested that i) toughness of expanded austenite was not improved with the compressive residual stress developed, since the fracture toughness values measured from the compressively stressed γ_N surface layers (synthesised on AISI 316 substrate) were significantly lower than that of untreated steels, and ii) the extensively observed surface cracks (in a direction perpendicular to the tensile stress) mainly nucleated at grain boundaries and defects during tensile testing. Noticeably, although the cracking features observed on γ_N-316 under tensile stress were similar to those of hard coatings on metals, "decohesion" that could be seen on coatings was not seen on γ_N-316 layer [161].

In this study, the extent of the decrease in abrasion wear rate of samples after TPN (**Table 5.3**) correlates well with the SF density and the volume fraction of ε-martensite observed in γ_N (i.e. increasing in the order: γ_N-330 → γ_N-304 → γ_N-AG17, as discussed in **Chapter 4**). Without the generation of SFs to accommodate nitrogen-introduced plastic flow in FCC grains during nitriding, γ_N-330 should have higher residual stress than γ_N-AG17 and γ_N-304, as also suggested by the volume push-out and grain boundary cracking observed of γ_N-330, but not of γ_N-AG17 and γ_N-304 (**Chapter 4**). The good correlation between abrasion wear rates and SF densities (rather than residual stress) of γ_N suggests that the increased level of lattice defects might contribute to degradation in layer toughness (thus degradation in abrasion performance), rather than (or to a lesser extent of) compressive residual stress.

However, as suggested by Christiansen et al. [160] and Hoeft et al. [161], layer brittleness of γ_N is likely to be a combined result from both residual stress and SF density in γ_N. Considering the layer brittleness of γ_N-316 under gaseous nitriding at high nitriding potential [160], the potential layer brittleness in this study could be eventually attributed to the high nitrogen absorbed (~ 23-34 at.% N, **Table 4.1**, **Chapter 4**) at material surface under high "nitriding potential" in an intensified 7:3 N_2:Ar (volume fraction) plasma atmosphere, which points to the need for future wear investigations of alloy AG17 and 330 under low-temperature TPN with lower nitrogen volume fraction (such as 3:7 N_2:Ar).

Apart from the potential layer brittleness under TPN at high nitrogen volume fraction, both the sharp drop in nitrogen content at layer/core interface and the insufficient layer thickness could also contribute to the accelerated wear rate of ASS after low-temperature TPN. Different to coatings or bulk materials (i.e. homogenous materials), γ_N layers are non-homogenous, having reducing nitrogen content from surface to core in the diffusion layer. Additionally, there is an characteristic abrupt drop in nitrogen content (and abrupt change in nitrogen composition-dependent properties) at the interface between γ_N and core [162].

More importantly, the γ_N layers synthesised have insufficient thickness (~4-5 μm as shown in **Fig. 5.2**) with respect to the ~3 μm (mean size) SiC powder used in slurry. Although the measured crater depths were all much smaller than the treatment layer depths, the 25 μm diameter stylus tip (used for crater profilometry) was not able to detect the narrow local 'indents' made by small SiC particles, which could have penetrated (across the layer/core interface) into the unmodified core and resulted in high abrasion wear rate. The 'real' abrasion-affected region could be much deeper than the measured values shown in **Table 5.3**.

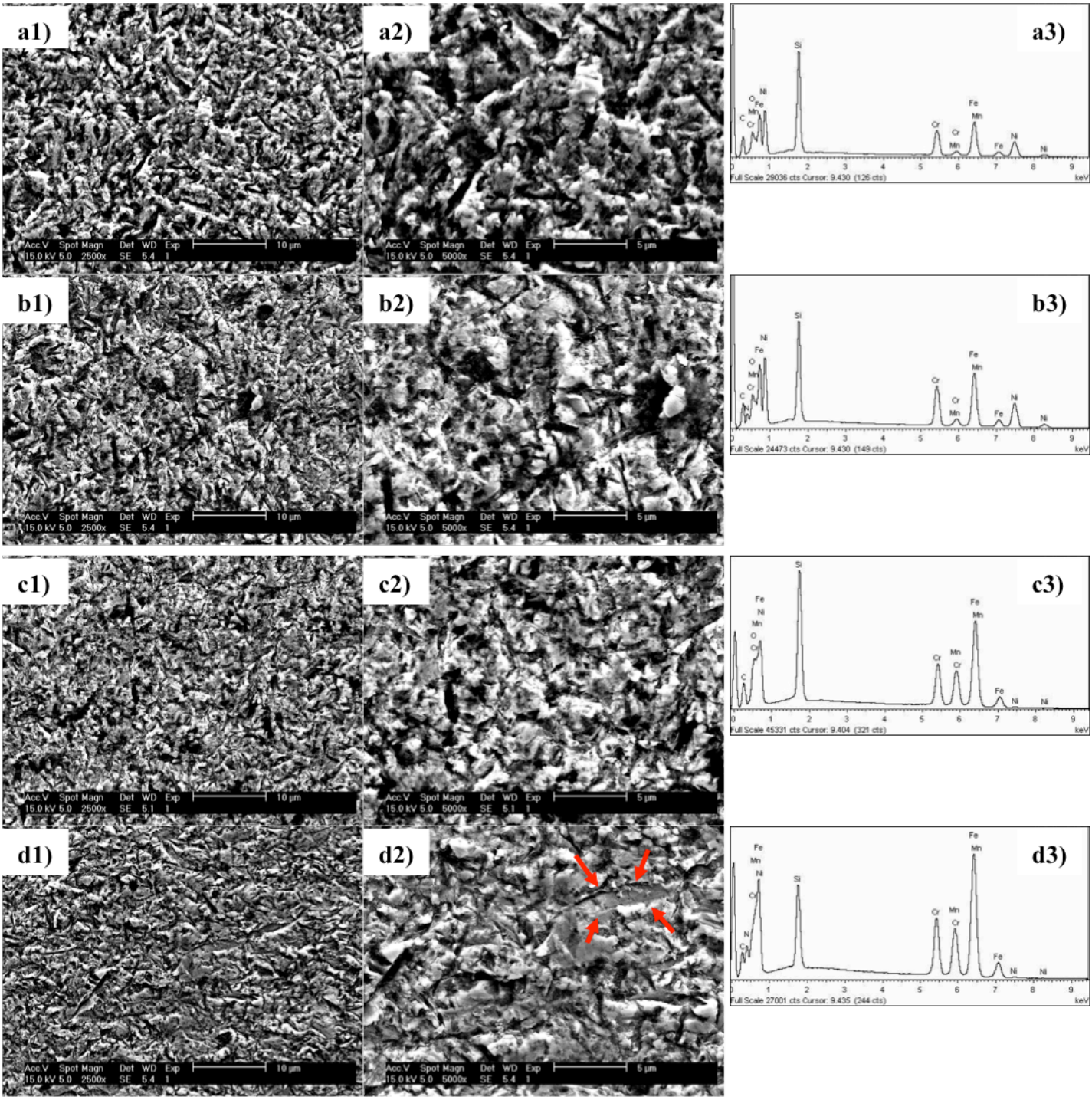

Fig. 5.6 SEM images, local SEM images and EDX profiles (corresponding to areas shown in local SEM images) for U-330 (a1-3, respectively), 400C20h-330 (b1-3, respectively), U-AG17 (c1-3, respectively) and 400C20h-AG17 (d1-3, respectively). For consistency, regions of interests were taken on the craters generated at normal load of 0.2N for abrasion distance of 2.39m and approximately halfway between the centres and the edges of the 'circular' craters observed under SEM.

As shown in **Table 5.3**, low-temperature TPN treatment (at 400°C and 20hrs) appears causing insignificant change and significant degradation in the surface abrasion performance of alloy 330 and alloy AG17, respectively. Therefore, the wear craters on alloy 330 and AG17 before and after low-temperature TPN were examined under SEM and EDX. Although no evident of 2-body abrasion (e.g. parallel abrasive grooves) were observed under OM, SEM images (in **Fig. 5.6**) clearly revealed – in addition to extensive 'indents' – several deep 'cutting grooves' on the abrasion crates of ASSs both before and after TPN treatment. Compared to the paralleled grooves usually seen in the craters generated under 2-body abrasion mode, the cutting grooves observed in **Fig. 5.6** are randomly oriented, short and discontinuous. Additionally, an intense Si Kα peak (at ~ 1.84 keV) and a strong C peak (at ~0.28 keV) are evident in all EDX profiles (**Fig. 5.6a3, b3, c4, d3**), suggesting embedment of SiC abrasive particles (after indenting and cutting) onto the abrasion craters. A clear N Kα peak is also evident (at ~0.4 keV) in the EDX profiles of the abrasion craters on TPN-treated samples (**Fig. 5.6b3, d3**), which originates from γ_N layers. However, both the indents and cutting marks appear small and deep under SEM (compared to the 25 μm diameter stylus used for measurement), confirming that the real abrasion penetration depths could be much deeper than those detected as shown in **Table 5.3**. The γ_N layers on TPN-treated ASSs were mostly likely penetrated by the sharp SiC particles during abrasion.

Compared to the wear morphology on the abrasion craters of other three samples (**Fig. 5.6a2, b2, c2**), the abrasion crater on 400C20h-AG17 (**Fig. 5.6d2**) appears rather 'flat'. The indentation or cutting marks on 400C20h-AG17 appear shallow under SEM, which could be attribute to the superior surface hardness of 400C20h-AG17. Compared to the EDX profile for U-AG17 (**Fig. 5.6c3**), the relative Si Kα peak intensity is clearly lower in the EDX profile

for 400C20h-AG17 (**Fig. 5.6d3**), indicating reduced SiC particle embedment on 400C20h-AG17.

More importantly, no brittle cracks could be identified in the abrasion craters on TPN-treated surfaces (**Fig. 5.6b2, d2**). Nevertheless, several flat regions are observed in the abrasion craters of 400C20h-AG17 (as indicated using red arrows in **Fig. 5.6d2**), but are not observed in the abrasion craters on U-AG17, U-330 and 400C20h-330. These flat areas hint at faceted brittle fracturing of γ_N-AG17 layer on 400C20h-AG17 during abrasion. Intriguingly, abrasion morphology appears similar between U-330 and 400C20h-330 without any sign of brittle failure after TPN, in which case the potential brittle fracture of γ_N during abrasion (as suggested by the facets observed in abrasion crater of 400C20h-AG17, **Fig. 5.6d2**) seems associate more with high SF number density rather than high residual stress.

Moreover, O was identified by INCA software (at ~0.525 keV) in EDX profiles (**Fig. 5.6a3, b3, c3**), hinting at another aspect for consideration (i.e. chemical reaction of sample surface in contact with wet SiC slurry). The surface of abrasion craters are, most likely, plastically deformed, oxidised and embedded with SiC particles (possibly fractured, if against TPN-hardened ASS surfaces). It points to the need of future studies on cross-sectional microstructure and chemical composition of the abrasion craters (probably under SEM/TEM after FIB sectioning/thinning).

To further investigate the potential brittle fracture of γ_N layers under 'multi-indentation' rolling-abrasion, several series of Vickers indents (with increasing indent load at 0.025, 0.05, 0.1 and 0.3 kgf) were carried out on the untreated and the 400°C 20hrs nitrided samples. The Vickers indents at 0.3 kgf are shown in **Fig. 5.7**. Some indentation-introduced traces (as

indicated by red arrows in **Fig. 5.7a**), which could be slip lines under plastic accommodation of indentation, were seen on U-304 without any sign of brittle failure.

After TPN at 400°C and 20hrs, however, 'circumferential' cracks (rather than radical cracks) were observed on all three ASS samples after indentation (as shown at indent load of 0.3 kgf, **Fig. 5.7b-d**). Considering the treated surfaces being compressed by indenter, the surface layers equivalently experienced a tensile component of stress/strain at directions towards indent centre (as indicated with the directions of the red arrows in **Fig. 5.7b-d**), where the cracks observed are at directions nearly perpendicular to the tensile components, similar to what was seen in Hoeft's study [161].

With these observations after Vickers indentation (**Fig. 5.7**), one could argue that the sharp ~3 μm SiC particles could introduced brittle cracking of the γ_N layers during 'multi-indentation' rolling-abrasion (especially after certain abrasion distances that the layer/core interfaces were affected by the 'indentation' from SiC particles), contributing to brittle fracture of nitrided surfaces and accelerating the abrasion wear rates.

Nevertheless, brittle cracking was not seen on all 400°C 20hrs nitrided ASS samples under Vickers microindents at low load (e.g. at 0.025 kgf for the microindentation hardness given in **Table 5.1**), but clearly seen at indent load of 0.3 kgf as shown in **Fig. 5.7**. These cracks seen on nitrided samples under indentation at higher indent loads could be associated to the increasing indent-affected deformation zone across the abrupt layer/core interface.

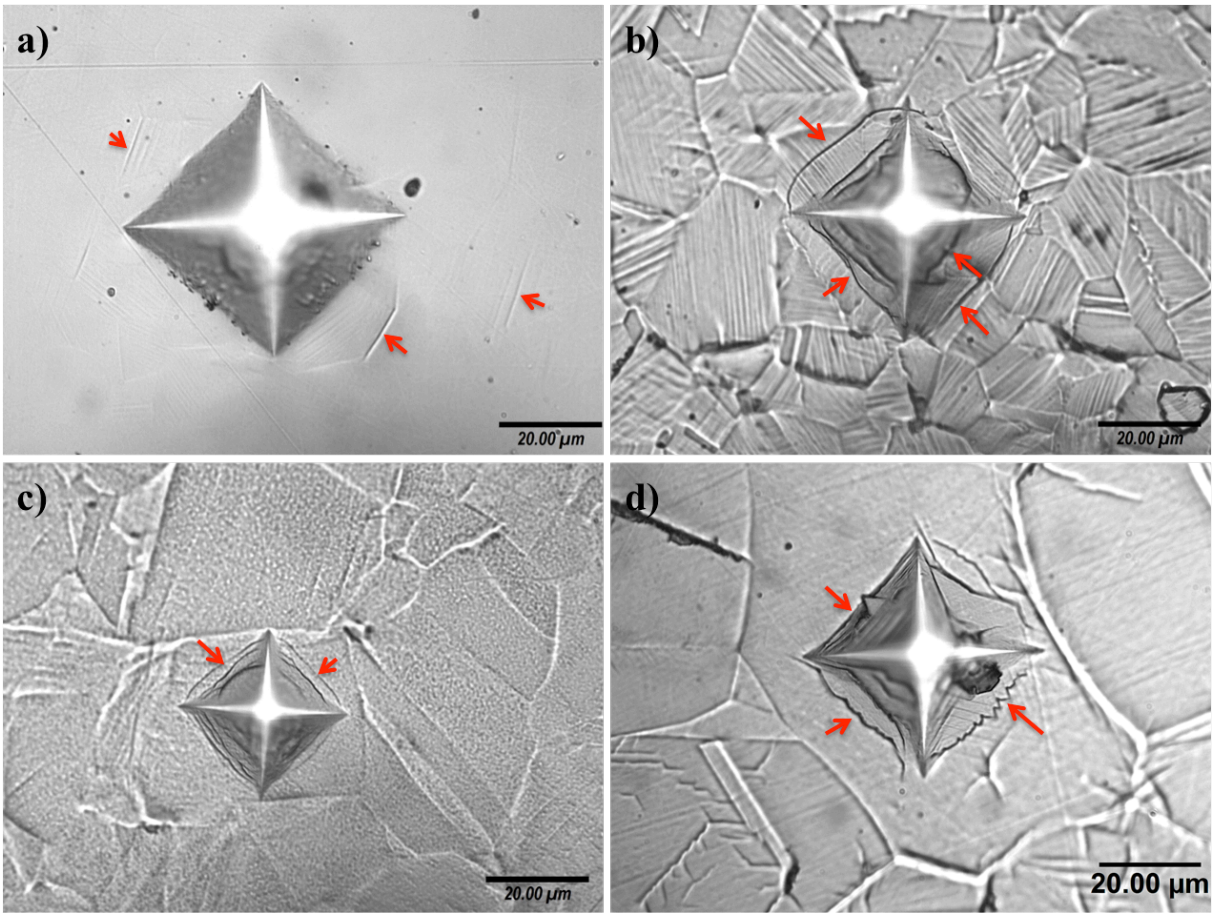

Fig. 5.7 Optical images of Vickers hardness indents (at 0.3 kgf) on a) U-304, b) 400C20h-304, c) 400C20h-AG17, and d) 400C20h-330

At indent load of 0.025 kgf, indent depths on all three nitrided samples are all less than 1 µm, using equation: $h = \frac{d}{2\sqrt{2}\tan\frac{136°}{2}} \approx \frac{d}{7.0006}$ (h is Vickers indent depth, d is the average length of diagonal and 136° is Vickers indenter angle). For the indents at 0.3 kgf on 400C20h-304, 400C20h-AG17 and 400C20h-330 **(Fig. 5.7b-d**), indent depths are ~6.6, ~4.6 and ~7.0 µm, respectively. Brittle cracks observed on nitrided samples under Vickers indentation (**Fig. 5.7b-d**) could be attributed to the insufficient load-bearing capacity of the unmodified core (and the abrupt layer/core interface) below thin γ_N layers on nitrided ASS samples. With this regard, the accelerated wear rate observed for ASS samples after nitriding (**Table 5.3**) under

the selected 3-body micro-abrasion condition appears to be a combined result from brittle fracturing and insufficient layer thickness.

5.3 Corrosion Performance

5.3.1 Open circuit potential

Open circuit potential curves are plotted in **Fig. 5.8**. The stabilised open circuit potentials at 3600s are shown in **Table 5.4**. After TPN at 400°C for 20hrs, OCP increased for Ni-stabilised austenitic 304 and 330, and increased very slightly for AG17. OCP of 304 and AG17 decreased significantly after TPN at 450°C for 20hrs, while there was no significant variation of OCP between 400C20h-330 and 450C20h-330.

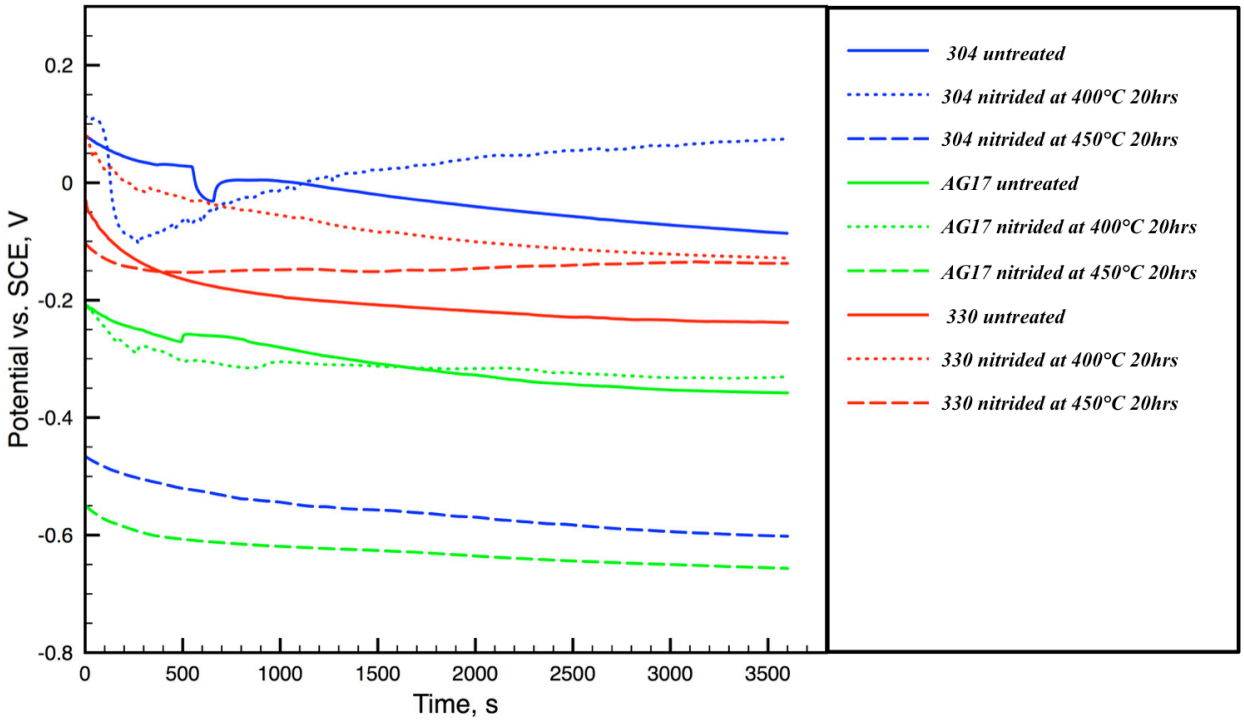

Fig. 5.8 OCP curves of samples in 3.5 wt.% NaCl

Table 5.4 OCP, Tafel potential and current of tested samples

Materials	OCP, V	Tafel potential, V	Tafel current, $\times 10^{-6}$ A/cm^2
U-304	-0.09	-0.46	1.56
400C20h-304	+0.08	-0.26	0.17
450C20h-304	-0.60	-0.72	1.42
U-AG17	-0.36	-0.47	1.70
400C20h-AG17	-0.33	-0.50	0.61
450C20h-AG17	-0.66	-0.75	1.61
U-330	-0.24	-0.41	1.05
400C20h-330	-0.13	-0.33	0.88
450C20h-330	-0.14	-0.33	1.13

5.3.2 Potentiodyanamic polarisation

Potentiodynamic polarisation curves are shown in **Fig. 5.9**. Tafel potentials (E_{corr}) and current densities (I_{corr}), which were derived via extrapolation of linear cathodic/anodic regions in the potentiodynamic polarisation curves, are given in **Table 5.4**. In terms of OCP, E_{corr} and I_{corr} values, low treatment temperature is preferred (but should be sufficiently high for the generation of considerably thick and useful nitrogen-supersaturated layer) for nitriding ASS without the loss of corrosion performance.

The nitrogen-supersaturated surfaces of ASS all showed improved corrosion performance after TPN at 400°C for 20hrs. For both Ni-stabilised austenitic 304 and 330 type ASS after low-temperature TPN, E_{corr} shifted to higher potentials and I_{corr} shifted to lower current densities. The enhancement in corrosion performance of the two Ni-stabilised ASSs (i.e. 304 and 330) upon colossal nitrogen-supersaturation at material surface (without formation of CrN) after TPN was obvious, with the evident shifts of the polarisation curves to the top-left (more noble) regions of the plot. Additionally, although E_{corr} of 400C20h-AG17 did not vary significantly as compared to U-AG17, I_{corr} of AG17 was clearly reduced after TPN at 400°C (**Table 5.4**), indicating much smaller corrosion rate at equilibrium corrosion potential, E_{corr}.

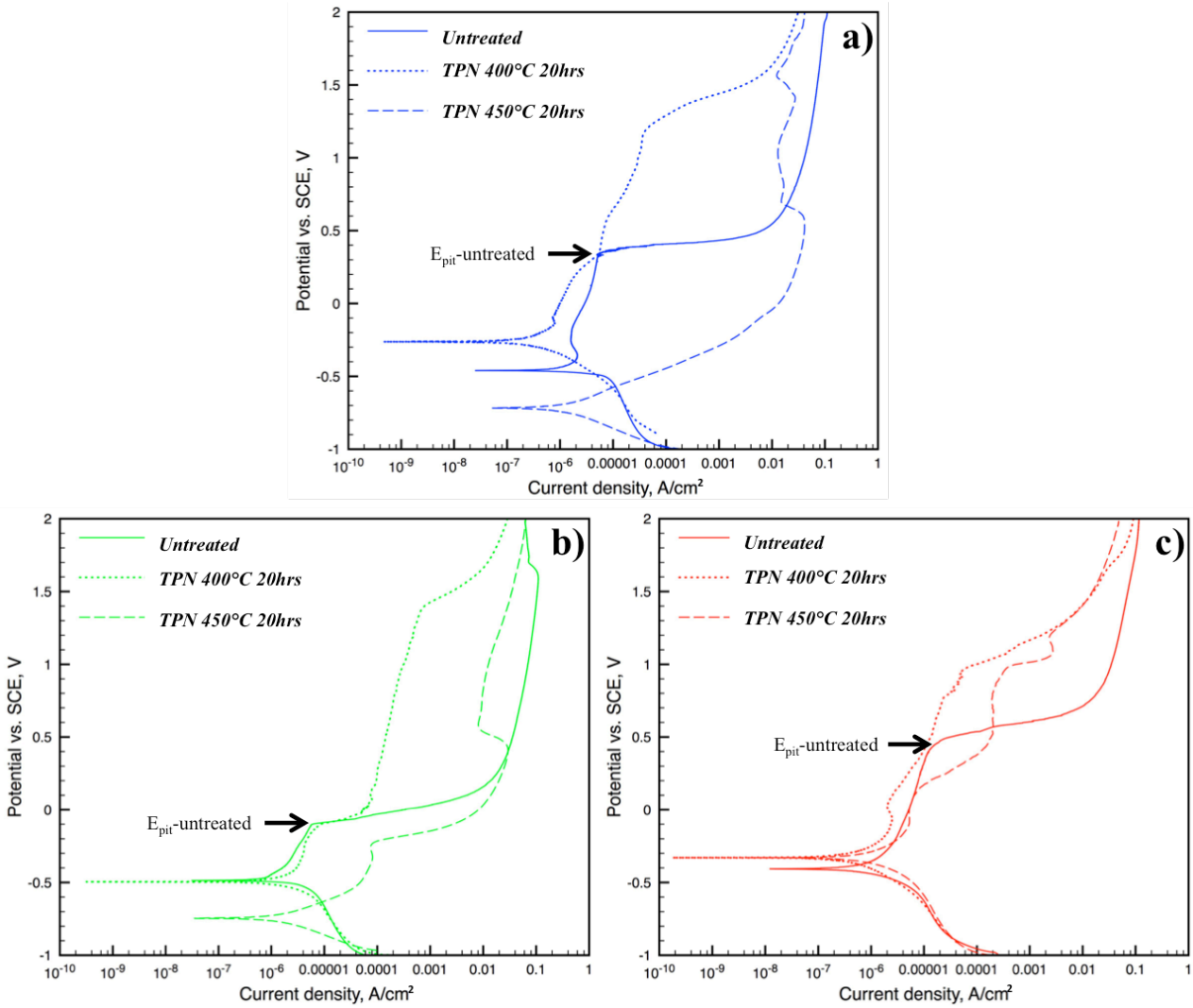

Fig. 5.9 Potentiodynamic polarisation curves of a) AISI 304, b) Staballoy AG17®, and c) RA330® before and after TPN at 400°C and 450°C for 20hrs

Degradation of corrosion performance can be confirmed for 304 and AG17 after TPN at upper treatment condition, because of the shifts of polarisation curve to the bottom-right (less noble regions) of the plot. Degradation of material corrosion performance could clearly be attributed to the lattice decomposition to CrN and Cr-depleted phase. However, E_{corr} of 450C20h-330 was at a potential similar to that of 400C20h-330 but higher than U-330, while I_{corr} was at a value higher than that of both 400C20h-330 and U-330. Intriguingly, compared to the γ_N-330 layer on 400C20h-330, the coherent nano-particles in inside γ_N-330 grains (i.e.

limited re-distribution of Cr) and incoherent nano-sized CrN precipitates at grain boundaries on 450C20h-330 (i.e. small volume fractions of complete Cr re-distribution) did not result in a drop in E_{corr}, but an increase in corrosion rate.

5.3.1 Corrosion passivity and features on corrosion sites

Austenitic stainless steels are known for their corrosion passivity owing to the protective Cr-rich oxide film that naturally forms at the material surface in oxidising environments (i.e. in the anodic reaction region for dissolution of metallic elements into the electrolyte, $M \rightarrow M^{n+} + ne^{-}$). The passivation and corrosion localisation of ASS in the anodic reaction region of the potentiodynamic polarisation curve (i.e. the upper part of potentiodynamic curves above E_{corr}) needs further discussion.

First of all, sudden increases in current density were observed for all three untreated alloys in potentiodynamic curves (at E_{pit}-untreated, as indicated in **Fig. 5.9**), which are due to breakdown of the passive film on ASS and localised pitting corrosion. Owing to the different alloy compositions, corrosion passivity is different for the three untreated ASS substrates. Generally, following an order from Mn-N stabilised to Ni-stabilised ASS, E_{pit} values were ~ -0.1V, ~0.3 V and ~0.5 V for U-AG17, U-304 and U-330, respectively. The high Mn-N U-AG17 had the smallest passivation region, whilst the high-Ni U-330 had the largest passivation region. High Ni content in ASS appears beneficial for large passivation region during corrosion in chloride solution.

For all three ASS after low-temperature TPN (at 400°C 20hrs, **Fig. 5.9**), the passivation regions were extended to higher corrosion potentials, while the corrosion current densities in the anodic reaction regions were reduced. Although U-AG17 and 400C20h-AG17 had similar E_{pit} values, 400C20h-AG17 exhibited much lower current density than U-AG17 after the first

breakdown of passivation at E_{pit} (**Fig. 5.9b**). Given an incompletely decomposed structure, 450C20h-330 showed higher current density than that of 400C20h-330 and U-330.

Additionally, the features observed on corrosion sites of samples after potentiodynamic polarisation (**Fig. 5.10**) also indicated improved pitting resistance in 3.5 wt.% NaCl solution. Firstly, corrosion pits are observed on all three untreated ASSs after corrosion (see OM images, **Fig. 5.10a, c, e**). After low-temperature nitriding, pitting corrosion was clearly reduced as shown in **Fig. 5.10b, d, f**. The enhancement of pitting corrosion resistance of ASS after addition of nitrogen (either in equilibrium solid solution [163] or under paraequilibrium interstitial supersaturation [164-170]) were attributed to the formation of ammonium ions, via reaction: $[N] + 4H^+ + 3e^- \rightarrow NH_4^+$, which neutralised local pH level and inhibited (acidic) pitting. Low-temperature nitriding of ASS appears beneficial in preventing pitting corrosion in chloride solution. However, some localised features were still seen on the corrosion sites (see dark-field OM images, as highlighted in **Fig. 5.10b, d, f**).

On the corrosion site of 400C20h-304 after potentiodynamic polarisation in 3.5 wt.% NaCl solution (**Fig. 5.10b**), some γ_N-304 grains showed slightly deeper corrosion depth than others. Parallel bright patterns were clearly revealed inside these grains in the dark-field image of **Fig. 5.10b**. Buhagiar et al. [170] presented similar patterns under SEM, which was attributed to stress-induced slip lines during corrosion, on low-temperature carbonitrided AISI 316 ASS after immersion corrosion test in Ringer's solution. The parallel patterns in **Fig. 5.10b**, which could also be stress-induced slip lines, on 400C20h-304 after potentiodynamic polarisation in 3.5 wt.% NaCl solution (i.e. a much less aggressive solution compared to Ringer's solution) could be associated to and hinted at a high residual stress in the γ_N-304 layer investigated.

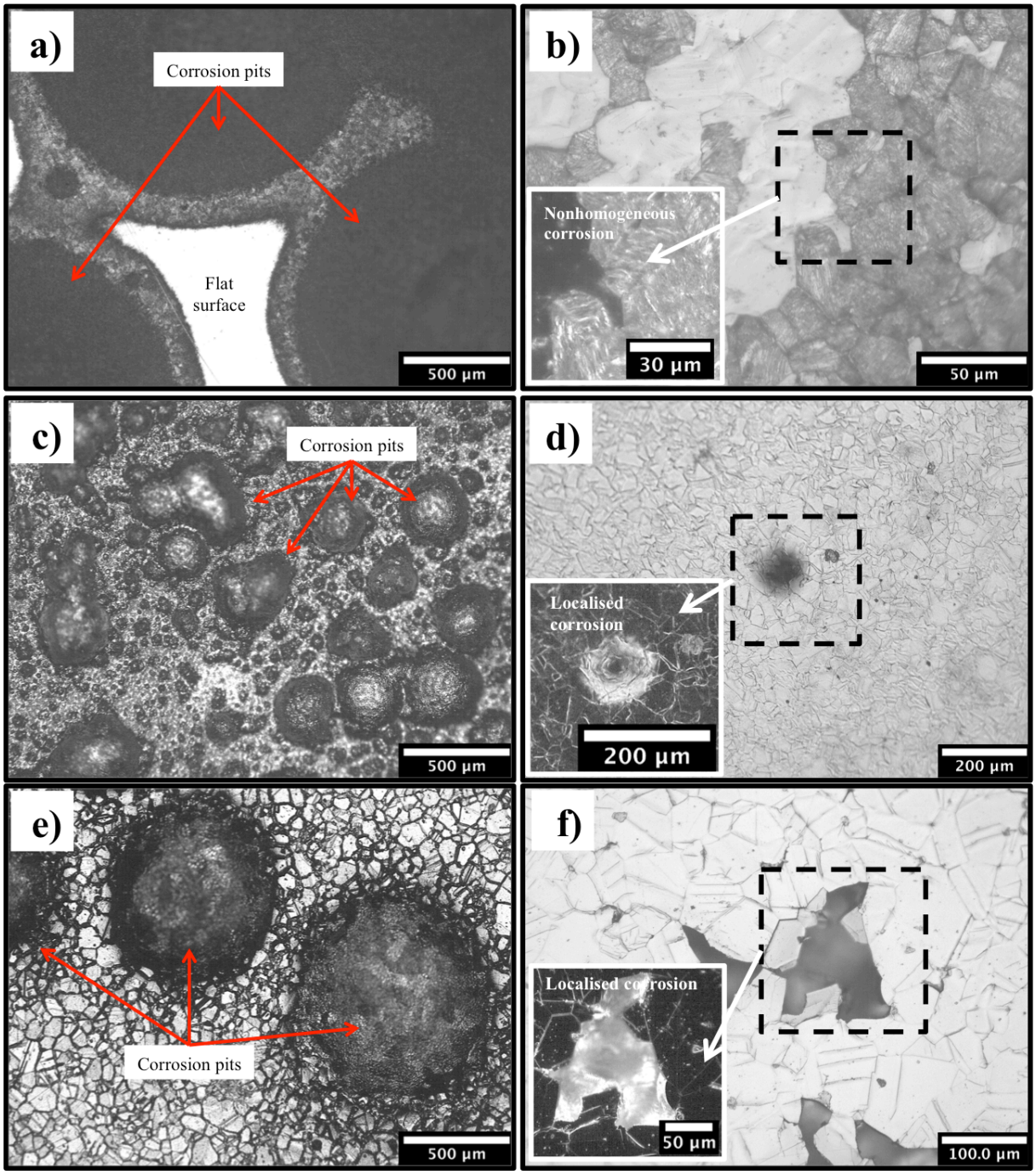

Fig. 5.10 OM showing features in the corrosion sites on untreated and 400°C treated surfaces for a, b) AISI 304; c, d) Staballoy AG17®; and e, f) RA330® (the local features are also highlighted under dark-field optical illumination at the left corner of image b, d, f)

The corrosion site of 400C20h-AG17 after potentiodynamic polarisation is shown in **Fig. 5.10d**. Small rounded pits (~20 μm diameter) were evidently seen. Compared to corroded U-AG17, which showed several large corrosion pits and large numbers of fine pits, corrosion pits on γ_N-AG17 were less in number and smaller (such that they can hardly be found). One could argue that the colossal nitrogen content in γ_N-AG17 inhibits both the initiation and growth of corrosion pits via contributing to NH_4^+ formation during corrosion. However, as compared to Ni-stabilised ASS, high Mn-N ASS appears more susceptible to pitting corrosion in chloride solution after low-temperature nitrogen-supersaturation, due to the small rounded pits observed on corroded 400C20h-AG17.

Relatively large features were observed on 400C20h-330, as shown in **Fig. 5.10f**. The rest of the surface of 400C20h-330 appeared very similar to that before corrosion testing (i.e. minimal corrosion). Considering the sharp and straight boundaries between these large features and the flat surface, this feature cannot be simply explained by (localised) corrosion, where surface volumes were dissolved in electrolyte; however, it could be due to a combined effect of both corrosion and the high residual stress in γ_N-330. Firstly, the volume displacements on 400C20h-330 along shear bands (as observed under TEM, **Chapter 4**) and possibly along grain boundaries (for the cracking observed) after TPN could expose the less nitrogen-supersaturated volumes in the underlying region. Secondly, once the surface volumes are dissolved away in the electrolyte, the high stresses (or strain energy) stored in the γ_N-330 layer on 400C20h-330 could be released further via such volume displacements, which in turn accelerate corrosion. Additionally, considering the tendency of γ_N-330 layer to crack along grain boundaries at elevated treatment temperature (**Chapter 4**), these large feature on the corrosion site of 400C20h-330 (**Fig. 5.10f**) could occur due to stress corrosion cracking, given the potentially highest residual stress in γ_N-330.

5.4 Summary

In this chapter, three surface hardened ASS after TPN at 400°C for 20hrs were evaluated under sliding/abrasion wear testings; and both the 400°C 20hrs and the 450°C 20hrs treated ASSs were evaluated by corrosion testing in 3.5wt.% NaCl water solution. Several conclusions can be drawn, as follows:

- Remarkable surface hardness enhancements were seen for all three ASSs after TPN treatment (**Fig. 5.1**). The superior nitrogen absorption in AG17 under low-temperature nitriding (associated with its ability to generate SFs under stain) provides this alloy with the highest surface hardness amongst the three investigated.

- The prolonged low-temperature TPN treatments appears beneficial to material (dry) sliding wear performance (**Table 5.2**), via reducing adhesive wear and enhancing load-bearing capacity of the treated surface during sliding against WC-Co ball; however, wear of the WC-Co counterface material tends to increase on the nitrided samples (**Fig. 5.3**).

- As indicated by abrasion results (**Table 5.3**) and surface cracking under Vickers indents (**Fig. 5.7**), the high surface nitrogen content in γ_N might have damaged the toughness of ASS under the selected high nitrogen volume fraction in the chosen plasma atmosphere. Under 3-body abrasive wear, the accelerated wear rate of ASS after TPN (**Table 5.3**) could be attributed to i) brittle fracturing of 'over-supersaturated' γ_N layers under the selected treatment parameters and ii) the relatively shallow diffusion layer depths with respect to the ~3 μm (mean size) particles used in abrasive slurry.

- The prolonged low-temperature treated samples (i.e. at 400°C and 20hrs) all showed improved corrosion performance in 3.5 wt.% NaCl solution compared to untreated ASS substrates (**Fig. 5.10**). Additionally, low-temperature TPN could also inhibit pitting corrosion of ASS (**Fig. 5.9** and **Fig. 5.10**). An expected loss of corrosion resistance was observed with the lattice decomposition of 304 and AG17 after TPN at 450 °C for 20hrs, whilst the sluggish decomposition at the surface of 450C20h-330 resulted in only a slight increase in I_{corr} as compared to U-330 (**Fig. 5.9**).

- The surface chemistry and the distribution of essential corrosion-resistant elements (such as Cr) are the dominant factors for material corrosion performance. Both the surface nitrogen content and the pre-existing substitutional elements in substrate (i.e. Ni or Mn levels) determined the corrosion performance of γ_N layers synthesised. The high SF number densities (and the formation of ε-martensite) in γ_N-304 and γ_N-AG17 and high residual stress in γ_N-330, which were potential influential factors on material mechanical/tribological performance, did not translate to a decrease in material corrosion resistance. However, residual stress of γ_N layer needs to be concerned for applications of low-temperature nitrided ASS in corrosive environments regarding the potential breakdown of passive films via volume displacements during corrosive attack (owing to the tendency of γ_N layer to relax its residual stress, such as the potential stress corrosion cracking in γ_N-330, **Fig. 5.10f**).

- Both the non-homogenous corrosion on γ_N-304 (**Fig. 5.10b**) and the large sharp features on γ_N-330 (**Fig. 5.10f**) suggested high levels of residual compressive stress, whilst no sign of high residual stress was seen on 400C20h-AG17 (**Fig. 5.10d**). A ranking order of residual stress level of γ_N layers, using the features observed after potentiodynamic

polarisation (**Fig. 5.10b,d,f**), could be given from high to low as γ_N-330, γ_N-304 and γ_N-AG17, which was inversely correlated to the SF densities observed in these N-rich layers.

6 Characterisation of two Cr-free austenitic steels after triode plasma nitriding

This chapter presents investigations on two Cr-free austenitic steels, Invar 36® (Fe-35Ni, in wt.%) and Hadfield steel (Fe-13Mn-1.2C, in wt.%) after TPN. Although Invar was reported by Williams et al. [87] under nitrogen ion beam processing at 400°C as showing two 'new' FCC structures after treatment, neither Invar nor Hadfield steel have been investigated under low-temperature nitriding in the open literature. Although Cr is believed being the essential element in formation of γ_N and short ranged ordered Cr-N clusters has been widely discussed, it might be possible to generate γN on Cr-free austenitic steels, given one of the key facts in γ_N formation is a sufficiently low temperature that phase transformation towards thermodynamic equilibrium is hindered. Apart from X-ray diffraction analysis with respect to the existing open database of powder diffraction patterns, a combination of techniques (such as EDX, BSE and TEM) is used, together with nano-indentation and Vickers indentation testing, to identify the 'new' surface phases formed on Invar and Hadfield samples under low-temperature TPN treatment – and to explore the possibility of nitrogen supersaturation in these alloys.

In **Section 6.1**, TPN-treated Invar (at equivalent treatment conditions to those of ASS in **Chapter 4**) is characterised and compared to nitrided 330 to reveal to role of Cr, where both substrate materials have ~35 wt.% Ni, but one without Cr and one with ~19 wt.% of Cr. The differences in material surface crystal structure and mechanical property (i.e. indentation hardness) after TPN are discussed between the selected two high-Ni steels. In **Section 6.2**, TPN-treated Hadfield steel (at a different chamber configuration and a lower treatment temperature of ~300°C for 4-20hrs) is characterised and discussed. The surface phase

compositions and hardness of Hadfield steel are revealed with respect to treatment times. Because of the different treatment conditions applied and the different Mn and N content between Had and AG17, results of the former are not directly compared to the latter, but reveal nevertheless the crystallographic response of such high Mn-C austenitic steel to nitrogen absorption at a much lower diffusion treatment temperature.

6.1 Characterisation of Invar, as compared to 330, after TPN treatment

6.1.1 General characterisation

6.1.1.1 Surface nitrogen content and Vickers hardness

Surface nitrogen content of Invar ranges from ~18 to ~20 at.% after TPN (**Table. 6.1**), which are all significantly higher than the equilibrium N solubility in γ-Fe (i.e. ~10.3 at.% at ~650°C [58]) and are very closed to that of γ′-Fe_4N (i.e. ~20 at.% for one N in the centre of each FCC Bravais lattice). Nitrogen content increases very slightly with increasing treatment time, but no significant change with temperature is observed. Comparing the surface nitrogen content between Invar and 330 at each TPN-treatment condition, the presence of Cr in austenitic lattice of the latter does appear to be beneficial in obtaining a higher surface nitrogen uptake.

Table 6.1 Surface nitrogen content (at.%) of Invar and 330 after TPN

Treatment	330	Invar
400°C 4hrs	23.1 ± 0.6	18.3 ± 0.4
400°C 20hrs	24.0 ± 0.8	19.8 ± 0.3
425°C 4hrs	24.1 ± 0.5	18.9 ± 0.3
425°C 20hrs	25.7 ± 0.9	20.6 ± 0.3
450°C 4hrs	22.6 ± 0.8	18.8 ± 0.6
450°C 20hrs	25.1 ± 0.5	19.6 ± 0.6

Surface Vickers hardness values of Invar and 330 after TPN are tabulated in **Table 6.2**. Material surface hardness increases with both treatment temperature and time, from ~200 $HV_{0.025}$ for U-Invar to a maximum of ~734 $HV_{0.025}$ for 450C20h-Invar. Comparing the surface Vickers hardness between Invar and 330 at each TPN-treatment condition, the stainless high-Ni alloy 330 possesses a significantly higher surface hardness, which is consistent with the much higher surface nitrogen content of 330 samples in **Table 6.1**. Nevertheless, nitrogen absorption and the consequent surface hardness enhancement needs to be discussed alongside the surface crystallographic structure and diffusion layer depths of the treated surfaces (as will be shown in the following Sections).

Table 6.2 Surface Vikers hardness, $HV_{0.025}$

Treatment	330	Invar
Untreated	210 ± 4	200 ± 3
400°C 4hrs	520 ± 10	390 ± 5
400°C 20hrs	1048 ± 62	498 ± 8
425°C 4hrs	515 ± 17	531 ± 8
425°C 20hrs	1494 ± 21	705 ± 25
450°C 4hrs	786 ± 26	638 ± 8
450°C 20hrs	1573 ± 18	734 ± 12

6.1.1.2 Surface morphology – OM on top of material surfaces

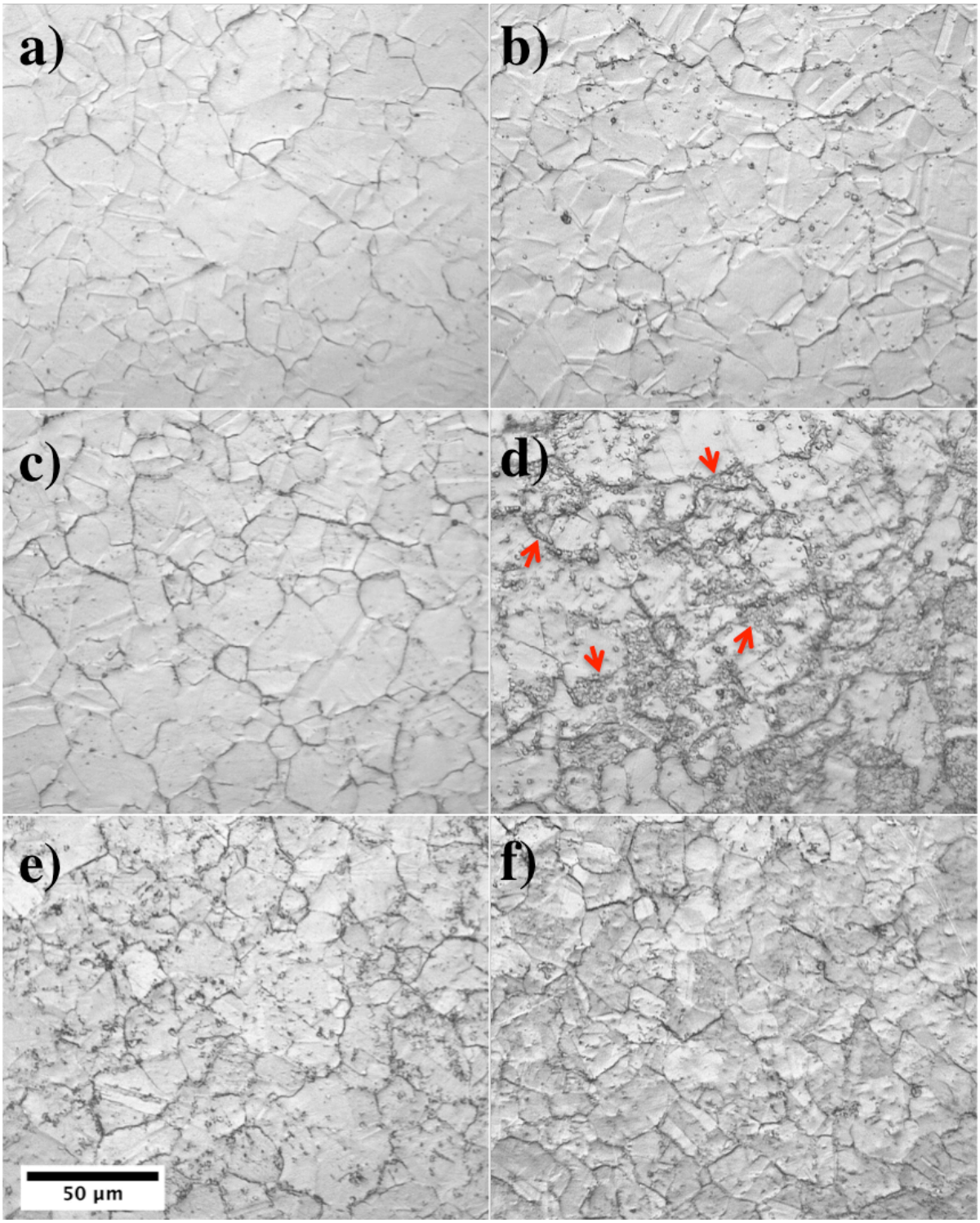

Fig. 6.1 Optical micrographs of Invar 36® after TPN at a) 400°C 4hrs, b) 400°C 20hrs, c) 425°C 4hrs, d) 425°C 20hrs, e) 450°C 4hrs, and f) 450°C 20hrs

Material surface morphology after TPN is revealed under optical microscopy, as shown in **Fig. 6.1**. Grains are revealed under OM, showing grain size ranging from ~20 to ~50 μm. The parallel traces or 'dimples' (as an indication of γ_N or CrN formation, respectively, as already shown in **Chapter 4**) were not observed on top of Invar after TPN. Noticeably, some particles are revealed (as indicated with red arrows in **Fig. 6.1d)** on top of material surface of 425C20h-Invar, which were examined under EDX being (Ti, W)-rich depositions. These particles, which could be due to a contaminated chamber environment (i.e. residual Ti-based depositions in the chamber from a previous coating process by other users), are not characteristic features to do with the nitrogen diffusion or phase transformation at the surface of Invar under TPN. Nevertheless, these contaminations (e.g. TiN particles) might introduce some errors in surface nitrogen content measurement during EDX of the treated surfaces of Invar, in which case 425C20h-Invar shows slightly higher nitrogen content than the other TPN-treated Invar samples (**Table 6.1**).

6.1.1.3 BSE imaging of sample cross-sections

The BSE images of the nitrided Invar cross-sections are shown in **Fig. 6.2**. Under BSE imaging, all the nitrided Invar surfaces show a discontinuous feature-containing surface zone, which grows thicker with increasing treatment temperature and time. No distinguishable features could be observed below these surface zones. Since Ni and Fe have similar atomic weight (of ~58.7 and ~55.8 g/mol) and N is much lighter (i.e. ~14.0 g/mol), these features observed under BSE imaging (in **Fig. 6.2**) should mainly originate from the distribution of nitrogen in the TPN-treated surfaces under nitrogen diffusion at different treatment temperatures and times.

Taking the dark features as being N-rich phase(s), two phase morphologies (i.e. a 'cellular' and a homogenous region) are observed in **Fig. 6.2**. At 400°C, the dark (N-rich) homogenous regions start forming discontinuously from the very surface of material (**Fig. 6.2a**) and then grow and coalesce with treatment time (**Fig. 6.2d**). At 425°C, the 'cellular' regions observed are evidently composed of two phases, which should be a N-rich one (dark under BSE) and a N-depleted one (bright under BSE) with interlamellar spacing of several tens of nanometers. At 450°C treatment temperature, the feature-containing zone appears to be double-layered, containing a top layer of homogenous phase and an underlying layer of cellular phases.

As shown in **Fig. 6.2**, neither the penetration depths nor the distributions of these N-rich features on nitrided Invar are homogenous, which is clearly different to the homogenous N-supersaturated layers observed on 330 after TPN (see **Fig. 4.7**, **Chapter 4)**. These feature-containing zones under BSE imaging on Invar after TPN (typically ~1-3 μm on 400C20h-Invar and ~3-5 μm on 450C20h-Invar) appear much thinner than those on alloy 330 after TPN (typically ~4 μm on 400C20h-330 and ~13 μm on 450C20h-330, **Chapter 4**).

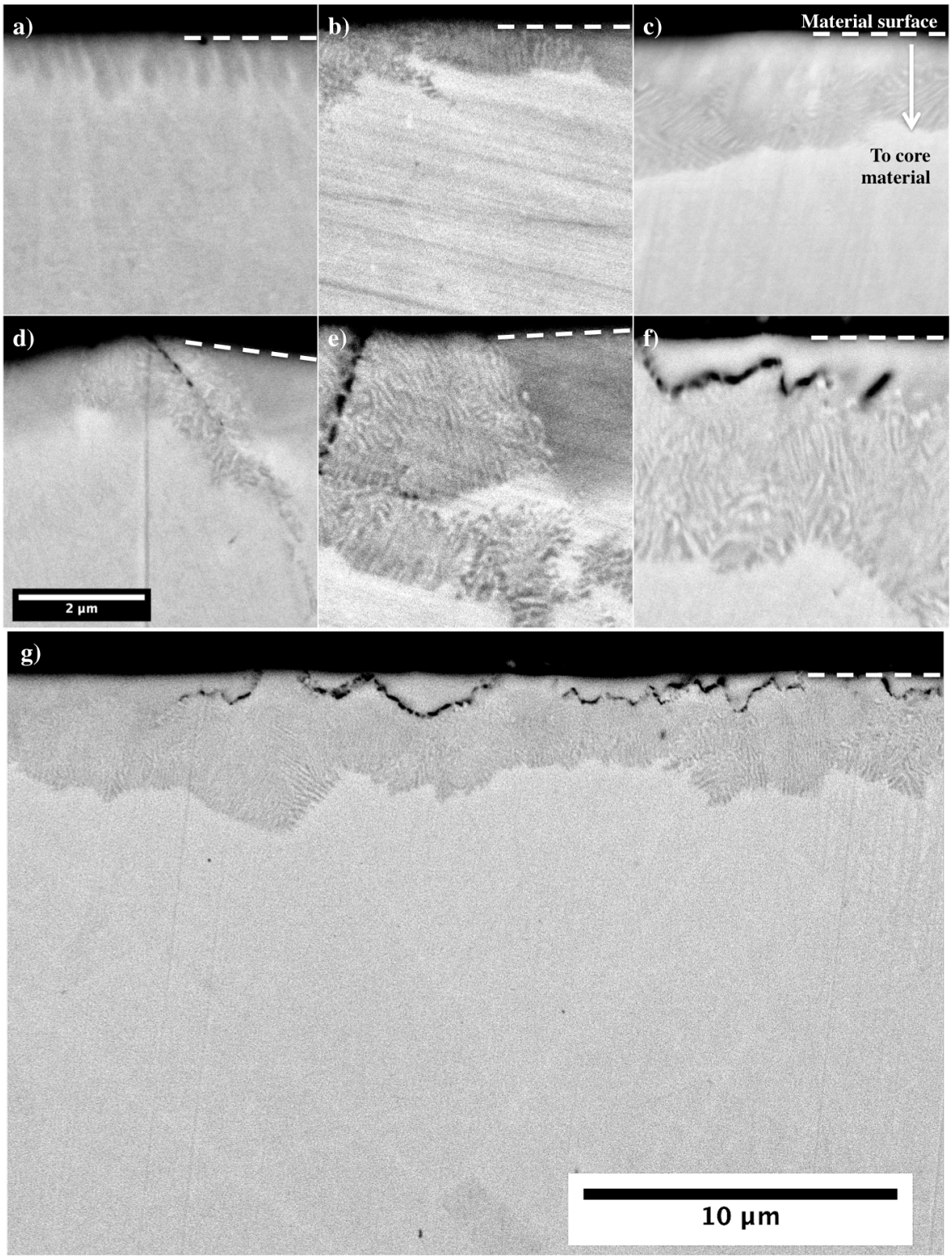

Fig. 6.2 Cross-sectional BSE images of Invar 36® after plasma nitriding at a) 400°C 4hrs, b) 425°C 4hrs, c) 450°C 4hrs, d) 400°C 20hrs, e) 425°C 20hrs, f-g) 450°C 20hrs. Image a-f were taken at same magnification (with scale bar shown in image d) for comparison reason, and image g was taken at a much lower magnification to show a larger cross-sectional surface area of this sample

6.1.2 Phase identifications

Nevertheless, as will be shown in this section, there are also rather deep zones of nitrogen solid solution, γ(N), on nitrided Invar below these feature-containing surface regions. As will also be discussed using GAXRD and TEM techniques in this section, all the dark features observed on nitrided Invar under BSE imaging in **Fig. 6.2** − i.e. both the dark homogenous feature and the dark features in 'cellular' regions − correspond to γ′ iron-nickel nitride, whilst the bright lamellae in the 'cellular' region correspond to N-depleted unexpanded γ-austenite.

6.1.2.1 GAXRD

Fig. 6.3a shows the GAXRD profiles (at 2° incident angle) of all of the nitrided Invar samples. The strong GAXRD peaks of the nitrided samples match well with the iron-nickel nitride: γ′-$Fe_{4-x}Ni_xN$ (PDF card 00-060-0479, stable for $0 < x < 3.3$ under experimental conditions [171]). Considering the constant Fe:Ni ratio of ~2.6:1.4 for Invar before and after TPN (under surface EDX), this γ′ phase is most likely $Fe_{2.6}Ni_{1.4}N$ (i.e. x=1.4 for γ′-$Fe_{4-x}Ni_xN$). A very weak γ′(110) peak is also observed for all the nitrided Invar samples, which is due to the N occupation at octahedral FCC centres – so that the FCC(110) plane is no longer 'forbidden' − and is consistent with the PDF card. The dark features observed under BSE imaging in **Fig. 6.2** could be attributed to this γ′ nitride.

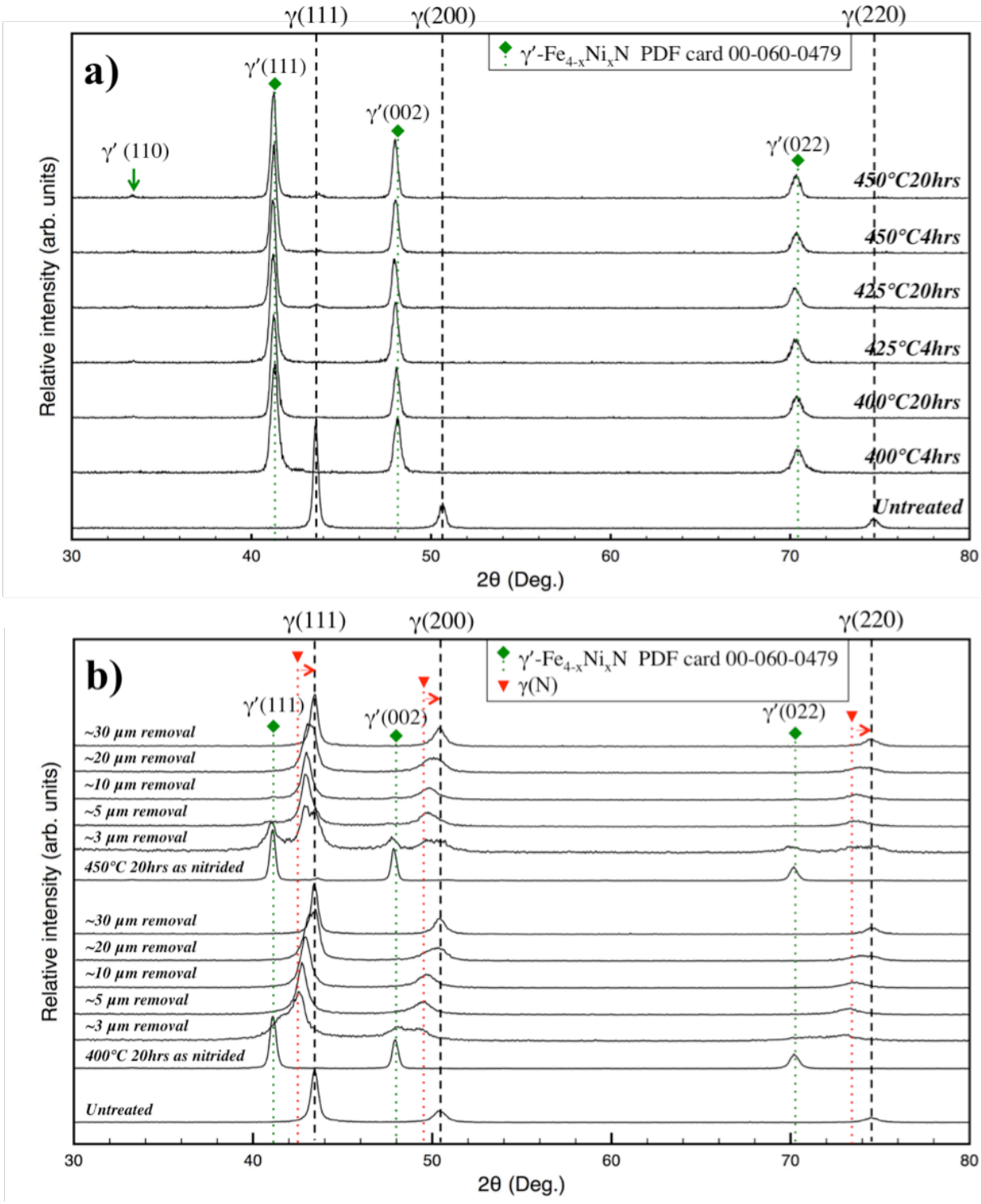

Fig. 6.3 GAXRD profiles of Invar 36® a) after nitriding at all treatment conditions, and b) 400C20h-Invar and 450C20h-Invar after successive layer removal (for ~3/5/10/20/30 μm, measured using a micrometer) by grinding the treated surfaces using P1200 SiC paper; γ′ – iron nickel nitride, γ(N) – isotropically expanded nitrogen solid solution, γ – substrate or unexpanded austenite

However, the BSE images in **Fig. 6.2** show that the surface layer is clearly not homogenous, but contains 'cellular' regions of bright lamellae (especially after higher treatment temperatures). Apart from γ′ peaks, weak γ(111) substrate peak can be seen on 425C20h-Invar, 450C4h-Invar and 450C20h-Invar in **Fig. 6.3a**. The bright lamellae in the 'cellular' region (under BSE imaging in **Fig. 6.2b,c,e,f**) could be attributed to the (N-depleted) γ phase. The cellular regions observed under BSE (**Fig. 6.2b,c,e,f**) could therefore be a mixture of γ′-$Fe_{4-x}Ni_xN$ and unexpanded γ.

Owing to the shallow X-ray attenuation depths (i.e. ~0.6 μm) for 2° GAXRD on Invar, the peaks observed only correspond to the phases existing at the very surface of the material. To investigate surface phase compositions at depth, 400C20h-Invar and 450C20h-Invar were selected and ground successively using P1200 SiC paper for ~3/5/10/20/30 μm layer-depth removal for GAXRD profiles at different depths of the treated surfaces, as shown in **Fig. 6.3b**.

Evidently, at depths from ~3 to 20 μm below the γ′-containing surface zone on both of the nitrided Invar samples, there is another FCC phase (indicated by the red arrow in **Fig. 6.3)** with continuously decreasing lattice parameter from surface to core until the unmodified substrate is reached. The gradually shifting FCC peaks (to higher 2θ angles at deeper regions within the treated surfaces) until γ-substrate could be attributed to isotropically expanded nitrogen solid solution in Invar, which has (presumably) decreasing nitrogen content from surface to core under nitrogen diffusion during TPN treatments. Noticeably, this γ(N) phase does not give rise to any distinguishable features under BSE imaging, probably due to the low nitrogen content of γ(N) and gradually decreasing nitrogen content in γ(N) towards core.

More importantly, comparing the GAXRD profiles between 400C20h-Invar and 450C20h-Invar at a depth of ~3 μm (**Fig. 6.3b**), the γ-FCC substrate peaks evidently seen at this depth on 450C20h-Invar are not observed on 400C20h-Invar. Considering the relatively deep penetration of the 'cellular' region on 450C20h-Invar in **Fig. 6.2f** (as compared to the γ′ penetration in **Fig. 6.2d**), the strong substrate γ peaks at ~3 μm on 450C20h-Invar correspond to the bright lamellae in the 'cellular' region, which confirms that the cellular region is a mixture of γ′ + γ. This cellular phase mixture is likely due to phase decomposition of N-saturated γ(N).

6.1.2.2 Cross-sectional TEM analysis

The phase distribution was then confirmed via investigations of cross-sectional TEM samples prepared from 400C20h-Invar and 450C20h-Invar, covering a volume from the surface to a depth of ~6 μm (**Fig. 6.4-6.6**). Using a ~0.5 μm diameter diffraction aperture, the selected area EDPs of the near surface volume for 400C20h-Invar shows diffraction spot for γ′ (as shown at the two zone axis, **Fig. 6.4b, e**). In good agreement with γ′(110) GAXRD peaks observed in **Fig. 6.3b**, the weak 'forbidden' electron diffraction spots − e.g. FCC(110), FCC(100) and FCC(201) as shown in **Fig. 6.4b,e** – are due to N-occupation in octahedral centres of FCC Bravais unit cell (i.e. in centres of corner-sharing octahedra in FCC lattice).

Using one of the 'forbidden' reflections, the DF-TEM image of **Fig. 6.4d** shows a bright γ′-containing region just below the treated surface, which is consistent with the BSE observations (**Fig. 6.2d**) and XRD analysis. Additionally, the selected area EDPs of the volumes below the γ′-containing region on 400C20h-Invar (as shown at the two zone axis, **Fig. 6.4c, f**) reveal only FCC diffraction reflections without those 'forbidden' reflections, confirming the precipitation-free nitrogen solid solution (as indicated under GAXRD, **Fig.**

6.3b). Under TEM, γ′ is coherent to the underlying γ(N), with the cubic-to-cubic structure-orientation relationships: <110>γ′//<110>γ(N) and <112>γ′//<112>γ(N).

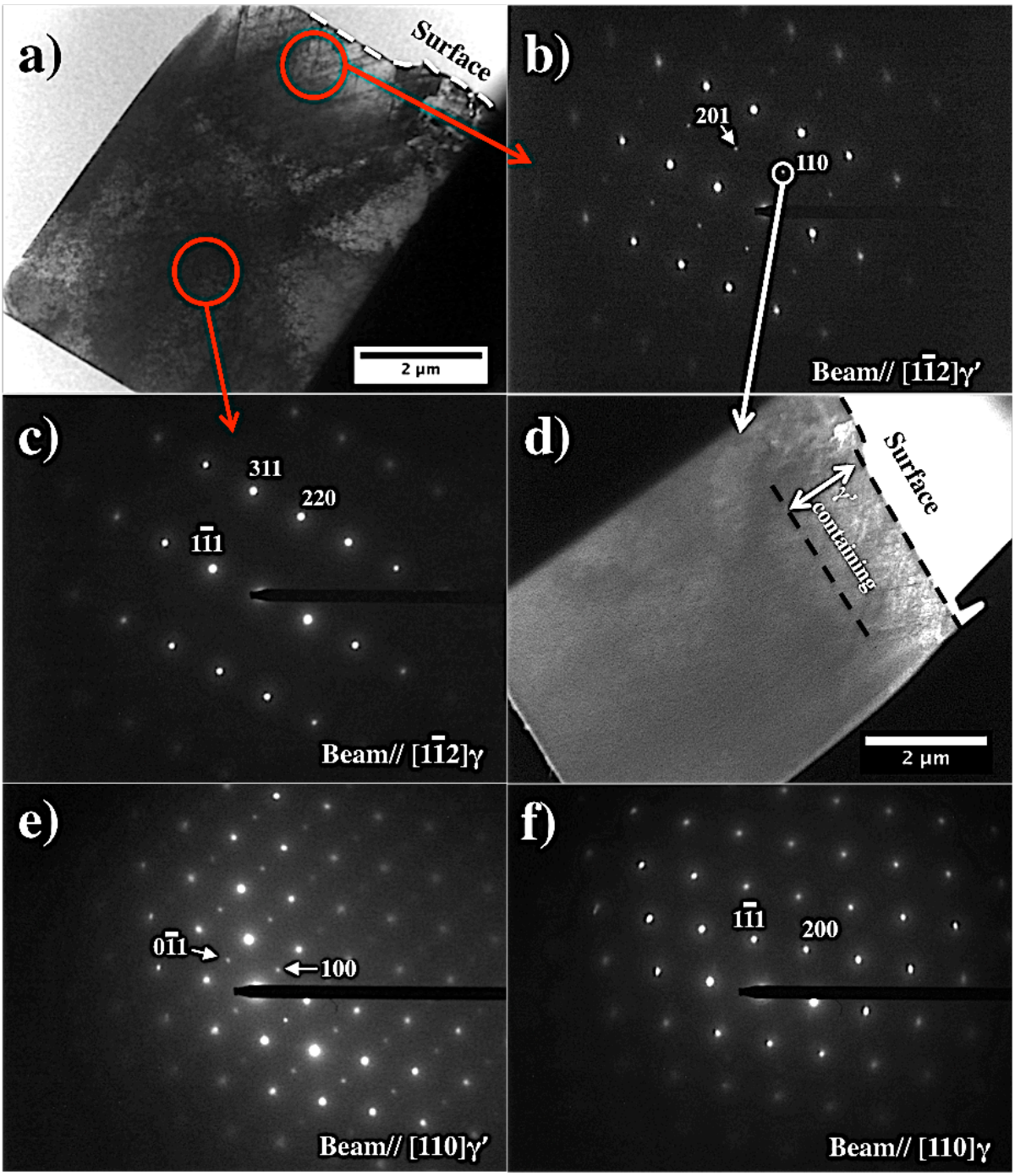

Fig. 6.4 TEM images of 400C20h-Invar. a) Low magnification BF-TEM image; b-c) selective area EDPs from regions as indicated in figure a; d) DF-TEM image constructed with electrons indicated in figure b; e-f) EDPs of the surface γ′-containing region and the underlying core, respectively, at another zone axis

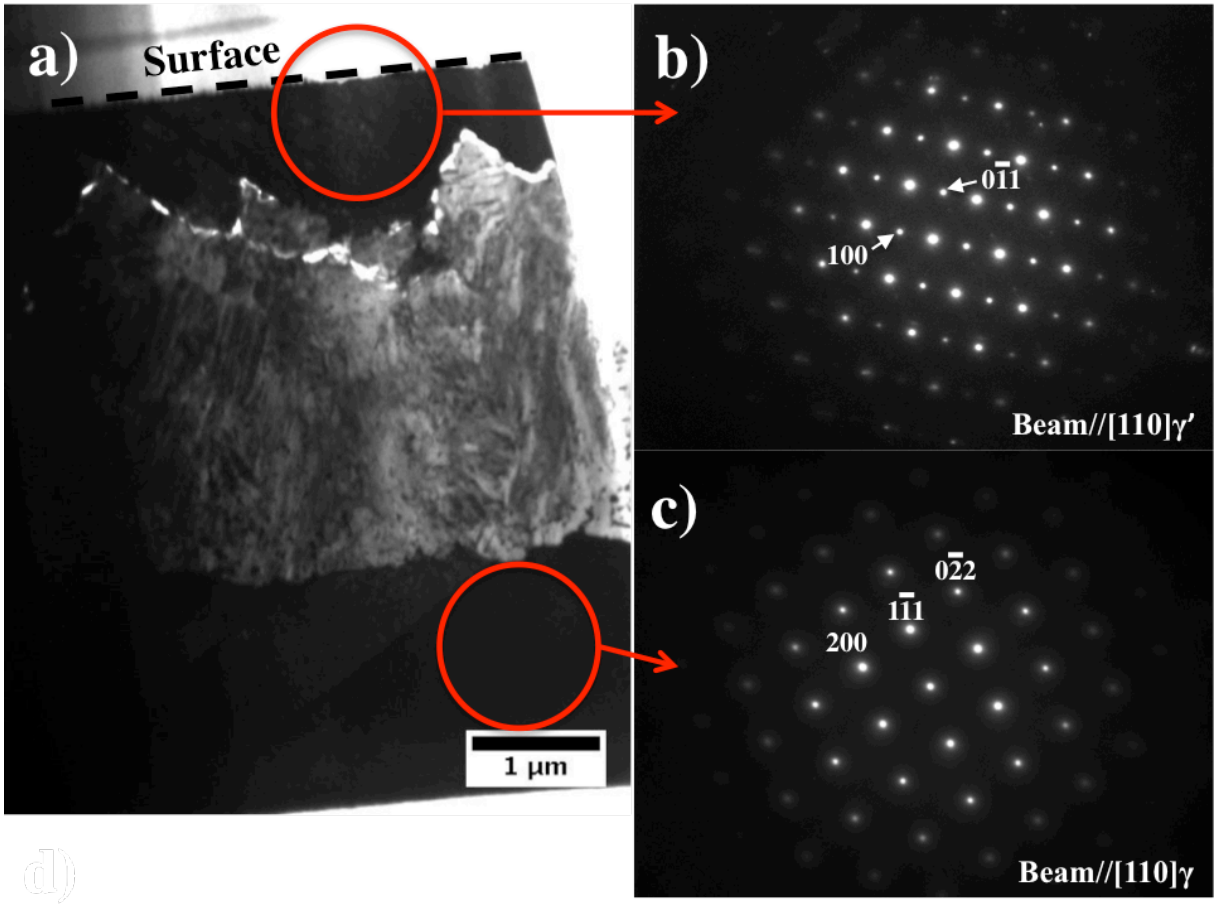

Fig. 6.5 TEM images of 450C20h-Invar. a) Low magnification BF-TEM image; b-d) selective area EDPs from regions as indicated in figure a

Similar to 400C20h-Invar, diffraction spots of γ′ (**Fig. 6.5b**) and γ(N) (**Fig. 6.5c**) are revealed at the very surface and at much deeper region on 450C20h-Invar. The topmost γ′ layer on 450C20h-Invar shares the same crystallographic orientation of γ(N). For the 'cellular' region at the surface of 450C20h-Invar (**Fig. 6.2f**), selected area EDPs present two sets of diffraction patterns (i.e. as shown at the two zone axis, **Fig. 6.6b, d**). Such double diffraction indicates a pair of coherent phases with lattice constant ratio at ~1.054, which agrees with the lattice constant ratio between γ′ and γ (i.e. ~1.055, determined from peak positions of γ′ and γ from GAXRD at ~3 μm depth for 450C20h-Invar). Using the (100)γ′ diffraction spot, DF-TEM

images (**Fig. 6.6a, c**) clearly show a lamellar mixture of γ′ and γ, consistent with the 'cellular' morphology observed under BSE in **Fig. 6.2f**.

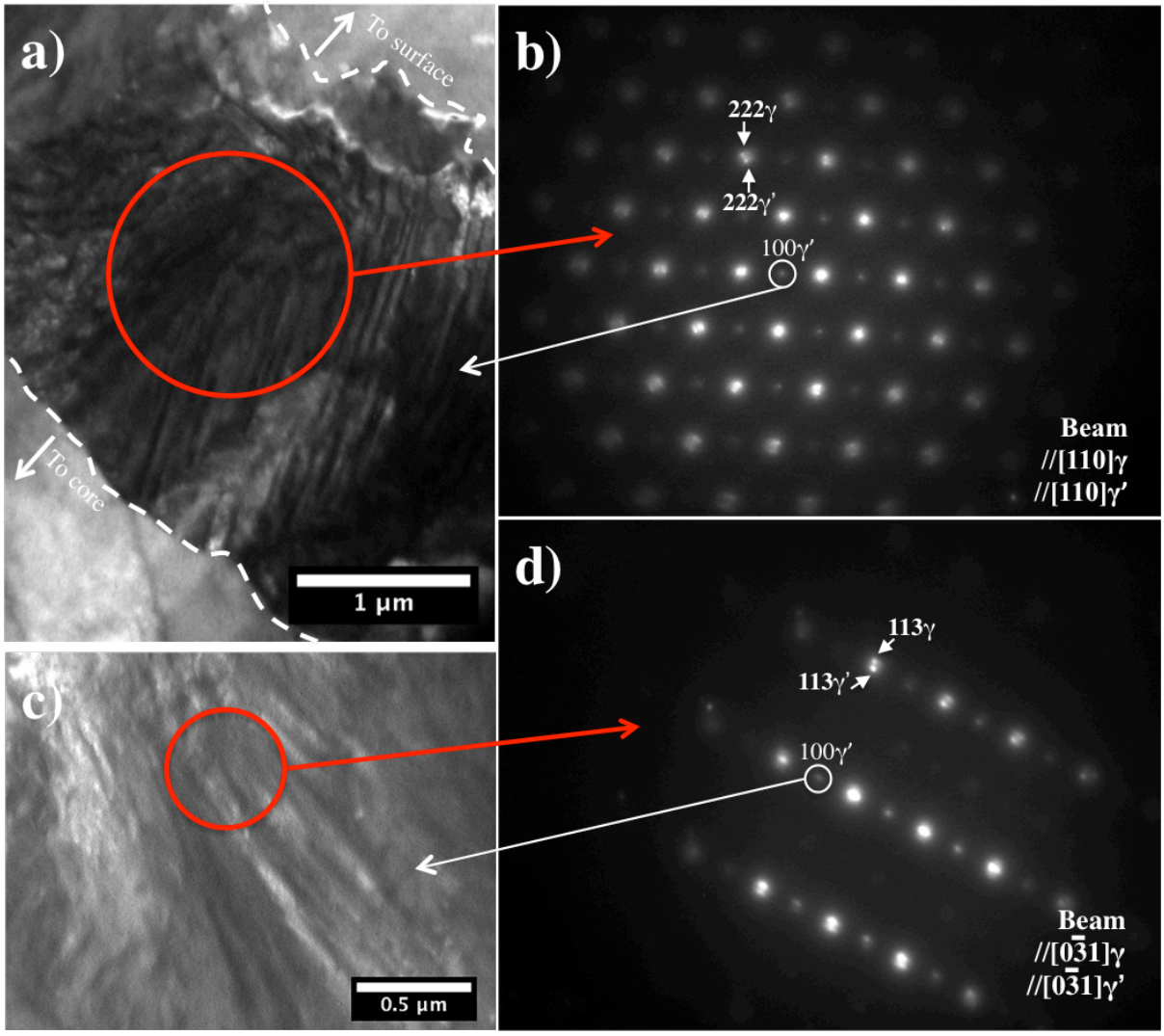

Fig. 6.6 TEM images of 450C20h-Invar. a) Low magnification BF-TEM image; b-d) selective area EDPs from regions as indicated in figure a

6.1.3 On the role of Cr in nitrogen supersaturation of Fe-based FCC lattices

As discussed above, N-rich phases (which are dark under BSE imaging in **Fig. 6.2**) are identified after GAXRD (**Fig. 6.3**) and TEM analysis (**Figs. 6.4-6.6)**. Following a (presumably) decreasing nitrogen content from surface to core on the nitrided Invar, there is i) a topmost zone containing mainly γ′-$Fe_{2.6}Ni_{1.4}N$ but also small fractions of γ′-$Fe_{2.6}Ni_{1.4}N$ + γ-$Fe_{2.6}N_{1.4}$ phase mixture, and ii) an underlying nitrogen solid solution in Invar with continuously reducing lattice constants from a depth of ~3 μm to ~20 μm.

6.1.3.1 On lattice expansion − XRD profiles and lattice parameters

The XRD profiles of Invar after TPN (under Bragg-Brentano θ-2θ geometry, **Fig. 6.7a**) appear analogous to that reported for Invar under nitrogen ion beam processing at 400°C by Williamson et al. [87], where two 'new' FCC structures were denoted as γ_{N1} and γ_{N2} (as highly expanded and less-expanded FCC structures, respectively). However, after **Section 6.1.2**, the XRD peaks of these two 'new' phases (**Fig. 6.7a**) could be attributed to γ′ nitride (i.e. γ′-$Fe_{2.6}Ni_{1.4}N$) and γ(N) (i.e. isotropically expanded nitrogen solid solution), respectively. Noticeably, due to different X-ray attenuation depths (i.e. ~2.4-4.4 μm for θ-2θ XRD and ~0.6 μm for GAXRD), the γ(N) observed on the treated surfaces under Bragg-Brentano θ-2θ geometry (**Fig. 6.7a**) is not detected under Seeman-Bohlin geometry (**Fig. 6.3a**). Additionally, the weak peak at substrate γ-FCC positions observed in XRD profiles above 425C20h-Invar (**Fig. 6.7a**) could be attributed to the unexpanded (N-depleted) γ-FCC component in the 'cellular' phase mixture.

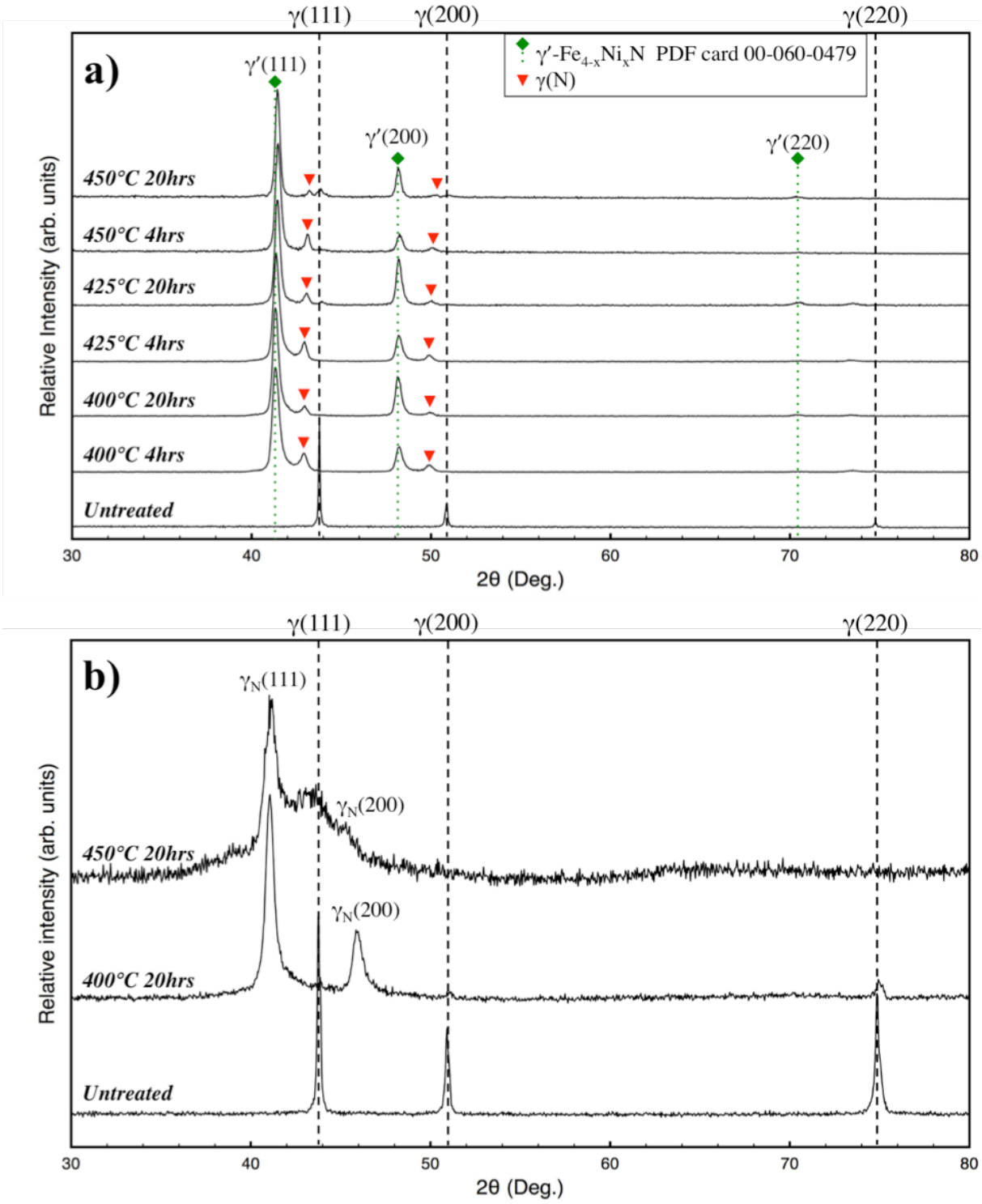

Fig. 6.7 Theta-2theta XRD profiles of a) Invar 36® and b) RA 330® before and after TPN, both Invar and RA 330® are nitrided at equivalent conditions at 400°C 20hrs and 450°C 20hrs; γ_N – anisotropic nitrogen-expanded austenite, γ′ – iron nickel nitride, γ(N) – isotropically expanded nitrogen solid solution, γ – substrate or unexpanded austenite

More importantly, comparing the results for Invar to those of alloy 330 after TPN (**Fig. 6.7b**), where the original γ-substrate peaks are shifted anomalously to lower 2θ angles for the latter (i.e. anisotropic lattice expansion under nitrogen supersaturation), the peak shifts on Cr-free Invar under TPN (**Fig. 6.7a**) are hkl-independent (i.e. isotropical lattice expansion, as also noticed by Williamson [87]). Lattice parameters of the three FCC structures identified in **Fig. 6.7** could be calculated from their experimental XRD peak positions. The derived lattice parameters − a(111) and a(200), as determined from FCC(111) and FCC(220) planes − are plotted in **Fig. 6.8**, where they are compared to the lattice constant of γ′-$Fe_{4-x}Ni_xN$ (PDF card 00-060-0479) and to those of γ_N-330 on 400C20h-330. Noticeably, the lattice parameters for γ_N and γ(N) derived here from XRD profiles correspond to material surface volumes with decreasing nitrogen content from surface to core.

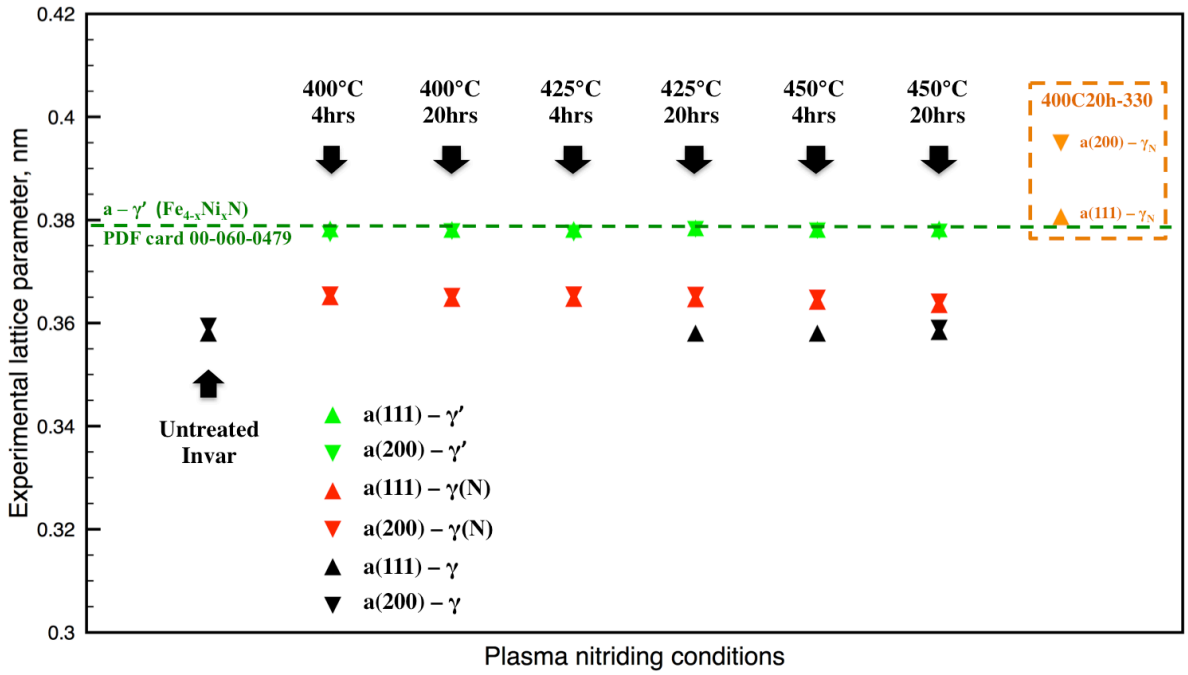

Fig. 6.8 Lattice parameters as determined from the FCC(111) and FCC(200) XRD peak positions of untreated and nitrided Invar, as compared to those of γ_N-330 on 400C20h-330 (as highlighted in orange dashed box) and γ′ from PDF card 00-060-0479 (as shown in green dashed line)

The black triangles at the bottom of the plot represent the derived lattice constants for the (solution-annealed) Invar substrate at ~0.359 nm in **Fig. 6.8**, which is similar to that of (solution-annealed) the 330 alloy substrate (see **Chapter 4**). Above ~0.359 nm, the phases synthesised on both substrates after TPN could be regarded as being expanded either isotropically (Invar) or anisotropically (alloy 330) from the unexpanded γ-substrate.

Firstly, the red triangles directly above the black triangles (of the γ-substrate) in **Fig. 6.8** indicate the lattice parameter of γ(N), which ranges from ~0.365 nm to ~0.363 nm. The lattice constants derived for γ(N) correspond to nitrogen levels in solid solution in Invar. The lattice constant for nitrogen at maximum solubility in pure Fe (~10.3 at.% N at ~650°C [58]) could be estimated as ~0.365 nm using $0.3572 + 0.00078 \times at.\%N$ from Ref. [63]. Although Ni addition in Fe is known to reduce nitrogen solid solubility in Fe-Ni alloys at high temperatures (e.g. under gaseous nitriding at ~900-1100°C [171]), it appears that this Fe-35Ni Invar alloy is capable of accommodating high nitrogen content in solid solution at a low nitriding temperature such as 400°C (probably to a level near ~10.3 at.% N, close to the equilibrium solid solubility limit of N in pure Fe).

Moreover, nitrogen solubility in γ(N) on TPN-treated Invar decreases with increasing treatment temperature and time, as suggested by the decreasing lattice constant of γ(N) from left to right in **Fig. 6.8**. Such variation of the lattice constant for γ(N) is pronounced at high treatment temperatures (i.e. 425°C and 450°C) accompanied with the 'cellular' regions observed under BSE imaging (**Fig. 6.2)**. In this case, the decrease in nitrogen solubility in γ(N) could be attributed to the cellular decomposition mechanism of N-rich isotropically-expanded γ(N) to γ′ nitride and N-depleted, unexpanded γ (which is enhanced at elevated treatment temperature), pointing to a need for further studies of Invar under TPN at even lower

treatment temperatures (<400°C) or lesser N_2:Ar volume ratios (<7:3), to suppress γ′ formation and explore the maximum solid solubility of N in Invar. Noticeably, the decrease in nitrogen content of γ(N) with increasing treatment temperature is also hinted at by GAXRD analysis (after successive layer removal) in **Fig. 6.3b**, where the γ(N) peak positions at a depth of ~3 μm are at slightly lower 2θ angles (i.e. slightly higher isotropic lattice expansion) in 400C20h-Invar compared to those of 450C20h-Invar at the same depth.

The solid solubility of N in Invar under TPN appears to be limited by the potency of γ′ nitride formation. The lattice parameter of γ′ (as extracted from PDF card 00-060-0479) is indicated using a horizontal green dashed line in **Fig. 6.8**. Different to the random nitrogen octahedral occupation in γ(N), γ′ (with lattice constant at ~0.383 nm provided by PDF card 00-060-0479) corresponds to ordered occupation (at ~20 at.% N in total) in the centres of corner-sharing octahedra in FCC lattice made by large metallic elements such as Fe and Ni.

Most importantly, in contrast to γ(N) on nitrided Invar, the hkl-dependent lattice parameters derived for γ_N-330 in 400C20h-330 (highlighted by the orange dashed box in **Fig. 6.8**) are clearly higher than the lattice constant of γ′. Having ~19 at.% of pre-existing Cr in substrate, alloy 330 is able to accommodate interstitial nitrogen (above 20 at.%, **Table. 6.1**) under anisotropic lattice expansion (i.e. γ_N), without isotropic lattice expansion into γ′-Fe_4N type nitride. Thus, the role of Cr in the formation of nitrogen-expanded austenite for alloy 330 under TPN can be understood via the prevention of γ′-Fe_4N-type nitride formation, owing to the strong chemical affinity between Cr and N. In accommodation of interstitial nitrogen in a rather 'rigid' FCC sub-lattice (i.e. 'immobile' substitutional elements) under TPN at selected low temperatures, the segregation of Cr is suppressed so that long-range ordering of the CrN nitride phase in the ASS substrate cannot be achieved; however, the preferential formation of

γ′ in a Cr-free FCC sublattice under equivalent TPN treatment is achieved rather easily, since the formation of γ′ could be achieved by ordered N occupation without migration of substitutional elements, as indicated by the same crystallographic orientation between γ′ and matrix (under TEM, **Fig. 6.4** and **Fig. 6.6**).

Moreover, Menthe et al. [115] and Riviere et al. [117] demonstrated a Cr-N chemical bonding, instead of Fe-N (for γ′ formation) in γ_N-304L layers. According to the XPS spectra obtained of γ_N-304L layers, nitrogen atoms in the nitrogen interstitial supersaturated FCC sub-lattice are always in nitride state [115, 117], while Fe was essentially detected in the metallic state [117]. In this case, the presence of Cr (to a large level such as ~17-19 wt.%) in ASS prohibits the preferential Fe-N bonding for the Fe-based FCC sub-lattice under nitrogen insertion.

In this regard, the difference between stoichiometric γ′ (isotropically-expanded from Invar) and γ_N (anisotropically-expanded from 330) is fundamentally reflected in the different chemical bonding between metallic elements (e.g. Fe, Ni and Cr) and nitrogen. Clearly, the γ′-Fe_4N structure (stoichiometric at ~20 at.% for N and isotropic expansion to the parent FCC lattice) tends to form under Fe-N bonding for Invar under TPN, while γ_N formed with high and non-stoichiometric N absorption under potential 'trapping of N by Cr and formation of short-ranged-ordered Cr-N clusters.

Comparing the EDP between γ′-$Fe_{2.6}Ni_{1.4}N$ (**Fig. 6.4e** and **Fig. 6.5b**) and γ_N-330 (**Fig. 4.16a** and **Fig. 4.18b**, **Chapter 4**) at 400°C 20hrs and 450°C 20hrs, the absence of 'forbidden' FCC reflections in γ_N-330 indicates that interstitial nitrogen atoms are not always occupying at octahedral centres. Considering both the absence of 'forbidden' FCC reflections and the preferential Cr-N bonding in γ_N, nitrogen atoms probably locate in interstitial sites in vicinity

to Cr (rather than corner-sharing octahedral sites in the case of γ′-Fe_4N) in FCC lattice of γ_N. Nevertheless, the 'forbidden' FCC reflections were observed in both γ_N-AG17 and γ_N-304 (**Chapter 4**) with higher nitrogen content than γ_N-330. Compared to the absence of 'forbidden' FCC reflections in γ_N-330, the observation of 'forbidden reflections' in γ_N-AG17 and γ_N-304 is probably due to the higher interstitial occupation in octahedral interstices (i.e. high N:Cr ratio).

6.1.3.2 On nitrogen diffusion mechanisms − cross-sectional hardness-depth profiles

Assuming N trap sites provided by the randomly distributed Cr in ASS during nitrogen diffusion, Parascandola et al. [172] proposed a nitrogen diffusion model in γ_N based on trapping and detrapping of nitrogen (rather than the random walk model demonstrated in **Chapter 2**), which was qualitatively consistent with depth profiles of nitrogen isotopes on AISI 316 ASS under low energy high flux nitrogen implantation at 400°C (firstly using ^{15}N and then using ^{14}N) [173].

As already shown in **Table 6.1**, the surface nitrogen content of alloy 330 under TPN is much higher than that of Invar. More importantly, under nitrogen diffusion during TPN, surface hardened zones are developed – owing to the N depth profiles developed − on both Invar and 330 with reducing hardness values from surface to core (**Fig. 6.9**). The transverse hardness profiles from surface to core on 400C20h-Invar and 450C20h-Invar (**Fig. 6.9a**) can be compared to 400C20h-330 and 450C20h-330 (**Fig. 6.9b**) to reveal the different transverse nitrogen distribution with and without Cr in a high-Ni Fe-based FCC lattice.

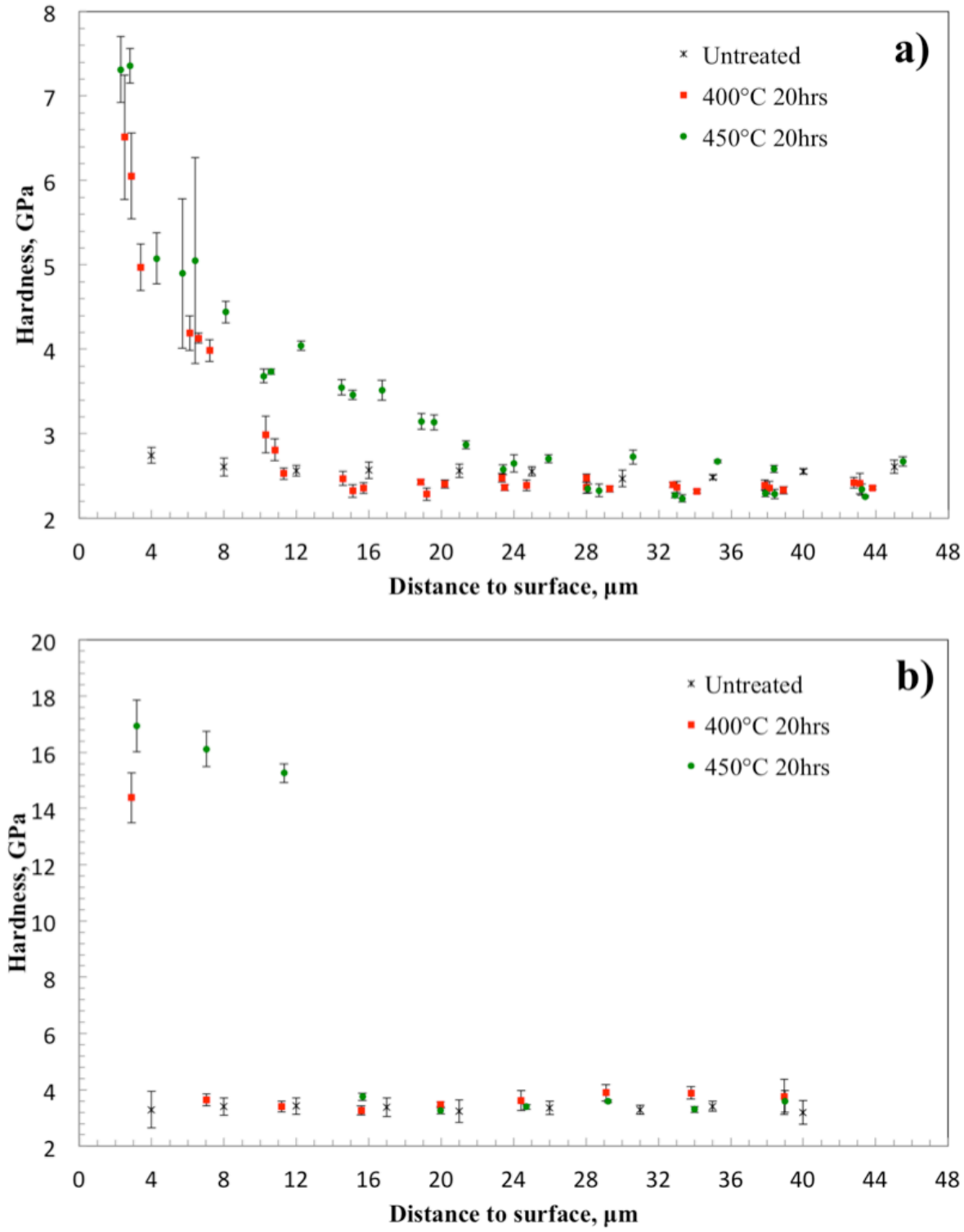

Fig. 6.9 Cross-sectional nanoindentation profiles of a) Invar 36® and b) RA 330® after plasma nitriding at 400°C and 450°C for 20hrs (error bars − ± 95% confidence interval at each depth level)

The surface hardened zone on 400C20h-Invar and 450C20h-Invar are, respectively, ~11 μm and ~24 μm thick (**Fig. 6.9a**). The diffusion layer depths of 330 after TPN are ~4.4 μm and ~12.9 μm for 400C20h-330 and 450C20h-330, respectively (as already determined from BSE images, **Chapter 4**), which are consistent with the hardness profiles (**Fig. 6.9b**). Comparing the nitrogen diffusion depths suggested by the hardened layer depths, the high Cr content in alloy 330 restricts the diffusion of N into deeper regions, which could be attributed to the nitrogen trapping effect from Cr.

In terms of the shape of N depth profile of γ_N, nitrogen content reduces slowly in a plateau-shape from surface to core and then drops abruptly in a sharp leading edge at the layer/core boundary [10]. In the hardness profiles, high hardness plateau (e.g. on 450C20h-330, **Fig. 6.9b**) and abrupt drops in hardness between diffusion layer and the unmodified core are revealed on nitrided 330, which suggests that the ~19 at.% of Cr in alloy 330 enables retaining (or trapping [172]) of high N nitrogen content at material surface under nitrogen diffusion at low treatment temperatures. Different to those of γ_N-330 layers (**Fig. 6.9b**), the hardness of nitrided Invar (**Fig. 6.9a)** − after dropping rather abruptly from the γ′-containing zone to γ(N) zone − generally reduces gradually towards core owing to the gradually reducing nitrogen content from surface to core for nitrogen in isotropically expanded solid solution in Fe-35Ni). The large errors obtained at depths of ~3 μm in 400C20h-Invar and at depth of ~6 μm in 450C20h-Invar could be attributed to the inhomogeneous penetration of γ′ nitride at material surface.

Both of the depths and shapes of hardness depth profiles (**Fig. 6.9**) suggest retaining of nitrogen at the treated surface by Cr, which could be attributed to the trapping of nitrogen by Cr as suggested in literature. Ni in the Fe-35Ni matrix does not provide such trapping effect

for interstitial nitrogen. Cr plays an important role for nitrogen supersaturation in ASS under low temperature nitriding and appears to be a key element under the topic of designation of low-temperature 'nitridable' alloys ('nitridable' in terms of γ_N formation after low-temperature nitriding), which points to future studies on the minimum content of Cr (or other strong nitride-forming elements that are able to 'capture' N) required for nitrogen supersaturation in ASS (or other FCC matrix).

6.2 Characterisation of Hadfield steel after TPN

6.2.1 General characterisation

6.2.1.1 Surface nitrogen content and Vickers hardness

The surface nitrogen content of treated Hadfield steel increases with treatment time (**Fig. 6.3**), until saturated at ~27 at.% after 12hrs at 300°C. Similar to those obtained for nitrided Invar, all nitrided surfaces of Hadfield steel have N-content higher than the equilibrium nitrogen solid solubility limit in γ-Fe (~10.3 at.%) [58]. The surface nitrogen content of TPN-treated Hadfield steel increases to a rather high value, near 27 at.%, after 12hrs of nitriding – which is higher than that of nitrided Invar (**Table 6.1**) and also higher than the minimum nitrogen content required for ε-Fe_3N_{1+x} type nitride formation (i.e. ~25 at.% N for ε-Fe_3N).

Table 6.3 Surface nitrogen content (at.%) and Vickers hardness ($HV_{0.025}$) for Hadfield steel after TPN

Treatment	Surface nitrogen content, at%	Vickers hardness, $HV_{0.025}$
Untreated	/	292 ± 6
300°C 4hrs	19.5 ± 1.2	424 ± 18
300°C 8hrs	24.4 ± 0.7	721 ± 72
300°C 12hrs	26.9 ± 0.6	937 ± 112
300°C 20hrs	26.8 ± 0.5	1080 ± 70

Surface Vickers hardness values of Hadfield steel after TPN are tabulated in **Table 6.3**, with remarkable surface hardness enhancement after TPN. Similar to the trend observed for the surface nitrogen content, the alloy surface hardness increases with treatment time as well, and such hardness enhancement with time slows down at a treatment time of 12hrs. The surface hardness achieved on 300C20h-Had (i.e. ~1080 $HV_{0.025}$) is significantly higher than that of nitrided Invar shown in **Table 6.1**. However, these observations could be due to nitride formation, which cannot prove the formation of γ_N and needs to be discussed in conjunction with XRD results – as will be shown in the following sections.

6.2.1.2 OM on top of material surfaces

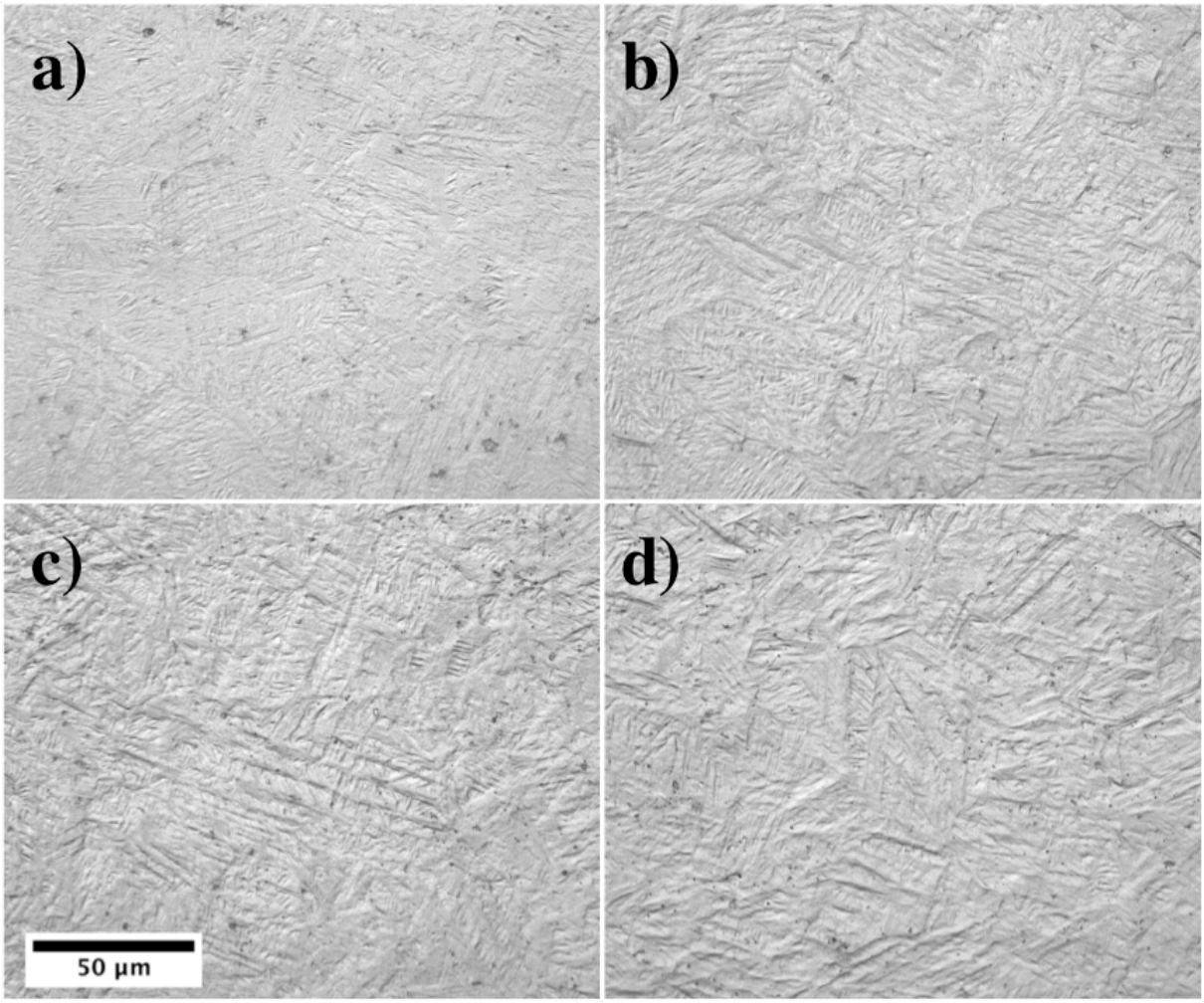

Fig. 6.10 Optical micrographs of a) 300C4h-Had, b) 300C8h-Had, c) 300C12h-Had and d) 300C20h-Had

The 300°C triode-plasma nitrided Had presents a 'woven' surface morphology (**Fig. 6.10**), where the expected austenitic grain boundary outlines are not clearly seen. The parallel traces (for plastic accommodation of supersaturated nitrogen) and 'dimples' (for decomposition of nitrogen-expanded austenite) observed for ASS under TPN (**Chapter 4**) are not seen on the nitrided Hadfield steel samples. Considering plasma etching effects during TPN, such morphology suggests formation of lamellar phases at the material surface.

6.2.1.3 BSE imaging of treatment cross-sections

Sample cross-sections were examined under BSE imaging, as shown in **Fig. 6.11a-d**). No evidence of homogeneous layers (which is a characteristic feature for γ_N) can be seen. Inhomogeneous dark phases are revealed in a rather bright diffusion zone at the treated surface of Had (**Fig. 6.11**). Diffusion layer grows inward with increasing treatment time. Based on **Fig. 6.11d**, a total layer depth of ~30 μm is achieved on 300C20h-Had.

At such low treatment temperature, the phase evolution of the Hadfield steel surface after TPN could only be attributed to the diffusion of interstitial elements. Under nitrogen diffusion, the counterintuitive bright (high mean atomic weight) background phase in the diffusion zone on nitrided Had (**Fig. 6.11**) could be due to carbon-depletion, potentially owing to carbides or carbonitrides formation in the diffusion-affected zone and/or surface decarburisation [174].

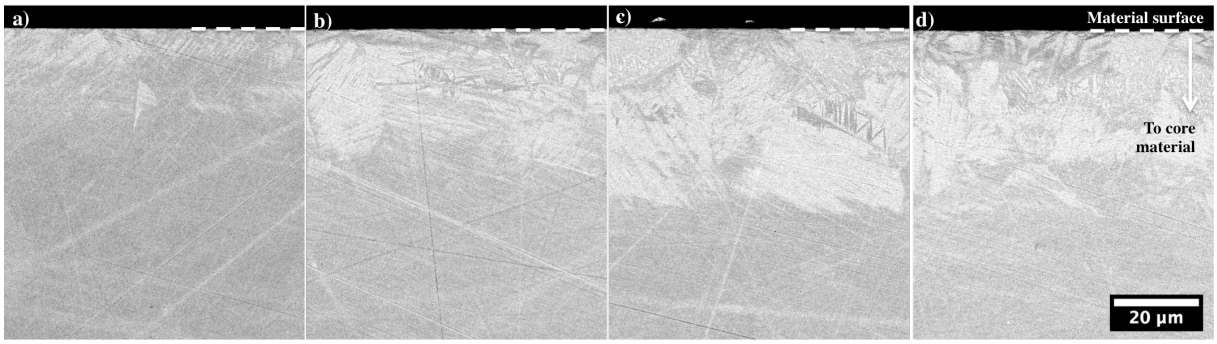

Fig. 6.11 Transverse BSE images of a) 300C4h-Had, b) 300C8h-Had, c) 300C12h-Had and d) 300C20h-Had

The dark precipitates at the top region in the diffusion-affected zone on nitrided Had (**Fig. 6.11**) present different brightness/contrast levels (as shown clearly in **Fig. 6.12b**), suggesting different types of iron manganese nitrides (or ε-carbonitrides) with significantly different

interstitial content. The lamellar morphology of the dark nitrides (**Fig. 6.12b**) agrees with the 'woven' morphology observed on top of material (**Fig. 6.10**).

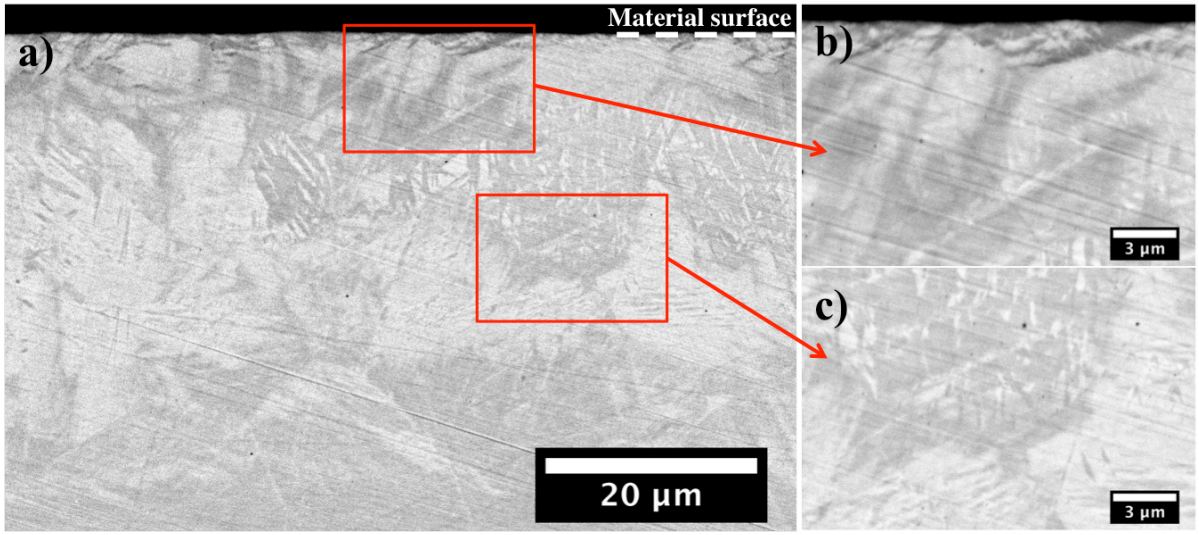

Fig. 6.12 Transverse BSE micrographs of 300C20h-Had in detail

6.2.2 Phase identification

6.2.2.1 XRD analysis of the treated surfaces

Nitrided Hadfield steel samples are examined via XRD under Bragg-Brentano θ-2θ geometry (**Fig. 6.13a**) and under Seeman-Bohlin geometry (**Fig. 6.13b**). No evidence of γ_N nor γ(N) formation can be seen. After nitriding, the observed XRD peaks match well with ε-$Fe_3N_{1.47}$ (PDF card 01-078-8900) and γ′-Fe_4N (PDF card 04-018-4772), suggesting formation of ε-Fe_3N_{1+x} type and γ′-Fe_4N type iron nitrides at the surface of Hadfield steel after TPN. Considering the high Mn-C content in Hadfield steel, nitride precipitates could be iron manganese carbonitrides ε-$(Fe, Mn)_3(N, C)_{1+x}$ and γ′-$(Fe, Mn)_4N$. The dark phases (under BSE imaging, **Fig. 6.12b**) and the greyish phase (under BSE imaging, **Fig. 6.12b** and **Fig. 6.12c**) could be identified as ε-type nitride (or carbonitrides) and γ′-type nitride, respectively.

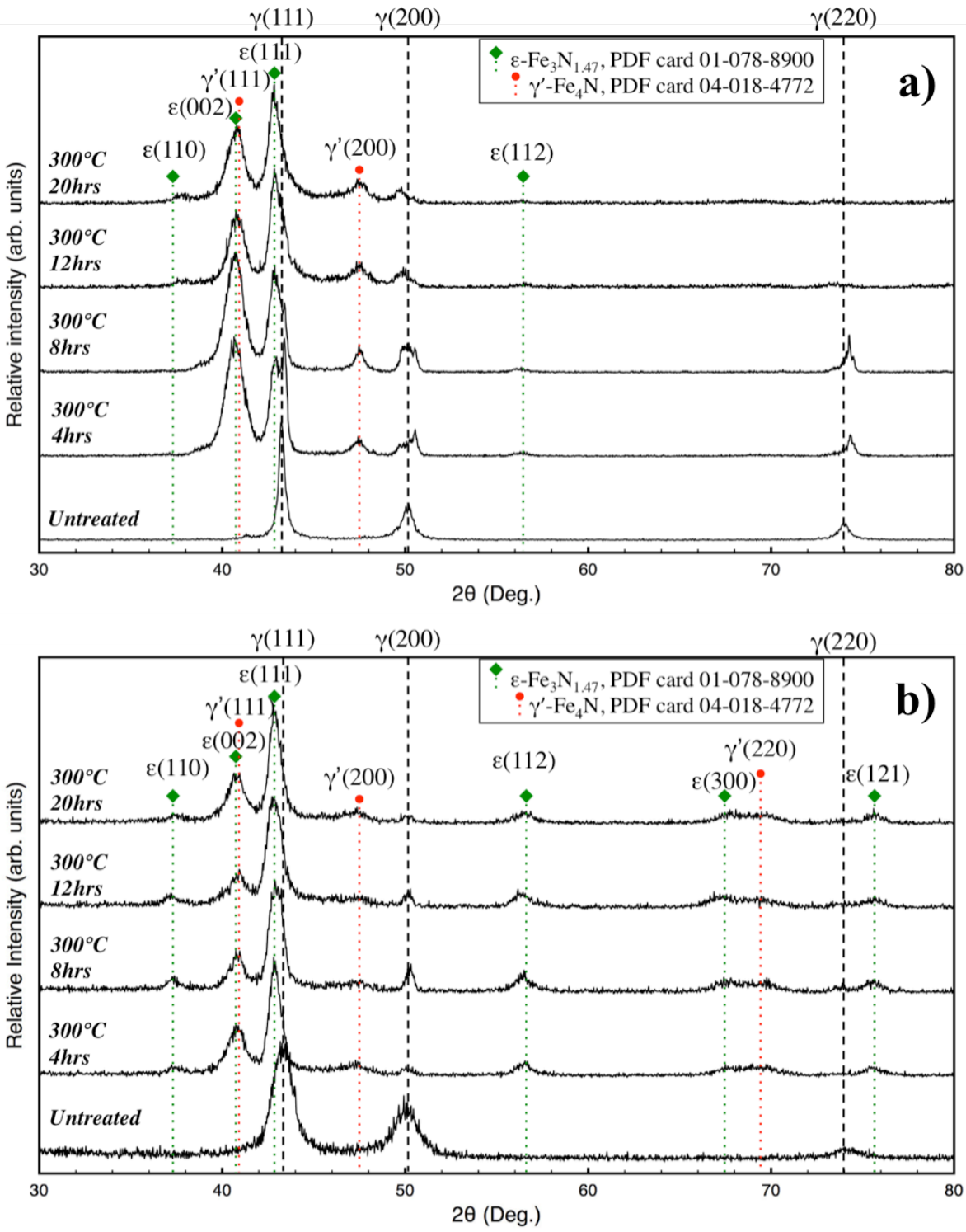

Fig. 6.13 X-ray diffractograms of Hadfield steel before and after TPN a) under Bragg-Brentano θ-2θ geometry, and b) Seeman-Bohlin geometry (at 2° glancing angle)

As suggested by the increasing ε(110) peak intensity with treatment time (**Fig. 6.13a**), the volume fraction of ε-nitrides (or ε-carbonitrides) increases with treatment time. According to the GAXRD profile of 300C4h-Had (**Fig. 6.13b**), both types of nitrides form on Hadfield steel after 4hrs of nitriding. Additionally, the different X-ray attenuation depths under different X-ray diffraction geometries (**Table 3.4, Chapter 3**) suggests that the XRD profiles in **Fig. 6.13a** corresponds to material surface volumes at depths of ~1.7-3.3 μm and the GAXRD profiles in **Fig. 6.13b** correspond to rather shallower surface regions to a depth of ~0.4 μm. Comparing the peak intensities observed for ε-nitride and γ′-nitride between **Figs. 6.13a** and **6.13b**, ε-nitride appears to reside at the very surface and γ′-nitride locate at regions much deeper than ε-nitride on the TPN-treated Hadfield steel. The nitride distributions suggested by XRD profiles (**Fig. 6.13**) are consistent with BSE images (**Figs. 6.11** and **6.12**).

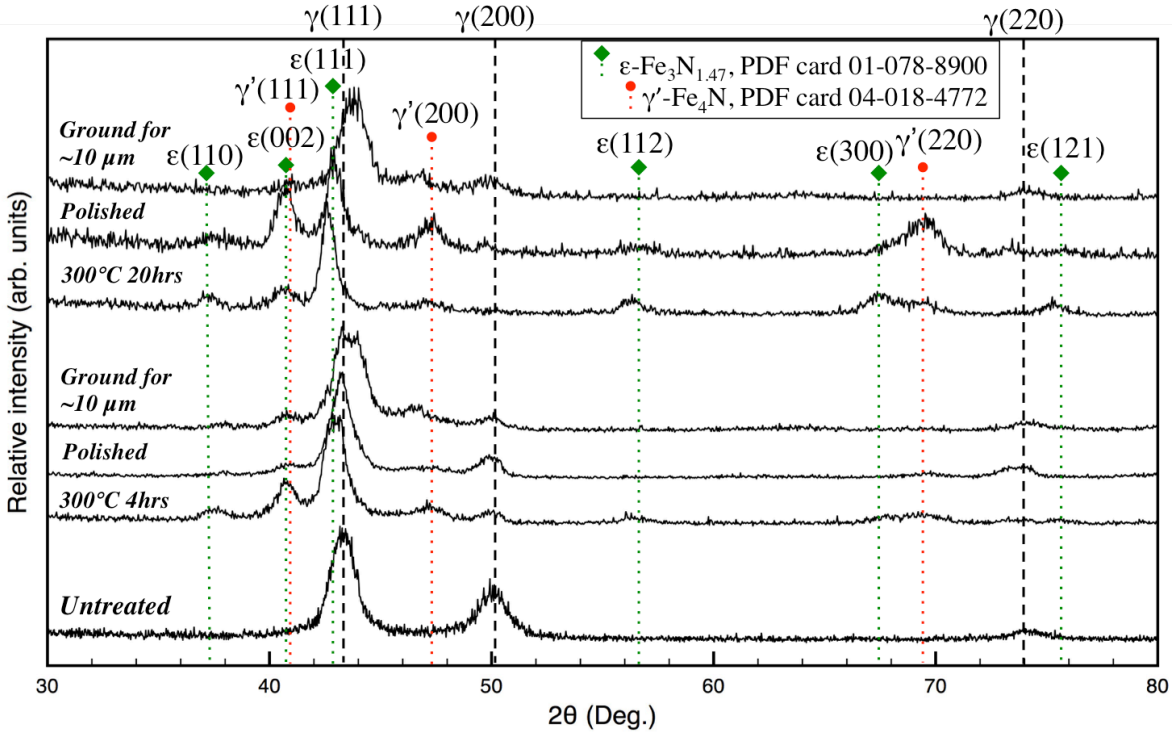

Fig. 6.14 GAXRD of 300C4h-Had and 300C20h-Had as nitrided, after polishing and after grinding (~10 μm surface layer removal)

To reveal the crystal structure in depth**,** 300C4h-Had and 300C20h-Had were further investigated under GAXRD after grinding (for ~10 μm layer removal, measured using a micrometer) and polishing as shown in **Fig. 6.14**. Neither γ_N nor γ(N) can be seen after grinding or polishing the TPN-treated Hadfield steel samples. At a depth of ~10 μm (**Fig. 6.14**), XRD profiles of both nitrided surfaces indicate γ′-nitride precipitate. Neither carbides nor ε-carbonitrides were clearly observed for TPN-treated Had after grinding and polishing under XRD in **Fig. 6.14**. However, the carbon depletion (indicated by the bright background phase under BSE imaging, **Fig. 6.11**) and the broad γ(111) peak at depth of ~10 μm (on 300C4h-Had and 300C20h-Had, **Fig. 6.14**) suggests potential formation of fine carbides in deeper regions of the diffusion-affected zone on nitrided Hadfield (in small volume fractions that were not clearly detected under XRD).

Different to TPN-treated Invar samples after TPN at 400-450°C, γ(N) is not observed in the diffusion zones on Had samples under TPN, which could be attributed to the low treatment temperature applied (i.e. 300°C for Hadfield steel is much lower than 400-450°C for Invar). Nitrogen diffusion at such low treatment temperature for Had most likely occurs along grain boundaries and the precipitate/matrix interfaces, rather than by bulk diffusion.

6.2.2.2 XRD analysis of core microstructure

Due to the high carbon content, Hadfield steel is vulnerable to carbide precipitation such as $(Fe, Mn)_3C$ during heat treatments between 300°C and 800°C [175]. The core microstructure (after etching) of Hadfield steel after TPN treatment presents a grain structure without visible precipitations, as shown in **Fig. 6.15a,b**. After grinding the treated samples using P1200 SiC paper (to depths of ~200 μm, measured with a micrometer), the core structures of Hadfield

steel after TPN are revealed under XRD as shown in **Fig. 6.15c**, where core material shows substrate peaks at positions close to U-Had without any detectable carbide formation.

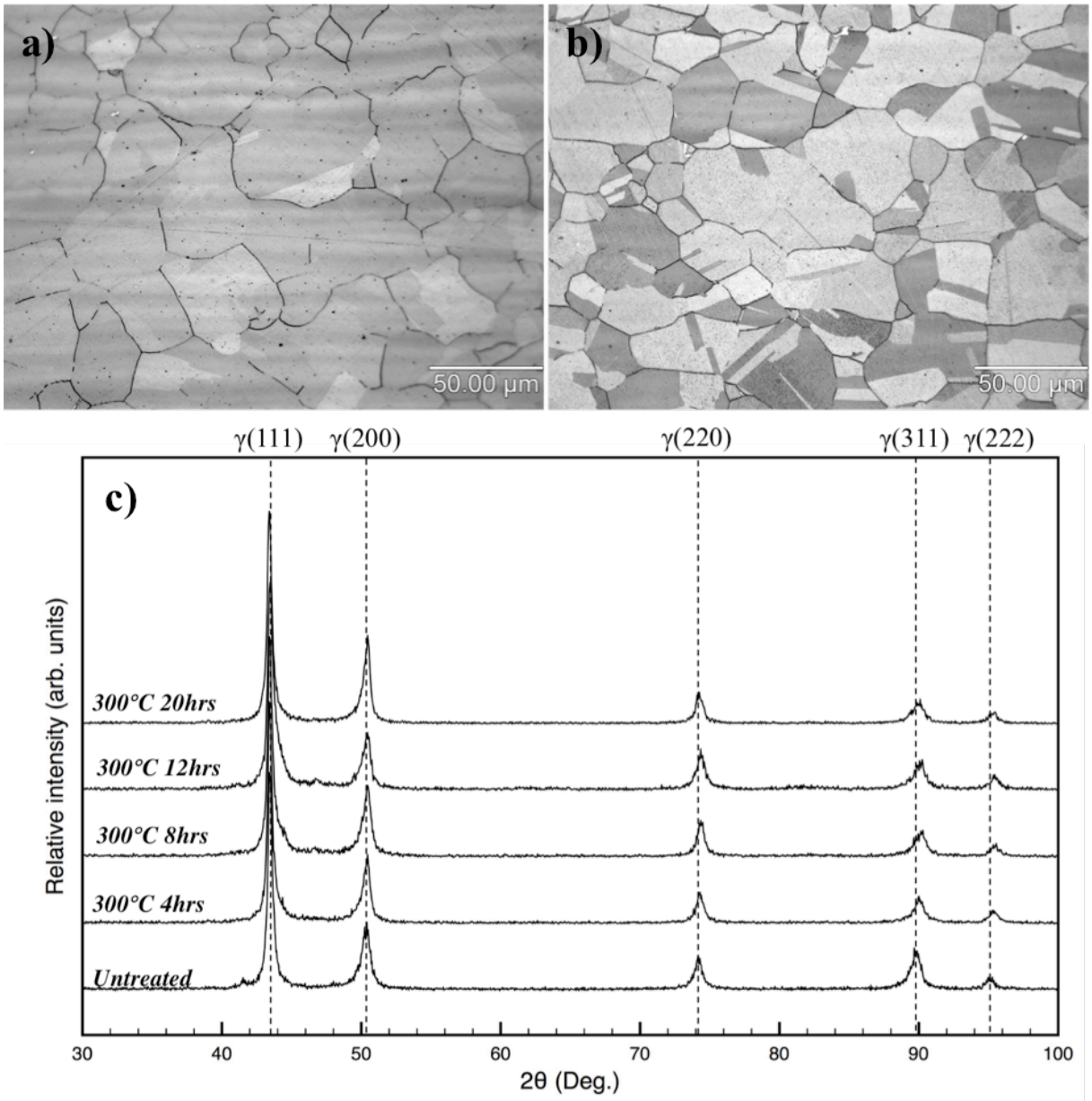

Fig. 6.15 OM images showing core microstructures of a) U-Had and b) 300C20h-Had (etched with 2% Nital); c) θ-2θ XRD profiles of core of Hadfield steels (at depths of ~200 µm after grinding)

6.2.3 Transverse nanoindentation hardness-depth profiles

Although γ_N does not form on nitrided Hadfield steel, the low temperature TPN treatment provides surface hardness enhancement (**Table 6.3**). As shown in cross-sectional nanoindentation hardness depth profiles (**Fig. 6.15)**, surface hardened layers are revealed, showing increasing hardness and depth with treatment time. A maximum hardness value, ~12.6 GPa, was revealed at a depth of ~4μm in 300C20h-Had, which is over 2.5 times higher than that measured for U-Had (~4.8 GPa). The hardened layer depth determined from **Fig. 6.16** correlates well to the penetration depths of dark precipitates revealed under BSE imaging in **Fig. 6.11** (e.g. ~30 μm on 300C20h-Had).

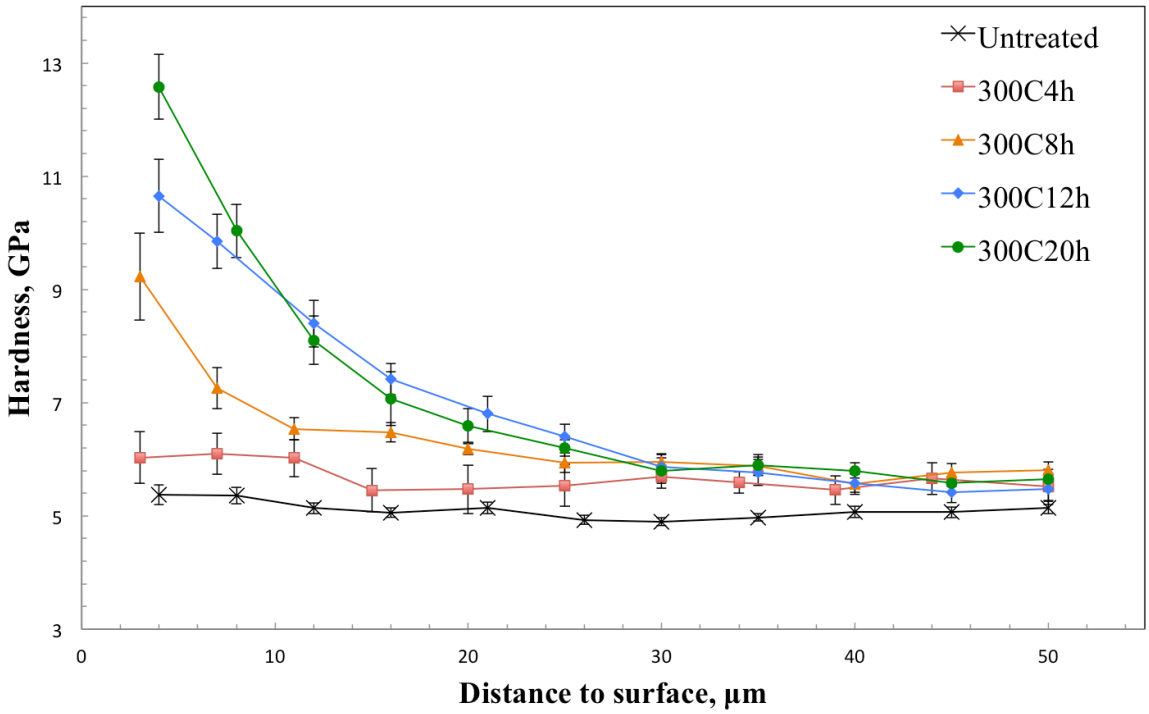

Fig. 6.16 Cross-sectional nanoindentation hardness profiles (at 5000 μN) of untreated and nitrided Hadfield steels

Comparing the hardness profiles of nitrided Had in **Fig. 6.16** to those of nitrided 330 in **Fig. 6.9b**, hardness of TPN-treated Had samples reduces gradually from surface to core (**Fig.**

6.16), whereby the hardness plateau and abrupt drop of hardness (characteristic of nitrogen-supersaturation) is not observed. Clearly, Mn in the Fe-based FCC lattice does not provide the trapping characteristic of Cr to interstitial N under low-temperature TPN.

6.3 Summary

In this chapter, Cr-free Fe-35Ni Invar alloy was compared to Fe-19Cr-35Ni ASS after TPN treatment under equivalent conditions, while Cr-free Fe-13Mn-1.2C Hadfield steel was also investigated after TPN, to explore the possibility of low temperature nitrogen supersaturation of Cr-free high-Mn steel. Nitrogen supersaturation was not observed on either of the selected Cr-free austenitic steels under the chosen nitriding conditions; however, several findings can be drawn, as follows:

- After investigations using a combination of techniques such as BSE (**Fig. 6.2**), GAXRD (**Fig. 6.3**) and TEM (**Figs. 6.4-6.6**), the surface phases on nitrided Invar under XRD (**Fig. 6.7**) could be identify as iron nickel nitride, γ'-$Fe_{2.6}Ni_{1.4}N$, and isotropically-expanded nitrogen solid solution, γ(N), respectively. Nitride precipitates were observed in the upper regions of the diffusion zone on the TPN-treated Invar (e.g. to depth of ~3-5 μm on 450C20h-Invar, **Fig. 6.2**), while the isotropically-expanded nitrogen solid solution (below the nitride-containing region) extended deep into the core material (e.g. to a depth of ~24 μm on 450C20h-Invar, as suggested by the nanoindentation hardness-depth profile, **Fig. 6.9**).

- Although Ni addition in Fe is known to reduce nitrogen solid solubility in Fe-Ni alloys at high temperatures, Invar alloy was capable of accommodating a rather large isotropic lattice expansion, from ~0.359 nm to ~0.365 nm under nitrogen dissolution at 400°C – without forming γ' – as shown in **Fig. 6.8** (c.f. a maximum lattice constant of ~0.365 nm for pure Fe with ~10.3 at.% N at equilibrium nitrogen solid solubility). However, such nitrogen dissolution in Invar under low temperature TPN was limited by γ' formation in the N-saturated matrix.

- Relatively high surface nitrogen content (and surface hardness) was observed on the Cr-free high-Mn Had under TPN at 300°C (**Table 6.3**); however, the high surface nitrogen content and hardness was owing to ε-Fe_3N_{1+x} type and γ′-Fe_4N type iron nitride formation at the near surface, rather than γ_N (**Fig. 6.13**). ε-type nitrides resided at the upper region and γ′-type nitrides formed at deeper regions in the diffusion zone. A relatively deep surface hardened layer (up to ~30 μm after 12hrs of TPN-treatment, **Fig. 6.16**) is observed on the nitrided Had surface, but it is due to precipitation (as suggested by BSE imaging **Fig. 6.11**) rather than γ_N or γ(N).

- Owing to the strong chemical affinity between Cr and N and the preferential Cr-N bonding under nitrogen supersaturation, the high amount of Cr in alloy 330 (~19 wt.%) prevented the formation of γ′ and Fe-N bonding for steels under low-temperature nitriding. In terms of the surface nitrogen content between Fe-35Ni and Fe-19Cr-35 under TPN (**Table 6.1**) and their transverse nitrogen distribution (as suggested by their hardness depth profiles, **Fig. 6.9**), Cr played an important role in retaining (or trapping) the interstitial nitrogen in the treated surface of ASS. Neither Ni nor Mn in Fe-based FCC matrix appeared to exhibit such trapping characteristics to interstitial nitrogen under low temperature TPN.

Conclusions

In this study, four specific austenitic steels and AISI 304 ASS (i.e. Fe-18Cr-8Ni, in wt.%) were investigated under triode-plasma nitriding at selected treatment conditions. In **Chapter 4**, the crystal structures of nitrogen diffusion layers developed on top of two proprietary ASS − i.e. AG17 (Fe-17Cr-20Mn-0.5N, in wt.%) and alloy 330 (Fe-19Cr-35Ni, in wt.%) after TPN treatment were compared under equivalent treatment conditions at 400°C, 425°C and 450°C for 4hrs and 20hrs, respectively. In **Chapter 5**, the surface hardening of three ASS after prolonged treatment at a low treatment temperature of 400°C were investigated under dry sliding wear and SiC wet-slurry abrasive wear conditions; the ASS samples after surface nitrogen modification at 400°C 20hrs and 450°C 20hrs were evaluated under open circuit potential and potentiodynamic polarisation in 3.5 wt.% NaCl water solution. In **Chapter 6**, the Cr-free high-Ni Invar (Fe-35Ni, in wt.%) was compared to the proprietary high-Ni ASS alloy 330 (Fe-19Cr-35Ni, in wt.%) under TPN at equivalent treatment conditions; and the Cr-free high-Mn/C Hadfield steel (Fe-13Mn-1.2C) was also investigated after TPN at a rather low treatment temperature of 300°C for 4, 8, 12 and 20hrs. Several conclusions could be drawn, as follows:

- Under plastic accommodation of nitrogen at low treatment temperature, two possible types of nitrogen composition-induced plasticity mechanism were proposed for the matrix lattice with respect to material SFE (i.e. dislocation glide in the high SFE alloy 330 and dislocation dissociation in the low SFE AG17).
- At elevated treatment temperature, two possible 'diffusional' phase transformation mechanisms were identified in association with CrN formation, which were: i) a uniformly-distributed eutectoid decomposition mechanism to CrN + α-Fe in AG17 (similar to 304), and ii) a sluggish precipitation mechanism to CrN + (Ni stabilised) γ-Fe in alloy 330.

- The symbiotic relationship between SF number density and nitrogen uptake in a low SFE alloy such as AG17 during thermochemical treatment appeared beneficial in achieving high nitrogen absorption and lattice expansion at a relative low treatment temperature, but also tended to result in accelerated phase decomposition at higher treatment temperatures.
- Given the potential for dislocation glide under lattice strain, high SFE alloys such as 330 tend to accommodate less interstitial nitrogen overall (with rapid saturation – and relatively low anisotropic expansion − occurring under thermochemical treatment), but exhibit better structural integrity and thermodynamic stability.
- Other than providing the basic (meta)stable room-temperature austenitic phase composition of the parent alloy, neither Mn nor Ni was essential for formation of γ_N.
- Nevertheless, both Mn and Ni had a pronounced effect on lattice structure and metastability of ASS under low-temperature thermochemical treatment, via their influences on material SFE – and particularly with regard to the onset of crystallographic phase instability (e.g. SF initiation) at the point of alloy 'over-supersaturation' with nitrogen (in Fe-Cr-Ni/Mn-N systems) for specific, alloy composition-dependent, time/temperature envelopes.
- The γ_N layers synthesised after low-temperature TPN provided beneficial load-bearing capacity and reduced adhesive wear to the treated ASS samples under dry sliding wear condition, hence remarkably enhanced material sliding wear resistance.
- Nevertheless, material surface hardness enhancement after formation of γ_N layers did not necessarily translate to good abrasive wear performance. The increased abrasion wear rate after TPN-treatment could be attributed to the brittleness of γ_N layers under nitrogen 'over-supersaturation' (as suggested by the cracking observed on γ_N layers after Vickers indentations) and relatively low layer thickness (of the order of the wear particle size).

- Improvements in corrosion performance (and inhibition of pitting corrosion) were evident for all three ASSs after TPN at 400°C for 20hrs – and the anticipated loss of corrosion resistance after CrN formation in γ_N was observed on ASS being treated at 450°C for 20hrs.
- The high SF number densities (and formation of ε-martensite) observed in γ_N-304 or γ_N-AG17 and the high residual stress in γ_N-330, which were influential factors on material mechanical/tribological performance, did not appear to decrease material corrosion resistance.
- However, the high residual stress developed (e.g. in γ_N-330) raised concerns for the application of γ_N in corrosive environments, where the relaxation of the high residual stress in γ_N layer during corrosion could lead to local breakdown of passive films in demanding corrosive environments (e.g. stress-corrosion cracking effects).
- A ranking order of residual stress level of the γ_N layers tested could be given from high to low as γ_N-330 → γ_N-304 → γ_N-AG17, which appeared inversely correlated to the SF densities observed in them.
- Surface nitrogen uptake, anisotropic lattice expansion, the resulting surface hardness and material tribological performance of γ_N layers could certainly be tailored via altering the nitriding parameters (voltage and/or gas mixture), but is also influenced by the elastic/plastic response of the N-rich lattice to the composition-induced lattice stress/strain during nitrogen interstitial diffusion. The compositional factors of ASS substrate (particularly on the Mn/Ni content and a selection criterion developed with respect to SFE) could also be ultilised to tailor the composition, structure and property/performance of γ_N layers.
- For the Cr-free FCC steels, γ′-$Fe_{2.6}Ni_{1.4}N$ and γ(N) nitrogen solid solution were identified in the diffusion zone of Invar under TPN at 400-450°C, whilst ε-Fe_3N_{1+x} type and γ′-Fe_4N type nitrides were identified in the diffusion zone of Hadfield steel under TPN at 300°C.

- Before γ′ formation, the FCC lattice of Invar was capable of accommodating an isotropic lattice expansion from ~0.359 nm to ~0.365 nm under nitrogen interstitial diffusion at 400°C.
- The strong chemical affinity between Cr and N (and the preferential Cr-N bonding) appear to prevent the formation of γ′ (and Fe-N bonding) for Fe-based FCC lattice under nitrogen insertion. For the formation of γ_N, Cr played an important role of retaining (or trapping) the interstitial nitrogen at the treated surfaces, whereas neither Ni nor Mn appeared to exhibit such characteristic to interstitial nitrogen under low temperature TPN.

This study explored the role of the main alloying elements in ASS substrates (such Cr, Mn and Ni) on the formation, crystal structure and structure metastability of nitrogen-expanded austenite under low-temperature TPN treatment, to i) extend the current understanding on γ_N formed particularly on two proprietary ASS substrates (ie. other than the commonly-investigated AISI 304 or 316) under low-temperature nitriding with respect to the SFE of substrates (varied with the different Mn/Ni content), ii) provide evidence on trapping characteristics of Cr to N for Fe-based FCC alloys during low temperature nitriding (not shown by Ni or Mn) and, more importantly, iii) contribute to a basic methodology for the development of 'nitridable' (in terms of the ability to achieve nitrogen supersaturation of austenite under low-temperature nitriding conditions) austenitic alloys for low-temperature thermochemical diffusion treatment in the future.

Further Work

The surface nitrogen content in this study was based on SEM-EDX and no composition-depth profile was given for respective surfaces. It is necessary to perform surface chemistry analysis of the nitrided surfaces (e.g. GDOES and XPS). Although positive results were observed in material sliding and corrosion performance (in 3.5 wt.% NaCl solution) for three ASS after low-temperature TPN, corrosion performance of γ_N in other corrosive media and the tribo-corrosion performance of γ_N still need to be studied in the future. The Ni-free Mn-N stabilised ASS and the high-Ni ASS (or the corrosion resistant Ni alloys) could be evaluated further with respect to their potential applications (e.g. biocompatibility testing or NACE corrosion testing, respectively, for biomedical and offshore applications).

The relatively shallow diffusion depths (for insufficient abrasion protection using ~3 μm abrasive particles) and the layer brittleness (as hinted at by the poor abrasion performance, that could be attributed to the high 'nitriding potential' employed) points to future studies on ASS under TPN at different nitriding parameters (e.g. nitrogen gas volume fraction, bias voltage and/or working pressure) to explore the influence of plasma nitriding parameters (especially in triode-plasma configuration) on the crystallographic instabilities in γ_N layers.

As discussed in this study, Cr played an important role in the formation of γ_N. However, it still remains unclear that: i) what is the minimum Cr content required in substrates (e.g. Fe-Cr, Ni-Cr and Co-Cr alloys) for the effective formation of nitrogen-expanded austenite, and ii) whether strong nitride-forming elements other than Cr (e.g. Ti, V, Nb, W) could also facilitate the formation of such metastable layers on candidate substrates. Additionally, apart from Mn and Ni, various other substitutional elements (e.g. Co, Cu, Al, Si, Mo, etc.) can also influence the SFE and/or lattice stability of austenitic iron and steel.

Under the scope of designing low temperature 'nitridable' austenitic alloys, future studies could be carried out on: i) low-SFE (e.g. Cr-containing TWIP/TRIP steels or Co-Cr alloys) or high-SFE (e.g. superaustenitic ASS or Ni-Cr alloys) materials and ii) on Fe/Ni/Co-based alloys containing different levels of Cr (or other strong nitride-forming elements). For example, the likely formation of coherent ε-martensite lamellae (or incoherent α′-martensite) in γ_N layers synthesised on Cr-containing TWIP or TRIP steels under low-temperature nitriding, which needs to be confirmed by respective studies in the future, could substantially influence material structure-property-performance considerations, particularly for optimal design of high-strength, light-weight steel structures in thin section.

Reference

[1] A. W. Machlet, "Hardening or treatment of steel, iron," United States Patent 1092925, 1914.

[2] A. Fry, "Process for hardening steel alloys," United States Patent 1487554, 1924.

[3] D. Pye, *Practical nitriding and ferritic nitrocarburizing*. United States ASM International, 2003.

[4] K. L. Hsu, T. M. Ahn, and D. A. Rigney, "Friction, wear and microstructure of unlubricated austenitic stainless steels," *Wear,* vol. 60, pp. 13-37, 1980.

[5] Z. L. Zhang and T. Bell, "Structure and corrosion resistance of plasma nitrided stainless steel," *Surface Engineering,* vol. 1, pp. 131-136, 1985.

[6] P. A. Dearnley, A. Namvar, G. G. A. Hibberd, and T. Bell, "Some observations on plasma nitriding austenitic stainless steel," presented at the Plasma surface engineering Garmisch-Partenkirchen, 1988.

[7] J. Flis, J. Mankowski, and E. Rolinski, "Corrosion behaviour of stainless steels after plasma and ammonia nitriding " *Surface Engineering,* vol. 5, pp. 151-157, 1989.

[8] K. Ichii, K. Fujimura, and T. Takase, "Structure of the ion-nitrided layer of 18-8 stainless steel," *Technology Reports of Kansai University,* vol. 27, pp. 135-144, 1986.

[9] M. A. J. Somers and T. Christiansen, "Low temperature surface hardening of stainless steel " in *Thermochemical Surface Engineering of Steels*, E. J. Mittemeijer and M. A. J. Somers, Eds., First ed Cambridge: Woodhead Publishing, 2015, pp. 557-579.

[10] H. Dong, "S-phase surface engineering of Fe-Cr, Co-Cr and Ni-Cr alloys," *International Materials Reviews,* vol. 55, pp. 65-98, 2010.

[11] T. L. Christiansen, K. Stahl, B. K. Brink, and M. A. J. Somers, "On the carbon solubility in expanded austenite and formation of Hagg carbide in AISI 316 stainless steel," *Steel Research International,* vol. 87, pp. 1395-1405, 2016.

[12] T. Christiansen and M. A. J. Somers, "Controlled dissolution of colossal quantities of nitrogen in stainless steel," *Metallurgical and Materials Transactions A,* vol. 37A, pp. 675-682, 2006.

[13] Y. Cao, F. Ernst, and G. M. Michal, "Colossal carbon supersaturation in austenitic stainless steels carburized at low temperature," *Acta Materialia,* vol. 51, pp. 4171-4181, 2003.

[14] E. I. Meletis, V. Singh, and J. C. Jiang, "On the single phase formed during low-temperature plasma nitriding of austenitic stainless steel," *Journal of materials science letters,* vol. 21, pp. 1171-1174, 2002.

[15] J. C. Jiang and E. I. Meletis, "Microstructure of the nitride layer of AISI 316 stainless steel produced by intensified plasma assisted processing," *Journal of Applied Physics,* vol. 88, pp. 4026-4031, 2000.

[16] G. M. Michal, F. Ernst, and A. H. Heuer, "Carbon paraequilibrium in austenitic stainless steel," *Metallurgy and Material Transactions A,* vol. 37A, pp. 1819-1824, 2006.

[17] F. Ernst, Y. Cao, G. M. Michal, and A. H. Heuer, "Carbide precipitation in austenitic stainless steel carburized at low temperature," *Acta Materialia,* vol. 55, pp. 1895-1906, 2007.

[18] T. Bell, "Current status of supersaturated surface engineered S-phase materials," *Key Engineering Materials,* vol. 373/374, p. 289, 2008.

[19] X. Y. Li, S. Thaiwatthana, H. Dong, and T. Bell, "Thermal stability of carbon S phase in 316 stainless steel," *Surface Engineering,* vol. 18, pp. 448-452, 2002.

[20] A. Leyland, K. S. Fancey, A. S. James, and A. Matthews, "Enhanced plasma nitriding at low pressures: a comparative study of d.c. and r.f. techniques," *Surface and Coatings Technology,* vol. 41, pp. 295-304, 1990.
[21] A. Matthews and A. Leyland, "Surface treatment of metals at low pressure," United Kingdom Patent GB2261227, 1993.
[22] A. Leyland, D. B. Lewis, P. R. Stevenson, and A. Matthews, "Low temperature plasma diffusion treatment of stainless steels for improved wear resistance," *Surface and Coatings Technology,* vol. 62, pp. 608-617, 1993.
[23] K. S. Fancey, "An investigation into dissociative mechanisms in nitrogenous glow discharges by optical emission spectroscopy," *Vacuum,* vol. 46, pp. 695-700, 1995.
[24] K. M. Winter, J. Kalucki, and D. Koshel, "Process technologies for thermochemical surface engineering," in *Thermochemical Surface Engineering of Steels*, E. J. Mittemeijer and M. A. J. Somers, Eds., First ed Cambridge: Woodhead Publishing, 2015, pp. 141-202.
[25] J. T. Slycke, E. J. Mittemeijer, and M. A. J. Somers, "Thermodynamics and kinetics of gas and gas-solid reactions," in *Thermochemical Surface Engineering of Steels*, E. J. Mittemeijer and M. A. J. Somers, Eds., First ed Cambridge: Woodhead Publishing, 2015, pp. 3-111.
[26] J. R. Davis, *Surface Hardening of Steels, Understanding the Basics*: ASM International, 2002.
[27] "Liquid Nitriding " in *Heat treating, Vol. 4, ASM Handbook*, ed: ASM International, 1991, pp. 410-419.
[28] H. Beyer, P. Biberbach, and C. Scondo, "Process for nitriding iron and steel in salt baths regenerated with triazine polymers," United States Patent 4019928, 1977.
[29] J. Elwart and R. Hunger, "Plasma (Ion) Nitriding and Nitrocarburizing of Steels," in *Steel Heat Treating Fundamentals and Processes, Vol. 4, ASM Handbook*, ed: ASM International, 2013, pp. 690-703.
[30] B. Berghaus, German Patent DPR 668639, 1932.
[31] B. Berghaus, German Patent DPR 851560, 1939.
[32] A. M. Ignatov and A. A. Rukhadze, "Plasmas in nature, laboratory and technology," in *Plasma Technology, Fundamentals and Applications*, C. M. and C. Gorse, Eds., First ed New York: Springer Science + Business Media, 1992, pp. 1-10.
[33] A. Fridman and L. A. Kennedy, *Plasma Physics and Engineering*, First ed. New York: Taylor&Francis Routledge, 2004.
[34] K. S. S. Harsha, *Principles of Vapor Deposition of Thin Films*, First ed. Online: Elsevier Science, 2005.
[35] M. A. Lieberman and A. J. Lichtenberg, *Principles of Plasma Discharges and Materials Processing*, Second ed. New Jersey: John Wiley & Sons, Inc, 2005.
[36] M. Capitelli and C. Gorse, *Plasma Technology Fundamentals and Applications*, First ed. New York: Springer Science+BusinessMedai, 1992.
[37] J. C. Maxwell, "Illustrations of the dynamic theory of gases. II. On the process of diffusion of two or more kinds of moving particles among one another," *Phil. Mag.,* vol. 20, pp. 21-37, 1860.
[38] J. C. Maxwell, "Illustrations of the dynamic theory of gases. I. On the motions and collisions of perfectly elastic spheres," *Phil. Mag.,* vol. 19, pp. 19-32, 1860.
[39] L. Boltzmann, "Uber die Natur der Gasmolecule," *Sitz. Math. Naturwiss. Cl. Acad. Wiss. Wien II.,* vol. 74, p. 55, 1877.
[40] H. Hertz, *Ann. Phys.,* vol. 17, p. 177, 1882.
[41] R. Clausius, "Uber die mittlere Lange der Wege, welche bei der Molecularbewgung gasformigen Korper von den einzelnen Moleculen zuruckgelegt werden, nebst einigen

anderen Bemerkungen uber die mechanischen Warmetheorie," *Ann. Phys.,* vol. 105, pp. 239-258, 1858.
[42] J. O. Hirschfelder, C. F. Curtiss, and R. B. Bird, *Molecular Theory of Gases and Liquids*, First ed. New York: Wiley, 1954.
[43] H. Fredriksson and U. Akerlind, "Properties of Gases," in *Physics of Functional Materials* 1st ed UK: John Wiley & Sons, 2008.
[44] K. S. Fancey, "An Investigation into Phenomena Which Influence the Optimisation of Ion Plating Systems," Doctor of Philosophy, University of Hull, 1989.
[45] B. N. Chapman, *Glow Discharge Process*, First ed. New York: Wiley, 1980.
[46] K. S. Fancey and A. Matthews, "Some fundamental aspects of glow discharges in plasma-assisted processes," *Surface and Coatings Technology,* vol. 33, pp. 17-29, 1987.
[47] W. D. Davis and T. A. Vanderslice, "Ion energies at the cathode of a glow discharge," *Phys. Rev.,* vol. 131, pp. 219-228, 1963.
[48] J. Rickards, "Energies of particles at the cathode of a glow discharge," *Vacuum,* vol. 34, pp. 559-662, 1984.
[49] D. A. Porter and K. E. Easterling, *Phase Transformations in Metals and Alloys*, Second ed. Hong Kong: Springer-Science+Business Media, B.V., 1992.
[50] L. S. Darken, "Diffusion of carbon in austenite with a discontinuity in composition " *Transactions AIME,* vol. 180, pp. 430-438, 1948.
[51] R. Abbaschian, L. Abbaschian, and R. E. Reed-Hill, *Physical Metallurgy Principles*, Fourth ed. United States: Cengage Learning, 2009.
[52] H. Mehrer, *Diffusion in Solids, Fundamentals, Methods, Materials, Diffusion-Controlled Processes*. Berlin, Heidelberg Springer-Verlag 2007.
[53] S. Lampman, "Introduction to Surface Hardneing of Steels," in *ASM Handbook Vol. 4: Heat Treating*, First ed United States of America: ASM International, 1991.
[54] C. Wells, W. Batz, and R. F. Mehl, "Diffusion coefficient of carbon in austenite," *Transactions AIME,* vol. 188, p. 553, 1950.
[55] W. P. Tong, N. R. Tao, Z. B. Wang, J. Lu, and K. Lu, "Nitriding Iron at lower tempeartures," *Science,* vol. 299, pp. 686-688, 2015.
[56] E.H. Du, Marchie van Voorthuysen, D.O. Boerma, and N. C. Chechenin, "Low Temperature extension of the Lehrer diagram and the iron-nitrogen phase diagram," *Metall. Mater. Trans. A,* vol. 33A, 2002.
[57] K. H. Jack, "The Iron-Nitrogen System: The preparation and the Crystal Structures of Nitrogen-Austenite and Nitrogen-Martensite," *Proceeding of the Royal Society A,* vol. A208, p. 200, 1951.
[58] H.A. Wriedt, N.A. Gokcen, and R.H. Nafziger, "The Fe-N (iron-nitrogen) system," *Bulletin of Alloy Phase Diagrams,* vol. 8, p. 355, 1987.
[59] *Alloy Phase Diagrams, ASM Handbook, Vol. 3*: ASM International, 1992.
[60] T.B. Massalski, *Ed. in Chief, Binary Alloy Phase Diagrams,* vol. 2nd ed., p. ASM International, 1996.
[61] S. Bhattacharyya, "Iron nitride family at reduced dimensions: a review of their synthesis protocols and structural and magnetic properties," *Journal of Physical Chemistry C,* vol. 119, pp. 1601-1622, 2014.
[62] P. Prenosil, *Härterei-Techn. Mitt.,* vol. 28, pp. 157-164, 1973.
[63] D. H. Jack and K. H. Jack, "Invited review: Carbides and nitrides in steel," *Materials Science and Engineering* vol. 11, pp. 1-27, 1973.
[64] K. H. Jack, "The Iron-Nitrogen System: The crystal Structure of elipsal-phase Iron Nitrides," *Acta Crystallographica* vol. 5, p. 404, 1952.

[65] N.I. Kardonina, A.S. Yurovshikh, and A. S. Kolpakov, "Transformations in the Fe-N system," *Metal Science and Heat treatment,* vol. 52, pp. 457-467, 2010.
[66] H. Jacobs, D. Rechenbach, and U. Zachwieja, "Structure determination of γ'-Fe4N and ε-Fe3N," *Journal of Alloys and Compounds,* vol. 227, pp. 10-17, 1995.
[67] T. Liapina, A. Leineweber, E.J. Mittemeijer, and W. Kockelmann, "The lattice parameters of e-iron nitridess: lattice strains due to a varying degree of N ordering," *Acta Materialia,* vol. 52, pp. 173-180, 2004.
[68] U. Schwarz, A. Wosylus, M. Wessel, R. Dronskowski, M. Hanfland, D. Rau, R. Niewa, "High-pressure high-temperature behavior of ζ-Fe2N and phase transition to ε-Fe3N1.5," *European Journal of Inorganic Chemistry* pp. 1634-1639, 2009.
[69] F. Tessier, A. Navrotsky, R. Niewa, A. Leineweber, H. Jacobs, S. Kikkawa, M. Takahashi, F. Kanamaru, F.J. DiSalvo, "Enegetics of binary iron nitrides," *Solid State Science* vol. 2, pp. 457-462, 2000.
[70] C. Navio, J. Alvarez, M. J. Capitan, F. Yndurain, and R. Miranda, "Nonmagnetic γ''-FeN thin films epitaxially grown on Cu(001): Electronic structure and thermal stability," *Physical Review B,* vol. 78, 2008.
[71] O. C. Shepard, "The effect of carbide precipitation and carburisation on the mechanical properties of type 304 stainless steel," U.S. AEC Report 1958.
[72] W. C. Hayes and O. C. Shepard, "Corrosion and decarburization of the ferritic chromium-molybdenum steels in sodium coolant systems," Atomics International1958.
[73] W. J. Anderson and G. V. Sneesby, "Carburization of austenitic stainless steel in liquid sodium," Atomics International1960.
[74] W. F. Holcomb, "Carburization of type 304 stainless steel in liquid sodium," *Nuclear Engineering and Design,* vol. 6, pp. 264-272, 1967.
[75] F. B. Litton and A. E. Morris, "Carburization of type 316L stainless steel in static sodium," *Journal of the Less-Common Metals,* vol. 22, pp. 71-82, 1970.
[76] S. P. Hannula and O. Nenon, "Surface structure and properties of ion-nitrided austenic stainless steels," *Thin Solid Films,* vol. 181, pp. 343-350, 1989.
[77] E. Angelini, A. Burdese, and B. De Benedetti, "Ion nitriding of austenitic stainless steels," *Metallurgical Science and Technology,* vol. 6, pp. 33-39, 1988.
[78] C. M. Zener, *Elasticity and anelasticity of metals*. Chicago: University of Chicago Press, 1948.
[79] S. Mandl and B. Rauschenbach, "Anisotropic strain in nitrided austenitic stainless steel," *Journal of Applied Physics,* vol. 88, pp. 3323-3329, 2000.
[80] Y. Sun, X. Y. Li, and T. Bell, "X-ray diffraction characterisation of low temperature plasma nitrided austenitic stainless steels," *Journal of Materials Science,* vol. 34, pp. 4793-4802, 1999.
[81] C. N. J. Wagner, J. P. Boisseau, and E. N. Aqua, *Transactions of the Metallurgical Society of AIME,* vol. 233, p. 1280, 1965.
[82] M. S. Paterson, "X-ray diffraction by face-centered cubic crystals with deformation faults," *Journal of Applied Physics,* vol. 23, pp. 805-811, 1952.
[83] B. E. Warren, "X-ray studies of deformed metals," *Progress in Metal Physics,* vol. 8, pp. 147-202, 1959.
[84] D. L. Williamson, L. Wang, R. Wei, and P. J. Wilbur, "Solid solution strengthening of stainless steel surface layers by rapid, high dose, elevated temperature nitrogen ion implantation," *Materials Letters,* vol. 9, pp. 302-308, 1990.
[85] D. L. Williamson and O. Ozturk, "Metastable phase formation and enhanced diffusion in f.c.c. alloys under high dose, high flux nitrogen implantation at high and low ion energies," *Surface and Coatings Technology,* vol. 65, pp. 15-23, 1994.

[86] O. Ozturk and D. L. Williamson, "Phase and composition depth distribution analyses of low engergy high flux N implanted stainless steel," *Journal of Applied Physics,* vol. 77, 1995.
[87] D. L. Williamson, J. A. Davis, and P. J. Wilbur, "Effect of austenitic stainless steel composition on low-energy, high-flux nitrogen ion beam processing," *Surface and Coatings Technology,* vol. 103-104, pp. 178-184, 1998.
[88] K. Marchev, C. V. Cooper, J. T. Blucher, and B. C. Giessen, "Conditions for the formation of a martensitic single-phase compound layer ion-nitrided 316L austenitic stainless steel," *Surface and Coatings Technology,* vol. 99, pp. 225-228, 1998.
[89] K. Marchev, R. Hidalgo, M. Landis, R. Vallerio, C. V. Cooper, and B. C. Giessen, "The metastable m phase layer on ion-nitried austenitic stainless steels Part 2, crystal structure and observation of its two-directional orientational anisotropy," *Surface and Coatings Technology,* vol. 112, pp. 67-70, 1999.
[90] K. Marchev, M. Landis, R. Vallerio, C. V. Cooper, and B. C. Giessen, "The m phase layer on ion nitrided austenitic stainless steel (III), an epitaxial relationship between the m phase and the γ parent phase and a review of structural identifications of this phase " *Surface and Coatings Technology,* vol. 116-119, pp. 184-188, 1999.
[91] Y. Hirohata, T. Abe, and T. Yamashina, "Preparation of iron oxide and nitride films by means of reactive sputtering," *Journal of the Vacuum Society of Japan,* vol. 21, pp. 73-79, 1978.
[92] A. Oueldennaoua, E. Bauer-Grosse, M. Foos, and C. Frantz, "Formation d'un nitrure metastable FeN de structure NaCl par pulverisation cathodique," *Scripta Metallurgica,* vol. 19, pp. 1503-1506, 1985.
[93] A. Bourjot, M. Foos, and C. Frantz, "Basic properties of sputtered 310 stainless steel-nitrogen coatings," *Surface and Coatings Technology,* vol. 43/44, pp. 533-542, 1990.
[94] A. Saker, C. Leroy, H. Michel, and C. Frantz, "Properties of sputtered stainless steel-nitrogen coatings and structural analogy with low temperature plasma nitrided layers of austenitic steels," *Material Science and Engineering A,* vol. 140, pp. 702-708, 1991.
[95] J. von. Stebut, A. Darbeida, A. Saker, A. Billard, and R. Rezakhanlou, "Optimization of the contact mechanical strength of magnetron-sputtered nitrogen-dope AISI 316L physically vapour deposited coatings," *Surface and Coatings Technology,* vol. 57, pp. 31-42, 1993.
[96] A. Saker, A. Billard, and R. Rezakhanlou, "Optimization of the surface mechanical strength of AISI 316L physically vapour deposited nitrogen-doped coatings on AISI 316L substrates," *Surface and Coatings Technology,* vol. 60, pp. 434-440, 1993.
[97] J. M. Schneider, C. Rebholz, A. A. Voevodin, A. Leyland, and A. Matthews, "Deposition and characterization of nitrogen containing stainless steel coatings prepared by reactive magnetron sputtering," *Vacuum,* vol. 47, pp. 1077-1080, 1996.
[98] K. L. Dahm and P. A. Dearnley, "S phase coatings produced by unbalanced magnetron sputtering," *Surface Engineering,* vol. 12, pp. 61-67, 1996.
[99] M. P. Fewell and J. M. Priest, "High-order diffractometry of expanded austenite using synchrotron radiation," *Surface and Coatings Technology,* vol. 202, pp. 1802-1815, 2008.
[100] F. A. P. Fernandes, T. L. Christiansen, G. Winther, and M. A. J. Somers, "On the determination of stress profiles in expanded austenite by grazing incidence X-ray diffraction and successive layer removal," *Acta Materialia,* vol. 94, pp. 271-280, 2015.
[101] T. Christiansen and M. A. J. Somers, "On the crystallographic structure of S-phase," *Scripta Materialia,* vol. 50, pp. 35-37, 2004.

[102] B. K. Brink, K. Stahl, T. L. Christiansen, J. Oddershede, G. Winthiner, and M. A. J. Somers, "On the elusive crystal structure of expanded austenite," *Scripta Materialia,* vol. 131 pp. 59-62, 2017.
[103] T. Christiansen, T. S. Hummelshoj, and M. A. J. Somers, "Expanded austenite, crystallography and residual stress," *Surface Engineering,* vol. 26, pp. 242-247, 2010.
[104] J. Oddershede, T. L. Christiansen, K. Stahl, and M. A. J. Somers, "Extended X-ray absorption fine structure investigation of nitrogen stabilized expanded austenite," *Scripta Materialia,* vol. 62, pp. 290-293, 2010.
[105] T. S. Hummelshoj, T. L. Christiansen, and M. A. J. Somers, "Lattice expansion of carbon-stabilized expanded austenite," *Scripta Materialia,* vol. 63, pp. 761-763, 2010.
[106] B. E. Warren, *X-ray Diffraction* First ed. New York: Dover Publications Inc., 1990.
[107] L. Velterop, R. Delhez, T. H. de Keijser, E. J. Mittemeijer, and D. Reefman, "X-ray diffraction analysis of stacking and twin faults in f.c.c. metals: a revision and allowance for texture and non-uniform fault probabilities," *Applied Crysallography,* vol. 33, pp. 296-306, 2000.
[108] J. C. Stinville, P. Villechaise, C. Templier, J. P. Riviere, and M. Drouet, "Lattice rotation induced by plasma nitridng in a 316L polycrystalline stainless steel," *Acta Materialia,* vol. 58, pp. 2814-2821, 2010.
[109] J. C. Stinville, C. Tromas, P. Villechaise, and C. Templier, "Anisotropy changes in hardness and indentation modulus induced by plasma nitriding of 316L polycrystalline stainless steel," *Scripta Materialia,* vol. 64, pp. 37-40, 2011.
[110] J. C. Stinville, J. Cormier, C. Templier, and P. Villechaise, "Modeling of the lattice rotations induced by plasma nitriding of 316L polycrystalline stainless steel," *Acta Materialia,* vol. 83, pp. 10-16, 2015.
[111] B. Clausen, T. Lorentzen, and T. Leffers, "Self-consistent modeling of the plastic deformation of F.C.C. polycrystals and its implications for diffraction measurements of internal stresses " *Acta Materialia,* vol. 46, pp. 3087-3098, 1998.
[112] X. Y. Li and Y. Sun, "Transmission electron microscopy study of S phase in low temperature plasma nitrided 316 stainless steel," in *Stainless Steel 2000: Thermochemical Surface Engineering of Stainless Steel*, T. Bell and K. Akamatsu, Eds., 1st ed London: Maney Publishing, 2001.
[113] D. Stroz and M. Psoda, "TEM studies of plasma nitrided austenitic stainless steel," *Journal of Microscopy,* vol. 237, pp. 227-231, 2010.
[114] K. Tong, F. Ye, H. Che, M. K. Lei, S. Miao, and C. Zhang, "High-density stacking faults in a supersaturated nitrided layer on austenitic stainless steel," *Journal of Applied Crystallography,* vol. 49, pp. 1967-1971, 2016.
[115] E. Menthe, K. T. Rie, J. W. Schultze, and S. Simsson, "Structure and properties of plasma-nitrided stainless steel," *Surface and Coatings Technology,* vol. 74-75, pp. 412-416, 1995.
[116] N. Yasumaru, "Low-temperature ion nitriding of austenitic stainless steels," *Materials Transactions - The Japanese Institute of Metals* vol. 39, pp. 1046-1052, 1998.
[117] J. P. Riviere, M. Cahoreau, and P. Meheust, "Chemical bonding of nitrogen in low energy high flux implanted austenitic stainless steel," *Journal of Applied Physics,* vol. 91, pp. 6361-6366, 2002.
[118] J. Buhagiar, X. Li, and H. Dong, "Formation and microstructural characterisation of S-phase layers in Ni-free austenitic stainless steels by low-temperature plasma surface alloying," *Surface and Coatings Technology,* vol. 204, pp. 330-335, 2009.
[119] J. Dudala, J. Gilewicz-Wolter, and Z. Stegowski, "Simultaneous measurement of Cr, Mn and Fe diffusion in chromium-manganese steels," *Nukleonika,* vol. 50, pp. 67-71, 2005.

[120] T. Christiansen and M. A. J. Somers, "Decomposition kinetics of expanded austenite with high nitrogen contents," *Z. Metallkd.,* vol. 97, pp. 79-88, 2006.
[121] G. A. Collins, R. Hutchings, K. T. Short, J. Tendys, X. Li, and M. Sammandi, "Nitriding of austenitic stainless steel by plasma immersion ion implantation," *Surface and Coatings Technology,* vol. 74-75, pp. 417-424, 1995.
[122] T. Bell and Y. Sun, "Low-temperature plasma nitriding and carburising of austenitic stainless steels," *Heat treatment of metals,* vol. 29, pp. 57-64, 2002.
[123] T. Makishi and K. Nakata, "Surface hardening of nickel alloys by means of plasma nitriding," *Meallurgical and Materials Transactions A,* vol. 35A, pp. 227-238, 2004.
[124] X. Y. Li, N. Habibi, and H. Dong, "Microstructural characterisation of a plasma caburised low carbon Co-Cr alloy," *Surface Engineering,* vol. 23, pp. 45-51, 2007.
[125] J. Lutz, J. W. Gerlach, and S. Mandl, "PIII nitriding of fcc-alloys containing Ni and Cr," *Physica Status Solidi A,* vol. 205, pp. 980-984, 2008.
[126] M. P. Fewell, D. R. G. Mitchell, J. M. Priest, K. T. Short, and G. A. Collins, "The nature of expanded austenite," *Surface and Coatings Technology,* vol. 131, pp. 300-306, 2000.
[127] B. K. Brink, K. Stahl, T. Christiansen, C. Frandsen, M. F. Hansen, and M. A. J. Somers, "Composition-dependent variation of magnetic properties and interstitial ordering in homogenous expanded austenite," *Acta Materialia,* vol. 106, pp. 32-39, 2016.
[128] B. H. Kolster, "Wear and corrosion resistant coatings on austenitic steels," *VDI-Berichte (The Association of German Engineers),* vol. 506, 1983.
[129] R. H. van der Jagt, B. H. Kolster, and M. W. H. Gillham, "Anti-wear/corrosion treatment of finished austenitic stainless steel components: the Hardcor process," *Materials & Design,* vol. 12, pp. 41-46, 1991.
[130] O. Rey and P. Jacquot, "Kolsterising: hardening of austenitic stainless steel," *Surface Engineering,* vol. 18, pp. 412-414, 2002.
[131] B. H. Kolster, "Mechanism of Fe and Cr transport by liquid sodium in non-isothermal loop systems," *Journal of Nuclear Materials,* vol. 55, pp. 155-168, 1975.
[132] J. P. Lebrun, "Applications of low-temperature surface hardening of stainless steels," in *Thermochemical Surface Engineering of Steels*, E. J. Mittemeijer and M. A. J. Somers, Eds., First ed Cambridge: Woodhead Publishing, 2015, pp. 633-647.
[133] S. Collins and P. Williams. (2006) Low-temperature colossal supersaturation. *Advanced Materials and Process*. 32-33.
[134] P. Williams and S. V. Marx, "Low temperature case hardening processes," United states Patent 6093303, 2000.
[135] P. Williams and S. V. Marx, "Selective case hardening processes at low temperature," United State Patent 6165597, 2000.
[136] P. Williams and S. V. Marx, "Low temperature case hardening " United States Patent 6461448 B1, 2002.
[137] P. Williams and S. V. Marx, "Modified low temperature case hardening processes " United States Patent 6547888 B1, 2003.
[138] J. P. Lebrun, H. Michel, and M. Gantois, *Memoires Scientifiques de la Revue Metallurgie,* vol. 10, pp. 727-738, 1972.
[139] L. Poirier, Y. Corre, and J. P. Lebrun, "Solutions to improve surface hardness of stainless steels without loss of corrosion resistance," *Surface Engineering,* vol. 18, pp. 439-442, 2002.
[140] J. P. Lebrun, "Plasma-assisted processes for surface hardening of stainless steel," in *Thermochemical Surface Engineering of Steels*, E. J. Mittemeijer and M. A. J. Somers, Eds., First ed Cambridge: Woodhead Publishing, 2015, pp. 615-632.

[141] H. Hertz and J. P. Lebrun, "Low pressure plasma nitriding of austenitic stainless steels (Nitruration en plasma basse pression d'aciers inoxydables austenitiques)," in *9th International Congress on Heat Treatment and Surface Engineering and 5th French Open International Conference on Heat Treatment*, Nice-Acropolis, 1994, pp. 301-310.
[142] Staballoy AG17® datasheet, accessed at March/2017 from http://www.atimetals.com.
[143] W. McGowan and L. Kerwin, *Can. J. Phys.,* vol. 42, p. 2086, 1964.
[144] G. Cassar, "Improvement in Tribological Characteristics of Titanium Alloys using Duplex Intensified Plasma Treatment," Doctor of Philosophy, Department of Materials Science and Engineering University of Sheffield, 2011.
[145] K. Adachi and I. M. Hutchings, "Wear-mode mapping for the micro-scale abrasion test," *Wear,* vol. 255, pp. 23-29, 2003.
[146] T. H. Lee, E. Shin, C. S. Oh, H. Y. Ha, and S. J. Kim, "Correlation between stacking fault energy and deformation microstructure in high-interstitial-alloyed austenitic steels," *Acta Materialia,* vol. 58, pp. 3173-3186, 2010.
[147] L. Mosecker and A. Saeed-Akbari, "Nitrogen in chromium-manganese stainless steels: a review on the evalution of stacking fault energy by computational thermodynamics," *Science and Technology of Advanced Materials,* vol. 14, p. 033001, 2013.
[148] S. Allain, J. P. Chateau, O. Bouaziz, S. Migot, and N. Guelton, "Correlation between the calculated stacking fault energy and the plasticity mechnisms in Fe-Mn-C alloys," *Material Science and Engineering A,* vol. 387-389, pp. 158-162, 2004.
[149] R. E. Schramm and R. P. Reed, "Stacking fault energies of seven commercial austenitic stainless steels," *Metallurgical Transactions A,* vol. 6A, p. 1345, 1975.
[150] J. Talonen and H. Hanninen, "Formation of shear bands and strain-induced martensite during plastic deformation of metastable austenitic stainless steels," *Acta Materialia* vol. 55, pp. 6108-6118, 2007.
[151] L. Vitos, J. O. Nilsson, and B. Johansson, "Alloying effects on the stacking fault energy in austenitic stainless steels from first-principles theory," *Acta Materialia,* vol. 54, pp. 3821-3826, 2006.
[152] J. Lu, L. Hultman, E. Holmstrom, K. H. Antonsson, M. Grehk, W. Li, L. Vitos, A. Golpayegani, "Stacking fault energies in austenitic stainless steels," *Acta Materialia,* vol. 111, pp. 39-46, 2016.
[153] V. Gavriljuk, Y. Petrov, and B. Shanina, "Effect of nitrogen on the electron structure and stacking fault energy in austenitic steels," *Scripta Materialia,* vol. 55, pp. 537-540, 2006.
[154] K. Morii, H. Mecking, and Y. Nakayama, "Development of shear bands in F.C.C. single crystals," *Acta Metallurgica* vol. 33, pp. 379-386, 1985.
[155] A. Korbel, J. D. Embury, M. Hatherly, P. L. Martin, and H. W. Erbsloh, "Microstructural aspects of strain localization in Al-Mg alloys," *Acta Metallurgica,* vol. 34, pp. 1999-2009, 1986.
[156] P. Wagner, O. Engler, and K. Lucke, "Texture development in Al-3% Mg Influenced by shear bands," *Textures and Microstructures,* vol. 14-18, pp. 927-932, 1991.
[157] Y. Sun and T. Bell, "Sliding wear characteristics of low temperature plasma nitrided 316 austenitic stainless steel," *Wear,* vol. 218, pp. 34-42, 1998.
[158] R. I. Trezona, D. N. Allsopp, and I. M. Hutchings, "Transitions between two-body and three-body abrasive wear: influence of test conditions in the microscale abrasive wear test," *Wear,* vol. 225-229, pp. 205-214, 1999.

[159] M. G. Gee, A. J. Gant, I. M. Hutchings, Y. Kusano, K. Schiffman, K. V. Acker, S. Poulat, Y. Gachon, J. von Stebut, P. Hatto, G. Plint, "Results from an interlaboratory exercise to validate the micro-scale abrasion test," *Wear,* vol. 259, pp. 27-35, 2005.
[160] T. Christiansen and M. A. J. Somers, "Low temperature gaseous nitriding and carburising of stainless steel," *Surface Engineering,* vol. 21, pp. 445-455, 2005.
[161] D. Hoeft, B. A. Latella, and K. T. Short, "Residual stress and cracking in expanded austenite layers," *Journal of Physics: Condensed Matter* vol. 17, pp. 2547-3558, 2005.
[162] M. A. J. Somers and T. Christiansen, "Gaseous processes for low temperature surface hardening of stainless steel," in *Thermochemical Surface Engineering of Steels*, E. J. Mittemeijer and M. A. J. Somers, Eds., First ed Cambridge: Woodhead Publishing, 2015, pp. 581-614.
[163] R. F. A. Jargelius-Pettersson, "Electrochemical investigation of the influence of nitrogen alloying on pitting corrosion of austenitic stainless steels," *Corrosion Science,* vol. 41, pp. 1639-1664, 1999.
[164] X. M. Zhu and M. K. Lei, "Pitting corrosion resistance of high nitrogen f.c.c. phase in plasma source ion nitrided austenitic stainless steel," *Surface and Coatings Technology,* vol. 131, pp. 400-403, 2000.
[165] M. K. Lei and X. M. Zhu, "In vitro corrosion resistance of plasma source ion nitrided austenitic stainless steels," *Biomaterials,* vol. 22, pp. 641-647, 2001.
[166] X. Y. Li and H. Dong, "Effect of annealing on corrosion behaviour of nitrogen S phase in austenitic stainless steel," *Materials Science and Technology,* vol. 19, pp. 1427-1434, 2003.
[167] C. X. Li and T. Bell, "Corrosion properties of active screen plasma nitrided 316 austenitic stainless steel," *Corrosion Science,* vol. 46, pp. 1527-1547, 2004.
[168] A. Fossati, F. Borgioli, E. Galvanetto, and T. Bacci, "Corrosion resistance properties of glow-discharge nitrided AISI 316L austenitic stainless steel in NaCl solutions," *Corrosion Science,* vol. 48, pp. 1513-1527, 2006.
[169] L. C. Gontijo, R. Machado, S. E. Kuri, L. C. Casteletti, and P. A. P. Nascente, "Corrosion resistance of the layers formed on the surface of plasma-nitrided AISI 304L steel," *Thin Solid Films,* vol. 515, pp. 1093-1096, 2006.
[170] J. Buhagiar and H. Dong, "Corrosion properties of S-phase layers formed on medical grade austenitic stainless steel," *Journal of Materials Science: Materials in Medicine,* vol. 23, pp. 271-281, 2012.
[171] P. Perrot, "Iron - Nitrogen - Nickel," in *Landolt-Bornstein - Group IV Physical Chemistry (Numerical Data and Functional Relationships in Science and Technology), Vol. 11D, Part 4*, G. Effenberg and S. Ilyenko, Eds., 1st ed Berlin, Heidelberg: Springer, 2008.
[172] S. Parascandola, W. Moller, and D. L. Williamson, "The nitrogen transport in austenitic stainless steel at moderate temperature," *Applied Physics Letters,* vol. 76, pp. 2194-2196, 2000.
[173] S. Parascandola, R. Gunzel, R. Grotzschel, E. Richter, and W. Moller, "Analysis of deuterium induced nuclear reactions giving criteria for the formation process of expanded austenite " *Nuclear Instruments and Methods in Physics Research B,* vol. 136-138, pp. 1281-1285, 1998.
[174] A. K. Srivastava and K. Das, "Microstructural characterization of Hadfield austenitic manganese steel," *Journal of Material Science* vol. 43, pp. 5654-5658, 2008.
[175] Oliver and Boyd, *Manganese Steel*, 1st ed. Edinburgh: Hadfields Limited, 1956.